



**University of  
Nottingham**

UK | CHINA | MALAYSIA

Department of Civil Engineering

Faculty of Engineering

# Investigation into UHI monitoring with GNSS sensor network

**By**

**Jorge Mendez Astudillo, B.Eng, M.Sc.**

Thesis submitted to the University of Nottingham for

the degree of Doctor of Philosophy

July 2019

# Abstract

Radio frequency (RF) signals are used in Global Navigation Satellite Systems (GNSS) for positioning applications, however, it can also be used to monitor the atmosphere. RF signals can be affected by changes in the atmospheric refractivity index along their propagation path. This change of refractive index along the path of the signal in the troposphere causes a delay to the signal known as the Tropospheric Delay (TD). The TD in the zenith direction (ZTD) has already been used to derive the amount of precipitable water at a given site because the refractive index of air in the atmosphere is proportional to the environmental variables: temperature (T), pressure (P) and water vapour partial pressure (e). However, other environmental variables such as T have not been derived from the ZTD. Thus, this thesis presents a novel algorithm to estimate temperature from GNSS data for monitoring urban heat island intensity (UHII).

An urban heat island (UHI) occurs when an urban area is warmer than its adjacent rural areas. It exacerbates heat waves, leading to increased energy consumption and adverse effects to the environment and to human health. UHIs are monitored using remote sensing techniques, which allow the monitoring of large geographical areas with low time resolution. However, the study of UHIs within a city requires better spatial and temporal resolution. It is also desired to monitor the UHI in real-time. The algorithm presented in this thesis allows UHI monitoring with higher spatial and temporal resolution using a GNSS network.

The algorithm developed in this research has 6 inputs: the thickness of the troposphere, air pressure, water vapor partial pressure and the vertical profile of the refractive index obtained with radiosonde data. Another input is the ZTD obtained from the Precise Point Positioning (PPP) technique. The algorithm solves for temperature at the point where the GNSS data was collected. To validate the output of the algorithm, estimated T at 5 locations at 00:00UTC and 12:00 UTC have been compared to values of T from meteorological data near the GNSS station at the same times. Hourly data for 20 days in year 2017 has been used. An average difference of less than 1 °C has been found for data collected during the summer.

In order to measure the intensity of the UHI, it is necessary to measure the temperature at two locations simultaneously: an urban and an adjacent rural location nearby. The algorithm has been tested and validated using two publicly available datasets containing daily GNSS and meteorological data from Los Angeles, California (LA), USA and Hong Kong Special Administrative Region, China (HK). Also, the algorithm has been tested with an experimentally collected dataset containing hourly GNSS and meteorological data from Ningbo, China (NB). It has been found that an UHI with an intensity of 3.5 °C existed in LA during the winter 2017. The UHI detected in HK during the summer 2017 had an intensity of 4 °C and in NB had an intensity of 2 °C.

# Acknowledgments

This PhD project was carried out at the International Doctoral Innovation Centre (IDIC). Financial support from the Ningbo Education Bureau, Ningbo Science and Technology Bureau, China's Ministry of Science and Technology, and from The University of Nottingham is acknowledged. The work was also partially supported by EPSRC grant No EP/L015463/1. I would like to express my appreciation to my supervisors, Dr. Lawrence Lau, Dr. Yu-Ting Tang and Prof. Terry Moore, for their support and guidance throughout this PhD study.

I would also like to thank all the UNNC staff who helped with the experimental setup, with special thanks to Huib de Ligt, for his time and guidance during this period.

I would further like to acknowledge the help given by Dr. Yiming Quan during data collection and thank all my friends in the PhD community for encouraging me during difficult times. Furthermore, special thanks to my friends Sofia, Aurelio, Alfredo, and Salvador, who helped make this PhD journey more enjoyable.

Finally, I would like to thank my parents and my brother who have supported and loved me throughout my life, and especially during the times of hard work for this PhD.

# Table of contents

ABSTRACT .....	I
ACKNOWLEDGMENTS .....	III
TABLE OF CONTENTS .....	IV
ACRONYMS AND ABBREVIATIONS .....	IX
LIST OF FIGURES.....	XII
LIST OF TABLES.....	XV
CHAPTER 1 INTRODUCTION.....	1
1.1 Introduction to GNSS meteorology.....	1
1.2 Aims and objectives.....	2
1.3 Research limitations and assumptions .....	3
1.4 Contribution to knowledge .....	4
1.5 Thesis outline .....	4
CHAPTER 2 RESEARCH BACKGROUND.....	6
2.1 GNSS systems .....	6
2.1.1 GPS.....	7
2.1.2 GLONASS.....	9
2.1.3 Galileo .....	10
2.1.4 BeiDou Satellite System (BDS) .....	11
2.2 GNSS positioning and navigation applications .....	12
2.3 The PPP concept .....	14
2.3.1 Observation equations .....	15
2.3.2 PPP correction models.....	17
2.3.3 PPP implementation.....	23
2.4 GNSS meteorology applications.....	33
2.5 Motivation for research: UHI monitoring .....	34
2.5.1 UHI definition.....	35
2.5.2 UHI effects .....	36
2.5.3 UHI classifications .....	38
2.5.4 Techniques used for UHI monitoring.....	41
2.5.5 UHI mitigation techniques .....	42
2.5.6 Relevance of UHI monitoring .....	45

2.6	Definitions of Urban and Rural areas.....	45
2.7	The Troposphere .....	47
2.7.1	Troposphere content .....	48
2.7.2	Environmental variables in the troposphere .....	48
2.7.3	Refractivity of the troposphere .....	54
2.8	Tropospheric Delay .....	57
2.8.1	Zenith hydrostatic delay .....	59
2.8.2	Zenith wet delay .....	62
<b>CHAPTER 3 METHODOLOGY AND DATA USED IN THE RESEARCH .....</b>		<b>64</b>
3.1	Data used to calculate the vertical profile of environmental variables in the troposphere.....	65
3.1.1	Data used to calculate the vertical profiles of T ...	65
3.1.2	Data used to find the refractivity profile of the troposphere .....	67
3.2	Evaluation of the input to the algorithm .....	68
3.2.1	Data used to evaluate the quality of PPP ZTD estimation .....	68
3.3	Calculation of the refractivity in the troposphere.....	70
3.3.1	Radiosonde data used to calculate the profile of the refractivity .....	70
3.3.2	Calculation of the height of the troposphere.....	71
3.3.3	Calculation of the amount of water vapor partial pressure .....	75
3.4	Algorithm to estimate temperature from GNSS data .....	76
3.4.1	GNSS data used to test the algorithm.....	76
3.4.2	Surface Meteorological data used to validate the algorithm.....	76
3.5	Development of an algorithm to monitor the UHI intensity from GNSS data.....	77
3.5.1	Site description: Los Angeles (LA) .....	78
3.5.2	Site description: Hong Kong (HK) .....	80
3.5.3	Site description: Ningbo (NB) .....	82
3.5.4	GNSS data used to test the algorithm in LA.....	85
3.5.5	GNSS data used to test the algorithm in HK .....	86
3.5.6	GNSS data used to test the algorithm in NB .....	88

- 3.5.7 Meteorological data used to validate the algorithm in LA 89
- 3.5.8 Meteorological data used to validate the algorithm in HK 90
- 3.5.9 Meteorological data used to validate the algorithm in NB 91

**CHAPTER 4 EVALUATION OF ZTD ESTIMATES DERIVED FROM DIFFERENT PPP IMPLEMENTATIONS..... 92**

- 4.1 Methodology ..... 92
  - where n is the total number of ZTD estimates available. 93
- 4.2 Results ..... 93
- 4.3 Discussion of results..... 102
- 4.4 Conclusions..... 105

**CHAPTER 5 DEVELOPMENT OF AN ALGORITHM TO COMPUTE TEMPERATURES FROM ZTD..... 107**

- 5.1 Calculation of the universal parameters ..... 108
  - 5.1.1 Calculation of water vapour partial pressure (e) 109
  - 5.1.2 Measuring pressure ..... 110
  - 5.1.3 Calculation of the refractivity profile ..... 111
  - 5.1.4 Relation between ZTD and troposphere refractivity 113
  - 5.1.5 Calculation of troposphere height..... 115
  - 5.1.6 Calculation of the local  $N_0$  ..... 115
  - 5.1.7 Calculation of temperature using local refractivity parameters ..... 117
- 5.2 Estimation of ZTD..... 118
- 5.3 Algorithm implementation ..... 120
- 5.4 Results and validation ..... 122
  - 5.4.1 Validation of the algorithm..... 125
- 5.5 Conclusion..... 128

**CHAPTER 6 DEVELOPMENT OF AN ALGORITHM TO MONITOR UHI USING GNSS DATA ..... 130**

- 6.1 Algorithm: Using GNSS data to monitor UHI Intensity.. 130
- 6.2 UHI monitoring in LA ..... 132
  - 6.2.1 Classification of type of GNSS station..... 132
  - 6.2.2 Classification of type of meteorological station.. 133

6.2.3	Pairs of GNSS-Meteorological data .....	133
6.2.4	UHI Monitoring in the Los Angeles metropolitan area: Methodology.....	136
6.3	Implementation of the Algorithm with data from LA. ....	136
6.3.1	Extract the ZTD from RTKLIB output file .....	136
6.3.2	Load local parameters based on latitude.....	138
6.3.3	Process Local $N_0$ .....	139
6.3.4	Calculation of temperature from $N_0_{local}$ .....	140
6.3.5	Calculation of UHI intensity .....	141
6.4	Validation of algorithm .....	144
6.4.1	Validation of the temperature estimated from GNSS data	144
6.4.2	Validation of the estimation of UHI intensity.....	149
6.5	UHI monitoring in HK.....	154
6.5.1	Classification of type of GNSS station.....	155
6.5.2	UHI monitoring in Hong Kong: methodology .....	155
6.6	Implementation if the algorithm with data from HK.....	156
6.6.1	Process Raw data .....	156
6.6.2	Process ZTD .....	156
6.6.3	Load Local Parameters .....	159
6.6.4	Process local $N_0$ .....	159
6.6.5	Calculation of temperatures from $N_0_{local}$ .....	159
6.6.6	Estimation of UHI intensity .....	162
6.7	Validation of algorithm .....	163
6.7.1	UHI intensity from meteorological stations .....	164
6.8	UHI monitoring in Ningbo, China .....	167
6.8.1	UHI monitoring in Ningbo: Methodology.....	168
6.8.2	Process raw data .....	168
6.8.3	Process ZTD .....	169
6.8.4	Load local parameters.....	169
6.8.5	Process local $N_0$ .....	170
6.8.6	Calculation of Temperature from $N_0_{local}$ .....	171
6.8.7	Estimation of the UHI Intensity .....	173
6.9	Validation of output of algorithm .....	174
6.10	Analysis of discrepancies .....	175
6.11	Discussion .....	176

CHAPTER 7 CONCLUSIONS AND FUTURE WORK .....	179
7.1 Summary .....	179
7.2 Conclusions .....	180
7.3 Main contributions of this research .....	182
7.4 Future work .....	183
REFERENCES.....	185
APPENDIX 1 .....	192
APPENDIX 2.....	200
APPENDIX 3.....	203

# Acronyms and Abbreviations

AltBOC	Alternate Binary Offset Carrier
ASL	Above Sea Level
AUHI	Atmospheric Urban Heat Island
BAS	British Antarctic Survey
BDS	BeiDou Navigation Satellite System
BPSK	Binary Phase Shift Keying
CDMA	Code Division Multiple Access
CLU	Canopy Layer Urban Heat Island
DCB	Differential Code Biases
ECA	Environment and Natural Resources Canada
EKF	Extended Kalman Filter
ERP	Earth Rotation Parameters
ESA	European Space Agency
FTP	File Transfer Protocol
GEO	Geosynchronous Earth Orbit
GLONASS	Globalnaya Navigatsionnaya Sputnikovay Sistema
GM	Google Maps
GMF	Global Mapping Function
GNSS	Global Navigation Satellite Systems
GNSS-R	GNSS Receiver Remote Sensing Instrument
GPS	Global Positioning System
HK	Hong Kong

IERS	International Earth Rotation and Reference System Services
IGRA	Integrated Global Radiosonde Archive
IGS	International GNSS Service
ISA	International Standard Atmosphere
ITRF	International Terrestrial Reference Frame
JMA	Japan Meteorological Agency
JPL	Jet Propulsion Laboratory
LA	Los Angeles
LEO	Low Earth Orbit
LRT1	First Lapse Rate Tropopause
LRT2	Second Lapse Rate Tropopause
LS	Least Squares
MBOC	Multiplexed Binary Offset Carrier
MEO	Medium Earth Orbit
NCDC	National Climatic Data Centre
NMF	Neil Mapping Function
NOAA	National Oceanic and Atmospheric Administration
NRCan	Natural Resources Canada
PPP	Precise Point Positioning
PWV	Precipitable Water Vapour
QPSK	Quadrature Phase Shift Keying
RMSE	Root Mean Square Error
RS	Radiosonde
STD	Standard Deviation

SUHI	Surface Urban Heat Island
T2m	2 m above the ground Temperature Sensor
TEC	Total Electron Content
TT&C	Tracking Telemetry and Command
UHI	Urban Heat Island
UHII	Urban Heat Island Intensity
UTC	Universal Coordinated Time
WMO	World Meteorological Organization
ZHD	Zenith Hydrostatic Delay
ZTD	Zenith Tropospheric Delay
ZWD	Zenith Wet Delay

# List of Figures

<b>Figure 2.1.</b> Examples of <b>a)</b> a rural area, and <b>b)</b> an urban area, in LA.	46
<b>Figure 2.2.</b> Annual temperature profiles for selected northern hemisphere stations. ....	51
<b>Figure 2.3.</b> Annual temperature profiles for selected southern hemisphere weather stations.....	52
<b>Figure 2.4.</b> Profiles of temperature, air pressure and relative humidity vs altitude.....	53
<b>Figure 2.5. a)</b> Profiles of refractivity vs geodetic height, at different latitudes. <b>b)</b> Fit to an exponential in order to find the mathematical relation between refractivity and height.....	56
<b>Figure 3.1.</b> Locations of the tropopause and the troposphere, and the troposphere temperature profile. ....	72
<b>Figure 3.2.</b> Height of the troposphere at different latitudes, found with radiosonde data, redrawn from (Feng et al., 2012).....	74
<b>Figure 3.3.</b> LA location map.....	79
<b>Figure 3.4.</b> Los Angeles city map and incorporated areas.....	80
<b>Figure 3.5.</b> HK location, on the southern coast of China.....	81
<b>Figure 3.6.</b> Population density in Hong Kong. Green= low density, yellow= medium density, orange= high density. ....	82
<b>Figure 3.7.</b> Ningbo location.....	83
<b>Figure 3.8.</b> Location of the testing sites in UNNC and a park nearby Source: GoogleMaps.....	84
<b>Figure 3.9.</b> LA metropolitan area map showing locations of the IGS stations used in this study. ....	85
<b>Figure 3.10.</b> HK station locations, from HKGSS (HKGSS, 2019).....	87
<b>Figure 3.11.</b> Panoramic view of the urban-like area inside the University of Nottingham campus, Ningbo, China. ....	89
<b>Figure 3.12.</b> Ningbo rural area where the GNSS and temperature receivers were placed.....	89
<b>Figure 4.1.</b> RMSE, in cm, for day 27, 2016.....	93
<b>Figure 4.2.</b> RMSE, in cm, for day 27, 2017.....	94
<b>Figure 4.3.</b> RMSE, in cm, for day 118. 2016.....	95
<b>Figure 4.4.</b> RMSE, in cm for day 117 2017.....	95
<b>Figure 4.5.</b> RMSE, in cm, for day 209, 2016.....	96
<b>Figure 4.6.</b> RMSE, in cm, for day 208, 2016.....	97
<b>Figure 4.7.</b> RMSE, in cm, for day 300, 2016.....	98
<b>Figure 4.8.</b> RMSE, in cm, for day 299, 2017.....	98
<b>Figure 5.1.</b> Block diagram of the steps used to develop the algorithm used to estimate temperature from ZTD.....	107
<b>Figure 5.2.</b> Example of raw data from a radiosonde sounding.....	108
<b>Figure 5.3.</b> Refractivity of the troposphere, using radiosonde data...	111

<b>Figure 5.4.</b> Refractivity of the troposphere after applying exponential fitting.....	112
<b>Figure 5.5.</b> ZTD is the area under the refractivity profile curve, between the height of the receiver ( $Z_{\text{site}}$ ) and the height of the troposphere ( $Z_{\text{trop}}$ ). .....	114
<b>Figure 5.6.</b> Height of the troposphere estimated using data from station ISTA for year 2017 .....	115
<b>Figure 5.7.</b> Graphical description of the procedure applied to obtain $N_0_{\text{local}}$ . .....	116
<b>Figure 5.8.</b> Block diagram of the algorithm applied to calculate temperature from ZTD. ....	118
<b>Figure 5.9.</b> ZTD for station ISTA, for 2017. The red line represents the value of ZTD estimated with RTKLIB, while the blue line represents fitting of the daily averages. ....	119
<b>Figure 5.10.</b> Daily profile of estimated ZTD, DOY 181, ISTA. ....	120
<b>Figure 5.11.</b> Profiles of the variables input into the algorithm. ....	121
<b>Figure 5.12.</b> Output of the algorithm for 5 stations for 20 days each. 5 days are in spring, 5 days in summer, 5 days in autumn and 5 days in winter. ....	125
<b>Figure 6.1.</b> Block diagram of the UHI monitoring algorithm .....	131
<b>Figure 6.2.</b> Satellite views and maps of GNSS and meteorological stations used to monitor UHI in LA. Taken from <a href="http://www.googlemaps.com">www.googlemaps.com</a> . .....	135
<b>Figure 6.3.</b> Block diagram of the methodology used to monitor the LA metropolitan area UHI. ....	136
<b>Figure 6.4.</b> ZTD estimated with RTKLIB for 4 stations, 8 days of the year. .....	138
<b>Figure 6.5.</b> 2017 profiles for the universal parameters input to the algorithm.....	139
<b>Figure 6.6.</b> Profile of the local $N_0$ required to calculate temperature. ....	140
<b>Figure 6.7.</b> Output of the algorithm: estimated temperature from GNSS data from stations in LA metropolitan area. ....	141
<b>Figure 6.8.</b> UHII at station LBCH in Long Beach, California. 8 days distributed in the four seasons are plotted. ....	142
<b>Figure 6.9.</b> UHII at station BILL in Redondo Beach, California. 8 days distributed in the four seasons are plotted.....	143
<b>Figure 6.10.</b> UHII at station CIT1 in Pasadena, California. 8 days distributed in the four seasons are plotted.....	144
<b>Figure 6.11.</b> Difference of temperature obtained from the algorithm and from weather station data for the station in Long Beach, during 8 days of the year. ....	146
<b>Figure 6.12.</b> Difference of temperature obtained from the algorithm and from weather station data for the station in Pasadena, during 8 days of the year. ....	146
<b>Figure 6.13.</b> Difference of temperature obtained from the algorithm and from weather station data for the station in Redondo Beach, during 8 days of the year. ....	147

<b>Figure 6.14.</b> Difference of temperature obtained from the algorithm and from weather station data for the station in Temecula, during 8 days of the year. ....	147
<b>Figure 6.15.</b> UHI intensity of LA in UTC time. LA local time is UTC-8. Taken from (Ramamurthy & Sangobanwo, 2016). ....	150
<b>Figure 6.16.</b> Intensity of the UHI between three urban and one rural station during DOY 90 and 91 2017. ....	150
<b>Figure 6.17.</b> Intensity of the UHI between three urban and one rural station during DOY 180 and 181 2017. ....	151
<b>Figure 6.18.</b> Intensity of the UHI between three urban and one rural station during DOY 270 and 271 2017. ....	151
<b>Figure 6.19.</b> Intensity of the UHI between three urban and one rural station during DOY 360 and 361 2017. ....	151
<b>Figure 6.20.</b> Block diagram of the methodology followed to monitor the HK UHI. ....	156
<b>Figure 6.21.</b> ZTD of stations in HK during the spring in 2017. ....	157
<b>Figure 6.22.</b> ZTD of stations in HK during the summer 2017. ....	157
<b>Figure 6.23.</b> ZTD of stations in HK during the autumn in 2017. ....	158
<b>Figure 6.24.</b> ZTD of stations in HK during the winter in 2017. ....	158
<b>Figure 6.25.</b> Temperatures during the spring, 4 stations in HK. ....	160
<b>Figure 6.26.</b> Temperatures during the summer, 4 stations in HK. ....	160
<b>Figure 6.27.</b> Temperatures during the autumn, 4 stations in HK. ....	161
<b>Figure 6.28.</b> Temperatures during the winter, 4 stations in HK. ....	161
<b>Figure 6.29.</b> UHI intensity from GNSS data stations in HK. ....	163
<b>Figure 6.30.</b> Profile of the UHI intensity in HK, taken from (Wai Siu & Hart, 2013) ....	164
<b>Figure 6.31.</b> Profile obtained with meteorological data of UHI during 4 seasons. ....	165
<b>Figure 6.32.</b> ZTD estimated from raw data collected in the park and at UNNC campus. ....	169
<b>Figure 6.33.</b> Profile of local $N_0$ obtained from ZTD data and universal parameters. ....	171
<b>Figure 6.34.</b> Profile of $e$ , for 2017 ....	172
<b>Figure 6.35.</b> Temperatures estimated from ZTD at two locations: a park in Ningbo and at the UNNC campus. ....	173
<b>Figure 6.36.</b> Temperatures calculated with the algorithm and with GNSS data ( $PARK_{ztd}$ and $UNNC_{ztd}$ ), and temperatures measured with a temperature sensor ( $PARK_{met}$ and $UNNC_{met}$ ). ....	174

# List of Tables

<b>Table 2.1.</b> GPS signal characteristics (Hofmann-Wellenhof et al., 2008). .....	9
<b>Table 2.2.</b> GLONASS signal characteristics (Hofmann-Wellenhof et al., 2008). .....	10
<b>Table 2.3.</b> Signal parameters for GNSS.....	12
<b>Table 2.4.</b> Capability comparisons for PPP implementation (Mendez Astudillo et al., 2018). .....	32
<b>Table 2.5.</b> UHI classification according to target medium. ....	39
<b>Table 2.6.</b> Summary of mitigation techniques. ....	43
<b>Table 2.7.</b> Values for the empirically determined refractivity constants (as K / hPa). .....	55
<b>Table 3.1.</b> Meteorological stations used to study temperature at different latitudes. .....	66
<b>Table 3.2.</b> Radiosonde stations used to compute troposphere refractivity profiles. .....	67
<b>Table 3.3.</b> Summary of the IGS stations used to evaluate the quality of ZTD estimation. ....	69
<b>Table 3.4.</b> Selected radiosondes and their locations.....	70
<b>Table 3.5.</b> Details of IGS ZTD data used in this thesis. The code, latitude, longitude and height were provided by the IGS.....	76
<b>Table 3.6</b> Details of the meteorological stations selected for algorithm validation. ....	77
<b>Table 3.7.</b> Summary of Los Angeles metropolitan area IGS station locations. The images used for classification of the type of area are shown in Appendix 1. ....	86
<b>Table 3.8.</b> Location of GNSS stations in Hong Kong. Classification of the stations shown in Appendix 3. ....	88
<b>Table 3.9.</b> Weather stations in LA metropolitan area used for validation of the algorithm. Classification done using images in appendix 2. ....	90
<b>Table 3.10.</b> HK meteorological stations used for validation.....	91
<b>Table 3.11.</b> Location of temperature and GNSS sensors in Ningbo ....	91
<b>Table 4.1.</b> RMSE values (in cm), by groups, for Jan 27 2016 and 2017. .....	99
<b>Table 4.2.</b> RMSE values (in cm), by groups, for April 27, 2016 and 2017. .....	100
<b>Table 4.3.</b> RMSE values (in cm), by groups, for July 27, 2016 and 2017. .....	100
<b>Table 4.4.</b> RMSE values (in cm), by groups, for October 26, 2016 and 2017. ....	100
<b>Table 4.5.</b> RMSE values (in cm), calculated for each software, and using all data.....	101
<b>Table 5.1.</b> Structure of the vector containing water vapour partial pressure data.....	110

<b>Table 5.2.</b> Structure of the vector containing pressure data.....	110
<b>Table 5.3.</b> Structure of ZTD data input in the algorithm.....	118
<b>Table 5.4.</b> Average of the differences at 00:00 UTC in °C.....	126
<b>Table 5.5.</b> Average differences at 12:00 UTC in °C .....	126
<b>Table 5.6.</b> Average differences using all data in °C.....	127
<b>Table 5.7.</b> RMSE in °C of the average differences using all data.....	127
<b>Table 6.1.</b> GNSS stations paired with meteorological stations, and their respective locations. ....	133
<b>Table 6.2.</b> Mean of the differences in °C between temperature estimated with the algorithm and measured with T2m sensors in a weather station. ....	148
<b>Table 6.3.</b> RMSE in °C of the differences between temperature estimated with the algorithm and measured with T2m sensors in a weather station. ....	148
<b>Table 6.4.</b> Average of the differences in °C for UHI intensity in Long Beach, Redondo Beach and Pasadena.....	152
<b>Table 6.5.</b> RMS value in °C for the differences of UHI intensity in Long Beach, Redondo Beach and Pasadena.....	152
<b>Table 6.6.</b> Average of the differences of UHI intensity in °C, for stations in Long Beach, Redondo Beach and Pasadena at 04:00 and 16:00 local time.....	153
<b>Table 6.7.</b> Average of the differences in °C of all available data at 04:00 and 16:00. ....	154
<b>Table 6.8.</b> Average and RMSE of the differences of UHII_GNSS and UHII_MET. In °C.....	166
<b>Table 6.9.</b> Average and RMSE of the seasonal differences UHII_GNS-UHII_MET in °C.....	166
<b>Table 6.10.</b> Average in °C of the differences defined in Equation 6.6 .....	167

# CHAPTER 1

## INTRODUCTION

### 1.1 Introduction to GNSS meteorology

Global Navigation Satellite Systems (GNSS) are constellations of satellites (such as GPS, GLONASS, BeiDou and Galileo) used for positioning applications using radio frequency signals. As the radio frequency signals propagate through the atmosphere, they are affected by changes to the refractivity index of the air in the atmosphere. Therefore, GNSS signals can also be used to monitor the atmosphere.

The troposphere is the layer of the atmosphere closest to the Earth's surface, and it affects the propagating signal in a manner which is translated into a delay in the measurement—and this is known as the tropospheric delay (TD). The TD in the zenith direction (ZTD) is a by-product of the Precise Point Positioning technique (PPP). PPP uses estimators such as the Extended Kalman Filter (EKF) or Least Squares (LS) to estimate the ZTD, the position of the receiver and other parameters. The ZTD is defined as the integral, in the path of the signal, of the refractivity of the troposphere. The refractivity of the troposphere is described in terms of the environmental parameters of temperature (T), pressure (P), and water vapour partial pressure (e). It is possible to

deduce values for the environmental variables using known data from two of the environmental variables. For example, the ZTD has been used to estimate the amount of precipitable water at the location of the receiver. However, pressure and temperature have not been monitored using GNSS data. An algorithm developed to measure temperature from GNSS data which is applied to UHI monitoring is presented in this thesis. The algorithm is used to monitor the Urban Heat Island effect in three metropolitan areas: Los Angeles, California, USA, the Special Administrative Region of Hong Kong, and Ningbo, China.

The use of GNSS data to monitor the atmosphere has the advantage of availability of data. GNSS receivers and networks are widely available throughout the world. In contrast, radiosonde data, which is typically used to monitor the atmosphere, is not widely available. In terms of availability of data, only two radiosonde soundings a day or less are available while GNSS data can be available every second. Therefore, GNSS data can be used for real-time or near real-time environmental monitoring.

## **1.2 Aims and objectives**

In this thesis, a novel algorithm is presented for monitoring UHI intensity using GNSS data. The following objectives have been established:

- Find the profiles of the environmental variables affecting GNSS signals as they propagate through the atmosphere (see Chapter 4).
- Find the refractivity profiles of the troposphere, using radiosonde data (see Chapter 5).

- Develop and test an algorithm to estimate temperature using GNSS data (see Chapter 5).
- Develop and test an algorithm to monitor the UHI intensity using GNSS data for selected cities (see Chapter 6).

### **1.3 Research limitations and assumptions**

- The algorithm developed is valid only when dual-frequency GNSS data is used in the algorithm; therefore, when applying the PPP technique, the ionosphere effect has been mostly eliminated.
- The research has been limited by radiosonde data availability. Missing radiosonde data is compensated for through mathematical fitting of the available data to an exponential function.
- The input of the algorithm requires the water vapor partial pressure at a given location. Since it is not a measurable variable it needs to be estimated using mathematical models. The highly variable profile of the water vapor partial pressure is built with available radiosonde data. Therefore, its highly variability is not clearly detected.
- It is assumed that the pressure at the location is obtained from direct measurements from a barometer or from the radiosonde.
- It is assumed that the temperatures measured and estimated are from a height of 2 m above the ground.

## **1.4 Contribution to knowledge**

- 1 Surface level refractivity called in this thesis  $N_0$  and the ratio of change of the refractivity profile through the troposphere called in this thesis  $N_h$ , have been calculated with radiosonde data.
- 2 The yearly profile of the refractivity for latitudes multiples of  $5^\circ$  have been constructed.
- 3 An evaluation of the quality of the ZTD estimation from different PPP implementations has been presented.
- 4 A novel technique to estimate the first Lapse Rate Tropopause from the ZTD has been described.
- 5 A novel algorithm to estimate temperature from GNSS data has been presented, tested and validated.
- 6 A novel algorithm to monitor the UHI using GNSS data has been presented, tested and validated.

## **1.5 Thesis outline**

The thesis is divided in 7 chapters. Chapter 2 covers the basics of the three topics in this thesis: GNSS, the PPP technique, and UHIs. Also, in Chapter 2, a literature review on the use of GNSS for positioning and the application of GNSS signals for weather monitoring has been included. Then, a review of the PPP technique including the equations and the estimators used has been included. In the last part of Chapter 2, the concept of UHIs has been explained and topics related to the UHI are discussed, including monitoring techniques, the relevance of UHI monitoring, negative effects of UHI, and mitigation techniques.

In Chapter 3, “the methodology and data used in the thesis are described”. In Chapter 4, “the following topics are covered: characteristics of the troposphere, the effect of the refractivity index of air on radio frequency signals, and the estimation of tropospheric delay”. Also, in Chapter 4, tropospheric delay estimates obtained using different software implementations of PPP have been compared and evaluated.

The novel algorithm developed to estimate temperature from ZTD is described in detail in Chapter 5. The algorithm has been validated by comparing its results with temperatures obtained from meteorological stations.

Chapter 6 describes in full detail an algorithm developed to monitor UHIs using GNSS data and the algorithm presented in Chapter 4. Data from Los Angeles (LA), Hong Kong (HK), and Ningbo (NB) are used to test the algorithm. Validation of the algorithm has been done using data from weather stations co-located with the GNSS stations.

In Chapter 7, “a summary of the work described in this thesis is presented”. Also, conclusions drawn from the work described in this thesis are presented. Furthermore, a proposal for future implementation of GNSS-based UHI monitoring using a crowdsourcing system is also presented.

# CHAPTER 2

## RESEARCH BACKGROUND

The three topics covered in this chapter are: GNSS used for monitoring the atmosphere, the PPP technique and UHIs. The first section in this chapter covers the description of all GNSS systems and details of their signals. Then, the application of GNSS for positioning is introduced. At this point, the PPP technique is explained in detail because this is the technique used in this research to estimate the ZTD. Then, the application of GNSS signals to atmospheric monitoring is explained in detail. The final two parts of the chapter discuss the UHI effect in general. Also, it discusses the negative impacts of UHI on energy consumption, air and water quality, on human health (Peng et al., 2012). The last part of Chapter 2 discusses the relevance of monitoring UHI and mitigation techniques of UHI. Definitions of urban and rural areas, as used in this thesis, are also included in this chapter.

### **2.1 GNSS systems**

The GNSS is formed by several constellations of satellites transmitting electromagnetic signals to receivers around the earth, and is used mainly for finding the positions of the receivers (Hoffmann et al., 2012). The GNSS constellations described in this chapter are the American Global

Positioning System (GPS), the Russian GLONASS, the European Galileo and the Chinese BeiDou (BDS).

### **2.1.1 GPS**

Development of the GPS was initiated in 1973, by the Joint Program Office directed by the US Department of Defense, with the goal to establish, develop, test, acquire, and deploy a space-borne positioning system (Hoffmann et al., 2012). It was originally designed to serve military purposes; however, the GPS became open to civilians in 1983, and has been used ever since in many devices such as smartphones and car navigation systems.

The GPS system is structured in three segments: the space segment, the control segment and the user segment. The space segment consists of 24 operational satellites placed in six nearly circular orbits, inclined to  $55^\circ$ , at an altitude of approximately 20,200 km above the earth, and an orbit period of approximately 12 sidereal hours. In 1995, its full operability was declared. With full constellation (24 operational satellites), there are four to eight simultaneously visible satellites above  $15^\circ$ , on a global level. Visible satellites above  $15^\circ$  reduce multipath and provide signals strong enough to estimate positioning. Lowering the elevation mask to  $5^\circ$  increases the number of visible satellites to up to 12. Until 2016, there were 31 satellites in orbit (including operational and non-operational satellites), 12 Block-IIR, 7 Block IIR-M, and 12 Block-IIF satellites. 8 satellites from Block IIA are in reserve, while one from Block IIR-M has been deemed unhealthy (National Coordination Office for Space-Based Positioning, 2019)

The control segment of the GPS includes a master control station, monitoring stations and ground antennae. The master control station is in Colorado Springs, Colorado, USA, and is responsible for satellite control and system operation. Five globally distributed monitoring stations continuously measure pseudoranges (refer to section 2.2) to all visible satellites, and forward data to the master control station for calculation of satellite orbit and clock parameters. Calculated ephemerides and clock information are forwarded to ground antennae and uploaded to each GPS satellite three times per day. This way, the navigation message is created.

The fundamental frequency of the GPS signal is 10.23 MHz. Two carrier waves, L1 and L2, are generated by multiplying the fundamental frequency by 154 and 120 respectively. This yields a frequency of 1575.42 MHz and a wavelength of approximately 19 cm, for carrier L1, and a frequency of 1227.60 MHz and a wavelength of approximately 24 cm, for carrier L2. Satellites launched in 2010 (Block-IIIF) include the carrier frequency L5, which has a frequency of 1176 MHz and a wavelength of approximately 25 cm.

The Code Division Multiple Access (CDMA) principle is used. Three ranging codes are modulated on two carrier frequencies, a Coarse/Acquisition code (C/A) and a Precise (P1) code on carrier L1, and a Precise (P2) code on carrier L2. The main characteristics of GPS signals are summarized in Table 2.1.

**Table 2.1.** GPS signal characteristics (Hofmann-Wellenhof et al., 2008).

Carrier	Factor (*f <sub>0</sub> )	Frequency [MHZ]	Wavelength [cm]	PRN codes
L1	154	1575.42	19.0	C/A
				P
				M
				L1C
L2	120	1227.60	24.4	L2C
				P
				M
L5	115	1176.45	25.5	L5C
				L5I
				L5Q

### 2.1.2 GLONASS

The Russian navigation satellite system (GLObalnaya NAVigatsionnaya Sputnikovaya Sistema) is a response to the American navigation system: GPS. Because, similar to GPS, GLONASS was born as a military system and was opened for civilian use in 1995. Full constellation was reached in 1996 (24 satellites) but due to funding issues, in 2001 only 6 satellites were in operation. In the year 2018, 24 satellites were operational.

The GLONASS space segment consists of 24 satellites which are placed in three circular orbital planes with an inclination of 64.8°, and a revolution period of 11 h 15 min 44 s. The satellites orbit 19,100 km above the earth's surface. At least five satellites are simultaneously visible from 99% of the earth's surface if the full constellation is fulfilled. The ground segment, located in Russia, consists of a System Control Centre located at the Krasnoznamensk Space Centre, the centre for GLONASS system time synchronization at Schlekovo, four Tracking Telemetry and Command (TT&C) stations, and five tracking stations.

GLONASS transmits signals on two carrier frequencies, on which the navigation message on two ranging codes are modulated: the standard-accuracy signal (C/A) on carrier G1, and the high-accuracy signal (P) on both carriers. GLONASS uses the Frequency Division Multiple Access (FDMA) channel access method. Carrier frequencies are defined as follows, where k indicates the frequency channel:

$$G1 = 1602.0 + 0.5625k \text{ [MHz]}$$

$$G2 = 1246.0 + 0.4375k \text{ [MHz]}$$

It is expected that the new generation GLONASS-K satellites will also include a signal on a third carrier (Hoffmann et al., 2012). The characteristics of the GLONASS signals are summarized in Table 2.2.

**Table 2.2.** GLONASS signal characteristics (Hofmann-Wellenhof et al., 2008).

Carrier	Frequency [MHz]	Increment [MHz]	Wavelength [cm]	PRN codes
G1	1602	0.56	18.7	C/A
				P
G2	1246	0.43	24.1	C/A
				P
G3	1204	0.42	24.9	C/A2
				P2

### 2.1.3 Galileo

The European system, Galileo, is a joint initiative of the European Commission and the European Space Agency (ESA). It is a civil navigation satellite system, in which the European Union is responsible for legal and political issues, while the ESA manages technical parts of

the program. The system was created by firstly augmenting the existing GNSS system, resulting in the geostationary navigation overlay system EGNOS, and then the global navigation system for civil use was deployed.

In the year 2018, there are 22 satellites in orbit, and they are expected to be fully operational by 2020 (EGSA, 2019). The satellites are in three orbital planes, inclined by  $56^\circ$  and orbiting 29,600 km above the earth, with a revolution period of 14 h 4 min 45 s. Galileo guarantees six visible satellites at anytime, anywhere on earth, with an elevation mask of  $10^\circ$ . The space segment is supported by ground infrastructure composed of two ground centres, five TT&C stations, nine C-band mission uplink stations and 20–25 planned Galileo sensor stations, distributed worldwide.

Galileo signals are based on the fundamental frequency of  $f_0 = 10.23$  MHz, and cover five frequency bands: E1, E6, E5, E5a and E5b. Each satellite will broadcast ten different navigation signals, making it possible for Galileo to offer open access (OS), safety-of-life (SoL), commercial (CS), search-and-rescue (SAR) and public regulated services (PRS). Signals E1 and E5a coincide with GPS signals, while E5b overlays with GLONASS G3. This overlay characteristic was chosen to increase the interoperability with those systems. The implemented modulation is Binary Offset Carrier, of rate (1, 1) (BOC (1,1)).

#### **2.1.4 BeiDou Satellite System (BDS)**

This is a GNSS developed by China. As of 2018 there were 23 satellites in orbit, and the complete constellation of 35 satellites is expected to be

fully operative by 2020. Satellites are in Geosynchronous Earth Orbit (GEO), Medium Earth Orbit (MEO) and Inclined Geosynchronous Satellites Orbit (IGSO). The GEO orbit has an altitude of 35,786 km, the IGSO orbit has an altitude of 35,786 km and an inclination of 55° to the equator, and the MEO orbit has an altitude of 21,527 km and an inclination of 55° to the equator. The modulation technique used is QPSK. (System, 2019). Signal characteristics for all GNSS systems are summarized in Table 2.3.

**Table 2.3.** Signal parameters for GNSS

System	Frequency band	Carrier Frequency [MHz]	Modulation
GPS	L1 C/A	1575.42	BPSK
	L1 C	1575.42	MBOC
	L2 C	1227.60	BSPK
	L5	1176.45	QPSK
GLONASS	L1	1598.06-1605.37	BPSK
	L2	1242.93-1248.62	
Galileo	E1	1575.42	CBOC
	E5a	1176.45	altBOC
	E5b	1207.14	
	E6	1278.75	
BDS	B1	1561.09	QPSK
	B2	1207.14	

## 2.2 GNSS positioning and navigation applications

GNSS signals are used for position determination, velocity determination and altitude determination (Hoffmann et al., 2012). However, other applications, such as monitoring the atmosphere (Yu et al., 2014) or the

environment (Awange, 2012), have been researched and will be explained later in this chapter.

Positioning a receiver with GNSS signals is possible because the satellites transmit an electromagnetic signal to the earth where the receiver is located. The basic parameter observable by the receiver is the travelling time of the signal. A measurement called “pseudorange” is derived (Sanz Subirana et al., 2013b) from the travelling time of the signal. The pseudorange is the apparent range between the satellite and the receiver. It is defined as shown in equation 2.1 (Hofmann-Wellenhof et al., 2008), in which  $c$  is the speed of light in a vacuum.  $t_r(T_2)$  is the time of signal reception, measured in the time scale given by the clock of receiver  $r$ ,  $t^s(T_1)$  is the time of signal transmission, measured in the time scale given by the satellite clocks.

$$R_p(t) = c[t_r(T_2) - t^s(T_1)] \quad (2.1)$$

Considering the geometric range between a satellite and receiver, the clock synchronism error and other terms due to signal propagation through the atmosphere, relativistic effects, instrumental delays, multipath and receiver noise, equation (2.1) can be re-written as shown in (2.2) (Hofmann-Wellenhof et al., 2008), where  $\rho$  is the geometric range (defined by a component in x, y and z axis) between satellite and receiver,  $dt_r$  and  $dt^s$  are the receiver and satellite clock offsets respectively.  $T$  is the tropospheric delay,  $Iono$  is the ionospheric delay,  $K_{p,r}$  and  $K_p^s$  are the receiver and satellite instrumental delays respectively, which are

dependent on the code and frequency.  $\mathcal{M}_p$  represents the effect of multipath and  $\varepsilon_p$  is the receiver noise.

$$R_p = \rho + c(dt_r - dt^s) + T + Iono + K_{p,r} - K_p^s + \mathcal{M}_p + \varepsilon_p \quad (2.2)$$

Similarly, the carrier phase can also be used to obtain a pseudorange, which is defined as shown in (2.3) (Hofmann-Wellenhof et al., 2008), with the same nomenclature as the code pseudorange (equation 2.2) and  $\lambda_L \omega$  is the wind-up due to the circular polarization of the electromagnetic signal and the integer ambiguity  $N_L$ .  $k_{L,r}$  and  $k_L^s$  are frequency-dependent, carrier phase instrumental delays associated with the receiver and satellite, respectively, while  $m_L$  represents the carrier phase multipath and  $\varepsilon_L$  represents noise.

$$\Phi_L = \rho + c(dt_r - dt^s) + T - Iono + k_{L,r} - k_L^s + \lambda_L N_L + \lambda_L \omega + m_L + \varepsilon_L \quad (2.3)$$

The observables are used in different models for positioning, such as Point Positioning, Differential Positioning, Relative Positioning and PPP (Hofmann-Wellenhof et al., 2008).

### 2.3 The PPP concept

The PPP technique was pioneered as a positioning technique in 1997 by Zumberge et al. (1997), who implemented their method into the GIPSY/OASIS-II GPS processing software developed by the Jet Propulsion Laboratory (JPL). International GNSS service orbit products were used in PPP to achieve a cm-precise level of positioning (Heroux & Kouba, 2001). Since that work, other groups, such as Bisnath & Langley

(2003) and Gao & Shen (2002) developed new algorithms with improved results. In 2008, Tolman (2008) introduced the Kalman Filter into the PPP algorithm. The filter state includes receiver position, clock bias, a residual zenith wet tropospheric delay and a phase bias for each satellite. According to Tolman (2008), adaptation of the filter to real-time operation and single frequency data processing is straight forward. The Kalman filter has been implemented in PPP software such as RTKLib©.

PPP is a positioning technique that uses undifferenced single- or dual-frequency pseudorange and carrier phase observations, from a single GPS receiver (Zumberge et al., 1997). PPP also requires precise orbit and clock correction products, which are provided by several sources, such as the International GNSS service (IGS) (Zumberge et al., 1997), the Jet Propulsion Lab or Natural Resources Canada (NRCan)(Gao, 2006), or by regional reference station providers. The advantages of PPP are the achievement of cm / mm positioning accuracy and that it only requires one GNSS receiver, reducing its implementation cost (Mendez Astudillo et al., 2018).

### 2.3.1 Observation equations

The un-differenced observation equations for code  $P_{R,i}^S$  and carrier phase  $L_{R,i}^S$  measurements, in metric units, are (Zumberge et al., 1997):

$$P_{R,i}^S = \left[ \vec{r}_R(t_R) - \vec{r}^S(t_R - \tau_R^S) \right] + c\Delta t_R - c\Delta t^S \quad (2.4)$$

$$L_{R,i}^S = \left[ \vec{r}_R(t_R) - \vec{r}^S(t_R - \tau_R^S) \right] + c\Delta t_R - c\Delta t^S + \lambda_i N_{R,i}^S \quad (2.5)$$

In equations (2.4) and (2.5),  $\vec{r}_R$  is the station geocentric vector at the time of signal reception  $t_R$ ,  $\vec{r}^S$  is the geocentric vector to the satellite at the time of signal emission  $t^S = t_R - \tau_R^S$ , with  $\tau_R^S$  being the signal travel time between satellite S and receiver R. Symbol  $i$  indicates the carrier frequency.

The offsets caused by satellite and receiver clocks are shown by  $c\Delta t^S$  and  $c\Delta t_R$ , respectively. The carrier phase measurements,  $L_{R,i}^S$ , have to account for the ambiguity factor  $\lambda_i N_{R,i}^S$  with  $\lambda_i$  being the wavelength of the respective carrier  $i$ , and  $N_{R,i}^S$  the number of full carrier cycles between satellite and receiver.

In addition to clock errors, there are additional corrections that need to be applied to pseudorange and carrier phase observations. To achieve the ultimate PPP accuracy, corrections to error effects up to the mm-level are needed. These effects can be grouped into satellite-specific corrections, receiver-specific corrections, site-specific effects and signal propagation errors.

In order to correct all the effects, observation equations 2.4 and 2.5 will adopt the expanded forms represented by (2.6) and (2.7) (Heroux & Kouba, 2001).

$$P_i = \rho + c\Delta t_R - c\Delta t^S + \Delta\rho_{iono,i} + \Delta\rho_{tropo} + \Delta\rho_{rel} + \Delta\rho_{mp,i} + c\beta_R \quad (2.6)$$

$$+ c\beta^S + \epsilon_{P,i}$$

$$L_i = \rho + c\Delta t_R - c\Delta t^S - \Delta\rho_{iono,i} + \Delta\rho_{tropo} + \Delta\rho_{rel} + \Delta\rho_{mp,i} + \lambda_i\omega \quad (2.7)$$

$$+ \Delta\rho_{pcv,i} + \lambda_i\alpha_{R,i} + \lambda_i\alpha_i^S + \lambda_i N_i + \epsilon_{L,i}$$

In (2.6) and (2.7):

- $P_i$  and  $L_i$  are the code and phase measurements respectively, with  $i$  noting the frequency
- $\rho$  is the geometric distance between satellite and receiver
- $c\Delta t_R$  and  $c\Delta t^S$  are receiver and satellite clock corrections multiplied by the speed of light  $c$
- $\Delta\rho_{iono,i}$  is the ionospheric delay (frequency dependent)
- $\Delta\rho_{tropo}$  is the correction due to the tropospheric refraction
- $\Delta\rho_{rel}$  is the correction due to relativistic effects
- $\Delta\rho_{mp,i}$  is the delay due to the multipath (frequency dependent)
- $\beta_R$  and  $\beta^S$  are respective code biases for the receiver and the satellite
- $\lambda_i\alpha_{R,i}$  and  $\lambda_i\alpha_i^S$  are phase biased for the receiver and the satellite respectively, multiplied by the respective wavelength  $\lambda_i$
- $\omega$  is a phase wind-up correction
- $\Delta\rho_{pcv,i}$  is a frequency-dependent delay due to phase centre variation
- $N_i$  is the ambiguity for the respective frequency  $i$
- $\epsilon_{P,i}$  and  $\epsilon_{L,i}$  are the remaining un-modelled errors and white noise for the code and phase measurements.

### 2.3.2 PPP correction models

PPP requires the following corrections models: Satellites antenna offsets, phase wind-up correction, site displacement effects, solid earth tides, ocean loading (stations near the ocean), earth rotation parameters,

system biases and multipath. The correction models needed in PPP are explained next.

### **2.3.2.1 Satellites antenna offsets**

Separation of the GPS satellite centre of mass and the phase centre of its antenna requires a satellite-specific correction. Measurements are made to the antenna phase centres. However, since the force models used for orbit modelling refer to the satellite centre of mass, the IGS GPS precise satellite coordinates and clock products will refer to a satellite's centre of mass. In contrast, the orbits broadcasted in the GPS navigation message, refer to satellite antenna phase centres. Knowing satellite phase centre offsets, one must also monitor the orientation of the offset vector in space while the satellite orbits Earth. The IGS conventional phase centres are offsets both in the body z coordinate direction, towards Earth, and in the body x coordinate direction, which is on the plane containing the sun.

### **2.3.2.2 Phase wind-up correction**

In GPS, the observed carrier phase depends on the mutual orientation of the satellite and receiver antennae, as the GPS satellites transmit right circularly polarized (RCP) radio waves. Therefore, a rotation of either receiver or satellite antenna around its bore axis will change the carrier phase up to one cycle, which corresponds to one complete revolution of the antenna. This effect is called Phase Wind-Up (Wu et al., 1993). The rotation can happen because satellites undergo slow rotations as their solar panels are being oriented towards the Sun, and this in turn leads to

changes in the station–satellite geometry. The effect of this rotation needs to be corrected to increase precision.

Phase wind-up can be derived using formulae by Wu, J. *et al* (1993), expressed as equations (2.8) and (2.9).

$$\delta\phi = \text{sign}(\xi)\cos^{-1}\left(\frac{\vec{D}' \cdot \vec{D}}{(|\vec{D}'||\vec{D}|)}\right) \quad (2.8)$$

In (2.8),  $\xi = \vec{k} \cdot (\vec{D}' \times \vec{D})$ ,  $\vec{k}$  is the satellite-to-receiver unit vector, and  $\vec{D}'$ ,  $\vec{D}$  represent the effective dipole vectors of the satellite and the receiver, computed from the unit vectors of the satellite's  $(\vec{x}', \vec{y}', \vec{z}')$  and the receiver's  $(\vec{x}, \vec{y}, \vec{z})$  body coordinate systems. The expressions for the effective dipole vectors are as shown in (2.9).

$$\begin{aligned} \vec{D}' &= \vec{x}' - \vec{k}(\vec{k} \cdot \vec{x}') - \vec{k} \times \vec{y}' \\ \vec{D} &= \vec{x} - \vec{k}(\vec{k} \cdot \vec{x}) - \vec{k} \times \vec{y} \end{aligned} \quad (2.9)$$

### 2.3.2.3 Site displacement effects

A station undergoes real or apparent periodic movements, amounting to a few tens of cm, which are not included in its International Terrestrial Reference Frame (ITRF) position. These movements need to be modelled by adding a site displacement correction to the conventional ITRF coordinates. The vector of receiver coordinates consistent with the current realization of the ITRF includes corrections for solid earth tides,  $\delta\vec{X}_{SET}$ , rotational deformation due to polar motion,  $\delta\vec{X}_{PM}$ , and ocean loading,  $\delta\vec{X}_{OL}$ , as shown in equation (2.10)

$$\vec{X}_{R,ITRF} = \vec{X}_R + \delta\vec{X}_{SET} + \delta\vec{X}_{PM} + \delta\vec{X}_{OL} \quad (2.10)$$

This equation was taken from the International Earth Rotation and Reference System Services (IERS) Convention, 2003. For more details, refer to McCarthy & Petit (2004).

#### **2.3.2.4 Solid earth tides**

The solid earth tides effect occurs due to permanent, periodic (semi-diurnal and diurnal) and long-periodic movements of a station, originating mainly from the gravitational forces of the moon and the sun. The periodic vertical and horizontal site displacements, caused by tides of spherical harmonic degree and order ( $n m$ ), are characterized by the Love number,  $h_{nm}$ , and the Shida number,  $l_{nm}$ , (radial and transverse components respectively). The effective values of these numbers weakly depend on station latitude and tidal frequency (Wahr, 1981), and need to be taken into account when an accuracy of 1 mm is desired in determining station positions.

According to McCarthy & Petit (2004) the site displacement vector of the station due to the tides is calculated in two steps. In the first step we consider degree 2 and degree 3 tides. In the second step we introduce the frequency dependences of Love and Shida numbers. The total displacement is the sum of the displacements induced by the moon and the sun. Nominal values for the Love and Shida numbers, are 0.6078 and 0.0847, respectively.

#### **2.3.2.5 Ocean loading**

Ocean loading is similar to solid Earth tides, as it also has predominantly diurnal and semi-diurnal periodicity but it is caused by the load of the ocean tides. Ocean loading is induced by the temporal variation of the

ocean mass distribution and is dominated by diurnal and semi-diurnal periods. For single epoch positioning, at the 5 cm precision level, or mm static positioning over a 24 h period, and for stations that are far from the oceans, ocean loading can be safely neglected (Heroux & Kouba, 2001). The loading displacement vector  $\Delta C$  can be expressed in simplified form as shown in equation (2.11), where  $f_j$  and  $u_j$  depend only on the longitude of the lunar node (McCarthy & Pétit, 2004). Angular velocity is given by  $\omega_j$ , and  $\lambda_j$  denotes the astronomical argument at time  $t = 0$ , corresponding to the tidal wave component  $j$ , represented by 11 tidal waves.

$$\Delta c = \sum_j f_j A_{cj} \cos(\omega_j t + \lambda_j + u_j - \Phi_{cj}) \quad (2.11)$$

Calculation of the station-specific amplitude,  $A_{cj}$ , and the phase,  $\Phi_{cj}$ , depends on the applied ocean tide model; for example, FES2004 (Finite Element Solution).

### **2.3.2.6 Earth rotation parameters (ERP)**

Earth Rotation Parameters (Pole position  $X_p$ ,  $Y_p$  and UT1-UTC), along with conventions for sidereal time, precession and nutation, facilitate accurate transformations between the terrestrial and inertial reference frames that are required in global GPS analysis. Then, the resulting orbits in the terrestrial conventional reference frame, ITRF, like the IGS orbit product, imply the underlying ERP, and so therefore, users working directly with ITRF need not worry about ERP.

### **2.3.2.7 System biases**

GNSS observation data are affected by hardware biases originating at both the satellite and the receivers. These can be sub-categorized as:

1. Inter-frequency biases: inter-frequency bias is an issue for ionospheric delay estimation when signals of at least two frequencies are used.
2. Intra-frequency biases: these are an issue if a network containing different receivers is processed, or in a single receiver scenario.
3. Inter-system biases: combining observations from two or more satellite systems brings up additional biases, such as inter-system time system and inter-system coordinate system offsets.

In a positioning scenario, the receiver's biases are usually absorbed by the receiver clock correction parameter, provided only one type of observable is being used. Therefore, only satellite biases have to be taken into account (Leandro et al., 2007).

Code observation data suffer from differential code biases (DCB). In the case of GPS, these biases are provided, with respect to C1, P1 and P2 signals. Instrumental biases are also present in the phase observations. In the PPP case, instrumental biases are mapped into the ambiguity parameter. It is not necessary to apply DCB when using the L3 linear combination and when the IGS clock products are held fixed or are constrained. DCB correction files are published regularly and are available for download from (<ftp://ftp.unibe.ch/aiub/CODE>).

#### **2.3.2.8 Multipath**

The multipath effect occurs when the signal arrives at the receiver's antenna from more than one path, via reflection, diffraction, scattering or a combination of these. Multipath is still referred to as one of the last large sources of un-modelled errors in GNSS analysis. Multipath is very hard

to model because of its site-specific nature, caused by the unique environment of each GNSS site; it is dynamic, in the temporal and spatial senses, and therefore cannot be differenced out. It affects both code and phase measurements and is both frequency and elevation dependent. The multipath effect on P-code, pseudorange measurements can total a few meters. The theoretical maximum of this effect is approximately 15 m. On carrier phase observations, multipath error reaches a maximum of approximately 5 cm (Langley, 1998).

### 2.3.3 PPP implementation

Assuming a dual-frequency receiver, the following code and phase ionospheric-free observation equations are defined (Tolman, 2008):

$$P_{if} = \rho + c\Delta t_R - c\Delta t^S + \Delta\rho_{trop} + \gamma_{P,if} \quad (2.12)$$

$$L_{if} = \rho + c\Delta t_R - c\Delta t^S + \Delta\rho_{trop} + b_{if} + \gamma_{L,if} \quad (2.13)$$

In (2.12) and (2.13), in  $P_{if} = \frac{f_1^2 P_1 - f_2^2 P_2}{f_1^2 - f_2^2}$  and  $L_{if} = \frac{f_1^2 L_1 - f_2^2 L_2}{f_1^2 - f_2^2}$

- $f_1$  and  $f_2$  denote the frequencies of any two carriers
- $\gamma_{P,if}$  and  $\gamma_{L,if}$  denote the remaining un-modelled biases for code and phase ionospheric-free observations
- $b_{if}$  is an ambiguity factor
- $\Delta\rho_{trop}$  is the delay to the GNSS signal caused by the troposphere.

The PPP technique is implemented in software using two different approaches—the Least Squares (LS) and the Extended Kalman Filter (EKF)—to estimate the parameters defined in equations 3.9 and 3.10. Both techniques will be explained in detail, but focus will be given to EKF,

because its implementation in software is easy and the estimation is very precise. Thus, many PPP software programs have implemented this estimator.

### LS adjustment

This adjustment can be performed on the principal assumption of Gaussian normally distributed observation noise and uncertainty. Therefore, any bias or outlier must be removed prior to applying the LS adjustment procedure (Moritz, 1972).

A vector of observations  $l$  is defined as shown in equation (2.14).

$$l = Ax + v \quad (2.14)$$

In equation (2.14):

- $l[n \times 1]$  is the vector of observations,  $n$  being the number of observations
- $x[u \times 1]$  is the vector of unknowns
- $A[n \times u]$  is a design matrix,  $u$  being the number of unknowns
- $v[n \times 1]$  is the residual vector with the expectation defined as  $E[v] = 0$ .

The dispersion matrix of the observation is defined as shown in (2.15), with  $\Sigma_{ll}$  being the covariance matrix of observation (Moritz, 1972). Symbol  $\sigma_0^2$  represents the *a priori* variance of unit weight and  $Q_{ll}$  represents the cofactor matrix commonly calculated as an inverse of the weight matrix P.

$$D[l] = \Sigma_{ll} = \sigma_0^2 Q_{ll} \quad (2.15)$$

The adjustment is achieved by minimizing the sum of squares of the residuals (Moritz, 1978), as shown in (2.16):

$$v^T P v = (l - Ax)^T P (l - Ax) = \text{minimum} \quad (2.16)$$

The estimated vector of unknowns  $\hat{x}$  will then be as shown in (2.17), where  $N$  is the normal equation matrix, and  $n$  is the measurement vector.

$$\hat{x} = (A^T P A)^{-1} A^T P l = N^{-1} n \quad (2.17)$$

The cofactor matrix of the estimated parameter vector,  $Q_{\hat{x}\hat{x}}$ , follows the covariance propagation law and is defined as shown in (2.18).

$$Q_{\hat{x}\hat{x}} = (N^{-1} A^T P) Q_u (N^{-1} A^T P)^T = N^{-1} \quad (2.18)$$

The *a posteriori* variance of unit weight is defined as shown in (2.19), with  $n-u$  defining the degrees of freedom:

$$\hat{\sigma}_0^2 = \frac{\hat{v}^T P \hat{v}}{n-u} \quad (2.19)$$

The vector of estimated residuals,  $\hat{v}$ , is calculated from the vector of estimated parameters  $\hat{x}$  as:

$$\hat{v} = l - A\hat{x} \quad (2.20)$$

The covariance matrix of the estimated parameters is finally defined as shown in equation (2.21):

$$\Sigma_{\hat{x}\hat{x}} = \hat{\sigma}_0^2 Q_{\hat{x}\hat{x}} \quad (2.21)$$

For more details about Least Squares adjustment, refer to Moritz (1972).

### **Extended Kalman Filter (EKF)**

The first work in the literature to implement the EKF was undertaken by Zumberge et al (1997); the EKF was used to estimate the parameters needed in PPP processing of ionosphere-free combinations of dual frequency pseudorange and carrier phase data with precise satellite ephemeris.

In the EKF, a state vector,  $\mathbf{x}$ , for unknown model parameters, and its covariance matrix,  $\mathbf{P}$ , can be estimated with a measurement vector,  $\mathbf{y}_k$ , at an epoch  $t_k$ , by applying equations (2.22), (2.23) and (2.24).

$$\hat{\mathbf{x}}_{k+} = \hat{\mathbf{x}}_{k-} + \mathbf{K}_k(\mathbf{y}_k - \mathbf{h}(\hat{\mathbf{x}}_{k-})) \quad (2.22)$$

$$\mathbf{P}_{k+} = (\mathbf{I} - \mathbf{K}_k \mathbf{H}(\hat{\mathbf{x}}_{k-}) \mathbf{P}_{k-}) \quad (2.23)$$

$$\mathbf{K}_k = \mathbf{P}_{k-} \mathbf{H}(\hat{\mathbf{x}}_{k-}) (\mathbf{H}(\hat{\mathbf{x}}_{k-}) \mathbf{P}_{k-} \mathbf{H}(\hat{\mathbf{x}}_{k-})^T + \mathbf{R}_k)^{-1} \quad (2.24)$$

In equations (2.22), (2.23) and (2.24),  $\hat{\mathbf{x}}_k$  and  $\mathbf{P}_k$  are the estimated state vector and its covariance matrix, at the epoch time,  $t_k$ . The positive (+) and negative (-) signs indicate after and before measurement updates of EKF, respectively. Symbols  $\mathbf{h}(\mathbf{x})$ ,  $\mathbf{H}(\mathbf{x})$  and  $\mathbf{R}_k$  are the measurement model vector, the matrix of partial derivatives and the covariance matrix of measurement errors, respectively (Zumberger et al 1997).

Assuming the system model to be linear, the time update of the state vector and its covariance matrix are expressed as shown in (2.25) and (2.26), where  $\mathbf{F}_k^{k+1}$  and  $\mathbf{Q}_k^{k+1}$  are the transition matrix and the covariance matrix of the system noise, from epoch time  $t_k$  to  $t_{k+1}$ .

$$\hat{\mathbf{x}}_{(k+1)-} = \mathbf{F}_k^{k+1} \hat{\mathbf{x}}_{k+} \quad (2.25)$$

$$\mathbf{P}_{(k+1)-} = \mathbf{F}_k^{k+1} \mathbf{P}_{k+} \mathbf{F}_k^{k+1T} + \mathbf{Q}_k^{k+1} \quad (2.26)$$

The state vector,  $\mathbf{X}$  (equation (2.27)), consists of three Earth-centred Earth-fixed Cartesian components for position: a clock bias, a residual zenith wet tropospheric delay, and a single-phase bias, for each visible satellite.

$$\hat{\mathbf{X}} = [\hat{\mathbf{x}} \ t \ T \ B^0 \ \dots \ B^j] \quad (2.27)$$

For more details about use of the EKF for PPP, refer to: Zumberge et al (1997), and Tolman and Gelb (2008).

### 2.3.3.1 PPP software

The PPP technique has been implemented by different software packages. Each of them either follow different estimation strategies, or use precise ephemeris from different sources. There are online services accessible through the Internet and software packages that must be installed and run locally in a computer.

The main difference between locally run and installed PPP software packages and PPP online services; is that the first allows the user to select the source files—such as different ephemeris or navigation files—used for the estimation of parameters. In contrast, PPP online services do not allow user input of different ephemeris or navigation files. Three PPP software and three PPP online services are described below, as examples of PPP implementation.

**gLAB** is an advanced, interactive, educational, multipurpose package used for processing and analysing GNSS data (Juan et al., 2012), developed by Catalonia Technical University and the ESA. It can process either single or dual-frequency, GPS-only data. It allows the user to input different navigation files and needs double frequency GNSS data.

The tropospheric delay is defined in terms of the elevation angle ( $\epsilon$ ) of the satellite, as presented in (2.28).

$$T_r(\epsilon) = T_{rz,dry}M_{dry}(\epsilon) + T_{rz,wet}M_{wet}(\epsilon) \quad (2.28)$$

In (2.28),  $T_{rz,dry}$  and  $T_{rz,wet}$  are the dry and wet slant tropospheric delays, which can be estimated with the simple model shown in (2.29) and (2.30).  $\alpha = 2.3m$ ,  $\beta = 0.116 \cdot 10^{-3}$ ,  $H$  is the height above sea level (m). Symbol  $T_{rz0,wet} = 0.1 m$  and is estimated either through a random walk process

in the navigation-Kalman-filter, together with the coordinates and other parameters (Juan et al., 2012; Sanz Subirana et al., 2013a, 2013b), or through the UNB-3 model.

$$T_{rz,dry} = \alpha e^{\beta H} \quad (2.29)$$

$$T_{rz,wet} = T_{rz0,wet} + \Delta T_{rz,wet} \quad (2.30)$$

Parameters  $M_{dry}$  and  $M_{wet}$  are the dry and wet parts of the Neill Mapping Function, which does not require any meteorological data. The multiplication of the mapping function and the slant delay yield the ZTD.

**POINT** is a software package developed by the University of Nottingham and is capable of processing L1 and L2 GPS data. It implements an EKF for positioning, employing double difference observables (Mohammed et al., 2016); it also needs double frequency GNSS data. The user needs to input the ephemeris and the clock data.

For estimating the tropospheric delay, the hydrostatic component of the ZTD is calculated using a model, such as the Saastamoinen, Hopfield or Ifadis models, and the Neill Mapping Function. The wet component is an unknown in the EKF, and the total zenith tropospheric delay is calculated as the sum of wet and dry components as shown in equation 2.31.

$$ZTD = ZHD_{model} + ZWD_{estimated} \quad (2.31)$$

**RTKLIB** is an open source positioning software, developed by T. Takatsu (<http://www.rtklib.com/>). It can implement different positioning techniques, among them PPP, which can be computed in either static or kinematic mode. All corrections are input to the software via its Graphic User Interface. The user can choose the source of the files containing the corrections.

The effect of the troposphere is modelled using a mapping function and zenith tropospheric delays. The mapping function, in terms of the elevation angle ( $El$ ) and the azimuth angle ( $Az$ ) between the satellite and the receiver, is calculated as shown in equation (2.32).

$$M(El) = M_w(El)\{1 + \cot(El)(G_N \cos(Az) + G_E \sin(Az))\} \quad (2.32)$$

In (2.32),  $Z_T$  is the tropospheric zenith total delay, in metres. This parameter is estimated from the EKF, together with the north ( $G_N$ ) and east ( $G_E$ ) components of the tropospheric gradient.

### 2.3.3.2 PPP online services

The **Automatic Precise Positioning Service** (APPS) (JPL, 2019) is an online service, provided by the Jet Propulsion Lab (JPL), which can estimate position coordinates and other parameters (clock states, tropospheric delay and carrier-phase ambiguities), as a single set in Static Mode, or as a time series in Kinematic Mode. APPS can only take dual-frequency GPS observations. The service allows the user to decide whether to use Final, Rapid or Ultra-rapid type products from the JPL, for satellite orbit and clock corrections.

In the APPS the Zenith Wet Delay (ZWD) is estimated as a random walk, with variance of  $3 \text{ mm}^2$  per hour. Moreover, the wet delay gradient is estimated as a random walk with variance of  $0.3 \text{ mm}^2$  per hour and the phase ambiguities are estimated as real numbers (JPL). The ZTD is estimated by applying the GMF troposphere mapping function, with an *a priori* hydrostatic delay of  $1.013 * 2.27 * e^{-0.000116 * h}$  m. Where  $h$  is the station height above the ellipsoid, in m, and an *a priori* wet delay of 0.1 metres. The wet delay is estimated together with positioning unknowns.

The **Canadian Spatial Reference System** (CSRS-PPP service) (Canada, 2019), by Natural Resources Canada, uses a dynamic filter to estimate station position. The estimation can be done in either static or kinematic mode, and provides station-clock states, local tropospheric zenith delays and carrier phase ambiguities. Precise corrections to the applicable satellite orbit and clock are made available by the IGS. Either single- or dual-frequency GNSS data can be used as an input, and the user may choose either the NAD83 or the ITRF2008 frame of reference to determine coordinates (Heroux & Kouba, 2001).

In the CSRS-PPP service, the approach used for ZTD estimation is to smooth the estimates by a backward substitution, with the final converged satellite ambiguity parameters held fixed for all epochs. This approach is implemented to obtain optimal station ZTD series, based on all observations within the observation session (Heroux & Kouba, 2001). The GMF is the mapping function used in CSRS-PPP.

The service of **MagicGNSS** (GMV, 2019), operated by GMV Aerospace and Defense, is made available through their website. The user can process data in the static and kinematic modes, at two frequencies. Also, the user can choose to use final and / or rapid products for corrections of orbits and clocks of satellites, made accessible by the IGS or GMV. The current version can process data from the constellations GPS, GLONASS, Galileo, and BeiDou. Coordinates for the calculated position can be determined in two frames of reference, ITRF2008 and ETRS89. MagicGNSS does not take parameters of the phase centre antenna into

account in calculation. **MagicGNSS** uses the same strategy as CSRS-PPP for its implementation and ZTD estimation.

**Table 2.4.** Capability comparisons for PPP implementation (Mendez Astudillo et al., 2018).

<b>Parameter</b>	<b>APPS</b>	<b>CSRS-PPP</b>	<b>MagicGNSS</b>	<b>gLAB</b>	<b>POINT</b>	<b>RTKLIB</b>
Version	GIPSY 6.4	1.05	N/A	5.0.0	N/A	2.4.3
Mode of calculation	Static/kinematic	Static/kinematic	Static/kinematic	Static / kinematic	Static/kinematic	Static/kinematic
Constellation	GPS	GPS, GLO	GPS, GLO, Galileo, BDS	GPS, GLO, Galileo	GPS, GLO	GPS, GLO, GPS + GLO
Frequency	L1,L2	L1,L2	L1,L2	L1,L2	L1,L2	L1,L2
Type of observation	Code and phase	Code and phase	Code and phase	Code and phase	Code and phase	Code and phase
Antenna model	Not taken into account	Taken into account	Not taken into account	Taken into account	Taken into account	Taken into account
Frame of reference	ITRF2008	ITRF2008	ITRF2008	ITRF2008	ITRF2008	ITRF2008
Orbits and clocks of satellites	JPL final	IGS final	GMV Rapid, IGS Rapid, IGS final	IGS final	IGS final	IGS final
Cut-off angle	10°	10°	10°	10°	10°	10°
Mapping Function	GMF	GMF	GMF	NMF	NMF	NMF

Table 2.4 shows the capabilities of six PPP implementations: three of them need to be locally installed and three of them available as online services. The software locally run in the user's computer allows users to input the clock and ephemeris data to be used. Either final or rapid products from different sources can be used such as the International GNSS Service (IGS) or Jet Propulsion Lab (JPL). In addition, the cut-off-angle can be changed in these implementations, and either  $10^\circ$  or  $5^\circ$  are typically used. Finally, the three software packages implement the Neil Mapping Function (NMF); refer to (Niell, 2000) for more details about the NMF.

In contrast, online PPP services do not allow the user to change the source of the ephemeris (or offer a few options). However, depending on the observation data, final or rapid products are used. The cut-off-angle is set, in all cases, to  $10^\circ$ , and cannot be changed. Finally, the mapping function used for the estimation of tropospheric delay is the Global Mapping Function (GMF); refer to (Boehm et al., 2006) for more details about the GMF.

## **2.4 GNSS meteorology applications**

Environmental monitoring (Awange, 2012) and atmosphere remote sensing (Yu et al., 2014) are other applications for GNSS signals. As indicated by equations (2.2) and (2.3), conditions in the troposphere and ionosphere delay signal transmission between a satellite and a receiver. Refracted, reflected and scattered GNSS signals have been successfully used to remotely sense the characteristics and conditions of the Earth's surface and atmosphere (Jin et al., 2011). For example, the ionosphere

effect can be detected using dual-frequency GPS arrays as shown in (Jin et al., 2008). Also, using GPS data, it has been possible to observe plasma bubbles (Haase et al., 2011).

GNSS observations have also been used in atmospheric sounding, including sensing precipitable water vapour (PWV) (Bevis et al., 1994; Rocken et al., 1995), and ionospheric total electron content (TEC) (Davies & Hartmann, 1997; Jin et al., 2011). 3D water vapour representations can be constructed using GNSS observations from different systems (Dong & Jin, 2018). Moreover, the integration of GNSS-derived Path Delay with microwave radiometer measurements can be used to find a precise wet tropospheric correction for altimetric products (Fernandes et al., 2015). In all the examples, the ZTD is the parameter used as input.

GPS reflectometry is another method that can be used to monitor the earth. It is achievable with a GNSS Receiver Remote Sensing Instrument (GNSS-R) that has been launched as an 8-satellite constellation called CYGNSS. GNSS-R is expected to generate new applications in various environmental remote sensing fields, such as monitoring sea ice, sea states, oceanic eddies and geohazards, with high spatial-temporal resolution and in near real-time (Jin et al., 2011).

## **2.5 Motivation for research: UHI monitoring**

The objective of the work described in this thesis is to use GNSS atmospheric monitoring capabilities to monitor the temperature in urban and rural areas where UHIs are likely to happen. This section reviews

recent research on the UHI effect (UHIE) and the relevance of UHI monitoring and mitigation.

### **2.5.1 UHI definition**

As a consequence of industrialization and rapid urbanization, major metropolitan areas have emerged (Golden et al., 2007). Modern large cities are characterized by high concentrations of population, industries and buildings (Wang & Xu, 2008). Consequently, there is little aeration and a general absence of green space, due to the associated changes in land use. In most cities, natural vegetation has been replaced by cement and asphalt ground, which retain more heat than natural vegetation, and this accumulated surface heat can result in the evaporation of more surface water (Wang & Xu, 2008). Because of these effects, an urban climate different from that in non-urban areas is created (Boufidou et al., 2011).

UHIs are defined as urban regions that experience temperatures warmer than those of their rural surroundings (Roth, 2013). UHI intensity is often quantified by the difference in air temperature between a weather station located in an urban centre and one in a less urbanized outskirts (Peng et al., 2012). The areas need to be monitored simultaneously and need to be relatively close to each other, so that they have similar climates (Memon et al., 2009). An example of a method to quantify UHI intensity is by measuring the difference between a 2-m above the surface temperature sensor (T2m) of a weather station in an urban area and the T2m sensor in a nearby rural area (Jauregui, 1997; Jin, 2012) .

The difference of the city climate is manifested in the increased temperature of the air close to the ground (especially among buildings), relative to the air temperature outside the city, at the same altitude (Klysiak & Fortuniak, 1999). The intensity of the UHI depends on the morphology and the size of the city and the applicable meteorological conditions. Higher wind speeds, higher cloud cover and higher relative humidity reduce the UHI. Furthermore, UHI's intensity also varies with space and time (Hoffmann et al., 2012).

UHI is considered as one of the major problems in the 21st century posed to human beings as a result of urbanization (Rizwan et al., 2008). The UHI is the most studied climate effect of cities (Roth, 2013) and has been gaining attention around the research world (Nuruzzaman, 2015) as urbanization proceeds at an unprecedented pace, primarily in arid and semi-arid hot climates (Golden et al., 2007).

### **2.5.2 UHI effects**

This section describes UHI effects on humans, the environment, energy consumption and local meteorology: including effects such as atmospheric stability, humidity, clouds and fog, precipitation, evaporation, and snow cover (Szymanowski & Kryza, 2011).

#### Effects on Humans

A UHI influences the quality of life and human well-being in urban areas (Schwarz et al., 2011). According to the report published by the US Environmental Protection Agency and the Keystone Centre (2017), a warm air mass over cities causes effects on humans that include

discomfort, morbidity, increased mortality rates (Memon et al., 2009; Rizwan et al., 2008) and reduced worker productivity. These effects are problematic, particularly for inhabitants of cities and areas in the tropics (Memon et al., 2009). Moreover, other effects include discomfort and inconvenience to the urban population, due to high temperatures, wind tunnel effects in streets, and increased use of energy for cooling purposes (Shahmohamadi et al., 2011). Elevated temperatures are a concern for those who are vulnerable to extreme heat, including the elderly, those with pre-existing health conditions, and those of lower socio-economic status (Shahmohamadi et al., 2011). Also, according to Harris and Coutts (2011) higher temperatures at night limit relief from daily heat stress, influencing mortality rates.

#### Effect on the environment

The UHI alters more environmental variables than temperature, including ground-level ozone levels (Memon et al., 2009; Rizwan et al., 2008), the provision of water resources (city water demand (Jauregui, 1997)), air quality (episodes of unhealthy air pollution levels (Jauregui, 1997)), and biodiversity (Schwarz et al., 2011). Water demand increases with heat, as it is used for both personal cooling and also for landscape irrigation. Air quality deteriorates as more pollutants are released from air conditioning and cooling devices. In addition, biodiversity depends on the climate, so temperature change may influence species' habitats.

#### Energy Consumption

The UHI causes increased electricity demand, due to both population growth (Golden et al., 2007) and to increased energy consumption from the air-conditioning of buildings (Kikegawa et al., 2003). As a result, more electrical energy production is needed and more greenhouse gas is emitted from combustion of fossil fuels (Yu & Hien, 2006). This leads to increased smog, and also contributes to increased pollutant emissions from power plants (Shahmohamadi et al., 2011).

Increased energy consumption contributes to global warming, which further increases temperatures and energy demand (Yu & Hien, 2006). Furthermore, buildings that are not designed for high energy efficiency, use more energy for air conditioning and more electricity for lighting (Shahmohamadi et al., 2011). Higher temperatures in cities also increase demand for water for landscape irrigation (Yu & Hien, 2006).

### **2.5.3 UHI classifications**

There are many UHI classifications, based on various characteristics. One classification has been done according to the target medium: air, surface, or sub-surface (Unger et al., 2010). A further two types of UHI have been distinguished: The Surface UHI (SUHI), and the Atmospheric UHI (AUHI), as described in Table 2.5.

**Table 2.5.** UHI classification according to target medium.

Type of UHI	Layer of the earth	Definition	Measuring method
SUHI	Surface	Extends over the entire 3-D envelope of the surface (Roth, 2013)	<ul style="list-style-type: none"> <li>• Thermal infrared (Roth, 2013)</li> <li>• Airborne and satellite-based instruments (Grimmond et al., 2010).</li> </ul>
AUHI	Canopy	From the ground to below treetops and roofs (Programs, 2017)	<ul style="list-style-type: none"> <li>• Remote sensing data</li> <li>• Vehicle-mounted sensors</li> <li>• Dense network of fixed sites (Hu &amp; Brunzell, 2015).</li> </ul>
	Boundary	Starts from the rooftop and treetop level and extends up to the point where urban landscapes no longer influence the atmosphere. Extends no more than 1.5 Km from the surface (Programs, 2017)	<ul style="list-style-type: none"> <li>• Airborne and tower mounted sensors (Hu &amp; Brunzell, 2015)</li> <li>• Tethered or free-flying balloons (Grimmond et al., 2010)</li> <li>• Sensors attached to an aircraft.</li> <li>• Remote sensing (Golden et al., 2007).</li> </ul>

### SUHI

SUHI is defined as change in temperature at the surface of the earth and exhibits strong spatial and temporal variability. It depends on the material type and orientation of the surface with respect to the sun (Pichierri et al., 2012), as well as on its thermal (e.g., heat capacity, thermal admittance) and radiative (e.g., reflectivity or albedo) properties (Roth, 2013).

It is monitored using thermal infrared measurements from ground-, airborne- or satellite-based instruments (Grimmond et al., 2010), and thermal remotely sensed data (Hu & Brunzell, 2015). It is important to monitor SUHIs because urban surface temperatures are considered a direct indicator of UHI, for purposes related to human comfort and energy use (Grimmond et al., 2010).

## **AUHI**

According to the United States Environmental Protection Agency (Programs, 2017), AUHIs are divided into two types, canopy layer UHI and boundary layer UHI.

*Canopy Layer UHI:* The canopy layer is the portion of the atmosphere between the ground and buildings or city tree height (Schwarz et al., 2011), and is of great interest to researchers as it is the predominant UHI phenomenon (Roth, 2013). Canopy layer air temperature measurements are directly referred to as the UHI in the canopy layer (Schwarz et al., 2011). Canopy layer UHI is the most important UHI, since it is felt by pedestrians and urban dwellers (Harris & Coutts, 2011).

*Boundary Layer UHI:* The second layer, situated above the canopy layer, is called the urban boundary layer (UBL) (Oke, 1976). This layer's properties are altered by the cities themselves, including effects on the distinct turbulence, temperature and moisture fields of the layer (Hoffmann et al., 2012).

#### **2.5.4 Techniques used for UHI monitoring**

The main technique used to monitor UHI intensity requires the use of remote sensed data, such as Landsat 7 data. After processing the data, different temperatures are detected and mapped (Harris & Coutts, 2011). Other techniques used to identify the UHI require measurements from at least two T2m sensors, two towers, weather balloons or radiosondes (Voogt, 2014), one in a rural area and another in an urban area.

**SUHI** is measured using satellite and airborne thermal remote sensing techniques, which became possible through advances in technology such as sensor miniaturization (Jin, 2012). Thermal remote observations through the use of satellites provide a mechanism for observing the surface temperature of an area much larger than traditional in-situ data (Streutker, 2003). These observations also, facilitate temperature measurement over a large area simultaneously. Furthermore, their surface temperature patterns are clear, making it much more efficient for temperature mapping at large scale (Harris & Coutts, 2011).

The main drawback of using satellite imagery is that the images need to be taken at a particular time of day and night to achieve good spectral resolution. There is the ever-present risk that capturing surface temperature might not be possible, due to weather conditions such as clouds blocking the view (Harris & Coutts, 2011). Additional advantages include global coverage and consistent periodicity, which overcome the weaknesses of ground observations related to the footprint (area where the measurement was taken), site distribution, and costs. (Hu & Brunsell, 2015). In addition, this technique provides extensive spatial coverage (Jin,

2012) and it is possible to define surface temperatures and display the SUHI formed within a city at high spatial resolutions (Voogt, 2014), making it possible to create heatmaps showing temperature differences in a city.

**Canopy Layer UHI (CLU)** is measured using direct techniques, such as thermocouples and thermistors (Voogt, 2014). This kind of UHI is monitored using T2m observations, from one or a few sites spread over urban and surrounding rural regions (Jin, 2012).

CLU can be measured in situ by sensors on tall towers—which makes high temporal resolution possible, and can avoid requiring corrections due to atmospheric influence (Voogt, 2014). In order to achieve better spatial resolution, larger networks have been employed, which has been made possible due to advances made in sensor miniaturization and data transmission technology (Awange, 2012). Examples of techniques used to measure CLU include radiosondes, tethered or free-flying balloons, aircraft, helicopters, and remote observation methods (Voogt, 2014).

**The boundary-layer UHI** has been studied less compared to the CLU, as it is harder to measure due to the height where this phenomenon is present. Therefore, not many characteristics of this UHI are known and it has not been described in the literature.

### **2.5.5 UHI mitigation techniques**

Techniques applied to mitigate the UHIE (summarized in Table 2.6) depend on many factors, some of which can be taken into account either during the planning stage (Takebayashi & Moriyama, 2007), or after the design and planning stages.

**Table 2.6.** Summary of mitigation techniques.

UHI mitigation techniques	
Stages	Measures
Urban Planning	Green parks, roadside trees (Takebayashi & Moriyama, 2007). Water bodies, pervious pavements and street width (Nuruzzaman, 2015).
Building Planning	Green roofs, high reflection roofs, wall plantings (Takebayashi & Moriyama, 2007), increasing roof thickness, inserting additional insulation, providing false ceilings (Jain & Rao, 1974).
After the design and planning stages	“Green infrastructure”, green areas, shade trees (Harris & Coutts, 2011). Switch off air conditioning (Rizwan et al., 2008).

The city environment traps hot air and reduces air flow, generating low-velocity winds that cannot disperse suspended particles and polluting gases due to the tall buildings and narrow streets that form the typical city environment. Therefore, there is a UHI effect on air pollution. Furthermore, the structures in a city, and the distribution of buildings and urban structures affect formation of the UHI. Because the distribution and characteristics of the built environment determine the absorption of solar radiation and air flows (Gago et al., 2013). Built structures absorb heat when the sun is shining, and when the sun sets, heat is radiated back to the atmosphere—and it is at this moment that the UHI is clearly visible with remote sensing techniques.

It has been suggested that anthropogenic heat release could be reduced through adoption of designs that use high albedo, cooler roofs, of suitable

building materials, and by focusing building design on reducing heat intensity, during the building planning stage (Center).

After the design and planning stage, further mitigation can be achieved if green roofs and shade trees are installed to increase evaporative cooling (Center). Vegetation or 'green infrastructure' is a key approach for UHI mitigation (Harris & Coutts, 2011). It is an attractive mitigation option because of the multiple benefits it can provide, including improved stormwater runoff quality and the removal of pollutants from the air (Harris & Coutts, 2011). Research has demonstrated the capacity of vegetation to support urban cooling (Harris & Coutts, 2011).

Another mitigation technique is reducing anthropogenic heat release. For example, by switching off air conditioners (Rizwan et al., 2008). This works because air-conditioning contributes to urban warming, through waste heat production, and contributes to greenhouse gas emissions when powered by electricity generated using fossil fuels (Harris & Coutts, 2011). Due to the contribution of UHI to greenhouse gas emissions, efforts must be made to reduce energy use and to promote green energies in the building industry. This reduction can be achieved by minimizing energy demand, by rational energy use, and by using more green energy (Shahmohamadi et al., 2011). Summer sees the highest demand for air conditioning, therefore, the UHI must be minimized during the hot season to save energy. Also it must be minimized to decrease impacts on human health and to increase pollutant removal (Yu & Hien, 2006).

### **2.5.6 Relevance of UHI monitoring**

It is relevant to monitor UHI because: 1) temperatures build up in urban areas, 2) there are energy impacts, and 3) there are public health concerns associated with UHIs, as pointed out by the study of the Keystone Centre (2017). Since it has negative impacts on the quality of the city life, better understanding of UHI intensity drivers is an important aspect of research into climate and its impacts (Peng et al., 2012).

In addition, the most important characteristics of a given UHI are its magnitude and spatio-temporal structure. This information can be used by town planners and municipal services. It can also be used as an input for various modelling studies, such as air pollutant dispersion (Szymanowski & Kryza, 2011). Furthermore, the UHIE needs to be taken into account when planning towns or cities, to prevent high concentrations of air pollution and to create optimal bioclimatic conditions (Klysik & Fortuniak, 1999). According to Rizwan et al. (2008), future research should focus on design and planning parameters that can be applied to UHIE reduction, in order to facilitate life in a better environment.

## **2.6 Definitions of Urban and Rural areas**

Definitions of Urban and Rural areas differ slightly depending on the application. In general, an urban area is defined as an area with many built structures used for different purposes such as living (residential areas), conducting commerce (commercial areas), or producing goods or services (industrial areas). In urban areas, there are anthropogenic sources of heat, such as the means of transportation and air conditioning

units, among others. In contrast, a rural area has few built structures, is mostly covered by nature and the numbers and types of anthropogenic heat sources are reduced. Usually rural and urban areas are attached to each other, with rural areas found outside the city or urban area.

In satellite imagery where a pixel of the picture represents several km, an urban area will be typically a city, and a rural area, its surroundings. However, when the remote sensing resolution is increased, an urban or rural area can be defined within a city. Examples of urban and rural areas in the Los Angeles (LA) metropolitan area are shown in Figure 2.1 a) and Figure 2.1 b), respectively.

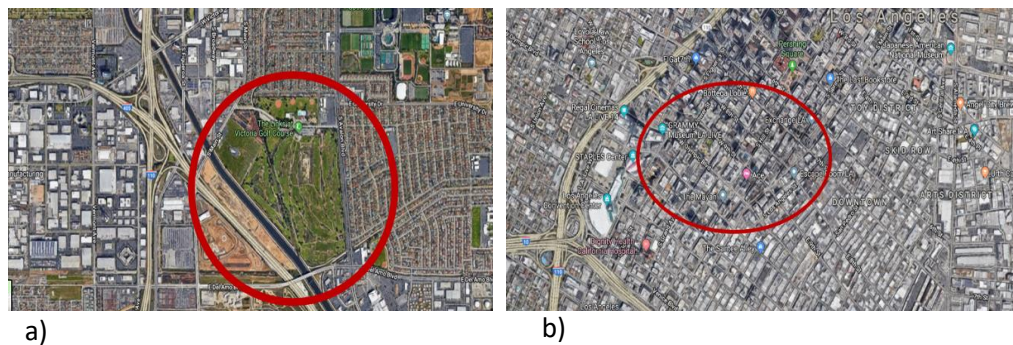


**Figure 2.1.** Examples of **a)** a rural area, and **b)** an urban area, in LA.

Figure 2.1 a) shows a rural area, in this case, a golf course in Carson, California. The golf course is a big green area with no built structures. It is surrounded by an expressway, which is a source for anthropogenic heat caused by the moving vehicles. However, the space is open air so the contribution to the UHIE is minimum. The golf course is also surrounded by low density housing areas, which contain gardens as well and have a low population density. In contrast, Figure 2.1 b) encircles an urban area, which is in downtown LA. The urban area contains many high

rising buildings very close to each other, as well as streets containing vehicles (source of anthropogenic heat). The downtown area is surrounded by other urban areas, which also have many built structures.

## 2.7 The Troposphere

The atmosphere is divided into several layers, including the ionosphere and the troposphere. The ionosphere is the ionized part of earth's upper atmosphere and is found from 60–1000 km above earth's surface. The troposphere is the layer closest to the earth's surface and is where all weather phenomena are located. There are no ionized gases in the troposphere; therefore, for electromagnetic waves in the radio-frequency spectrum (up to 15 GHz of fundamental frequency), the troposphere is a non-dispersive medium (Seeber, 2008).

GNSS signals are susceptible to experiencing delays during their transmission from the satellite to the receiver, due to the properties of the propagation media. In positioning applications, the induced delay of the signal is translated into positioning errors. Mathematically, the propagation delay,  $\Delta\rho$ , is defined as an integral of the refractive index, ( $n$ ), of the media along the ray path,  $s$ , between the satellite **S** and the receiver **R** (Seeber, 2008), as shown in equation (2.33).

$$\Delta\rho = \int_S^R (n - 1) ds \quad (2.33)$$

The refractive index ( $n$ ) is defined as the ratio of the propagation velocity of the signal in a respective medium ( $v$ ) and the propagation velocity of the signal in the vacuum ( $c$ ). The tropospheric delay in the zenith direction is a by-product of the PPP technique. The effect of the ionosphere can

be eliminated up to 98% by using dual-frequency GNSS data as input to PPP technique. Therefore, in this work, it is assumed that the effect of the ionosphere is eliminated by the PPP technique.

### **2.7.1 Troposphere content**

The troposphere is the closest layer of the atmosphere to the earth's surface, with altitudes reaching up to more than 20 km at the equator, and 7 km or more at the poles. The troposphere contains approximately 75% of Earth's total atmospheric mass and 99% of its total water vapour (Speight, 2017). Apart from water vapour, the troposphere comprises nitrogen (78%), and oxygen (20%) with the remaining 2% made up of other gases (Liang, 2013; Speight, 2017). The composition of gases within the troposphere is essentially homogenous, except for water vapour which shows high temporal and spatial variability.

### **2.7.2 Environmental variables in the troposphere**

All the weather phenomena are found in the troposphere and it is also where temperature, pressure and water vapour—all of which change with altitude—can be measured. The vertical profile of each parameter is derived next.

#### **2.7.2.1 Pressure in the troposphere**

Pressure is defined as force per unit of area (Speight, 2017). According to the International Standard Atmosphere (1975) at Mean Sea Level, the pressure is 1013.25 hPa. By definition 1013.25 hPa, equals a pressure of 1 kg/cm<sup>2</sup> of surface area. Due to gravity and decreased air density, air pressure decreases exponentially with increased height above the

surface. The pressure at the surface of the earth can be measured using a barometer, and at different altitudes, using radiosondes. The vertical profile of pressure vs altitude is shown in Figure 2.4.

### **2.7.2.2 Relative humidity in the troposphere**

Humidity is defined as the amount of water vapour in the air. It's temporal and spatial distribution is highly heterogeneous (highly variable) horizontally and vertically. For these reasons, it is hard to model or simulate with simple mathematical models. Furthermore, it has been discovered that humidity is found almost entirely within the first 10 km above the surface of the earth.

Several measures are used to characterize water vapour:

- Water vapour pressure—expressed in hPa or mbar.
- Absolute humidity—the amount of water vapour in the air, expressed in  $\text{g}/\text{m}^3$ .
- Specific humidity—the ratio between the density of water vapour and the density of wet air.
- Relative humidity—the ratio of water vapour pressure to saturation vapour pressure, expressed in %.
- Mixing ratio—the ratio of the density of water vapour to dry air.

Humidity is mostly measured as relative humidity, by sensors at surface level, such as weather stations (T2m). Another measurement typically available with humidity sensors is the Dew Point, which is the temperature at which enough water vapour is in the air for saturation to

occur. A vertical profile for relative humidity, obtained using data from weather sensors, can be found in Figure 2.4.

### **2.7.2.3 Temperature in the troposphere**

The temperature varies depending on several factors, including altitude, latitude, and time. In the tropospheric region, temperature decreases with increasing altitude, at a rate of about -5 to -7 Kelvin / km. The decrease of temperature is due mainly to greater heat absorption by the sun-heated earth's surface, which via conduction then heats up the air closer to the ground. At a certain altitude—the first boundary of the tropopause—the temperature increases at a different rate to its decrease. After that, when the stratosphere layer is reached, the temperature remains constant. The vertical profile of temperature vs altitude is shown in Figure 2.4.

Temperature also varies depending on the latitude where it is measured and the day of the year (DOY). Yearly data from each of the stations described in Table 3.1 has been processed to plot the temperature throughout the year. For simplicity, the stations in the northern and southern hemisphere have been shown in different plots, being Figure 2.2. and Figure 2.3, respectively.

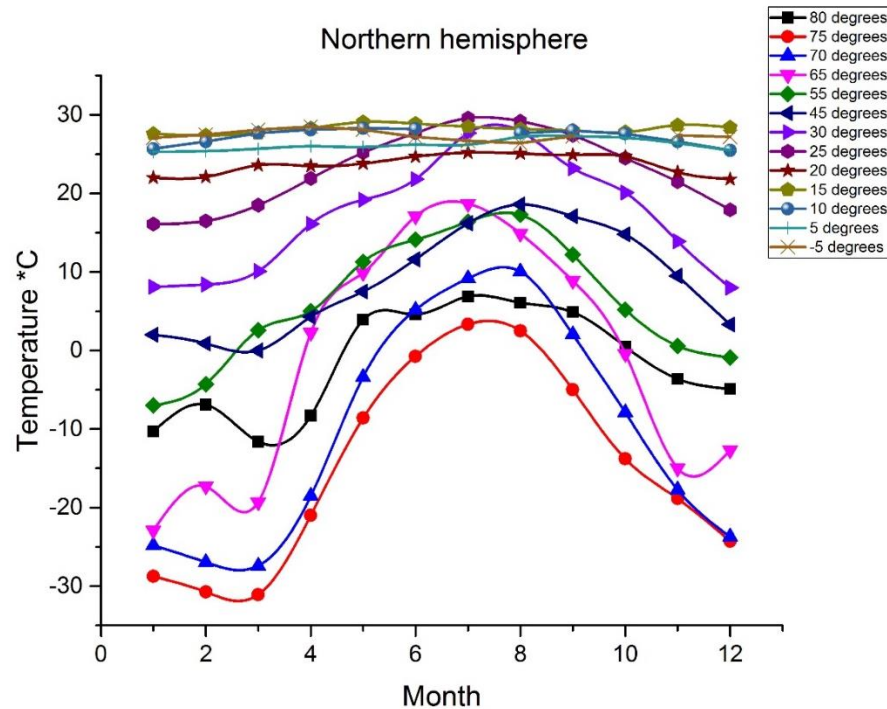


**Figure 2.2.** Annual temperature profiles for selected northern hemisphere stations.

As shown in Figure 2.2, the temperature has its maximum in the summertime, between the sixth and eighth months (between June and August) and the minimum is found between the second and third months (February and March). The stations in the arctic region (Svalbard and Resolute) exhibited extreme temperatures; during winter, the average temperature is around  $-30^{\circ}\text{C}$ , while in the summer the temperatures reach an average of  $0^{\circ}\text{C}$ , making an annual temperature fluctuation of approximately  $30^{\circ}\text{C}$ . On the other hand, stations near the equator, such as those in Chumphon, Thailand and Saint-Laurent, French Guiana, show smaller temperature differences between summer and winter, as can be seen in Figure 2.3, where their temperatures hardly deviate through the year.

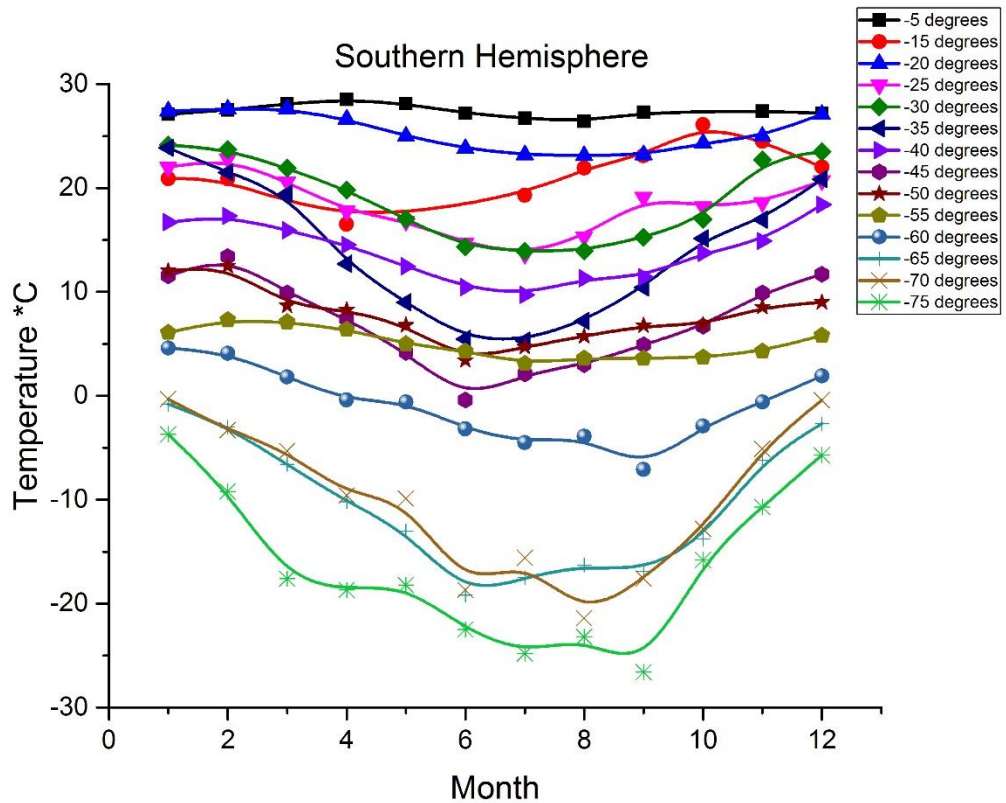


**Figure 2.3.** Annual temperature profiles for selected southern hemisphere weather stations.

Figure 2.3 shows the yearly temperature profiles for southern hemisphere stations, which are the opposite of those for the northern hemisphere. During the northern summer, the coldest monthly average temperatures are found. In contrast, in the northern winter, the warmest monthly average temperatures are found. Similar to the pattern observed in the northern hemisphere, stations further away from the equator exhibited more extreme annual temperature fluctuations. In contrast, those nearer the equator maintained relatively stable temperatures year-round.

From the temperature profiles presented in Figures 2.2 and 2.3, it can be concluded that stations in the northern hemisphere have their maxima

mid-year. It can also be concluded that those stations in the southern hemisphere have their maxima in the first and last months of the year, showing inverse behaviour. It can also be seen that stations near the equator exhibit smaller temperature fluctuations than those further away from the equator.

#### 2.7.2.4 Profile of P, T and RH vs Height

Radiosonde data described in Table 3.2 has been processed to calculate the profiles of P, T and RH vs height. These profiles are sketched in Figure 2.4

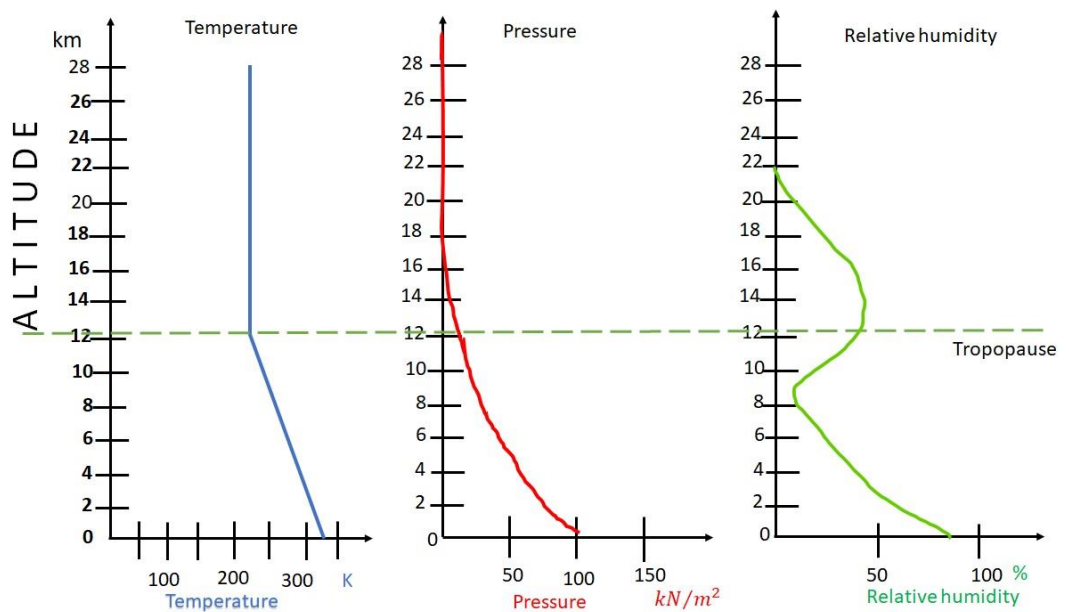


**Figure 2.4.** Profiles of temperature, air pressure and relative humidity vs altitude.

Figure 2.4 shows that temperature decreases as altitude increases up to the tropopause. Then, the temperature increases at a different rate, until the second tropopause. After which the temperature remains constant. According to the International Standard Atmosphere (1975) the average

sea level temperature is 27 °C, while the minimum at the tropopause is -64 °C. Pressure decreases in an exponential fashion—as an inverse to altitude—and reaches almost 0 at a point in the tropopause layer. Humidity also behaves exponentially, decreasing up to 10 km altitude (this 10 km layer is where most of the moisture of air is concentrated) and then behaving in an irregular way through higher altitudes.

### 2.7.3 Refractivity of the troposphere

The refractivity of the troposphere ( $N$ ) depends on environmental variables at the point of measurement, as shown in equation (2.34).  $k_1$ ,  $k_2$  and  $k_3$  are empirically determined coefficients,  $p$  is the air pressure in hPa,  $T$  is the absolute temperature in Kelvin and  $e$  is the water vapour partial pressure in hPa.  $Z_d$  and  $Z_w$  are unit-less compressibility factors for dry air and water vapour, respectively (Essen & Froome, 1951).

$$N = \left( k_1 \cdot \frac{p-e}{T} \right) Z_d^{-1} + \left[ k_2 \cdot \frac{e}{T} + k_3 \cdot \frac{e}{T^2} \right] Z_w^{-1} \quad (2.34)$$

The compressibility factors are corrections to account for the deviation of atmospheric constituents from an ideal gas. For an ideal gas, the compressibility factors equal 1. For simplicity, when estimating the ZTD, it has been assumed that the troposphere constitutes an ideal gas.

Values for the empirically determined refractivity constants  $k_1$ ,  $k_2$  and  $k_3$  have been investigated by several authors, including Thayer (1974), Smith and Weintraub (1953) and Bevis *et al.* (1994)—and their published values are listed in Table 2.7.

**Table 2.7.** Values for the empirically determined refractivity constants (as K / hPa).

	$k_1$	$k_2$	$k_3$
Thayer (1974)	77.6	72	$3.75 \cdot 10^5$
Smith and Weintraub (1953)	77.61	64.8	$3.77 \cdot 10^5$
Bevis et al (1994)	77.6	70.4	$3.73 \cdot 10^5$

The first term in equation (2.34) is the refractivity caused by the induced dipole moment of the dry constituents of the atmosphere. The second term is the induced dipole moment of water vapour, and the third term shows the effect of the permanent dipole of the water vapour molecules (Davis et al., 1985).

Since each of the environmental parameters that are needed to calculate the refractivity of the troposphere using equation (2.34) depend on altitude, the refractivity profile will also depend on altitude. The refractivity vs altitude profile is derived next.

In order to compute the profile of  $N$  vs altitude, radiosonde data from 2017 has been collected and processed for each of the stations described in Table 3.2. Values at the same height have been averaged, and a single value per height has been used. The values of  $p$ ,  $T$  and  $e$ , at different altitudes were input into equation 2.34 to compute the refractivity at different heights. A year of data has been processed, so all the values at each height have been averaged to produce the plot shown in Figure 2.5. The procedure has been done for each of the 12 stations described in Table 3.2. It has been found that all the profiles of the refractivity of the

troposphere have a similar shape and values. Therefore, it is safe to illustrate the refractivity of the troposphere using data from one station only as shown in Figure 2.5.

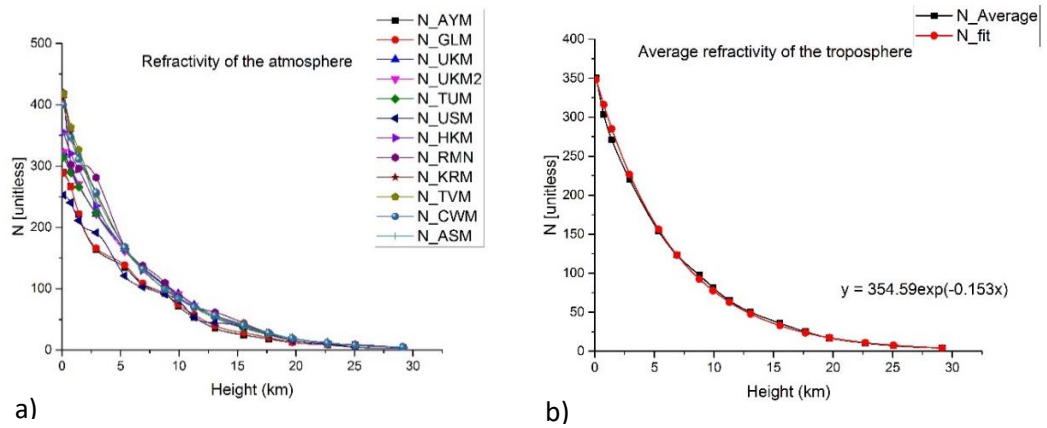


**Figure 2.5. a)** Profiles of refractivity vs geodetic height, at different latitudes. **b)** Fit to an exponential in order to find the mathematical relation between refractivity and height.

Figure 2.5 a) shows the troposphere refractivity profile for different stations, during one day in 2017. In order to find a mathematical relationship between refractivity and altitude, and to complete missing values, the data has been averaged and fitted to an exponential function. It is concluded from the plots shown in Figure 2.5 a) and Figure 2.5 b) that the shape of the refractivity profile was independent of station location, even when the value of  $N$  at height 0 m was different for each station. The mathematical expression of the relationship between  $N$  and altitude is described in equation (2.35).

$$y = 354.59e^{-0.153x}$$

$$N = N_0e^{-N_hZ} \quad (2.35)$$

Equation 2.35 has been used to compute the universal refractivity profile for a given latitude, using one year's data.

## 2.8 Tropospheric Delay

The troposphere causes a delay to the signal  $\Delta\rho_{tropo}$  (in m) which can be expressed as an integral of the total refractivity  $N$  along propagation path  $s$  from receiver  $r$  to satellite  $w$  (Hofmann-Wellenhof et al., 2008):

$$\Delta\rho_{tropo} = 10^{-6} \int_r^w N ds \quad (2.36)$$

The tropospheric delay can also be separated into two components, the dry component, related to temperature and air pressure, and the wet component related to the amount of water vapour available in the troposphere. The dry component is relatively stable, while the wet component fluctuates a lot (Hofmann-Wellenhof et al., 2008). Nevertheless, Equation 2.36 can be written as:

$$\Delta\rho_{tropo} = 10^{-6} \int_r^w N_{dry} ds + 10^{-6} \int_r^w N_{wet} ds \quad (2.37)$$

According to McCarthy and Pétit (2004), the total delay in the line of sight between a GNSS receiver and a GNSS satellite is derived as the sum of the hydrostatic (or dry) and wet delays, in the zenith direction, multiplied by respective mapping functions and a gradient correction. Equation (2.38) represents the tropospheric delay, where  $\Delta\rho_h^z$  and  $\Delta\rho_\omega^z$  are the hydrostatic and wet zenith delays, respectively, with associated hydrostatic and wet mapping functions  $m_h(\epsilon)$  and  $m_\omega(\epsilon)$ . Symbol  $\epsilon$  represents elevation angle of the satellite.

$$\Delta\rho_{tropo} = \Delta\rho_h^z \cdot m_h(\epsilon) + \Delta\rho_\omega^z \cdot m_\omega(\epsilon) + m_g(\epsilon)[G_N \cos\alpha + G_E \sin\alpha] \quad (2.38)$$

The term  $m_g(\epsilon)[G_N \cos\alpha + G_E \sin\alpha]$  is called the tropospheric gradient correction and accounts for the azimuthal dependence of the tropospheric path delay. In equation 2.38,  $m_g(\epsilon)$  stands for the gradient mapping function, with respect to elevation angle  $\epsilon$ .  $G_N$  and  $G_E$  denote the horizontal delay gradients in the north and east directions, respectively.  $\alpha$  is the azimuth angle of the received signal, measured from east to north.

The tropospheric delay in the zenith direction is called the Zenith Tropospheric Delay (ZTD). It can be determined as an integral of refractivity  $N$ , in the zenith direction (Wilgan et al., 2016).

$$ZTD = 10^{-6} \int_{zenith\ direction} N ds \quad (2.39)$$

The ZTD is defined as the sum of the Zenith Hydrostatic Delay (ZHD) and the Zenith Wet Delay (ZWD) (Hofmann-Wellenhof et al., 2008).

$$ZTD = ZHD + ZWD \quad (2.40)$$

The tropospheric delay and the ZTD are related to each other using the relation shown in (2.41) (Hofmann-Wellenhof et al., 2008).  $m_h(\epsilon)$  and  $m_w(\epsilon)$  are the hydrostatic and wet mapping functions, depending on the elevation angle.

$$\Delta\rho_{tropo} = ZHD * m_h(\epsilon) + ZWD * m_w(\epsilon) \quad (2.41)$$

According to Vedel et al. (2001), the ZTD can also be defined as the integral of the refractivity over a vertical column of the neutral atmosphere, as represented by (2.42).  $\rho$  is the density of air,  $z$  is the geometric height,  $R$  is the gas constant,  $T$  is the temperature,  $z_{site}$  is the height of the receiver with respect to the ground and  $z_{top}$  is the height of the troposphere.

$$ZTD = 10^{-6} \int_{z_{site}}^{z_{top}} \left( k_1 R_d \rho_d + \left( k_2 + \frac{k_3}{T} \right) R_w \rho_w \right) \delta z \quad (2.42)$$

Subscripts  $d$  and  $w$  represent dry and wet components respectively. Symbols  $k_1$ ,  $k_2$  and  $k_3$  are empirically determined constants, with  $k_1 = 7.76 * 10^{-1} \text{ K / Pa}$ ,  $k_2 = 7.04 * 10^{-1} \text{ K / Pa}$  and  $k_3 = 3.739 * 10^3 \text{ K}^2 / \text{Pa}$  (Essen & Froome, 1951). In order to solve the integral, it is important to use appropriate geometric heights for  $z$ , rather than the geopotential heights widely used in meteorology (Vedel et al., 2001). According to equation 2.40, the ZTD can be divided into the Zenith Hydrostatic Delay and the Zenith Wet Delay. These delays will be explained next.

### 2.8.1 Zenith hydrostatic delay

Equation 2.41 can be written in terms of the environmental variables, as shown in equation (2.43), where  $m_d$  is the molar mass of dry air ( $m_d = 28.9644 \pm 0014 \text{ g / mol}$ ) and  $R$  is the universal gas constant ( $R = 8.314345 \pm 00007 \text{ Pa} * \text{m}^3 / \text{K} * \text{mol}$ ) (Davis et al., 1985):

$$\Delta \rho_{tropo} = 10^{-6} \left[ \int_S^R \left( k_1 \frac{R}{m_d} \rho \right) ds + \int_S^R \left( k_2 \frac{e}{T} Z_w^{-1} \right) ds + \int_S^R \left( k_3 \frac{e}{T^2} Z_w^{-1} \right) ds \right] \quad (2.43)$$

A new constant factor,  $k_2'$ , is defined as in (2.44), in terms of the total density, where  $k_1$  and  $k_2$  are the same constants defined in Table 2.5.

$$k_2' = k_2 - k_1 \frac{m_w}{m_d} = 22.1 \pm 2.2 \text{ K/hPa} \quad (2.44)$$

From equation 2.42, the path delay due to hydrostatic refractivity is defined as in (2.45).

$$\Delta\rho_h = 10^{-6} \int_S^R \left( k_1 \frac{R}{m_d} \rho \right) ds \quad (2.45)$$

The vertical profile is defined by applying the condition of hydrostatic equilibrium  $\frac{dp}{dz} = -\rho(z)g(z)$  (Davis et al., 1985), where  $g(z)$  is acceleration due to gravity along the vertical coordinate,  $z$ . Symbol  $\rho(z)$  is the density of air along the vertical coordinate  $z$ . Integration of the vertical profile from antenna  $a$  of the receiver to infinity leads to equation (2.46).

$$\int_a^\infty \rho(z) dz = \int_a^\infty -\frac{dp}{g(z)} dz = \frac{p_0}{g_{eff}} \quad (2.46)$$

In (2.46),  $p_0$  is the pressure at the antenna and  $g_{eff}$  is the effective gravity, representing gravity acceleration at the centre of mass of the vertical column of the atmosphere above the site.

The hydrostatic delay in the zenith direction (ZHD) is defined as shown in equations (2.47) and (2.48).

$$ZHD = 10^{-6} k_1 \frac{R}{m_d} \frac{p_0}{g_{eff}} \quad (2.47)$$

$$g_{eff} = \frac{\int_a^\infty \rho(z)g(z) dz}{\int_a^\infty \rho(z)} \quad (2.48)$$

Modelling the ZHD is straightforward, as models can only differ in the choice of refractivity constant and on the basis of the modelling of the height and latitude dependence of the gravity term (Mendes, 1999).

The model proposed by Saastamoinen (1972) is an example of how the ZHD is modelled. According to Saastamoinen,  $g_{eff}$  can be approximated

as shown in (2.49), with  $\phi$  denoting the latitude of the station and  $h$  the height of the antenna above the geoid.

$$g_{eff} = 9.7840(1 - 0.00266\cos(2\phi) - 0.28 \cdot 10^{-6}h) \quad (2.49)$$

Denoting the expression in parenthesis in equation 2.48 as  $f(\phi, h)$ , Saastamoinen derived the ZHD, in m, as shown in (2.50).

$$ZHD = 0.0022768 \frac{p_0[hPa]}{f(\phi, h)} \quad (2.50)$$

Other models have been developed, such as the modified Saastamoinen model (Davis et al., 1985), the UNB3m latitude and height dependent model (Leandro, 2009), the Hopfield model (Hopfield, 1969) and the GPT model developed by Böhm *et al* (2007). These models are used in different software, while the Saastamoinen model is the most common and is the one implemented in PPP software.

Another ZHD derivation was done by Vedel et al. (2001). Assuming hydrostatic equilibrium in the troposphere, expression (2.51) was derived for the contribution of the ZHD (Vedel et al., 2001).

$$\Delta ZHD \approx \frac{k_1 R_d p_1}{g_1} \left\{ 1 + 2 \frac{R_d T_1}{r_1 g_1} + 2 \left( \frac{R_d T_1}{r_1 g_1} \right)^2 \right\} \quad (2.51)$$

For this derivation, it was also assumed that temperature was constant towards the top of the known profile, and that  $g(r) = g_1 (r_1/r)^2$ , where  $r$  is the distance to the centre of the earth. Symbols  $T_1$ ,  $g_1$ ,  $r_1$  and  $p_1$  are the values at the top of the known profile. Use of this model required assuming that temperature was constant in that part of the atmosphere, an assumption that doesn't represent reality. According to Vedel et al.

(2001), the equation has to be solved using numerical integration techniques together with interpolation techniques, and there is no solution after 80 km. In addition, the same authors found that an altitude difference of 8 m corresponds to 1 hPa, which corresponds to 2.3 mm in ZHD (Vedel et al., 2001).

The hydrostatic path delay is in fact responsible for approximately 90% of the total tropospheric delay and in typical meteorological conditions it can be about 2.3 m at sea level in the zenith direction.

### 2.8.2 Zenith wet delay

The derivation of a model to account for the ZWD is more challenging than for the hydrostatic delay, due to the high variability and unpredictability of the amount of water vapour in the troposphere. This is the reason why numerous models have been developed, using either Saastamoinen's or Hopfield's model, or their slight modifications, to determine hydrostatic delay. Usually, in GNSS processing, the ZWD is estimated as an additional parameter, along with station coordinates, during the least square adjustment or EKF. Nevertheless, some models can be used to give an initial value. For example, Saastamoinen (1972) proposed calculation of ZWD based on ideal gas laws, as shown in (2.52), where  $e$  is water vapour pressure and  $T$  is temperature:

$$ZWD = 0.0022768(1255 + 0.05T) \frac{e}{T} \quad (2.52)$$

Hopfield (1969) proposed the following expression for ZWD:

$$ZWD = \frac{10^{-6}}{5} N_w^{trop}(0) h_w \quad (2.52)$$

In (2.52),  $N_w^{trop}(0)$  is the refractivity of wet air at the surface and a mean value of  $h_w = 11000$  m is applied for the height of the troposphere up to which water vapour exists. Ifadis (1986) proposed the modelling of ZWD as a function of surface pressure, partial water vapour pressure and temperature. Mendes and Langley (1998) derived a linear relation between ZWD and water vapour partial pressure. All of these models have been developed to model the effect of water vapour on the travelling GNSS signal, due to its complexity and variability.

# CHAPTER 3

## METHODOLOGY AND DATA USED IN THE RESEARCH

In this chapter, the methodology followed to develop the algorithm is explained. Also, the data used to test and validate the algorithm is described. This chapter describes the data used in the order it is used to develop and validate the algorithm. The first step is to calculate the vertical profile of environmental variables in the troposphere in order to build a profile of the refractivity of the troposphere with height. The refractivity of the troposphere is related to the tropospheric delay obtained in the Precise Point Positioning technique. Furthermore, the refractivity is related to the environmental variables, therefore, it is important to understand how the environmental parameters related to the refractivity of the troposphere change with height. Section 3.2 describes the data used to test the quality of the ZTD which is an input to the algorithm. Section 3.3 shows the description of the radiosonde data used to produce the vertical profile of the refractivity at different heights. The algorithm requires the height of the troposphere and the water vapor partial pressure at the site of measurement. Therefore, radiosonde data and GNSS data used for such purpose is described in section 3.3.

The algorithm developed to monitor the UHI intensity using GNSS data requires an intermediate step which is the estimation of temperature from GNSS data. The data used to test and validate this algorithm is described in section 3.4. The UHI intensity is monitored with GNSS data by estimating the temperature at two sites, an urban and a nearby rural area using the algorithm to estimate temperature from GNSS data. GNSS data (ZTD) is used as input to the algorithm. Meteorological data is used to validate the algorithm. The algorithm has been tested and validated with GNSS and meteorological data from stations in Los Angeles, California, USA; Hong Kong and Ningbo, China. Section 3.5 displays the description of the sites used for testing the algorithm and describes the GNSS data and the meteorological data used to test and validate the algorithm.

### **3.1 Data used to calculate the vertical profile of environmental variables in the troposphere.**

The refractive index of the troposphere is described by the environmental variables available in the troposphere: pressure ( $p$ ), temperature ( $T$ ) and water vapor partial pressure ( $e$ ). It is necessary to understand how these variable change with altitude in order to understand the change of the refractivity index of the troposphere at different heights. In this section, the vertical profiles of  $p$ ,  $T$  and  $e$  in the troposphere are obtained with radiosonde and meteorological data described here.

#### **3.1.1 Data used to calculate the vertical profiles of T**

The vertical profile of T is obtained using surface temperature data. Yearly meteorological data from 26 meteorological stations near the earth's surface—described in Table 3.1 for different latitudes—has been processed. All meteorological stations chosen have temperature sensors at 2 m above the surface (T2m). Also, these stations have been strategically chosen to cover all latitudes of the earth.

**Table 3.1.** Meteorological stations used to study temperature at different latitudes.

Station code	Country	City/place	Latitude (deg)	Longitude (deg)	Height (m)
634-01008-000	NOR	Svalbard, AP	78.25	15.46	26.82
71924	CAN	Resolute bay, Nunavut	74.72	-94.97	67.7
YHI-2502502	CAN	Ulukhakrok, NWT	70.76	-117.81	36
425-70261-000	USA	Fairbanks, AK	64.81	-147.87	135.3
638-26781-000	RUS	Smolensk	54.75	32.06	238
403-71600-000	CAN	Sable Island, NS	43.93	60	5
Fuke	JAP	Fuke, Japan	32.68	128.81	9
Taipei	CN	Taipei, Taiwan	24.96	121.16	203.12
425-91285-000	USA	Hilo, Hawaii	19.72	155.06	10.4
425-91212-000	USA	Guam, Mariana Island	13.47	144.79	75.3
228-48517-000	THA	Chumphon, Thailand	10.49	99.18	5.95
315-81401-000	FRA	Saint-Laurent, French Guiana	5.48	-54.03	5
138-63980-000	SYC	Seychelles	-4.66	55.51	3
155-67665-000	ZMB	Lusaka, Zimbabwe	-15.31	28.45	1154
129-61990-000	MUS	Plaisance, Mauritius	-20.43	57.68	57
303-83842-000	BRA	Curitiba, Brazil	-25.41	-49.26	924
501-94610-000	AUS	Perth, Australia	-31.92	115.97	20
501-94926-000	AUS	Canberra, Australia	-35.3	149.2	577.6
934390	NZL	Wellington, New Zealand	-41.33	174.8	12
304-85874-000	CHL	Balmaceda, Chile	-45.91	-71.49	516
888910	FKL	Stanley	-51.68	-57.77	22.9
MAC1	ANT	Macquarie Island	-54.50	158.94	-6.69
PALM	ANT	Palmer station	-64.78	-64.05	31.24
CAS1	ANT	Casey	-66.28	110.52	22.6
SYOG	ANT	Syowa	-69.01	39.58	50.09
MCM4	ANT	McMurdo	-77.84	166.67	98.02

### 3.1.2 Data used to find the refractivity profile of the troposphere

Radiosondes are small, expendable instruments suspended below a large balloon inflated with hydrogen or helium. As the radiosonde rises (at approximately 300 m/min), sensors on the radiosonde transmit pressure, temperature, relative humidity and GPS position data every second. Therefore, radiosonde data is used to compute the vertical profile of the refractivity of the troposphere with p, T and e data at different heights.

The Integrated Global Radiosonde Archive (IGRA), run by the National Ocean and Atmosphere Administration: NOAA (NOAA, 2019), contains radiosonde data from more than 2500, globally distributed stations. Most stations contain data from two daily soundings (00:00 UTC and 12:00 UTC). 12 IGRA radiosonde stations described in Table 3.2 have been used to calculate the profile of the refractivity shown in Chapter 4.

**Table 3.2.** Radiosonde stations used to compute troposphere refractivity profiles.

Station	Latitude (deg)	Longitude (deg)	Altitude (m)	Location
GLM00004320	76.76	-18.66	11	DANMARKSHAVN
UKM00003005	60.13	-1.18	82	LERWICK
UKM00003882	50.89	0.31	52	HERSTMONCEUX
TUM00017064	40.9	29.15	18	ISTANBUL BOLGE (KARTAL)
USM00072376	35.23	-111.81	2179	AZ FLAGSTAFF
HKM00045004	22.37	114.186	24	KOWLOON
RMM00091376	7.08	171.39	3.4	MAJURO / MARSHALL IS. INTNL.
KRM00091610	1.35	172.91	2	TARAWA
TVM00091643	-8.51	179.21	1	FUNAFUTI
CWM00091843	-21.2	-159.81	7	RAROTONGA
ASM00094610	-31.92	115.97	20.4	PERTH AIRPORT
AYM00089571	-68.57	77.96	18	DAVIS

## **3.2 Evaluation of the input to the algorithm**

The input to the algorithm developed in this research is the ZTD estimated from PPP technique. There are at least 6 implementations of the PPP technique in software available online or as stand-alone software. Each implementation follows a different strategy to estimate the PPP parameters as described in Chapter 4. In order to choose a PPP implementation for this research, the quality of the estimations in each of the implementations needs to be evaluated.

The quality of the ZTD estimation is evaluated by comparing the estimates from different PPP implementation and the IGS Tropospheric product. The Root Mean Square Error (RMSE) of the differences is used as indicator of the quality of the estimations. It is found that no significant difference exist, therefore, any of the software packages described can be used to estimated ZTD from PPP. The quality test of the ZTD estimations from PPP implementations is described in Chapter 4.

### **3.2.1 Data used to evaluate the quality of PPP ZTD estimation**

Data publicly available from the International GNSS Service (IGS) was used for this study. The IGS provides daily and hourly observation and navigation files, for 505 GNSS stations distributed globally. It also provides other products, such as satellite ephemeris, earth rotation parameters and tropospheric delays with different latencies. Their data is publicly available through their File Transfer Protocol (FTP) site (<ftp://cddis.gsfc.nasa.gov/gnss>). The tropospheric delay product is generated from ground-based GNSS data using Bernese GPS Software

version 5.0. A cut-off angle of  $7^\circ$ , IGS final satellite, orbit and EOP products are used in the computation (IGS, 2019). This shows that the IGS ZTD product is available approximately 3 weeks after the observation date, once the final products are available. The product contains a clock estimation and a receiver position estimation, which is presented as a constant. The estimation of the zenith delay, in mm—which is done as a random walk with a variance of 3 cm/hr—is also included in the tropospheric product. Atmospheric gradients—estimated as a random walk, with variance of 0.3 cm/hr—are also included in the tropospheric product. The temporal resolution of the zenith delay estimates is 5 min, and the mapping function is the GMF.

For this comparison, GNSS observation data from the nine IGS stations listed in Table 3.3 has been processed with each of the PPP implementations described in Chapter 4. The results have been compared with the IGS tropospheric product of the same stations for eight days. The days chosen for the comparison were the 27<sup>th</sup> calendar day of January, April, July and October 2016 and 2017, since these dates covered weather conditions across all four seasons, in both hemispheres.

**Table 3.3.** Summary of the IGS stations used to evaluate the quality of ZTD estimation.

Station	City	Country	Latitude (deg)	Longitude (deg)	Height (m)
ALGO	Algonquin Park	Canada	45.95	-78.07	202
REYK	Reykjavik	Iceland	64.13	-21.95	93.1
TIXI	Tixi	Russian Federation	71.63	128.86	46.9
MAL2	Malindi	Kenya	-2.99	40.19	-20.4
RIOP	Riobamba	Ecuador	-1.65	-78.65	2793.0
NAUR	Nauru	Nauru	-0.55	166.92	46.3
PARC	Punta Arenas	Chile	-53.13	-70.87	22.3

MAW1	Mawson	Antarctica	-67.60	62.87	59.1
MAC1	Macquarie Island	Australia	-54.49	158.93	-6.7

### 3.3 Calculation of the refractivity in the troposphere.

The profile of the refractivity (N) in the troposphere is an input to the algorithm developed in this research. N is related to pressure (P), Temperature (T), water vapor partial pressure (e) and ZTD. Therefore, this is the variable used to estimate temperature from ZTD as shown in Chapter 5. The profile of the refractivity in the troposphere is calculated from radiosonde data at different latitudes. 32 radiosondes around the world (Table 3.4) have been processed to calculate N. 10 years of radiosonde data has been processed for each station. It was found that the annual variation of the vertical profile of the refractivity (N vs height) is negligible. Therefore, the average of the profile of the refractivity per station can be used with data from any year.

#### 3.3.1 Radiosonde data used to calculate the profile of the refractivity

The 32 stations processed to calculate the profile of the refractivity of the troposphere at different latitudes are described in Table 3.4

**Table 3.4.** Selected radiosondes and their locations.

Radiosonde stations					
Code	Lat (deg)	Lon (deg)	Height (m)	City	Start
RSM00020046	80.63	58.06	21	POLARGMO IM. E.T. KRENKELJA	1957
SVM00001028	74.50	19.00	20	BJORNOYA	1957
JNM00001001	70.94	-8.67	9	JAN MAYEN	1949
SWM00002185	65.54	22.11	17	LULEA-KALLAX	1949
UKM00003005	60.14	-1.18	82	LERWICK	1941
RSM00027612	55.93	37.51	187	MOSKVA (DOLGOPRUDNYJ)	1934

UKM00003882	50.90	0.31	52	HERSTMONCEUX	1993
HRM00014240	45.82	16.03	123	ZAGREB/MAKSIMIR	1955
TUM00017064	40.90	29.15	18	ISTANBUL BOLGE (KARTAL)	1951
USM00072376	35.23	-111.82	2179	AZ FLAGSTAFF	1995
IRM00040841	30.25	56.97	1748	KERMAN	1967
CHM00056778	25.01	102.68	1892	KUNMING	1956
CHM00059758	20	110.25	64	HAIKOU	1956
INM00043192	15.48	73.82	58.4	GOA/PANJIM	1954
RPM00098646	10.32	123.98	23	MACTAN	1973
MYM00048601	5.30	100.27	3	PENANG/BAYAN LEPAS	1968
BRM00082099	0.05	-51.07	16	MACAPA (AERO)	2005
IDM00097180	-5.07	119.55	14	UJUNG PANDANG/HASANUDDIN	1973
BRM00082917	-10	-67.8	142	RIO BRANCO (AERO)	2004
BRM00083378	-15.87	-47.93	1061	BRASILIA (AERO)	1966
BRM00083650	-20.50	-29.317	5	TRINDADE (ILHA)	1967
MAM00067197	-25.03	46.95	8	TAOLAGNARO	1972
BRM00083971	-30	-51.18	3	PORTO ALEGRE (AERO)	1950
ASM00094910	-35.16	147.46	220.7	WAGGA WAGGA AMO	1946
SHM00068906	-40.35	-9.88	54	GOUGH ISLAND	1957
ARM00087860	-45.78	-67.5	58	COMODORO RIVADAVIA AERO	1958
FKM00088889	-51.82	-58.45	74	MOUNT PLEASANT AIRPORT	1990
ASM00094998	-54.50	158.94	6	MACQUARIE ISLAND	1948
AYM00089055	-64.23	-56.72	208	BASE MARAMBIO	1982
AYM00089611	-66.28	110.52	40	CASEY	1957
AYM00089002	-70.66	-8.25	50	NEUMAYER	1984
AYM00089022	-75.45	-26.21	30	HALLEY	1957

Also, the height of the troposphere and the amount of water vapor partial pressure has been calculated from the same radiosonde data.

### 3.3.2 Calculation of the height of the troposphere

Between the troposphere and the stratosphere there is a layer called the tropopause, which is defined using the vertical profile of temperature vs altitude. Figure 3.1 shows the approximate location of the tropopause.

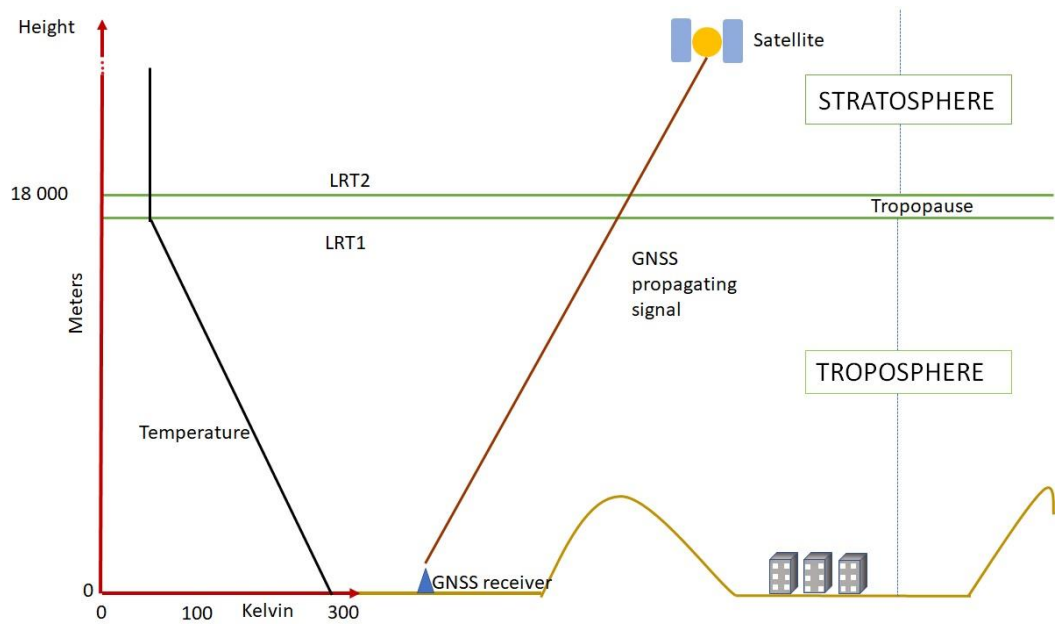


**Figure 3.1.** Locations of the tropopause and the troposphere, and the troposphere temperature profile.

The World Meteorological Organization (WMO) defines tropopause boundaries using its first and second lapse rates. The lower boundary of the tropopause can be determined using the first tropopause lapse rate (LRT1). According to the WMO, the LRT1 is defined as the lowest level at which the lapse rate (change of temperature with height) decreases to  $2\text{ }^{\circ}\text{C} / \text{km}$  or less, provided also that the averaged lapse rate between this level and levels within the next 2 km vertically does not exceed  $2\text{ }^{\circ}\text{C} / \text{km}$ . (WMO, 1957) If above the LRT1 the average lapse rate between any level and all higher levels with 1 km exceeds  $3\text{ }^{\circ}\text{C} / \text{km}$ , then a second tropopause (LRT2) is defined. This tropopause may be either within or above the 1 km layer (WMO, 1957). The tropopause is defined from the vertical profile of the temperature vs height. According to Hoinka (1998), at the height of the tropopause, air pressure equals values between 300 hPa at the poles and 70 hPa at the equator.

Figure 3.1 shows the total path of the propagating signal and the vertical temperature profile. The heights of LRT1 and LRT2 have been calculated, using radiosonde data (Feng et al., 2012; Seidel & Randel, 2006), GPS occultation (Rieckh et al., 2014), VHF radars (Hall et al., 2011) and a new method based on GNSS data combined with radiosonde data, which has been developed during this research.

#### Height of the tropopause calculated using radiosonde data

A detailed study of the LRT1 and LRT2 using radiosonde data has been presented by Feng et al. (Feng et al., 2012). Figure 3.2 shows the altitude of LRT1 and LRT2 at different latitudes (figure redrawn from (Feng et al., 2012)).

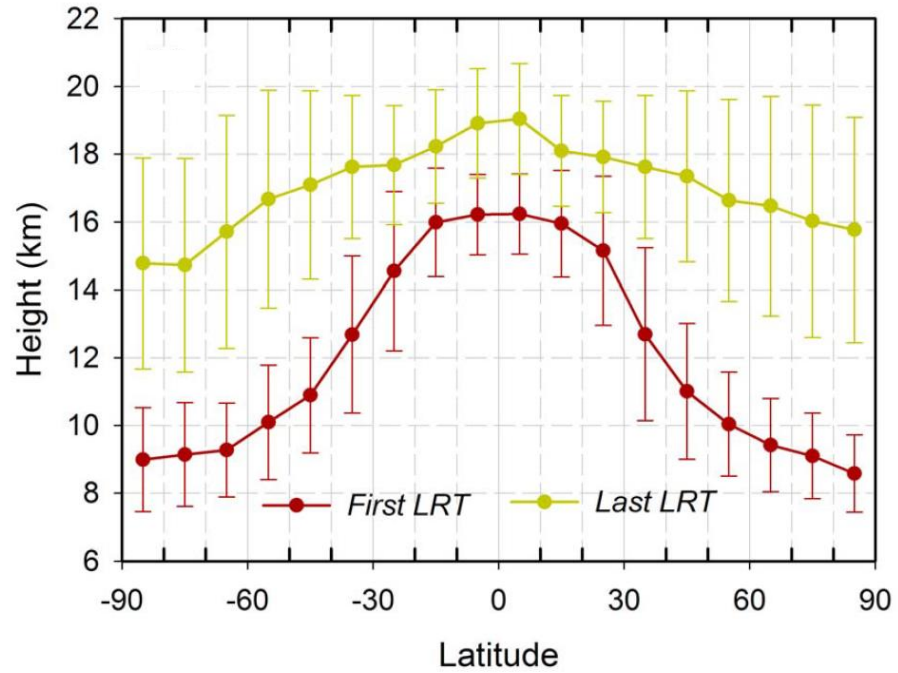


**Figure 3.2.** Height of the troposphere at different latitudes, found with radiosonde data, redrawn from (Feng et al., 2012).

As shown in Figure 3.2, LRT1 has its highest values in latitudes near the equator and its lowest values in latitudes near the poles. As well, it can be seen that tropopause thickness is greatest in the Polar Regions.

#### Height of the troposphere calculated using GNSS data

Another method derived during this research requires only GNSS data. For this method, the distance between LRT1 and LRT2 obtained with radiosonde is used to calculate an adjustment parameter called A1. Using the ZTD and the profile of the refractivity, equation (3.1) was derived:

$$h_{trop} = \frac{\ln\left(\frac{N_h ZTD \times 10^{-3} + 1}{N_0}\right)}{N_h} \quad (3.1)$$

where  $h_{\text{trop}}$  is the height of the troposphere,  $N_h$  is the ratio at which the refractivity decreases as height increases and  $N_0$  is the refractivity at point zero.

### 3.3.3 Calculation of the amount of water vapor partial pressure

The amount of water vapour present in the troposphere is hard to model and it cannot be measured directly from radiosonde data. To address this, mathematical models have been developed to relate water vapour pressure to other measurable or estimable variables, such as temperature or the zenith wet delay (ZWD). For example, an approximate relation between water vapour pressure and ZWD is shown in (Younes, 2016):

$$ZWD \approx \frac{0.217e}{T} \quad (3.2)$$

Assuming that water vapour exists until a height of 2 km, the earth's surface  $e_0$  is approximated as in (3.3) (Younes, 2016):

$$ZWD \approx 748 \frac{e_0}{T^2} \quad (3.3)$$

Also, models without the ZWD have been developed, such as that using Antoine's relation for ideal gases (4.3), where A, B and C are Antoine's constants ( $A = 8.071$ ,  $B = 1730.63$  and  $C = 233.43$ ) and T is the temperature, in Kelvin (Thomson, 1996).

$$e = \frac{10^{A - \frac{B}{C-T}}}{0.75} \quad (3.4)$$

All the existing models used in the estimation of water vapour partial pressure depend on the temperature complicating its modelling when temperature is an unknown, such as in the algorithm described in the

next section. Therefore, the  $e$  is empirically calculated using temperatures at different heights, using Antoine's equation (equation 3.4) and radiosonde data.

### 3.4 Algorithm to estimate temperature from GNSS data

The temperature is estimated using the relation of refractivity and environmental variables  $P$ ,  $e$  and the ZTD at a given site as described in Chapter 5. The algorithm is tested using the ZTD estimated using RTKLIB from observation data of 5 IGS stations around the world. The IGS stations used are described in Table 3.5 and the results of the algorithm are shown in Chapter 5.

#### 3.4.1 GNSS data used to test the algorithm

**Table 3.5.** Details of IGS ZTD data used in this thesis. The code, latitude, longitude and height were provided by the IGS.

GNSS stations					
Code	Latitude (deg)	Longitude (deg)	Height (m)	Location	Country
QAQ1	60.72	-46.05	110.40	Qaqortoq / Julianehaab	Greenland
HERS	50.87	0.34	76.50	Hailsham	United Kingdom
ISTA	41.10	29.02	147.20	Istanbul	Turkey
NAUR	-0.55	166.93	46.30	Nauru, Yaren District	Nauru
XMIS	-10.45	105.69	261.58	Christmas Island	Australia

#### 3.4.2 Surface Meteorological data used to validate the algorithm

In order to validate the results achieved by the algorithm, meteorological data has been collected at the same latitudes as GNSS stations. The International GNSS Service provides weather data for some stations in an ".m" file, which contains daily temperature, pressure and humidity data, at 15 min intervals. There are no standards for either the variables or the data formats, so some stations provide different measurements or use

different file formatting. Data can be downloaded from the IGS' FTP server: <ftp://cddis.gsfc.nasa.gov/gnss/data/daily/2017>. The meteorological stations have T2m sensors (2 m above the earth's surface) that report temperature. Table 3.6 contains the details of the meteorological stations whose data was used for validation purposes.

**Table 3.6** Details of the meteorological stations selected for algorithm validation.

Station code	Country	City/place	Latitude (deg)	Longitude (deg)	Height (m)
QAQ1	GRL	Qaqortoq / Julianehaab	60.72	-46.05	110.4
HERS	ENG	Hailsham	50.87	0.34	76.5
ISTA	TUR	Istanbul	41.1	29.02	147.2
NAUR	NAR	Nauru, Nauru	-0.55	166.92	46.3
XMIS	AUS	Christmas Island	-10.44	105.68	261.58

Observation data from days of the year 88,89,90,91,92 (spring), 178,179,180,181,182 (summer), 268,269,270,271, 272 (autumm), 358,359,360,361 and 362 (winter) for the stations described in Table 3.5 and 3.6 has been proceesed with RTKLIB to estimate the ZTD and validate the output. Chapter 5 shows the output of the algorithm and its validation.

### **3.5 Development of an algorithm to monitor the UHI intensity from GNSS data**

The algorithm developed to monitor the UHI intensity from GNSS data is explained in Chapter 6. It requires the estimation of temperature in an urban and a rural area from PPP estimated ZTD. The algorithm is tested using GNSS observation data from three metropolitan areas, Los Angeles (34.05349° N, -118.24532° E), California, USA, the Special

Administrative Region of Hong Kong (22.279812° N, 114.161766° E) and Ningbo (29.86569° N, 121.53916° E), China. The validation of the results is done by comparing the outputs of the algorithm with the temperatures reported by weather stations near the GNSS stations. The results and validation of the algorithm are shown in Chapter 6.

### **3.5.1 Site description: Los Angeles (LA)**

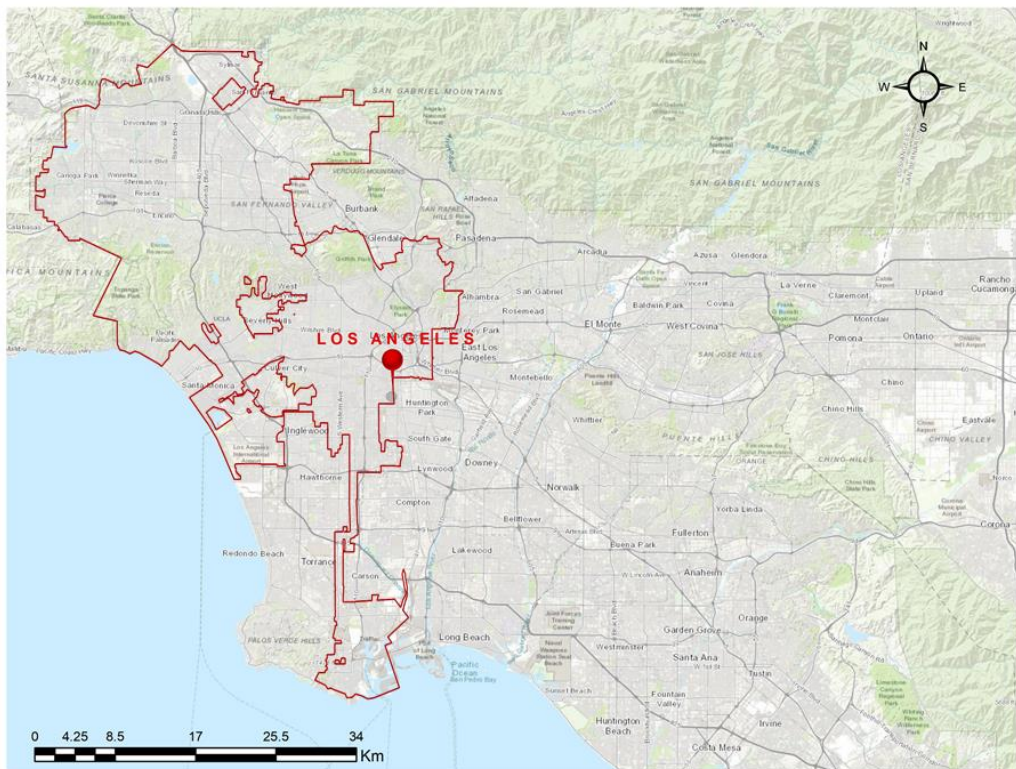
According to the Britannica encyclopaedia (Britannica, 2019b) LA is the second most populous city and metropolitan area in the United States of America, after New York. In 2010, the total population including the LA-Long Beach-Santa Ana metropolitan areas, was 12,828,837 inhabitants (Britannica, 2019b). Today, it is an important economic centre on the US west coast and is located across a broad coastal plain between mountains and the Pacific Ocean. LA County contains 90 incorporated cities, including Beverly Hills, Pasadena and Long Beach. The County encompasses 2300 km<sup>2</sup> of desert and 120 km of seacoast. LA's location in the USA shown in Figure 3.3.



**Figure 3.3.** LA location map.

The LA climate is typically classified as semi-arid or Mediterranean, as the region's latitude is far enough south to dissipate the most severe North Pacific winter storms; a cooling layer of marine air moderates the summer sun and the mountains to the east shield the region from potentially intense blasts of desert heat and cold. According to historic weather data, the city's mean temperature is approximately 18°C (Britannica, 2019b). In terms of built environment layout, the city is composed of a series of widely dispersed settlements, loosely connected to downtown. LA was chosen as an algorithm test site due to its dispersed distribution and the fact that there are different geographical conditions across the settlement, such as mountains, the Pacific Ocean and desert.

Another factor favouring LA as a test location was the availability of GNSS and meteorological data; there are several IGS GNSS stations in the different environments within the boundary of the LA metropolitan area. Similarly, weather data is collected at different points of the metropolitan area. The layout of LA City and its metropolitan area is shown in Figure 3.4.



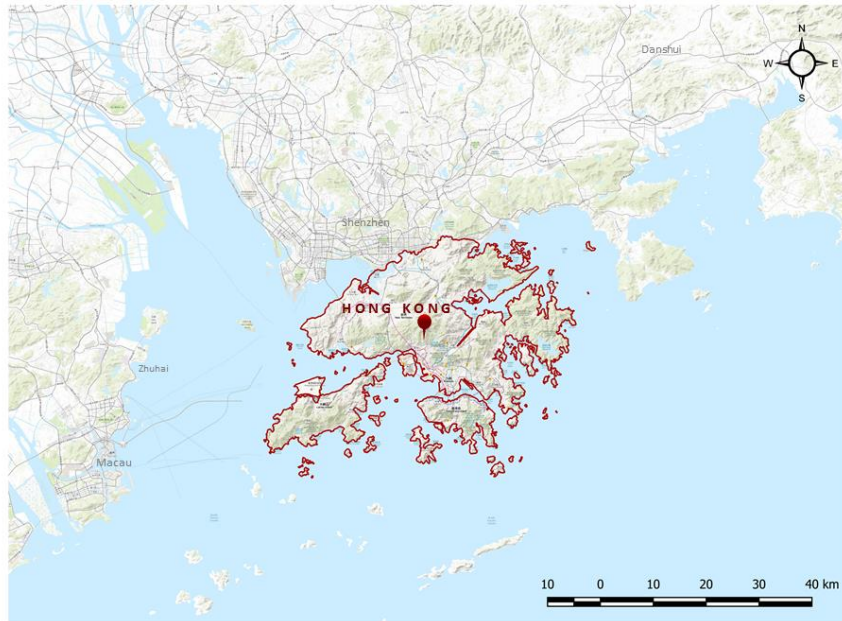
**Figure 3.4.** Los Angeles city map and incorporated areas.

Figure 3.4 shows the LA County boundary in red. The metropolitan area, although partly in other counties, is physically attached to LA County.

### **3.5.2 Site description : Hong Kong (HK)**

HK is a Special Administrative Region of China, located to the east of the Pearl River estuary on the Chinese south coast. The region is bordered

by Guangdong province and by the South China Sea to the east, south and west. It consists of Hong Kong Island, the southern part of Kowloon Peninsula and Stonecutters (Ngong Shuen) Island and the New Territories on the mainland. There are 230 large and small offshore islands (Britannica, 2019a). Figure 3.5 shows the HK location.



**Figure 3.5.** HK location, on the southern coast of China.

HK is located at the northern fringe of the tropical zone, and so its monsoon-based seasonal changes are well marked, with hot, humid summers and cool, dry winters. The mean January temperature is 16 °C and the mean for July is 29 °C. The average annual rainfall is approximately 2,220 mm; more than half of the rainfall falls during summer and 10% falls in the dry period extending from November–March. HK is affected by five or six typhoons annually, on average (Britannica, 2019a).

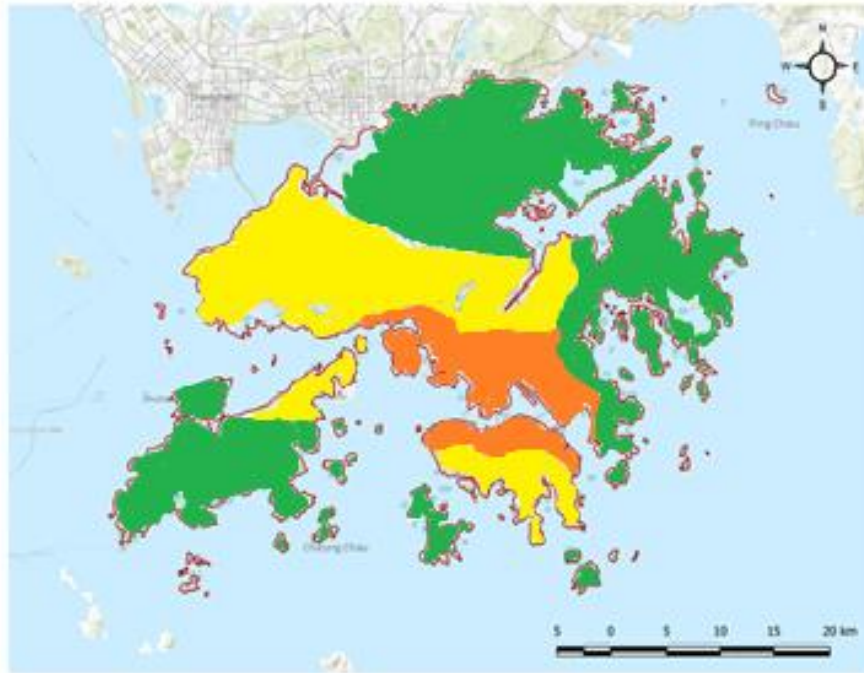


**Figure 3.6.** Population density in Hong Kong. Green= low density, yellow= medium density, orange= high density.

Given the limited space available, the city is densely populated. Figure 3.6 shows a map of the population density in HK in 2018 according to the Census and Statistics department. The green areas have a low population density (< 4000 inhabitants per km<sup>2</sup>), the yellow areas have a medium population density (4001-10 000 inhabitants per km<sup>2</sup>) and the orange areas have a high population density (>10001 inhabitants per km<sup>2</sup>). The amount of built structures is higher as the population density increases.

### **3.5.3 Site description: Ningbo (NB)**

Ningbo is situated in the coastal plain of the Yong River, approximately 25 km upstream from its mouth in Hangzhou Bay. Its land area is 9,816 km<sup>2</sup>, and its oceanic territory amounts to 9,758 km<sup>2</sup>. In total, the territory has 1,562 km of coastline, consisting of 788 km of mainland coastline

and 774 km of island coastline. There are 531 islands under the city's administration (Britannica, 2019c) and the 2012 population estimate for Ningbo was 7,639,000 inhabitants. The location of Ningbo is shown in Figure 3.7.

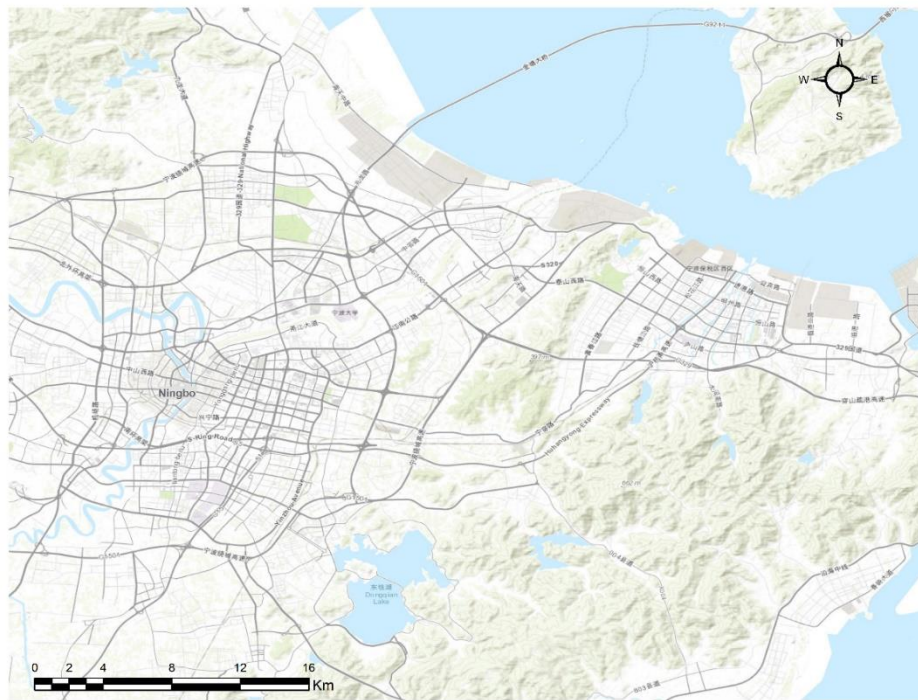


**Figure 3.7.** Ningbo location.

The Ningbo climate is classified as humid subtropical, with four distinct seasons, characterized by hot, humid summers and cold, cloudy and drier winters. The mean annual temperature is 16.53 °C, the city receives an average annual rainfall of 1440 mm and is affected by the 'plum rains' of the Asian monsoon, in June. Ningbo can experience typhoons from August–October (Britannica, 2019c).

The city of Ningbo is divided in six urban districts, with the district of Yinzhou the one relevant to this study. Yinzhou District is in the southern part of the city and has wide roads, large residential areas and big parks

with abundant vegetation—which makes it a good test site in terms of urban- and rural-type areas. Figure 3.8 presents a map of the location of the receivers taken from GoogleMaps.

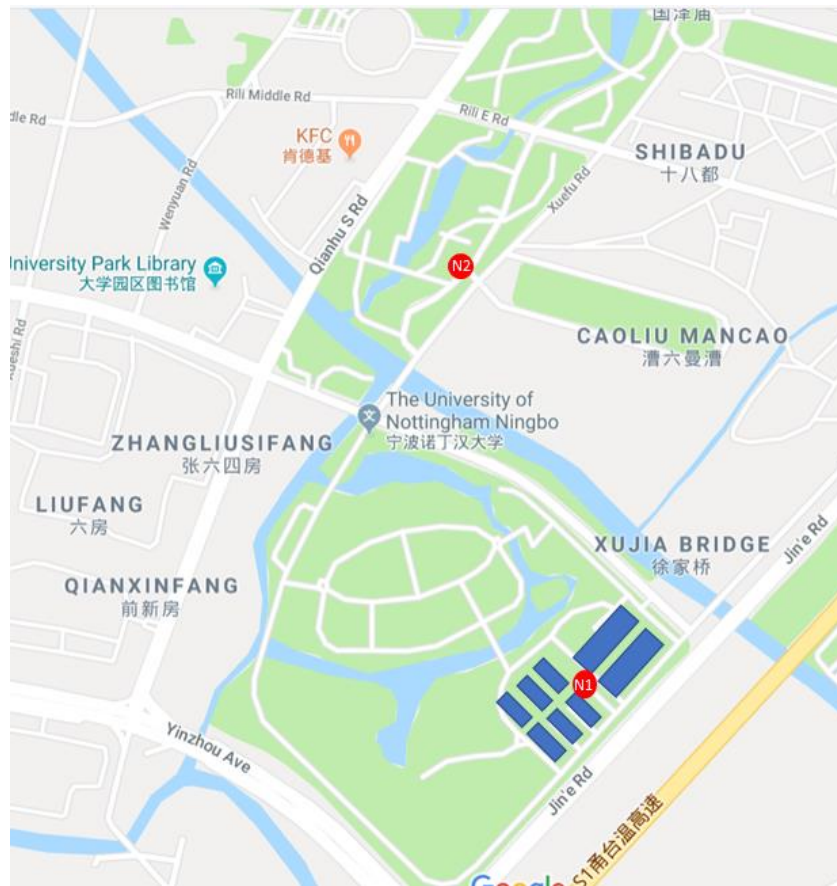


**Figure 3.8.** Location of the testing sites in UNNC and a park nearby  
Source: GoogleMaps

The test site was in the grounds of the University of Nottingham Ningbo campus (UNNC) (location: 29.80 121.556 30) and in park near UNNC (location: 29.81 121.56 14.18) as shown in Figure 3.8. At both points, GNSS data and meteorological data were collected. GNSS data has been used to calculate the temperature and meteorological data has been used to validate algorithm results.

### 3.5.4 GNSS data used to test the algorithm in LA

The map in Figure 3.9 shows the location of 16 IGS GNSS stations in the LA metropolitan area. Each station is in a different environment, including mountains, near water bodies and near the desert.

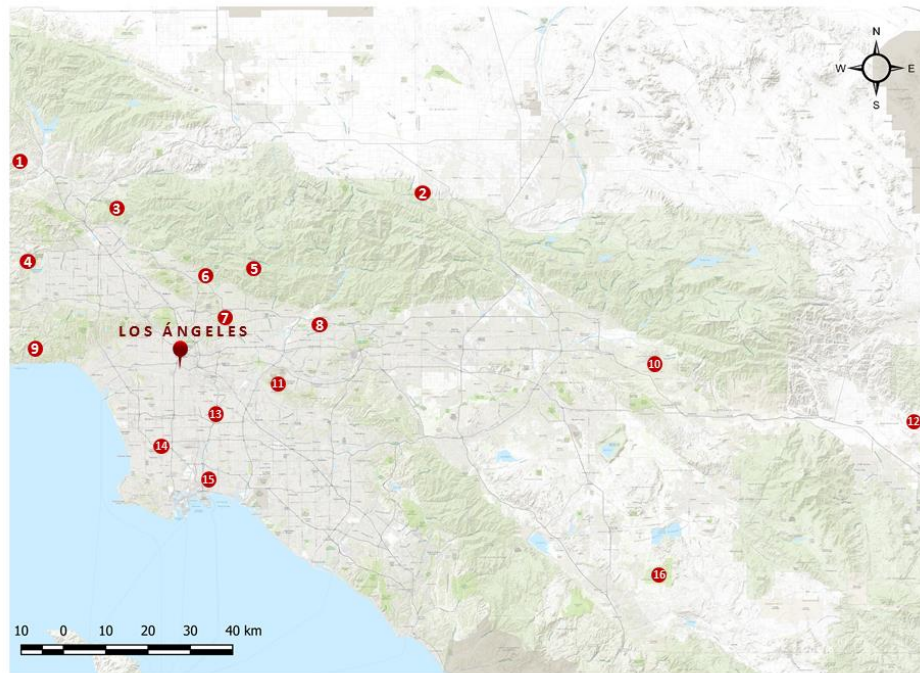


**Figure 3.9.** LA metropolitan area map showing locations of the IGS stations used in this study.

Table 3.7 indicates the map number, the IGS code, the latitude, longitude and height of the stations, as reported by the IGS, together with the name of the county or city where the station is located. The last column indicates the type of station, being either rural (R) or urban (U). The classification of the type of area was done *a-priori*, by looking at station surroundings and applying the definition of urban and rural areas described in Section 2.5. Stations were classified prior to their data being processed. The images used for classification of the type of area are shown in Appendix 1.

**Table 3.7.** Summary of Los Angeles metropolitan area IGS station locations. The images used for classification of the type of area are shown in Appendix 1.

Number in the map	IGS code	Latitude (deg)	Longitude (deg)	Height (m)	City/County	Type
1	SFDM	34.46	-118.75	291.52	Piru	R
2	TABL	34.38	-117.67	2228.03	Wrightwood	R
3	CMP9	34.35	-118.41	1137.99	Sylmar	R
4	ROCK	34.23	-118.67	553.39	Simi Valley	R
5	WLSN	34.23	-118.05	1705.26	Mt. Wilson	R
6	JPLM	34.20	-118.17	423.98	Pasadena	R
7	CIT1	34.13	-118.12	215.35	Pasadena	U
8	AZU1	34.12	-117.89	144.75	Azusa	U
9	SPK1	34.05	-118.64	440.13	Saddle Peak	R
10	CRFP	34.04	-117.10	688.82	Yucaipa	R
11	WHC1	33.98	-118.03	94.25	Whittier	U
12	WIDC	33.93	-116.39	445.04	Sky Valley	R
13	HOLP	33.92	-118.16	-6.71	Hollydale	U
14	TORP	33.79	-118.33	-5.22	Torrance	U
15	LBCH	33.79	-118.20	-27.58	Long Beach	U
16	BILL	33.58	-117.06	470.06	Temecula	R

### 3.5.5 GNSS data used to test the algorithm in HK

Raw GNSS data is provided by Hong Kong Geodetic Survey Services (HKGSS), part of the Land Department of the Survey and Mapping Office of the Special Administrative Region of Hong Kong. Data from 19 stations can be downloaded from their website: (HKGSS, 2019). One h data can be obtained in 5 s or 10 s intervals. Daily observations (24 h) can be downloaded in 5 or 30 s intervals, and daily data in 30 s intervals was chosen for this study. The whole network operated by the HKGSS is mapped in Figure 3.10.

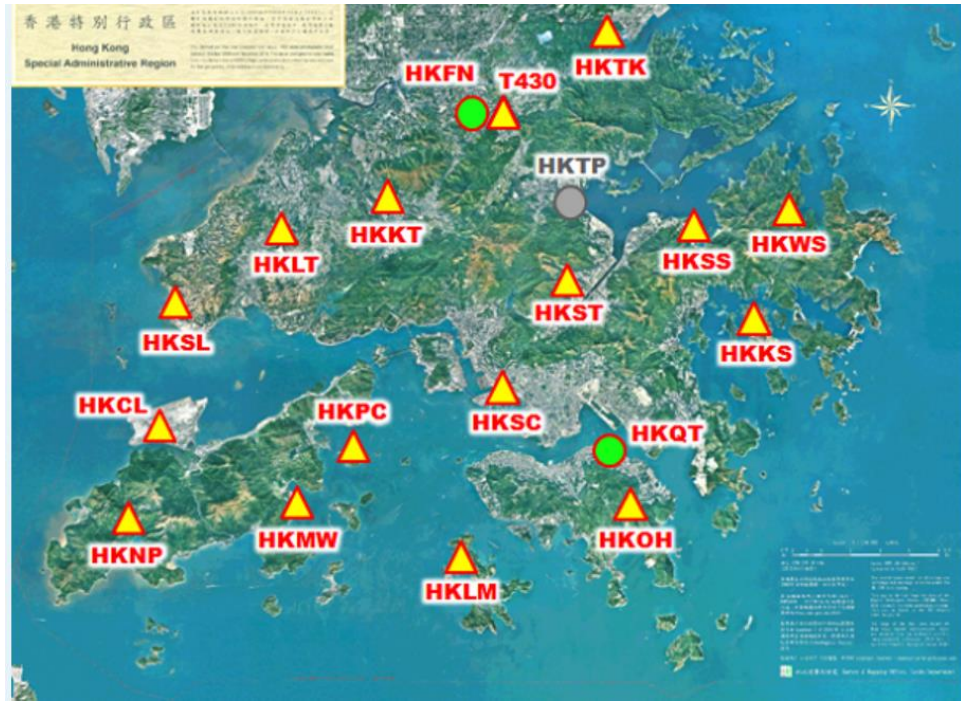


**Figure 3.10.** HK station locations, from HKGSS (HKGSS, 2019).

Figure 3.10 shows all the GNSS HK stations operated by HKGSS. The station classification type, either rural or urban, was done following the same visual procedure applied to the LA metropolitan area stations. The locations of the GNSS stations depicted in figure 3.10 are shown in Table 3.8. The classification of the type of station is shown in Appendix 3.

**Table 3.8.** Location of GNSS stations in Hong Kong. Classification of the stations shown in Appendix 3.

	latitude			Longitude			Height (m)
	deg	min	sec	deg	min	sec	
HKCL	22	17	45.03	113	54	27.79	7.71
HKFN	22	29	40.87	114	8	17.40	41.21
HKKS	22	22	4.43	114	18	42.96	44.71
HKKT	22	26	41.66	114	3	59.63	34.57
HKLM	22	13	8.25	114	7	12.21	8.55
HKLT	22	25	5.28	113	59	47.84	125.92
HKMW	22	15	20.92	114	0	11.43	194.94
HKNP	22	14	56.63	113	53	37.94	350.67
HKOH	22	14	51.67	114	13	42.78	166.40
HKPC	22	17	5.81	114	2	16.22	18.13
HKQT	22	17	27.72	114	12	47.57	5.17
HKSC	22	19	19.81	114	8	28.27	20.23
HKSL	22	22	19.21	113	55	40.73	95.29
HKSS	22	25	51.84	114	16	9.45	38.71
HKST	22	23	42.97	114	11	3.27	258.70
HKTK	22	32	47.64	114	13	23.80	22.53
HKWS	22	26	3.416	114	20	7.35	63.79
KYC1	22	17	2.58	114	4	34.70	116.38
T430	22	29	40.99	114	8	17.51	41.32

### 3.5.6 GNSS data used to test the algorithm in NB

GNSS data was collected with a GS10 Leica Receiver every second. The GS10 Leica receiver can receive GPS, GLONASS, BeiDou, Galileo and QZSS signals. One receiver was placed in the living area of the UNNC campus—which was defined as an urban area because there is a fountain in the middle of the living area, surrounded by seven-storey buildings, in a busy pedestrian area. A panoramic picture of the UNNC location where the GNSS and the temperature sensors were located is shown in Figure 3.11.



**Figure 3.11.** Panoramic view of the urban-like area inside the University of Nottingham campus, Ningbo, China.

The second receiver was placed in a rural area located in a park near the UNNC campus. The park is a big open space with a few trees scattered around; it is a very quiet area, with few pedestrians or vehicles. A panoramic view of the park where the GNSS and temperature sensors were placed is shown in Figure 3.12.



**Figure 3.12.** Ningbo rural area where the GNSS and temperature receivers were placed.

GNSS and meteorological data were captured for September 18 and 19, 2017 (DOY 262 and 263), due to the availability of resources and the clear weather of those late summer days. Summer days were chosen as that is when the UHIs are most easily detected.

### **3.5.7 Meteorological data used to validate the algorithm in LA**

The Meteorological data used for validation has been collected from a crowdsourcing system called Weather Underground (Underground, 2019) (WU). WU is formed by more than 250000 privately owned personal weather stations that report weather variables every hour: temperature, dew point, humidity, wind direction, wind speed, wind gust, pressure, precipitation, precipitation accumulated and condition of the weather.

Access to WU site is free and it enables the user to see microclimates around his exact location. Most of the personal weather stations available are concentrated in North America, Europe and Japan. WU reports hourly temperature for all available stations. However, only stations in airports, weather balloons and stations with high quality report historic data. Validation of the algorithm has been done with hourly data from days 90, 91,180,181,270,271, 360 and 361 of the year 2017. The stations are all located in Los Angeles metropolitan area, they are described in Table 3.9. The image used to classify the type of area (urban or rural-like) are show in Appendix 2.

**Table 3.9.** Weather stations in LA metropolitan area used for validation of the algorithm. Classification done using images in appendix 2.

Code	Location	Latitude (deg)	Longitude (deg)	Type
Temecula	McClellan Airport CA	33.12	-117.32	R
Pasadena	Bob Hope Airport, CA	34.15	-118.34	U
Redondo	Los angeles International Airport, CA	33.94	-118.38	U
Long Beach	Long Beach Daugherty Airport, ca	33.81	-118.14	U

### 3.5.8 Meteorological data used to validate the algorithm in HK

Two sources of data were used: data reported by GNSS stations in a meteorological file (.m), which contained pressure, temperature and relative humidity at the same rate of the GNSS observation data. The other source is data provided by Weather Underground ([www.weatherunderground.com](http://www.weatherunderground.com), WU) from the Hong Kong international Airport. Table 3.10 shows the code, source and locations of the meteorological data used for validation.

**Table 3.10.** HK meteorological stations used for validation

<b>Name</b>	<b>Lat (deg)</b>	<b>Long (deg)</b>	<b>Source</b>	<b>Type</b>
Hong Kong international Airport	22.26	113.95	WU	R
Hong Kong Observatory	22.49	114.14	IGS	U

### **3.5.9 Meteorological data used to validate the algorithm in NB**

The location of the temperature sensors used for validation of the algorithm is detailed in Table 3.11.

**Table 3.11.** Location of temperature and GNSS sensors in Ningbo

<b>CODE</b>	<b>Latitude</b>	<b>Longitude</b>	<b>Height</b>	<b>Type</b>
N1	29.80	121.56	23.19	U
N2	29.81	121.56	14.18	R

Meteorological data was collected from a location (Table 3.11) next to the GNSS receiver, using an Si 7013 temperature sensor (Silicon labs). This is a humidity and temperature sensor, with sensitivities of  $\pm 3\%$  RH and  $\pm 0.4\text{ }^{\circ}\text{C}$ . The sensor came with an evaluation kit (Si7013USB-Dongle) which is connected to a computer to download measurements. The software controlling the sensor and recording the measurements is provided by Silicon Labs Data, and it recorded data every minute.

# CHAPTER 4

## Evaluation of ZTD estimates derived from different PPP implementations

In this chapter, a comparison between ZTDs estimated using different PPP software packages and PPP online services is done. The comparison is done in order to evaluate the quality of the estimations and justify the selection of the software used for ZTD estimation. These results have been published in the journal *Sensors*, as Mendez Astudillo et al. (2018).

### **4.1 Methodology**

Observation data from the nine IGS stations in Table 3.3 has been processed with each software package described in section 2.3.3. The days chosen for the comparison were the 27<sup>th</sup> calendar day of January, April, July and October 2016 and 2017, since these dates covered weather conditions across all four seasons, in both hemispheres. In all implementations, the ZTD was estimated in kinematic mode. The quality of the estimation was assessed by comparing the estimation obtained with the software, with the ZTD available in the IGS Tropospheric product.

The Root Mean Square Error (RMSE) has been used as the quality indicator in this performance assessment

$$RMSE = \sqrt{\frac{\sum_{i=1}^n (ZTD_{estimated} - ZTD_{IGS})^2}{n}} \quad (4.1)$$

where n is the total number of ZTD estimates available.

## 4.2 Results

The RMSE values for each station with data from the different software and from the IGS tropospheric product are shown in Figures 4.1–4.8. In all the Figures, the first three stations are in the northern hemisphere, the next three are near the equator and the last three are in the southern hemisphere.

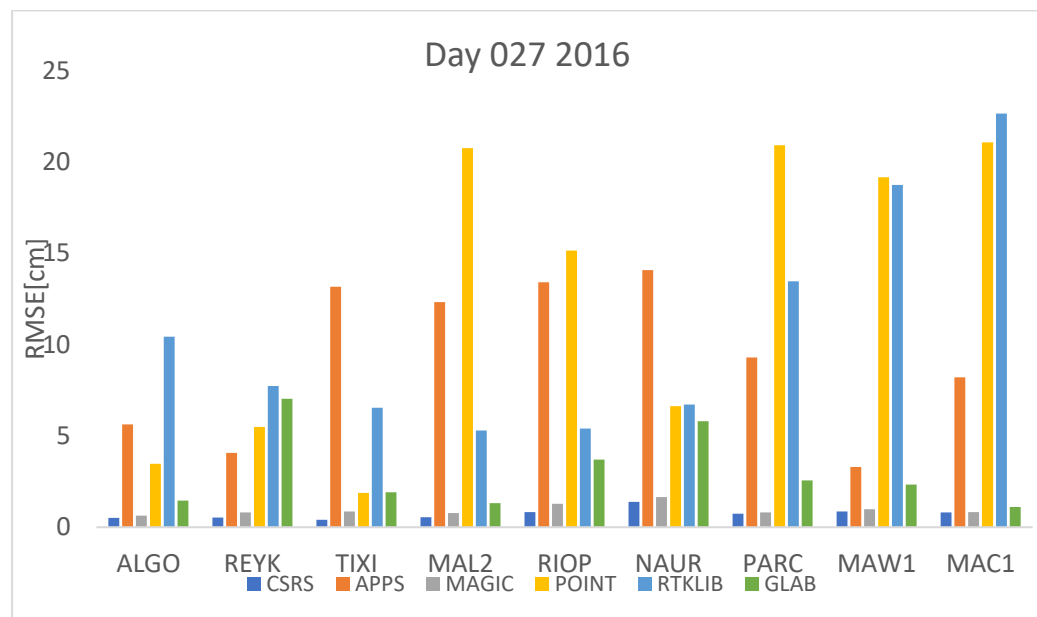


**Figure 4.1.** RMSE, in cm, for day 27, 2016.

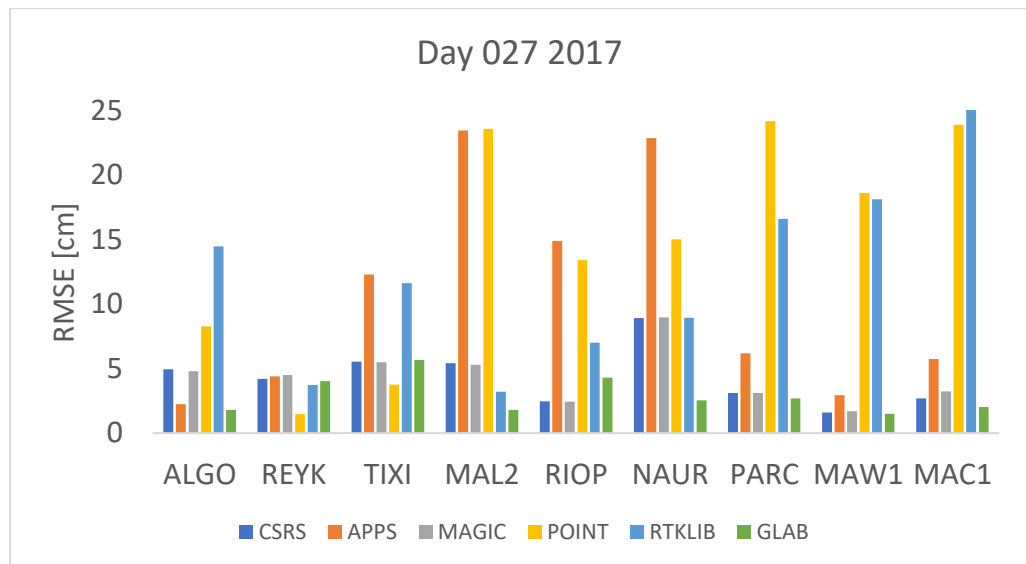


**Figure 4.2.** RMSE, in cm, for day 27, 2017.

Figure 4.1 and 4.2 represent 27 January 2016 and 2017, respectively, which is winter in the northern hemisphere and summer in the southern hemisphere. It can be seen in both figures that the estimates obtained with APPS and POINT for stations MAL2 and NAUR were different from the value obtained with the IGS tropospheric product. In addition, stations MAL2 and RIOP produced very high RMSE values with POINT and APPS. However, in both days, the RMSE obtained with CSRS-PPP and MagicGNSS were < 5 cm, for all stations, while high RMSE values for stations PARC, MAW1 and MAC1 were obtained with RTKLIB and POINT.

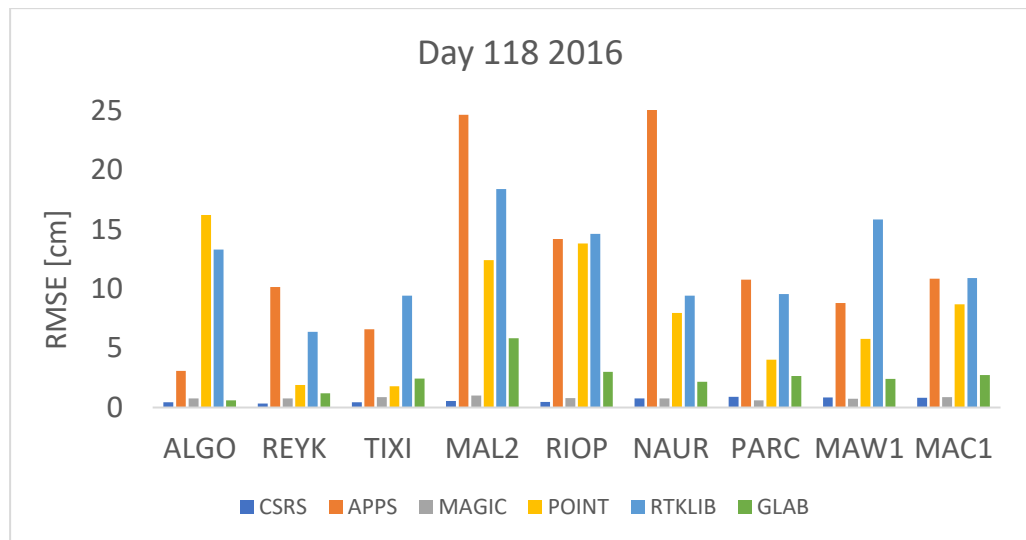


**Figure 4.3.** RMSE, in cm, for day 118. 2016

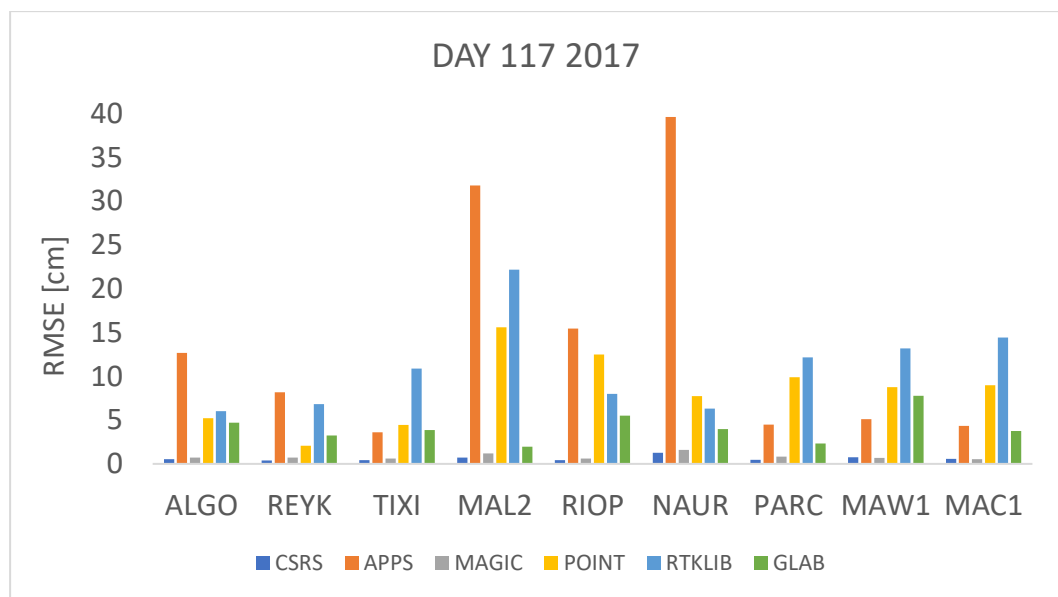


**Figure 4.4.** RMSE, in cm for day 117 2017.

April 27, 2016 and 2017 are days 118, 2016, and 117, 2017, respectively, which are spring days in the northern hemisphere and autumn days in the southern hemisphere, indicating that mild changes of temperature are to be expected. The RMSE values of the differences between the estimated ZTD and the IGS tropospheric product values are depicted in

Figure 4.3 and Figure 4.4. It can be seen that APPS, POINT and RTKLIB obtained high RMSE values for stations MAL2 and NAUR. In contrast, it can be seen that the RMSE value was very low in all stations (< 5 cm) for the estimates obtained using CSRS-PPP and MagicGNSS.

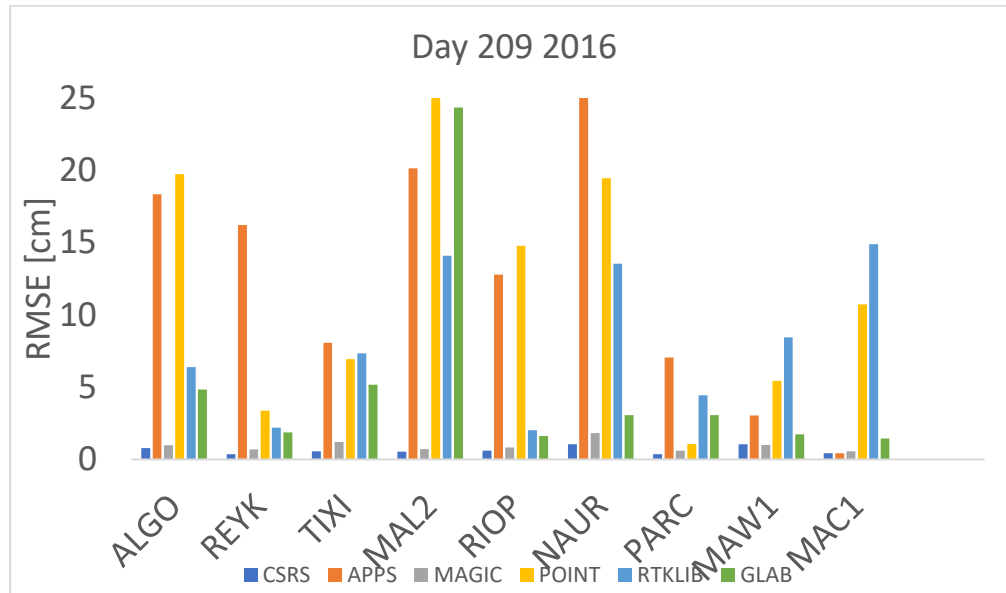


**Figure 4.5.** RMSE, in cm, for day 209, 2016.

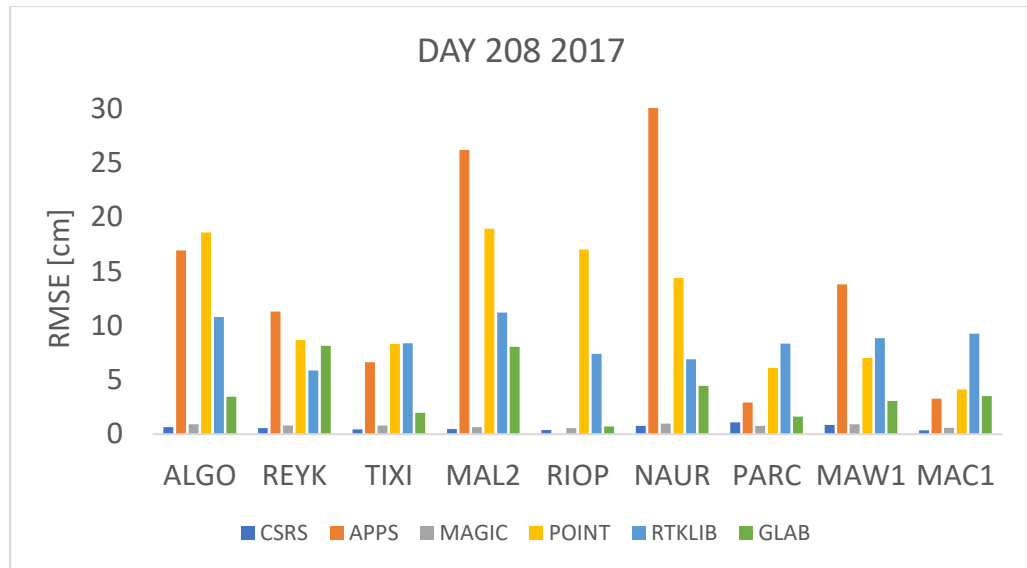


**Figure 4.6.** RMSE, in cm, for day 208, 2016.

Day 209, 2016 and 208, 2017, corresponded to 27 July 2016 and 2017, respectively. It was a summer day in the northern hemisphere, with high temperatures expected, and a winter day in the southern hemisphere, with low temperatures expected. Figures 4.5 and 4.6 depict the RMSE values for days 209, 2016 and 208, 2017 respectively. It can be seen that the highest RMSE values were found with data from stations NAUR, MAL2 and RIOP, processed with APPS, POINT and RTKLIB. In contrast, the lowest RMSE values were those computed using CSRS-PPP and MagicGNSS, for all stations.

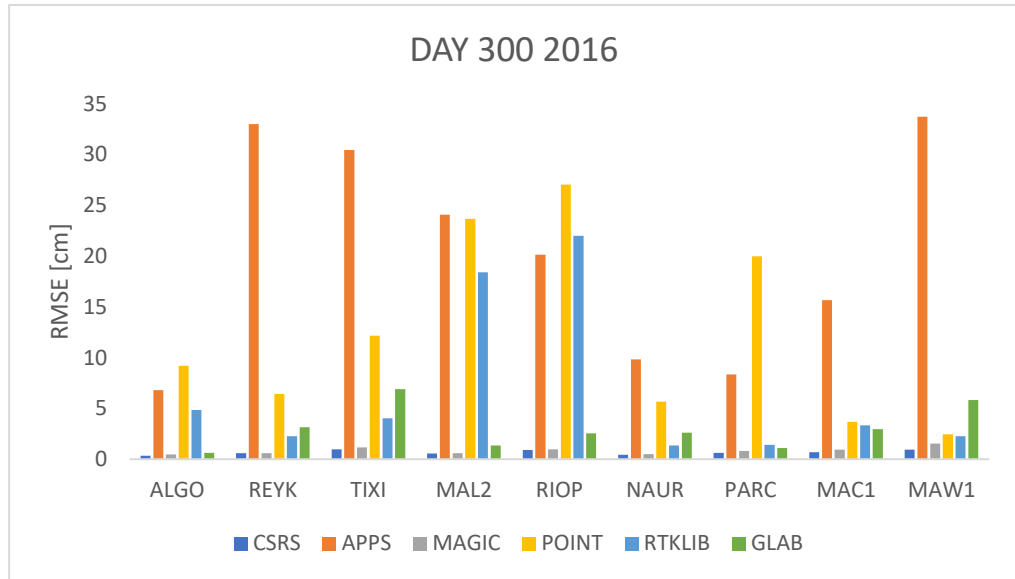


**Figure 4.7.** RMSE, in cm, for day 300, 2016.

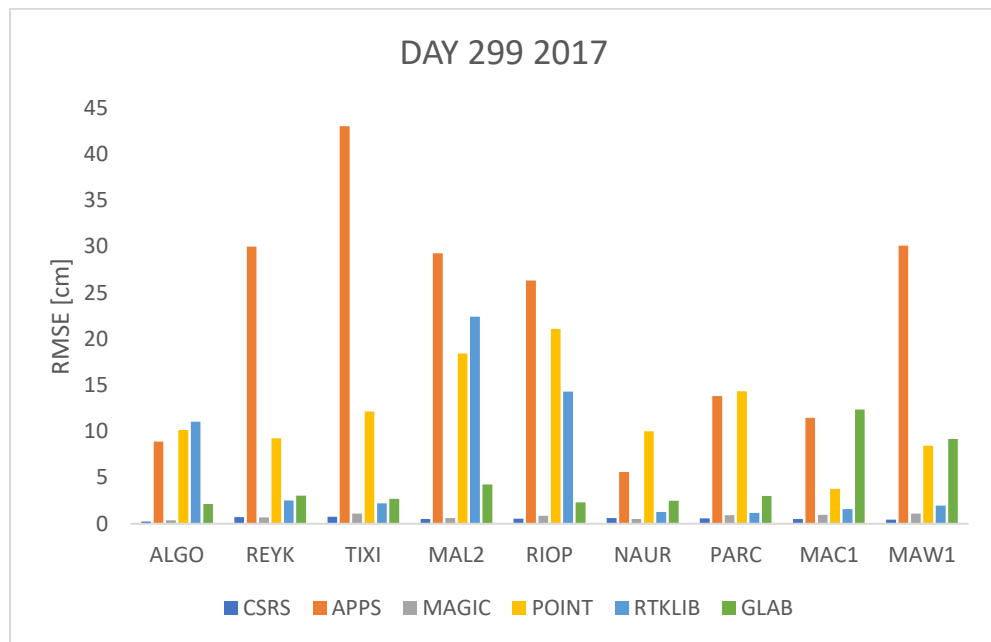


**Figure 4.8.** RMSE, in cm, for day 299, 2017.

Figure 4.7 and 4.8 show the RMSEs for data from 26 October 2016 and 2017 (days 300 and 299 respectively). This is an autumn day in the northern hemisphere, with colder temperatures expected, and a spring day, with mild temperatures expected, in the southern hemisphere.

According to the data presented in figures 4.7 and 4.8, the RMSEs obtained using APPS were very high (> 20 cm), for stations REYK, TIXI and MAW1, while those obtained with CSRS-PPP and MagicGNSS remained at < 2 cm, for all cases. Figures 4.1–4.8 show a trend in which, in most cases, the RMSEs obtained with data from stations near the equator were higher than those obtained for other stations, with most of the software packages used to apply the PPP technique.

In order to further study the ZTD estimation quality at different latitudes, the stations were divided into three groups, based on their latitude. The GNSS data from the stations at the same latitude was compared to the respective IGS Tropospheric Product. The RMSEs of all the differences from the stations in the group were then calculated, and the results are listed in Tables 4.1–4.4.

The regions were defined as follows: North included ALGO, REYK and TIXI; Centre included MAL2, RIOP and NAUR; and South included PARC, MAW1 and MAC1. Finally, Table 4.8 shows the RMSE for all differences estimated by applying each software and each online PPP service.

**Table 4.1.** RMSE values (in cm), by groups, for Jan 27 2016 and 2017.

	CSRS	APPS	MAGIC	POINT	RTKLIB	GLAB
North 2016	0.48	8.59	0.78	3.90	8.40	4.29
Centre 2016	0.98	27.61	1.29	19.06	5.84	4.04
South 2016	0.80	7.39	0.87	20.39	18.67	2.12
North 2017	4.92	7.64	4.96	5.32	10.93	4.12
Centre 2017	6.15	25.71	6.18	17.82	6.82	3.07
South 2017	2.55	5.15	2.77	22.36	20.46	2.13

**Table 4.2.** RMSE values (in cm), by groups, for April 27, 2016 and 2017.

	<b>CSRS</b>	<b>APPS</b>	<b>MAGIC</b>	<b>POINT</b>	<b>RTKLIB</b>	<b>GLAB</b>
North 2016	0.42	7.18	0.80	9.22	10.10	1.6
Centre 2016	0.60	31.26	0.86	11.66	14.62	3.99
South 2016	0.86	10.18	0.75	6.45	12.39	2.61
North 2017	0.45	8.96	0.69	3.82	8.19	3.62
Centre 2017	0.87	30.64	1.21	12.36	14.09	3.61
South 2017	0.62	4.66	0.69	9.24	13.29	4.76

**Table 4.3.** RMSE values (in cm), by groups, for July 27, 2016 and 2017.

	<b>CSRS</b>	<b>APPS</b>	<b>MAGIC</b>	<b>POINT</b>	<b>RTKLIB</b>	<b>GLAB</b>
North 2016	0.60	14.89	0.98	8.85	5.76	3.17
Centre 2016	0.77	20.96	1.22	20.23	11.35	1.77
South 2016	0.68	4.45	0.75	6.97	10.22	2.03
North 2017	0.55	12.36	0.83	12.78	8.59	4.5
Centre 2017	0.57	29.70	0.75	16.88	8.71	4.71
South 2017	0.82	8.36	0.77	5.88	8.82	1.38

**Table 4.4.** RMSE values (in cm), by groups, for October 26, 2016 and 2017.

	<b>CSRS</b>	<b>APPS</b>	<b>MAGIC</b>	<b>POINT</b>	<b>RTKLIB</b>	<b>GLAB</b>
North 2016	0.7	21.81	1.07	5.9	3.65	3.6
Centre 2016	0.71	18.75	0.8	23.75	16.59	1.77
South 2016	0.7	26.59	0.8	8.59	2.79	4.37
North 2017	0.41	27.93	0.87	7.92	6.54	8.94
Centre 2017	0.54	24.05	0.81	18.11	15.36	3.31
South 2017	0.7	41.32	0.8	10.53	2.06	2.73

According to the results shown in Tables 4.1–4.4, CSRS-PPP was the online software that performed best for all stations, as its derived RMSEs were consistently lower than those achieved using other software. It can also be seen that most of the software (APPS, POINT and RTKLIB) gave their highest RMSEs with data from equatorial stations, while MAGIC had most of its highest RMSE values in stations in the equatorial region, with the exception of data from July 2017, and October 2016 and 2017. Similarly, CSRS had its highest RMSE for stations near the equator for five days, and for three days the highest RMSE was found for stations in the southern hemisphere. In contrast, GLAB did not show a clear pattern; for three days, the highest RMSE was found for the stations in the North. For two days it was in the equatorial region and for three days the highest RMSEs were found for stations in the southern hemisphere.

In order to evaluate the quality of ZTD estimates derived using each software, RMSEs were calculated for all the differences (ZTD estimated from all stations with the same software, minus IGS tropospheric product), with the results (in cm) shown in Table 4.5.

**Table 4.5.** RMSE values (in cm), calculated for each software, and using all data.

	CSRS	APPS	MAGIC	POINT	RTKLIB	GLAB

January 27 2016	0.78	17.13	1.01	16.23	12.29	3.62
January 27 2017	4.77	15.67	4.85	16.75	13.96	3.21
April 27 2016	0.65	19.45	0.80	9.36	12.51	2.91
April 27 2017	0.67	18.64	0.90	9.45	12.14	4.03
July 27 2016	0.69	15.06	1.00	13.68	9.42	2.4
July 27 2017	0.66	17.39	0.78	12.67	8.71	3.85
October 26 2016	0.70	22.60	0.89	14.97	9.94	3.35
October 27 2017	0.56	31.99	0.83	12.90	9.71	5.83

Table 4.5 shows that the ZTD estimates calculated using the two online services CSRS-PPP and MAGIC achieved values closer to the IGS tropospheric product than the other three software packages, with the  $RMSE \leq 1$  cm, for most cases. DOY 27 for year 2017 proved to be an exception. From the three PPP software packages run locally, GLAB exhibited the lowest RMSE.

### 4.3 Discussion of results

Every software used for the analysis presented in this study uses a similar strategy to estimate the ZTD, particularly, the same model to estimate the hydrostatic slant delay (HSL). After the estimation of HSL, a mapping function is used to estimate the delay in the zenith direction. Then, the wet delay is estimated as an unknown in a parameter estimation process typically done with an EKF or LS. The online PPP software used the GMF based on numerical weather model data. The locally run PPP processing software implemented the Niell Mapping Function, which depends only on the site coordinates and day of the year. Because the GMF involves use of weather model data near the receiver, it models the delay caused by the troposphere better. On the basis of

these results, it is concluded that use of the GMF is one of the reasons why the online services that were tested obtained estimations closer to that of the IGS tropospheric product.

The effect of the ionosphere is another reason why the estimated value and the ZTD value obtained from the IGS tropospheric product differed. The model applied to correct the ionosphere effect used by the online PPP services was not stated, while for the other three, locally-run software packages, no ionosphere model was used. However, the carrier phase and code combinations were used to obtain ionosphere-free pseudoranges. This combination only eliminated the first order ionosphere effect, however residual effects were not eliminated, and they affect the signal.

The different cut-off angle set up in the software provided a third reason for the discrepancies between estimated ZTD and the values in the IGS tropospheric product. The IGS tropospheric product has a cut-off angle of  $7^\circ$ . All the software packages and online PPP services used for this study allow the cut-off angle to be set, however, the RTKLIB version used for this study only allowed use of angles in multiples of five, and so  $10^\circ$  was used as the closest option. In the other software packages, the cut-off angle was set to  $10^\circ$ . It is possible that this  $3^\circ$  difference had an effect on the ZTD estimates, since some satellites might be discarded for the solution. Furthermore, multipath affects the signal as well.

According to the results presented in this study, POINT and RTKLIB had very high RMSE values for stations near the equator, which meant that the model currently used does not clearly represent the tropospheric

effect at these latitudes. Possible reasons for this are that the thickness of the troposphere on the equatorial region is higher than in the polar region and that different weather conditions prevail near the equator. In addition, APPS and MAGIC obtained the highest RMSE values for stations nearer the equator, for DOY 27 of 2016 and 2017, 118 of 2016, 117 of 2017 and 209 of 2016. However, for the other days, the highest values were found for the southern and northern hemisphere respectively. Thus, confirming that the equatorial region has specific atmospheric conditions that were not properly accounted for by the models or the parameters used for the estimation. CSRS-PPP and GLAB obtained high RMSE values with data from different latitudes, at different days. However, the results with CSRS-PPP were always  $< 1$  cm (except for day 27, 2017), and in the case of GLAB, the results were consistently in the range 2–6 cm, which meant that both of these software packages obtained estimates very close to the IGS tropospheric value, with all data. The solution with GLAB takes one epoch to converge, so the first epoch was not considered in the RMSE analysis.

This comparison only included eight days of data, however the same days in different years were chosen, plus, the selected stations were globally distributed. It can be anticipated that similar weather conditions will prevail on the same days in two different years, therefore a trend can be found for how close the estimations were to the IGS tropospheric product. The stations are located in different latitudes, which allowed the study of how the different models used for the tropospheric model were influenced by the differing weather conditions of different latitudes.

## 4.4 Conclusions

In this chapter, the troposphere has been described in detail and the vertical profiles of pressure, humidity and temperature have been computed and displayed. The effects of latitude changes and DOY on the temperature profile have also been presented. The profile of the refractivity of the troposphere has been calculated because it causes the tropospheric delay. Radiosonde data has been used to calculate the profile of the refractivity of the troposphere.

The refractivity profile calculated with radiosonde data is assumed to be the same every year, at the given location. Therefore, it is considered to be a universal parameter, and is an input to the algorithm presented in Chapter 5.

Finally, the estimated ZTD obtained with APPS, CSRS-PPP, MagicGNSS, POINT, RTKLIB and gLAB software packages are compared with the ZTD provided by IGS. RMSEs are used to indicate estimation accuracy, as this technique indicates how different the estimated value is from a reference case. In this case, the IGS tropospheric product was taken as the reference case, since it is calculated using precise ephemeris.

Three trends have been found. Firstly, it has been found that CSRS-PPP obtains ZTD estimates very close to the value from the IGS tropospheric product. Second, it has been found that the tropospheric models currently implemented in RTKLIB and POINT do not account properly for weather or atmospheric conditions in the equatorial region. The corrections used by CSRS-PPP and MAGIC are very precise, so estimates closer to the

true value have been found. The third trend found is that GLAB also estimates the ZTD to a value very close to that derived by using the IGS tropospheric product.

Seasonal changes have not impact significantly on the ZTD estimation results obtained by applying the PPP software to the selected data sets. If precise ZTD estimates are needed for GNSS meteorology or numeric weather models, CSRS-PPP can provide very accurate estimates, followed by MagicGNSS and then gLAB. The average RMSE for RTKLib was 11.08 cm. However, the estimation is very close to the trospospheric product so it is assumed that there is no significant difference between the outputs of all software. In this research, RTKLIB is the PPP implementation used to estimate ZTD from GNSS data.

# CHAPTER 5

## DEVELOPMENT OF AN ALGORITHM TO COMPUTE TEMPERATURES FROM ZTD

In this chapter, a novel algorithm based on the ZTD and radiosonde-derived refractivity is presented to calculate temperature around the GNSS receiver. As shown in Figure 5.1, the algorithm is divided into three steps: calculation of the universal parameters, calculation of local parameters and then estimation of temperature using these local parameters. In this chapter, each of these steps is fully explained and the algorithm is tested with data from 32 globally distributed GNSS stations, and then validated with meteorological data.

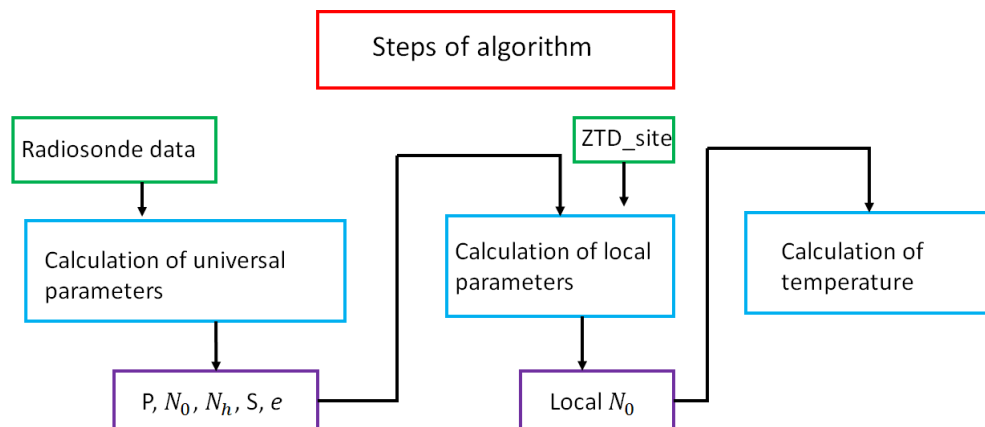


**Figure 5.1.** Block diagram of the steps used to develop the algorithm used to estimate temperature from ZTD.

The algorithm requires *a priori* values for the height of the troposphere ( $S$ ), air pressure at the place of measurement ( $P$ ) and the water vapour

partial pressure ( $e$ ) at the site of measurement. These values are obtained from radiosonde data, are called the universal parameters.

## 5.1 Calculation of the universal parameters

In order to obtain the vertical profile of troposphere refractivity vs height, as a universal profile, it is necessary to use yearly measurements at different heights of pressure, temperature and water vapour partial pressure. The structure of the file containing data collected during one radiosonde sounding is illustrated in Figure 5.2.

	E.T	P	Gph	Temp	RH	Dpd	W dir	W speed		
#TUM00017064	2018	05	01	00	2334	89	ncdc-gts		409000	291500
21	-9999	101100A	-9999	126A	-9999	20	60	10		
10	-9999	100000	109A	128A	-9999	28	35	10		
20	-9999	97800	-9999	-9999	-9999	-9999	245	15		
20	-9999	96500	-9999	110A	-9999	24	-9999	-9999		
20	-9999	94300	-9999	-9999	-9999	-9999	240	15		
10	-9999	92500	766A	180A	-9999	180	245	31		
20	-9999	91100	-9999	-9999	-9999	-9999	275	36		
20	-9999	90100	-9999	188A	-9999	430	-9999	-9999		
20	-9999	89400	-9999	190A	-9999	490	-9999	-9999		
20	-9999	89000	-9999	188A	-9999	490	-9999	-9999		
10	-9999	85000	1487A	164A	-9999	400	325	57		
20	-9999	79000	-9999	-9999	-9999	-9999	260	36		
20	-9999	73200	-9999	64A	-9999	120	-9999	-9999		
10	-9999	70000	3099A	40A	-9999	150	240	46		
20	-9999	66500	-9999	-9999	-9999	-9999	200	26		
20	-9999	66300	-9999	-1A	-9999	160	-9999	-9999		
20	-9999	61000	-9999	-9999	-9999	-9999	155	46		
20	-9999	60000	-9999	-65A	-9999	230	140	57		
20	-9999	59700	-9999	-67A	-9999	230	-9999	-9999		
20	-9999	58000	-9999	-79A	-9999	160	-9999	-9999		
20	-9999	55200	-9999	-109A	-9999	170	-9999	-9999		
20	-9999	53000	-9999	-137A	-9999	140	-9999	-9999		
10	-9999	50000	5720A	-171A	-9999	180	105	57		
20	-9999	45500	-9999	-225A	-9999	210	-9999	-9999		
20	-9999	44600	-9999	-241A	-9999	170	-9999	-9999		
20	-9999	43400	-9999	-9999	-9999	-9999	85	57		
10	-9999	40000	7350A	-299A	-9999	180	80	51		

**Figure 5.2.** Example of raw data from a radiosonde sounding

Figure 5.2 shows an example of raw data from a radiosonde sounding of IGRA's radiosonde TUM00017064 (Located in Istanbul, Turkey). This

data is used to calculate the refractivity profile at the location of the station. The first line is the header (starts with '#'), indicating the ID of the station, the date and time of the sounding (in this case 1 May, 2018), the hour of measurement and the release hour (in this case 23:34). After the time information, the number of levels or data records that are reported is indicated, followed by the data source code for pressure levels and for non-pressure levels in the sounding (ncdc-gts refers to the Global Telecommunications System messages receiver at NCDC from the National Centers for Environmental Prediction). Finally, the header indicates the latitude and longitude at which the sounding was taken. After the header, raw data is displayed, in which 10 indicates standard pressure and 20 means another pressure level. The columns with -9999 indicate a missing value. The columns indicate: Elapsed time since launch (E.T in Figure 5.2), pressure (P in Figure 5.2), geopotential height (m ASL, Gph in Figure 5.2), temperature in degrees °C (temp in Figure 5.2), relative humidity (as %, to tenths, RH in Figure 5.2), dew point depression (°C to tenths, Dpd in Figure 5.2), wind direction (degrees from north, w dir in Figure 5.2) and wind speed ( $\text{ms}^{-1}$  to tenths, w speed in Figure 5.2). The variables T, P and Gph obtained with radiosondes are used to compute the troposphere refractivity profile.

### **5.1.1 Calculation of water vapour partial pressure (e)**

The calculation of  $e$  was done using MATLAB and radiosonde data described in Table 3.4. The values for  $e$  were saved in a matrix, which was indexed through latitude. The matrix was formed by vectors, with the

structure described in Table 5.1, and it contained 365 values per latitude, with one value for each day of the year.

**Table 5.1.** Structure of the vector containing water vapour partial pressure data.

<b>Latitude (deg)</b>	<b>Water vapour partial pressure (hPa)</b>
1 value	365 values

### 5.1.2 Measuring pressure

The algorithm developed requires input data on the pressure at the site of measurement. Pressure can be measured using radiosondes, barometers or sensors integrated in hand-held devices, such as smartphones. Pressure information used in this algorithm was obtained from radiosonde data. The pressure measured at the first height of the sounding was recorded in a matrix, with the structure shown in Table 5.2. Pressure change during the day and throughout the year is very small, basically negligible, and so the pressure can be considered as a constant for a given latitude. The following matrix, with its 32 rows, is used as an algorithm input.

**Table 5.2.** Structure of the vector containing pressure data.

<b>Latitude (deg)</b>	<b>Longitude (deg)</b>	<b>Height (m)</b>	<b>Pressure (hPa)</b>
1 value from PPP	1 value from PPP	1 value from PPP	1 value from Radiosonde

### 5.1.3 Calculation of the refractivity profile

The daily troposphere refractivity profile at different heights is calculated using the values of pressure, relative humidity, temperature and geopotential height, obtained from radiosonde data in Table 3.4. This information is then used to solve equation (3.2) presented in chapter 3.

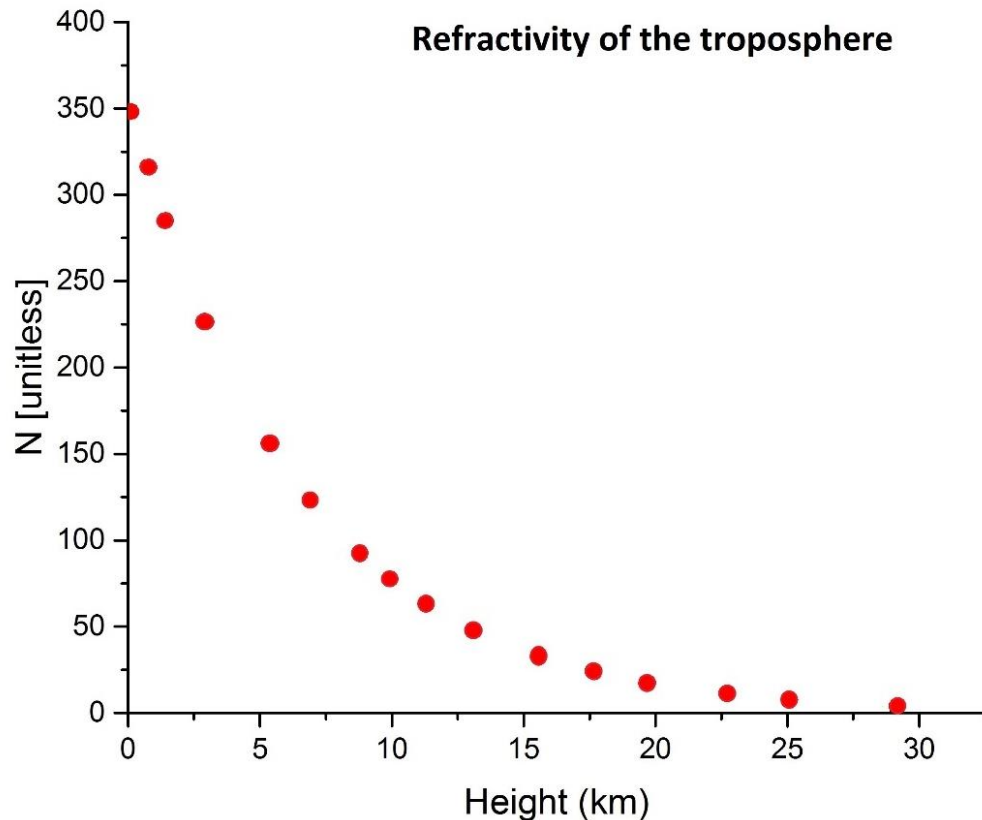


**Figure 5.3.** Refractivity of the troposphere, using radiosonde data.

Figure 5.3 is a graphical representation of refractivity found using radiosonde data. The points are fitted to an exponential function, in order to find a continuous line and a mathematical representation.

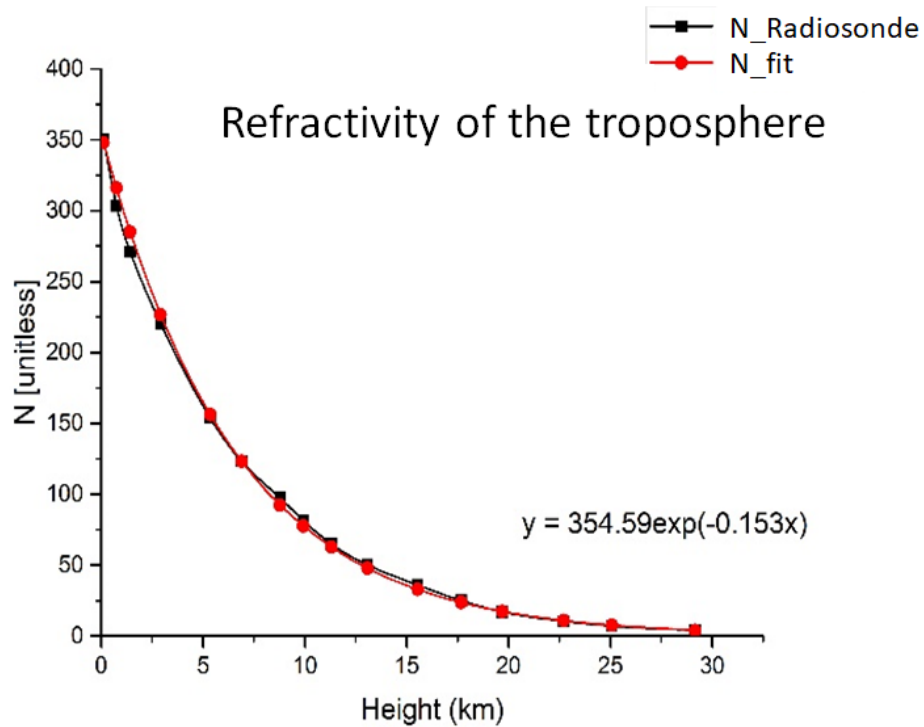


**Figure 5.4.** Refractivity of the troposphere after applying exponential fitting

Figure 5.4 shows the fitting of the points calculated with radiosonde data to an exponential function to find an expression similar to the equation for refractivity derived in chapter 3.  $N$  is the refractivity of the troposphere,  $N_0$  is the refractivity at the lowest point of the troposphere or level 0 and  $N_h$  is the ratio at which the refractivity value decreases, with increased height.

$$N = N_0 e^{-N_h z} \quad (5.1)$$

In the example shown in Figure 5.4,  $N_0 = 354.59$  and  $N_h = 0.153$ . Daily radiosonde data allows calculation of daily curves and daily values of  $N_0$  and  $N_h$ . In order to find an annual refractivity profile, daily curves and daily values for  $N_0$  and  $N_h$  are averaged, resulting in one value for  $N_0$  and  $N_h$ , per year.

Calculations for the refractivity profile at different latitudes show little change to the values of  $N_0$  and  $N_h$  throughout the year. However, all changes are cyclical, from year to year. Thus, only data from one year is used to compute troposphere refractivity and there is no need to re-compute the refractivity profile for other years. The refractivity profile used in the developed algorithm was obtained using radiosonde data from 2017.

#### **5.1.4 Relation between ZTD and troposphere refractivity**

The mathematical relation between ZTD and troposphere refractivity is shown in equation (4.5), where  $N_0$  is the troposphere refractivity at ground level and  $N_h$  is a factor that indicates exponential decay as the refractivity changes with respect to height.  $Z_{site}$  is site height with respect to ground level and  $Z_{top}$  is troposphere height at the point of measurement.

$$ZTD = 10^{-6} \int_{Z_{site}}^{Z_{top}} N_0 e^{-N_h z} dz \quad (5.2)$$

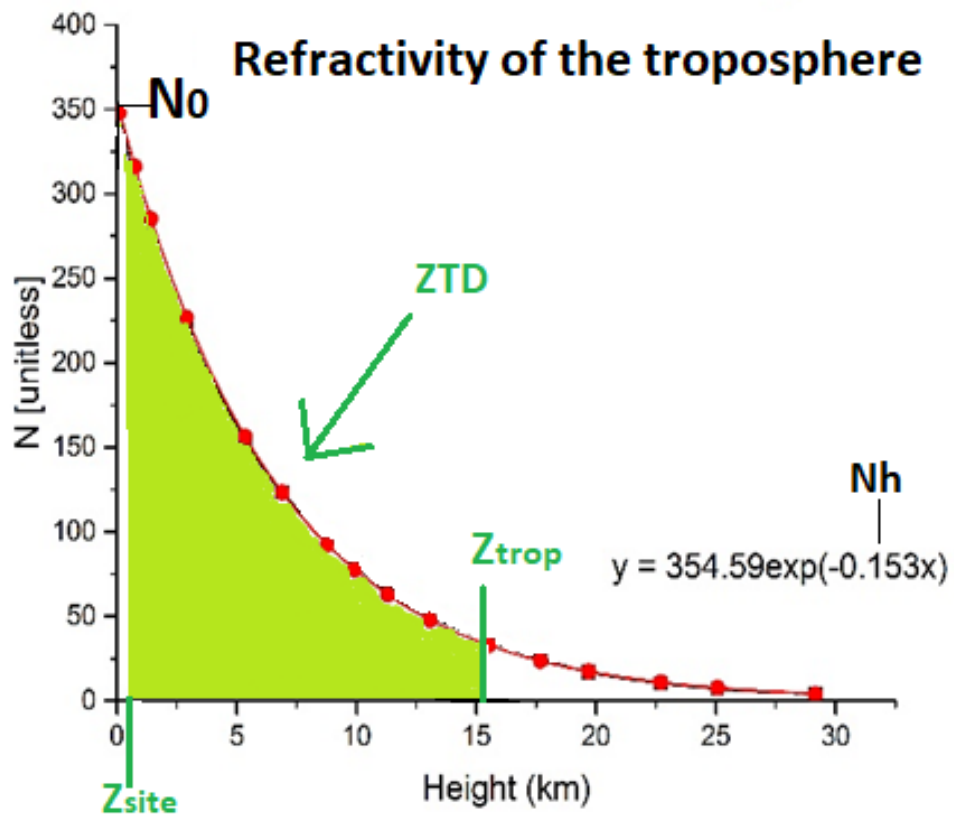
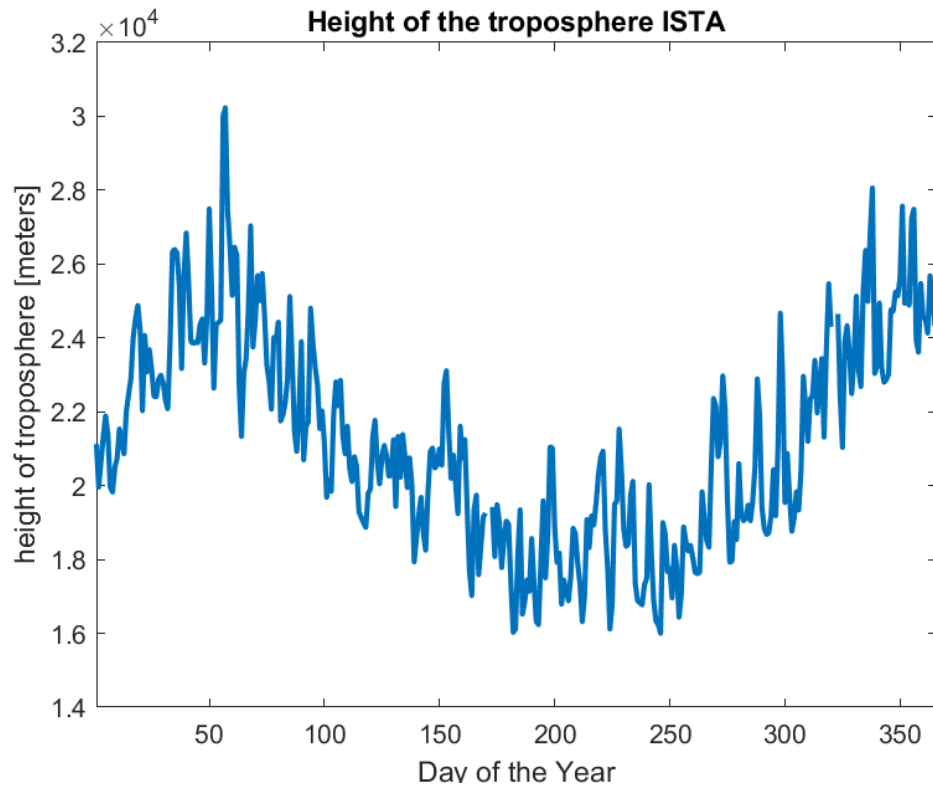


**Figure 5.5.** ZTD is the area under the refractivity profile curve, between the height of the receiver ( $Z_{\text{site}}$ ) and the height of the troposphere ( $Z_{\text{trop}}$ ).

As shown in Figure 5.5, the ZTD is equivalent to the area under the curve of the vertical refractivity profile vs height between receiver height and troposphere height. The  $Z_{\text{site}}$  is the altitude of the receiver, usually found with the positioning technique and  $Z_{\text{trop}}$  is the height of the troposphere, which can be defined as the height of the first lapse rate tropopause (LRT1). LRT1 is latitude-dependent and can be calculated from radiosonde or GNSS data.

### 5.1.5 Calculation of troposphere height

The height of the troposphere can be calculated using radiosonde data (Table 3.5) and applying the WMO definition of LRT1 and LRT2, as discussed in Chapter 3.



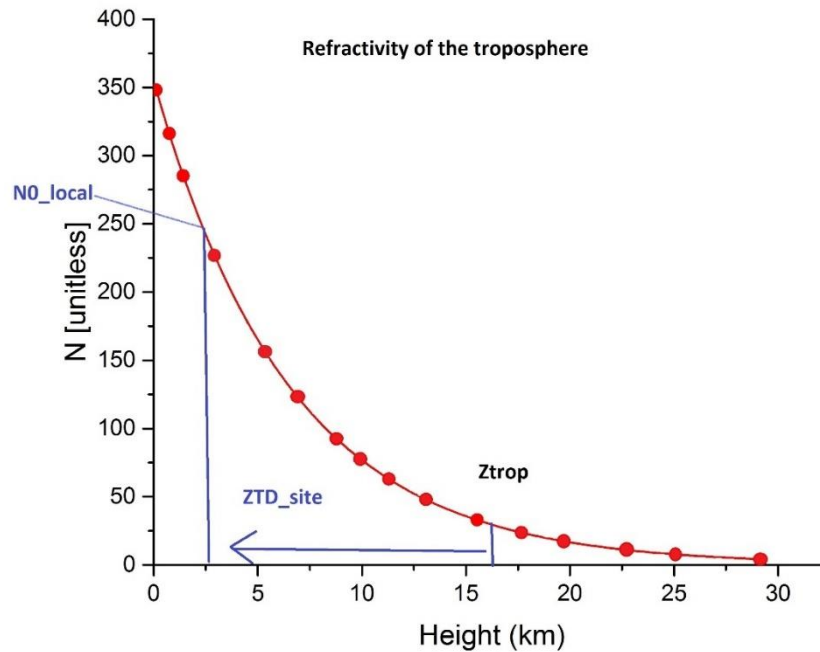
**Figure 5.6.** Height of the troposphere estimated using data from station ISTA for year 2017

Figure 5.6 shows an example of troposphere height computed using 2017 daily GNSS data, from station ISTA (Istanbul, Turkey).

### 5.1.6 Calculation of the local $N_0$

The second block in the diagram shown in Figure 5.1 relates to calculation of the local  $N_0$ . For this step, a ZTD is provided ( $ZTD_{site}$ ) and the corresponding  $N_0$  value is calculated by integrating the refractivity profile from  $Z_{trop}$  (corresponding to the latitude where the receiver is

located) to the height of the site and recording the corresponding  $N_0$  value ( $N_{0\_local}$ ), as shown in Figure 5.7



**Figure 5.7.** Graphical description of the procedure applied to obtain  $N_{0\_local}$ .

Mathematically, the operations performed are as shown in (5.3).

$$N_{0\_local} = \frac{ZTD}{10^{-6} \int_{z_{site}}^{z_{trop}} e^{-N_h z} dz} \quad (5.3)$$

Temperature  $T$  is found by combining Equations 3.2 and 3.6 defined in Chapter 3 into equation (5.4).

$$ZTD = 10^{-6} \int_{zenith\ direction} \left[ k_1 \cdot \frac{p-e}{T} + k_2 \cdot \frac{e}{T} + k_3 \cdot \frac{e}{T^2} \right] ds \quad (5.4)$$

$N_{0\_local}$  is used to estimate the temperature. Only one value of  $N_{0\_local}$  is found for each  $ZTD\_site$ , so the number of  $N_{0\_local}$  inputs available for

temperature estimation on a given day depends on the number of ZTD<sub>site</sub> inputs available on that day.

### 5.1.7 Calculation of temperature using local refractivity parameters

$N_{0\_local}$  is used to calculate the temperature from ZTD values by making equation (5.4) equal to 0, then, the equation is arranged into quadratic form, as shown in (5.5).

$$N_{0\_local}T^2 - T(k_1P - (k_1 + k_2)e) - k_3e = 0 \quad (5.5)$$

Solving (5.5) for temperature  $T$  requires using the solution for quadratic equations  $x = \frac{-b \pm \sqrt{b^2 - 4ac}}{2a}$ . The values for  $T$ , in degrees Kelvin, are found using the substitutions shown in (5.6), where  $N_{0\_local}$  is obtained with Equation 5.3,  $k_1$ ,  $k_2$ ,  $k_3$  are empirically calculated constants described in Table 3.1,  $p$  is the pressure at the site of measurement and  $e$  is the water vapour partial pressure at the site of the measurement (both  $p$  and  $e$  are known from radiosonde data).

$$a = N_{0\_local}$$

$$b = -k_1p + (k_1 + k_2)e \quad (5.6)$$

$$c = -k_3e$$

This entire algorithm is depicted schematically in Figure 5.8.

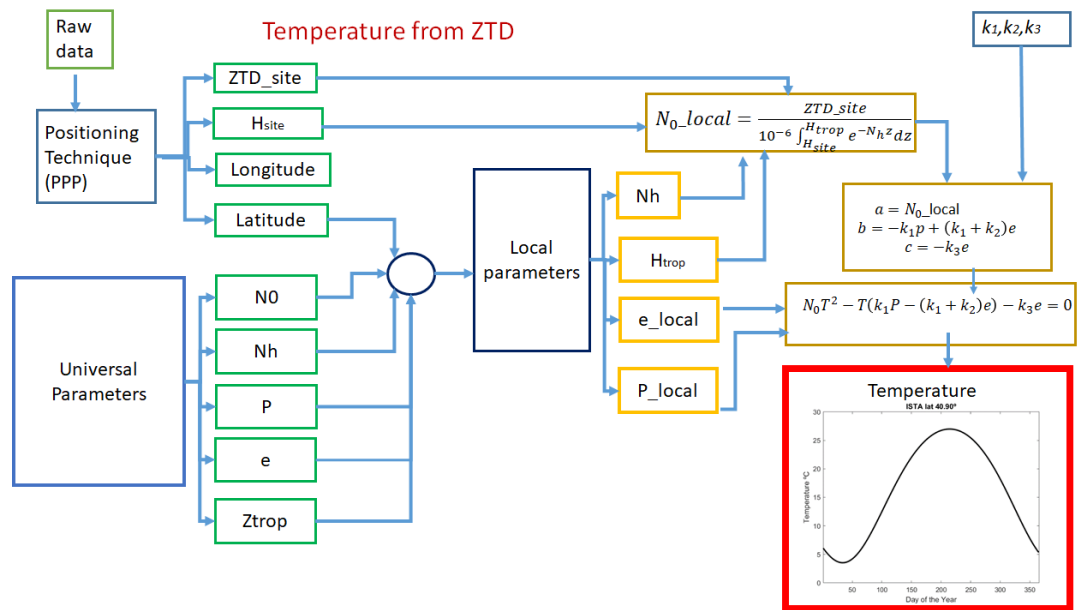


**Figure 5.8.** Block diagram of the algorithm applied to calculate temperature from ZTD.

In the algorithm represented as the block diagram in Figure 5.8, T was calculated using MATLAB and then tested using GNSS data and meteorological data from stations around the world.

## 5.2 Estimation of ZTD

The ZTD is estimated using an implementation of the PPP technique. In this case, observation data from stations described in Table 3.4 was processed with RTKLIB. MATLAB was used to create a matrix of 5 rows with the latitude, longitude, height and the 2880 ZTD values per day from the output of RTKLIB, in each vector. Table 5.3 shows the structure of the vector used to record the ZTD.

**Table 5.3.** Structure of ZTD data input in the algorithm.

Latitude (deg)	Longitude (deg)	Height (m)	ZTD (m)
1 value: from PPP technique	1 value: from PPP technique	1 value: from PPP technique	288 values

The ZTD is processed yearly and daily. Figure 5.9 shows the annual behaviour of the ZTD estimated with RTKLIB at station ISTA.

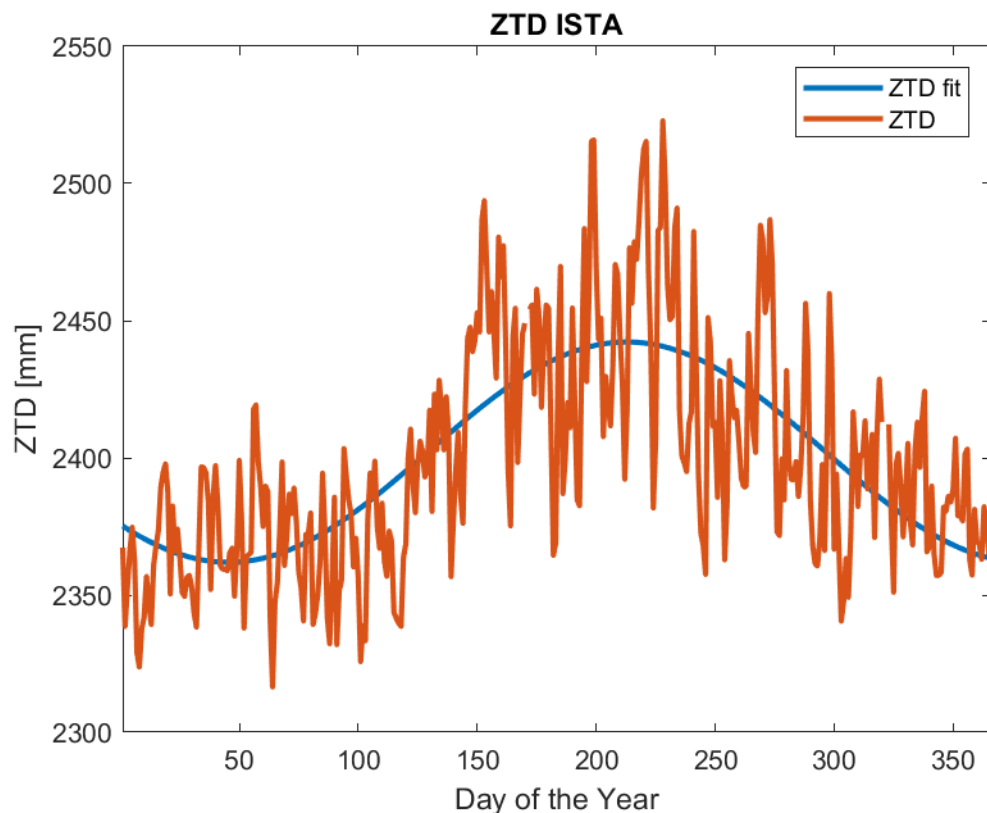


**Figure 5.9.** ZTD for station ISTA, for 2017. The red line represents the value of ZTD estimated with RTKLIB, while the blue line represents fitting of the daily averages.

The yearly profile of the ZTD behaves like temperature, that is, the lowest values are found around DOY 50, while the highest values are found around DOY 200. DOY 50 is during the winter in the northern hemisphere and DOY 200 is during the summer in the northern hemisphere, so the lowest and the highest temperatures are also found around the same days. The ZTD for other years has shown the same shape.

The daily profile of ZTD estimated for the DOY 181 at station ISTA is shown in Figure 5.10

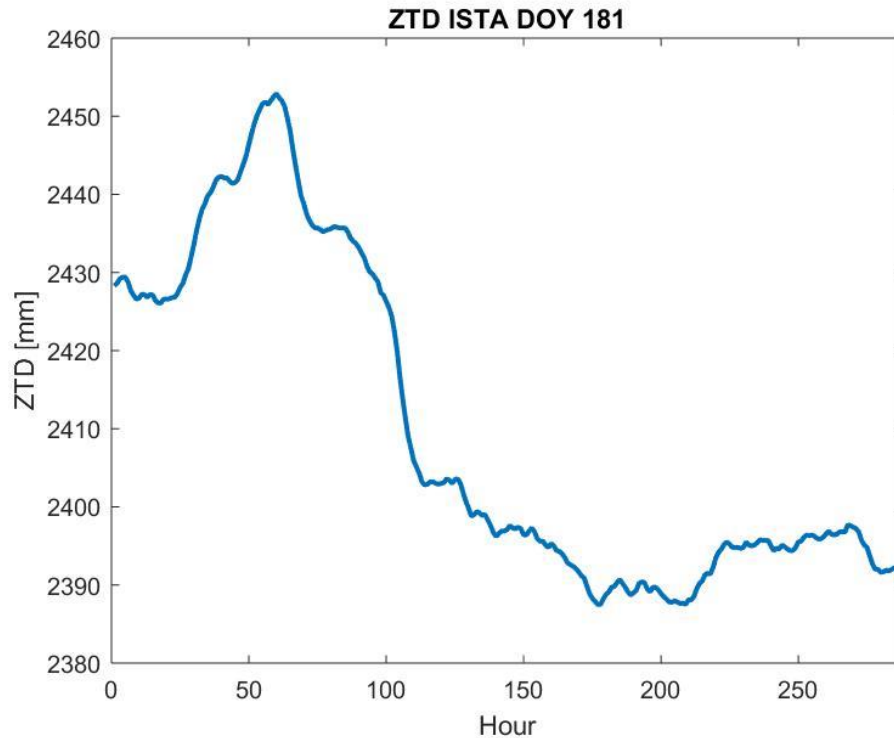


**Figure 5.10.** Daily profile of estimated ZTD, DOY 181, ISTA.

The daily profile of the ZTD estimated with RTKLIB is different every day. However, the values are higher for days closer to DOY 200. In general, the ZTD is higher during the hours of morning when the temperature rises and during the evening the values are lower. However, the amount of precipitable water available during the day affects the behaviour of the ZTD.

### 5.3 Algorithm implementation

A MATLAB code was created to process radiosonde data and create a matrix containing the universal values of  $N_0$ ,  $N_h$ ,  $e$  and  $P$  for 32 latitudes covering the whole earth (Table 3.4). In the case of  $e$ , whenever available, two profiles were found one at 00:00 UTC and one at 12:00 UTC. The

other variables were fit into smoothed curves as shown in the next example for the radiosonde in the same latitude as GNSS station ISTA.

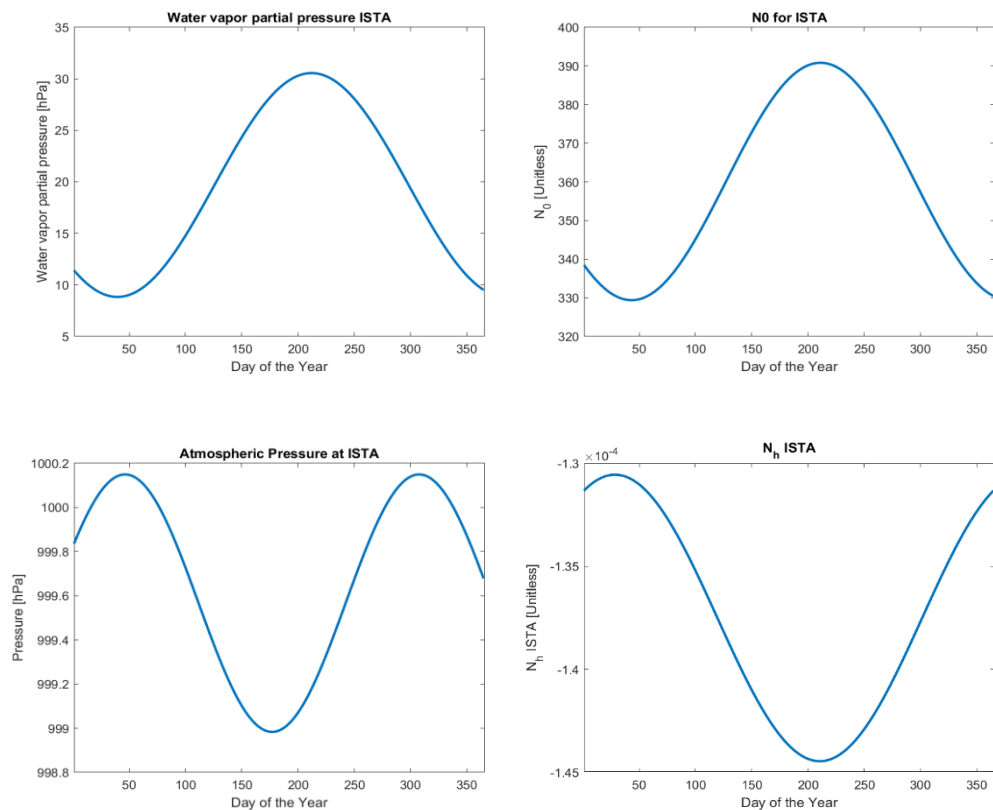


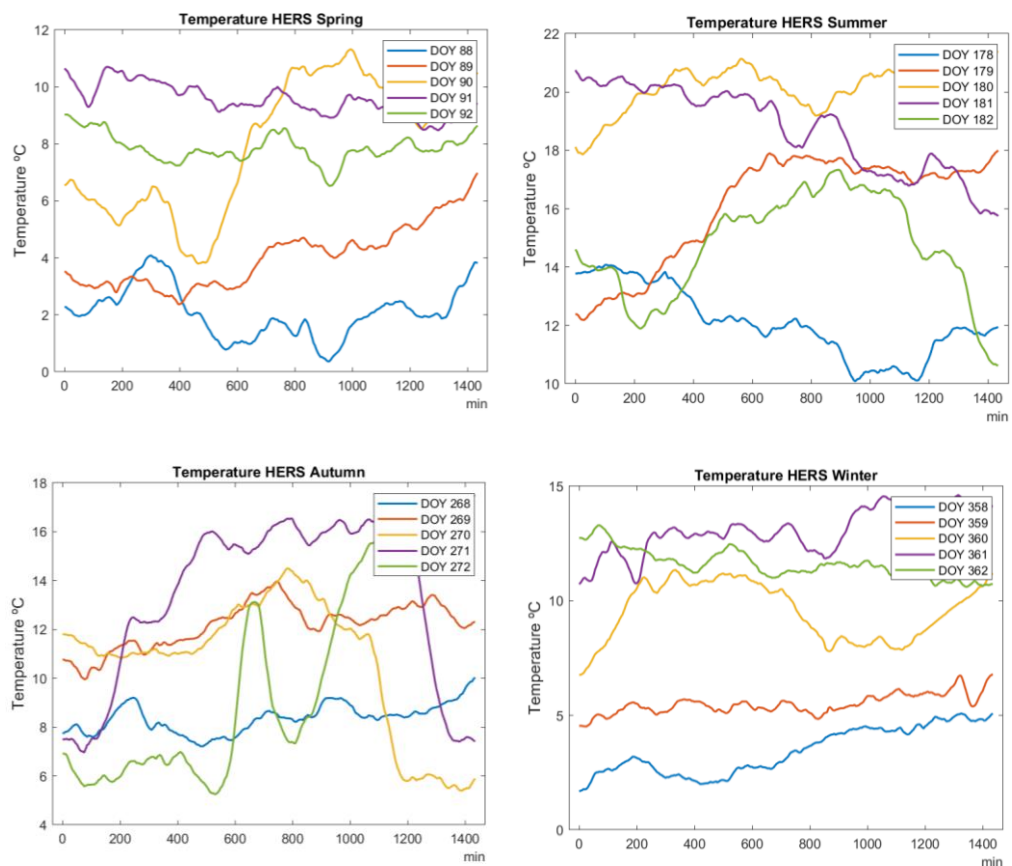
**Figure 5.11.** Profiles of the variables input into the algorithm.

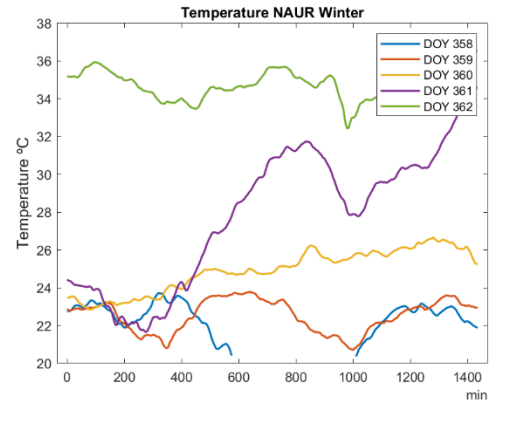
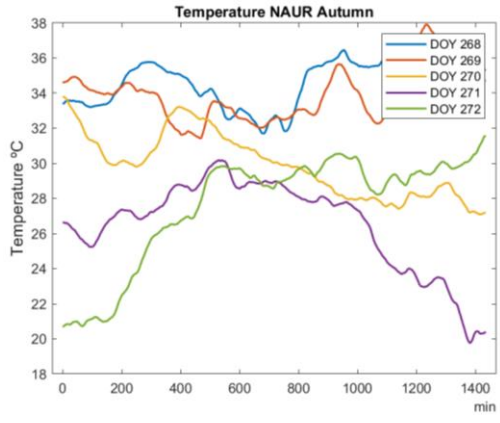
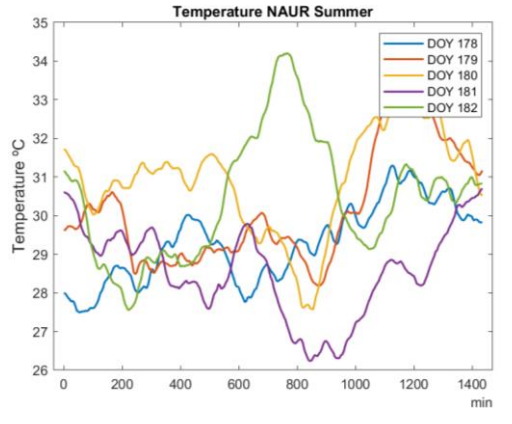
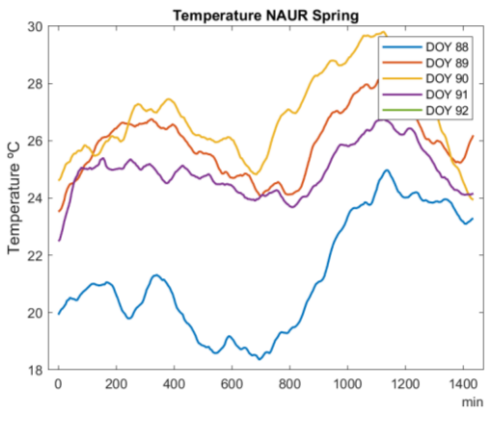
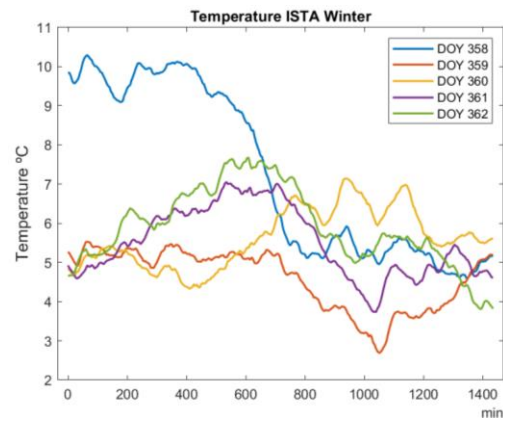
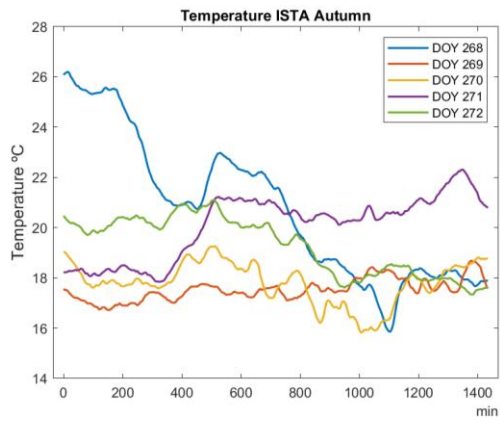
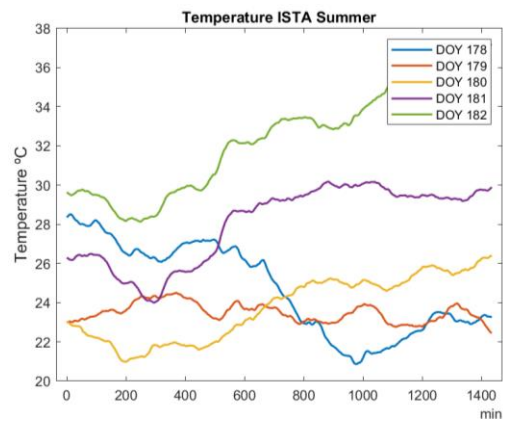
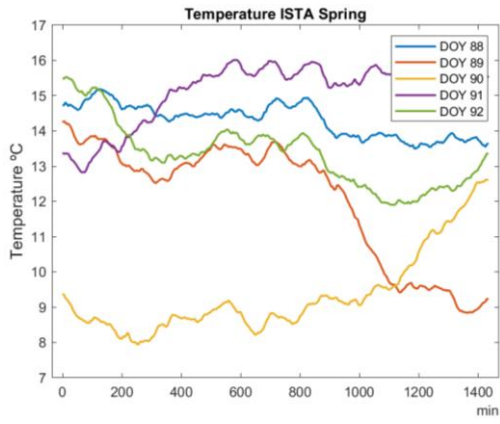
ZTD estimates from RTKLIB are processed using MATLAB. 20 days distributed in all the seasons have been processed. DOY 88, 89, 90, 91, 92, 178, 179, 180, 181, 182, 268, 269, 270, 271, 271, 358, 359, 360, 361 and 362. Observation data is available every 5 minutes, therefore, 288 values of ZTD are obtained every day. Equation 5.5 and 5.6 are solved using the methodology explained in the previous section. In section 5.4 the output of the algorithm and the validation are shown. The validation is

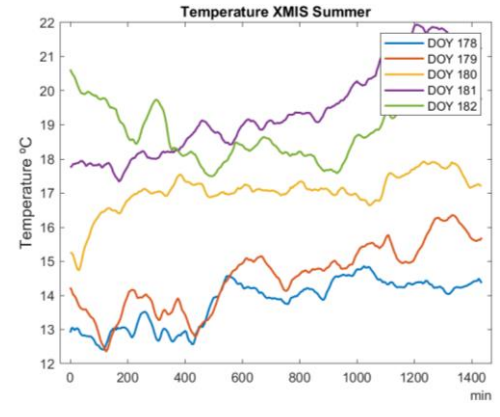
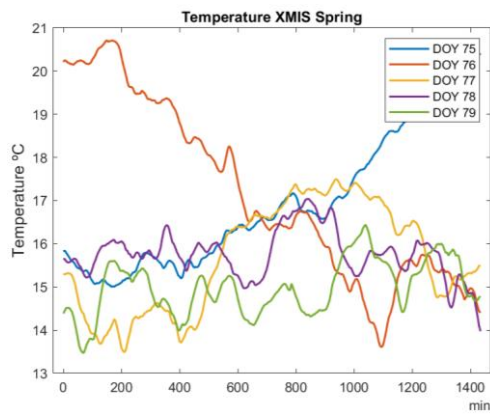
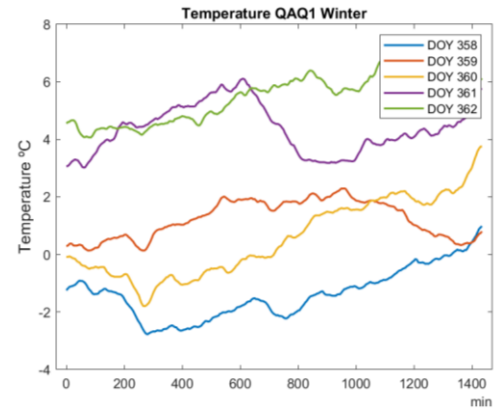
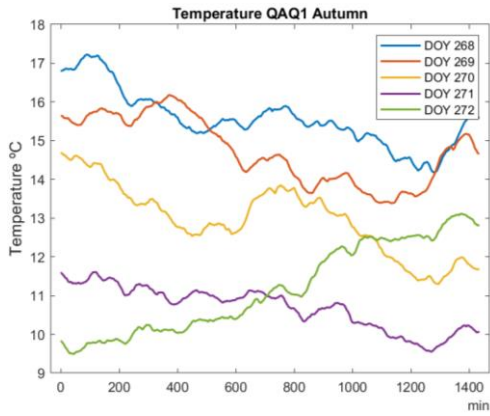
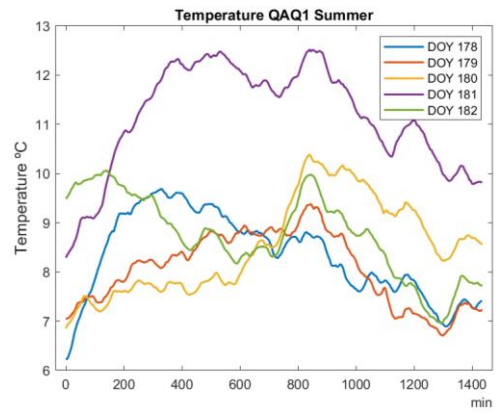
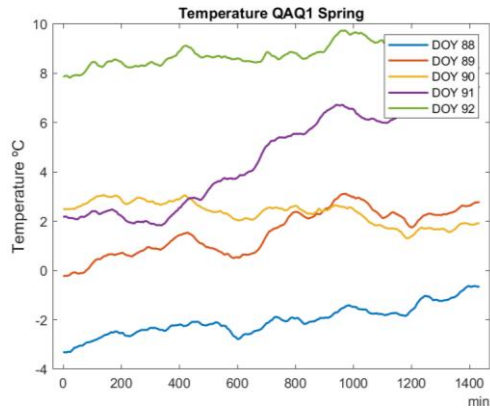
done by comparing the output of the algorithm ( $T_{algo}$ ) with the temperature reported by a weather station in the same location ( $T_{met}$ ).

## 5.4 Results and validation

The daily temperatures obtained with the algorithm have been plotted and are displayed in Figure 5.12. Each figure represents the temperature obtained at 5 different days. The days are grouped as spring (DOY 88, 89, 90, 91, 92), summer (DOY 178,179,180,181,182), Autumn (DOY 268,269,270,271,271) and Winter (DOY 358,359,360,361 and 362). The station XMIS do not report data from days 79 to 100. Therefore, the output shown are for DOY 75,76,77,78 and 79.







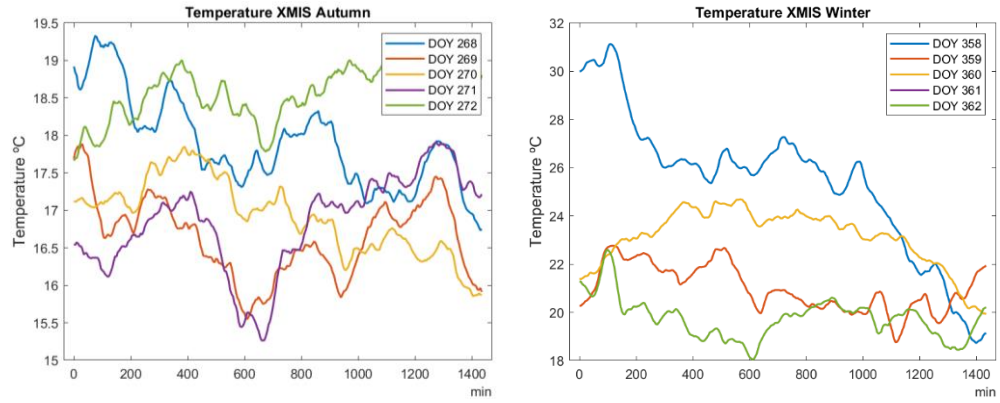


**Figure 5.12.** Output of the algorithm for 5 stations for 20 days each. 5 days are in spring, 5 days in summer, 5 days in autumn and 5 days in winter.

Figure 5.12 shows that the temperatures obtained for 5 GNSS stations during 20 days of the year. The results of the algorithm are compared with meteorological data at the same locations during the same days.

#### 5.4.1 Validation of the algorithm

The IGS GNSS stations reported in Table 3.5 report both, GNSS observations and meteorological data. Meteorological data is reported from T2m sensors (sensor at 2 meters of height above the surface). The result curves show the same shapes as the T found with the algorithm.

In order to evaluate the accuracy of the algorithm, comparisons were conducted between the temperature obtained with the algorithm and the temperature at the same epoch measured with weather stations. The following mathematical relationship was used (5.7), where  $T_{al}(t)$  is the temperature estimated with the algorithm at time  $t$  and  $T_{ws}(t)$  is the temperature measured with a weather station at time  $t$ .

$$Diff = T_{AL}(t) - T_{ws}(t) \quad (5.7)$$

The average of the differences and the RMS of the differences are calculated and used as the parameters to measure algorithm results quality. The algorithm requires the calculation of the  $e$  which is done from radiosonde data. The  $e$  affects the results of the algorithm and it varies with temperature. Therefore, radiosondes with two soundings, one at 00:00 UTC and 12:00 UTC have been processed. One value of  $e$  each of the soundings has been reported. The value of  $e$  is used to calculate a temperature at the same times. The temperatures obtained with the algorithm at 00:00 UTC and 12:00 UTC are compared with the measurements of temperature reported by the weather stations at the same times. The statistical analysis is shown in Tables 5.4-5.7.

**Table 5.4.** Average of the differences at 00:00 UTC in °C

	Spring	Summer	Autumn	Winter
HERS	<b>3.63</b>	<b>1.82</b>	<b>3.28</b>	<b>1.15</b>
ISTA	<b>5.70</b>	<b>3.29</b>	<b>1.85</b>	<b>3.03</b>
NAUR	<b>6.65</b>	<b>2.52</b>	<b>0.38</b>	<b>4.73</b>
QAQ1	<b>3.60</b>	<b>0.32</b>	<b>0.89</b>	<b>2.14</b>
XMIS	<b>0.30</b>	<b>0.28</b>	<b>6.83</b>	<b>5.32</b>

**Table 5.5.** Average differences at 12:00 UTC in °C

	Spring	Summer	Autumn	Winter
HERS	<b>6.94</b>	<b>0.42</b>	<b>4.03</b>	<b>0.58</b>
ISTA	<b>0.97</b>	<b>5.28</b>	<b>1.39</b>	<b>6.31</b>
NAUR	<b>3.99</b>	<b>5.33</b>	<b>2.17</b>	<b>0.23</b>
QAQ1	<b>7.10</b>	<b>2.82</b>	<b>1.32</b>	<b>1.50</b>
XMIS	<b>0.76</b>	<b>0.28</b>	<b>5.74</b>	<b>4.19</b>

Table 5.4 and Table 5.5 show the average of the differences between the output of the algorithm and the meteorological data measured by the T2m sensors at 00:00 UTC and 12:00 UTC. The lowest average differences at 00:00 UTC are found during the summer and the autumn, while the

highest are found at NAUR station during the spring. At 12:00 UTC, the lowest average differences are found during the summer and autumn while the biggest difference is found for station QAQ1 during the spring.

For all stations, the differences at 00:00 UTC and 12:00 UTC were averaged to make a conclusion about the quality of the estimations.

**Table 5.6.** Average differences using all data in °C

	Spring	Summer	Autumn	Winter
HERS	5.28	0.70	3.65	0.86
ISTA	3.33	0.99	0.23	4.67
NAUR	5.69	0.51	0.89	2.48
QAQ1	5.35	1.57	1.10	1.82
XMIS	0.53	0.28	5.29	4.76

Table 5.6 indicates that the lowest average differences have been found during the summer, while the highest was found during autumn and during the spring.

**Table 5.7.** RMSE in °C of the average differences using all data.

	Spring	Summer	Autumn	Winter
HERS	5.28	3.69	4.23	3.71
ISTA	5.32	5.42	3.98	6.20
NAUR	6.02	1.98	3.54	5.62
QAQ1	8.46	1.57	1.10	1.82
XMIS	1.26	2.10	5.35	5.83

The results showing an RMSE value of  $\leq 5$  °C are deemed to be good estimations, and it was considered that the algorithm could be used without modification to calculate temperatures at those sites.

## 5.5 Conclusion

An algorithm to calculate temperature using the ZTD has been presented in this chapter. The algorithm requires calculation of universal parameters that characterize the refractivity—the pressure, the thickness of the troposphere, the profile of the refractivity and the troposphere water vapour partial pressure—at the site of measurement. These parameters have been estimated with radiosonde data at different latitudes covering the whole world. Only two soundings per day are available in some Radiosonde stations. Therefore, the availability of the universal parameters is the mayor limitation of the algorithm. In particular, the value  $e$  is a mayor limitation since the amount of water vapor in the troposphere changes a lot over time and it is unpredictable. When two soundings are available, these are used to calculate two values of the water vapor partial pressure for one day instead of only one value per day. The pressure and the profile of the refractivity is mostly constant, therefore, once computed, its values can be used with data from different years. The universal parameters depend on latitude only.

The algorithm has been implemented with MATLAB, and the ZTD estimated with RTKLIB from 5 stations around the world during 20 days of the year has been used as an input to the algorithm. The algorithm has been validated by comparing the output of temperature with the temperature obtained with T2m sensors in weather stations at the same location as the GNSS station.

It has been found that during the summer and the autumn, the algorithm has a good accuracy (less than 5 °C), however, during the spring, the values for the RMSE are the highest (highest value found for station QAQ1= 8.43 °C). This is explained by the fact that during the summer the highest temperatures are found while during the spring the temperature difference between the maximum and the minimum is smaller. Therefore, when the variation of temperature in the site of measurement is bigger, the algorithm performs worse than when the temperatures are less variable. The station QAQ1 which reported a big RMSE value for spring is found at a very far north location. In this location, the temperature is extreme, with very low temperatures during the evening and high temperature during the day. However, during the spring the average temperature is near 5 °C which causes a difficulty when estimating the water vapor partial pressure with Antoine's equation explained in Chapter 3. Negative air temperatures cannot be estimated with Antoine's equations as the vapor at that those temperatures freezes, and it becomes ice fog. Antoine's equation does not account for temperatures below 0 °C. Therefore, a model to estimate the water vapor partial pressure from ice fog needs to be investigated.

# CHAPTER 6

## DEVELOPMENT OF AN ALGORITHM TO MONITOR UHI USING GNSS DATA

In this chapter, a novel algorithm to monitor the intensity of the UHI (UHII) based on GNSS data is presented. The algorithm requires temperature estimates from GNSS data at urban and rural sites simultaneously. The UHI intensity is monitored by studying the differences between these temperatures. The algorithm is tested and validated using GNSS data, radiosonde data and data from weather stations in three metropolitan areas: Los Angeles, California, USA (LA); Hong Kong Special Administration Region, China (HK) and Ningbo, Zhejiang, China (NB).

### **6.1 Algorithm: Using GNSS data to monitor UHI Intensity**

A UHI is detected when the measured temperature at a given point of time in an urban area is higher than the temperature in an adjacent rural area by at least 1 °C as described in Chapter 2. The intensity of the UHI is defined by the difference between the two temperatures. An algorithm

developed to estimate the UHI from GNSS data is shown in a block diagram in Figure 6.1.

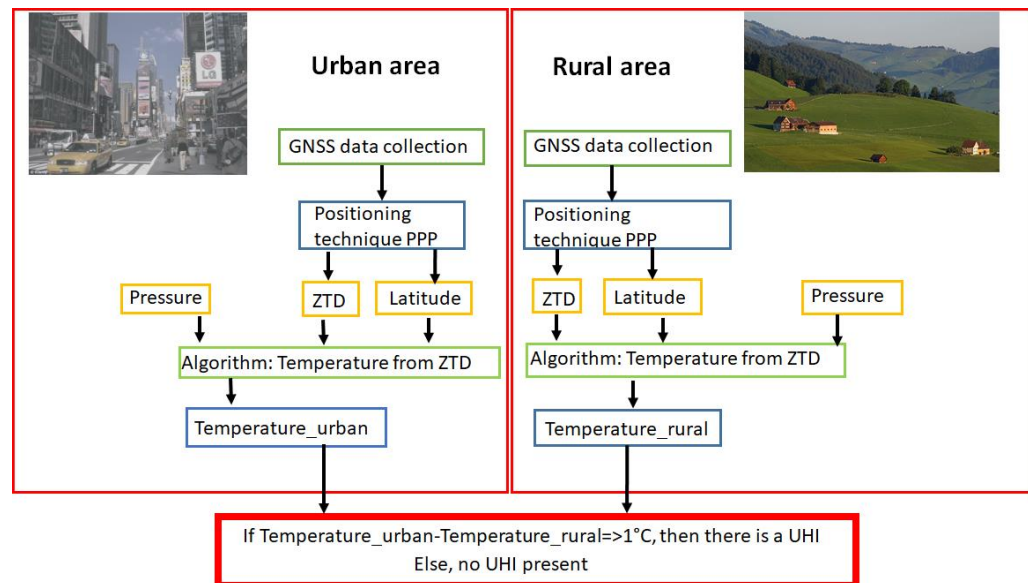


**Figure 6.1.** Block diagram of the UHI monitoring algorithm

As shown in Figure 6.1, the UHI can be monitored using GNSS by following 4 steps simultaneously in two locations:

- Collecting raw GNSS data
- Processing the GNSS data to obtain position coordinates and ZTD, using PPP
- Using the algorithm explained in Chapter 5 to compute temperature from ZTD
- Computing the UHI intensity

The algorithm requires simultaneous estimation of two temperatures, one in an urban and one in a rural area. Therefore, classification of the type of area where stations are located is needed. The classification of type of area is done visually from a satellite picture by seeing the elements

present in the surroundings of the stations or locations. The definition of urban and rural areas described in Chapter 2 is used for the visual classification.

In this chapter, the UHI is monitored using GNSS data in three different metropolitan areas. One metropolitan area is LA (Lat: 34.05, Long: -118.34°). The second metropolitan area is HK (Lat: 22.39, Long: 114.11). The third metropolitan area is Ningbo (Lat: 29.86, Long: 121.53).

## **6.2 UHI monitoring in LA**

GNSS raw data has been collected from stations in the metropolitan area described in Table 3.7 shown in Chapter 3. The data has been processed using RTKLIB for DOY 90,91, 180,181, 270,271, 360 and 361. Each day, 288 values of ZTD have been found. The first step of the algorithm to monitor the intensity of the UHI in LA metropolitan area is the classification of the data sources as urban or rural stations.

### **6.2.1 Classification of type of GNSS station**

The classification of the type of station requires knowledge of its surroundings and assessment as to whether it is mostly surrounded by built structures or nature. The online tool used for this purpose was Google Maps (GM), which provides satellite views of the LA metropolitan area. The terms and conditions of GM allow its use for research (Google, 2019). The satellite images provided by GM were taken in 2018; the coordinates of the station locations were input, and GM provided the corresponding satellite pictures. GM was accessed via its website (Google, 2019).

The visual classification for the environment around each station is shown in Appendix 1.

### 6.2.2 Classification of type of meteorological station

The meteorological data described in Section 3.5.7 is used to validate the algorithm and to calculate the UHI intensity from surface measurement. The stations need to be classified as urban or rural applying the same definitions as the ones used for the classification of type of GNSS stations as shown in the previous section (Section 6.2.1). Satellite photos obtained from Google Maps (GM) are used as the source for classification. The classification of meteorological stations is shown in Appendix 2.

For validation purposes, it is necessary to have the GNSS station and the meteorological station in the same place. However, since the GNSS stations and the weather stations are operated by different operators, the stations chosen, need to be close to each other. Therefore, pairs of meteorological and GNSS stations have been defined and are shown in Table 6.1. The IGS code has been assigned to the pair of stations.

### 6.2.3 Pairs of GNSS-Meteorological data

**Table 6.1.** GNSS stations paired with meteorological stations, and their respective locations.

Pair number	GNSS stations			Meteorological stations		
	Code	Lat (deg)	Long (deg)	Code	Lat	Long
1	WLSN	34.23	-118.06	→ USC00046006	34.23	-118.07
2	CIT1	34.14	-118.13	→ USC00046719	34.15	-118.14
3	WHC1	33.98	-118.03	→ USR0000CWHH	33.98	-118.01
4	TORP	33.80	-118.33	→ USC00047326	33.83	-118.37
5	LBCH	33.79	-118.20	→ USW00023129	33.81	-118.14

The paired stations shown in Table 6.1 are located near each other, with a maximum separation distance of 1.6 Km, for stations CIT1 and USC00046719. Figures 6.2 a)–e) show the GM satellite view and GM street view of the locations of the meteorological and GNSS station pairs. These data is used to classify the pair as either urban or rural, if both are in the same kind of environment. For example, the GNSS station in Mount Wilson (WLSN) and the meteorological station in Mount Wilson (USC00046006) are both in a rural area, so therefore, the pair WLSN has been classified as being in a rural area.

Google Map Satellite view	Google Map	
		<p><b>Pair 1:</b> Mount Wilson, both stations are in rural areas</p>
		<p><b>Pair 2:</b> Pasadena, both stations are in urban areas</p>
		<p><b>Pair 3:</b> Whittier, GNSS station in an urban area while the meteorological station is in a rural area</p>
		<p><b>Pair 4:</b> Torrance, both stations are in urban areas</p>
		<p><b>Pair 5:</b> Long Beach, both stations are in urban areas</p>

**Figure 6.2.** Satellite views and maps of GNSS and meteorological stations used to monitor UHI in LA. Taken from [www.googlemaps.com](http://www.googlemaps.com).

## 6.2.4 UHI Monitoring in the Los Angeles metropolitan area:

### Methodology

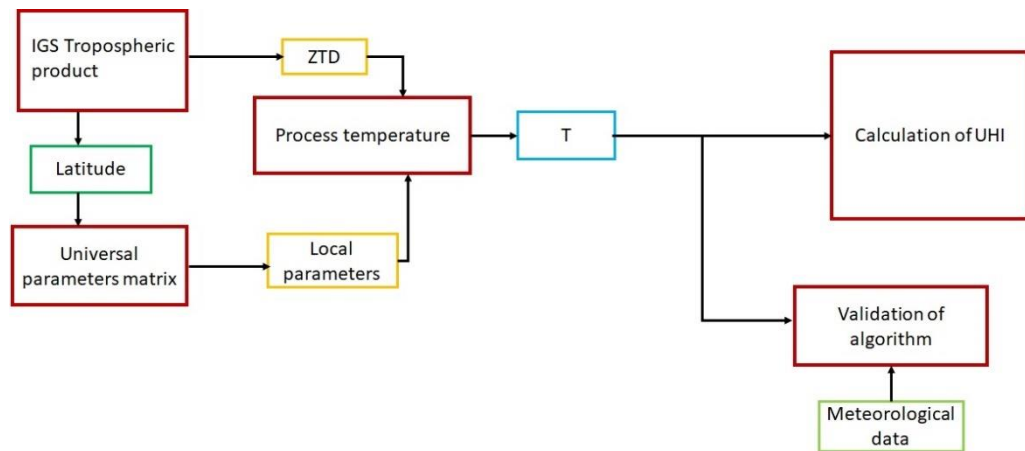


**Figure 6.3.** Block diagram of the methodology used to monitor the LA metropolitan area UHI.

The methodology used to monitor the LA UHI, shown in Figure 6.3, can be summarized in 5 steps:

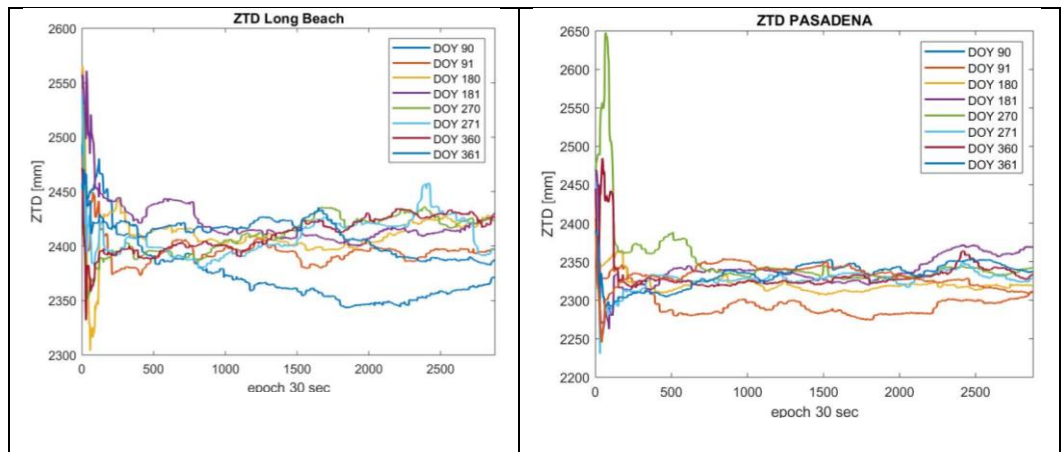
- Extract ZTD from output of RTKLIB.
- Load local parameters based on the latitude of receiver
- Process local  $N_0$
- Calculate temperature from local  $N_0$ .
- Calculate the UHI intensity

Each of these steps will be explained in detail in this chapter and at the end of the section, the effect of height on ZTD, on the local refractivity profile and on temperature will be shown.

## 6.3 Implementation of the Algorithm with data from LA.

### 6.3.1 Extract the ZTD from RTKLIB output file

MATLAB has been used to extract the receiver location latitude, longitude, height, time of measurement and ZTD from the RTKLIB output file. A matrix has been created, indexed by latitude with the output variables of 8 days of the year 2017. The days have been equally distributed in the four seasons of the year. Figure 6.4 shows the ZTD output from RTKLIB for 8 days in 4 GNSS stations in LA metropolitan area. Only 4 stations have been used to monitor the UHII in LA because for validation purposes there are only 4 weather stations with hourly temperature data in LA chosen for this study.



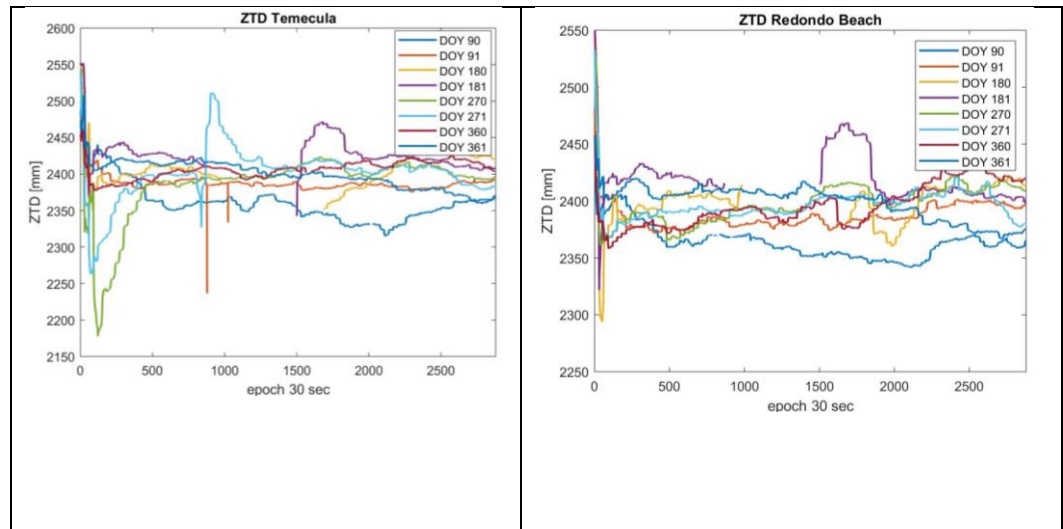


**Figure 6.4.** ZTD estimated with RTKLIB for 4 stations, 8 days of the year.

RTKLIB takes around 15 minutes to converge that is the reason why in all graphs presented in Figure 6.4, the values during the first 15 minutes are highly variable.

### 6.3.2 Load local parameters based on latitude

The  $N_h$ ,  $Z_{trop}$ ,  $e$  and  $P$  annual profiles are imported into MATLAB, based on the latitude where the GNSS station is located and the day of the year.

Figure 6.5 shows the yearly profiles for the universal parameters in 2017.

$P$  is considered a constant, as its annual fluctuation is negligible.

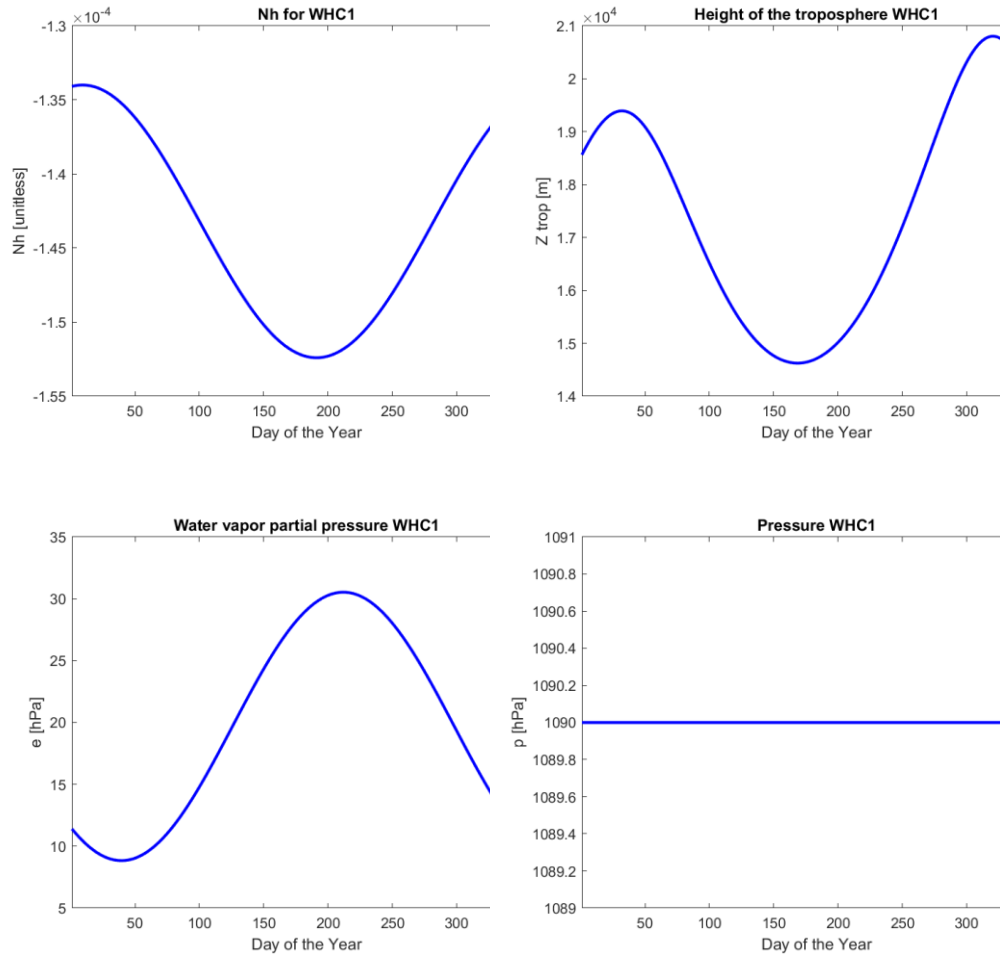


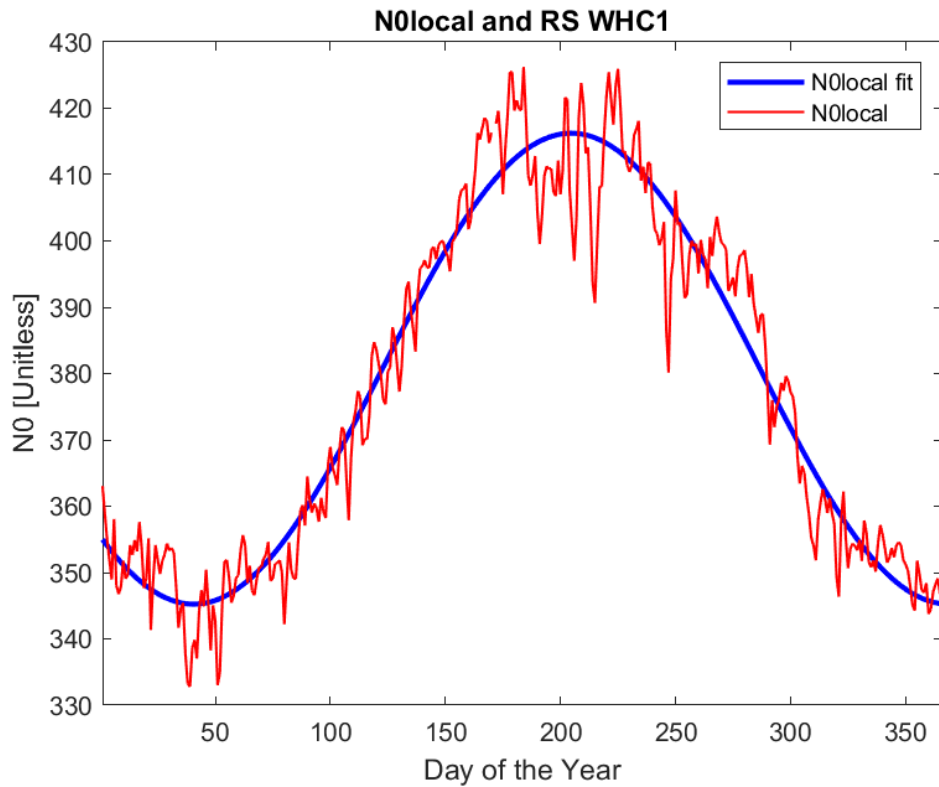
**Figure 6.5.** 2017 profiles for the universal parameters input to the algorithm.

### 6.3.3 Process Local $N_0$

As described in Chapter 5: the local  $N_0$  is found using  $N_h$ ,  $Z_{trop}$ , the altitude of the receiver ( $Z_{rec}$ ) and the ZTD. Formula (6.1) is used for the calculation of  $N_{0\_local}$

$$N_{0\_local} = \frac{ZTD}{q \int_{z_{rec}}^{z_{trop}} e^{N_h z} dz} \quad (6.1)$$

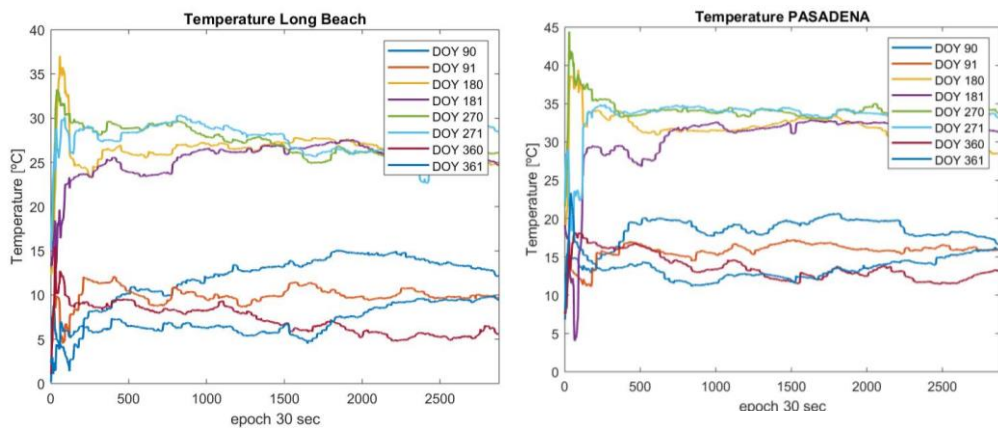
The results from calculation of  $N_{0\_local}$  are depicted graphically in Figure 6.6.



**Figure 6.6.** Profile of the local  $N_0$  required to calculate temperature.

### 6.3.4 Calculation of temperature from $N_0\_local$

The temperature is calculated using the universal parameters, the local refractivity profile and equation (5.4) as explained in Chapter 5. The temperatures estimated with the algorithm are shown in figure 6.7.



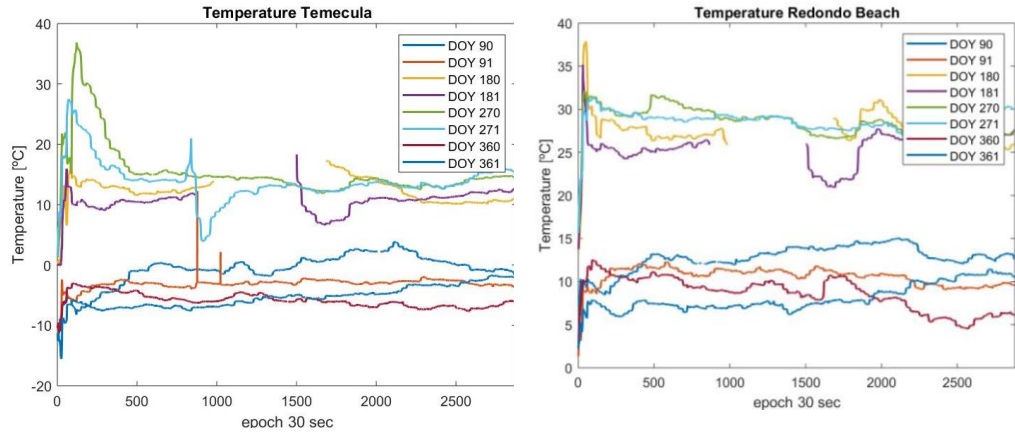


**Figure 6.7.** Output of the algorithm: estimated temperature from GNSS data from stations in LA metropolitan area.

Figure 6.7 shows the output of the algorithm which is the temperature estimated from ZTD. All the lines in the graphs have the same shape as the shape of the ZTD (Figure 6.4). The peak found during the first 15 minutes is due to the time needed by RTKLIB to find an stable value for ZTD.

### 6.3.5 Calculation of UHI intensity

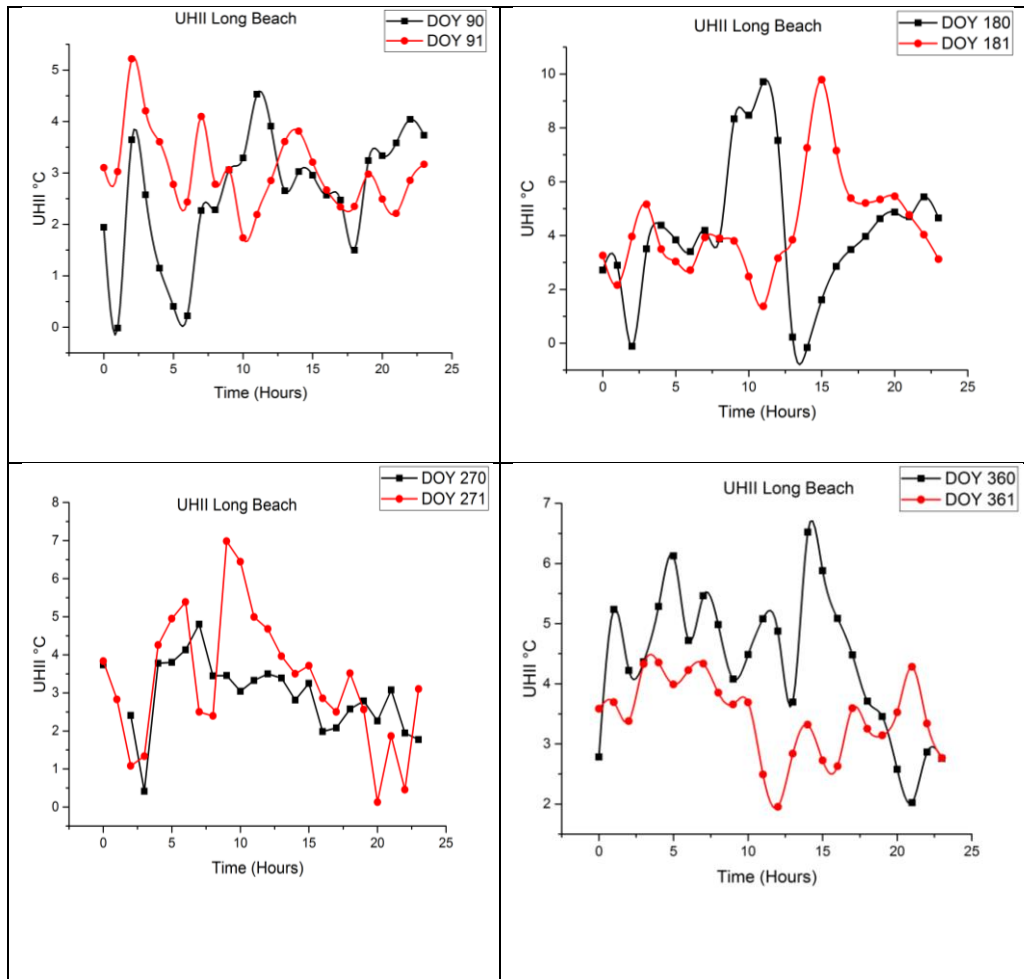
The UHI intensity is measured by subtracting the temperature at an urban station with the temperature at a rural station. In this case, the rural station is in Temecula and the other three stations are urban stations. The following mathematical relations are used to monitor the UHI intensity (UHII) at DOY 90,91,180,181,270,271,360,361:

$$UHII_{LBCH} = T_{alg}(Long\ Beach) - T_{alg}(Temecula)$$

$$UHII_{BILL} = T_{alg}(Redondo\ Beach) - T_{alg}(Temecula) \quad (6.2)$$

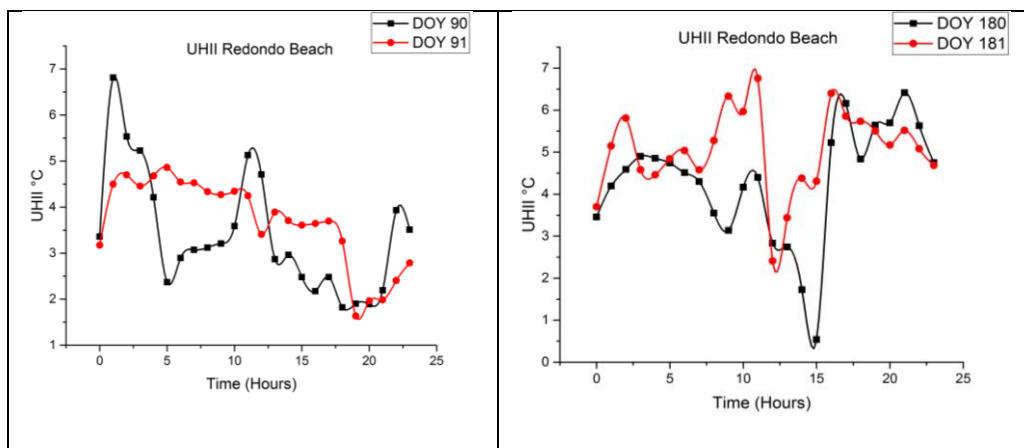
$$UHII_{CIT1} = T_{alg}(Pasadena) - T_{alg}(Temecula)$$

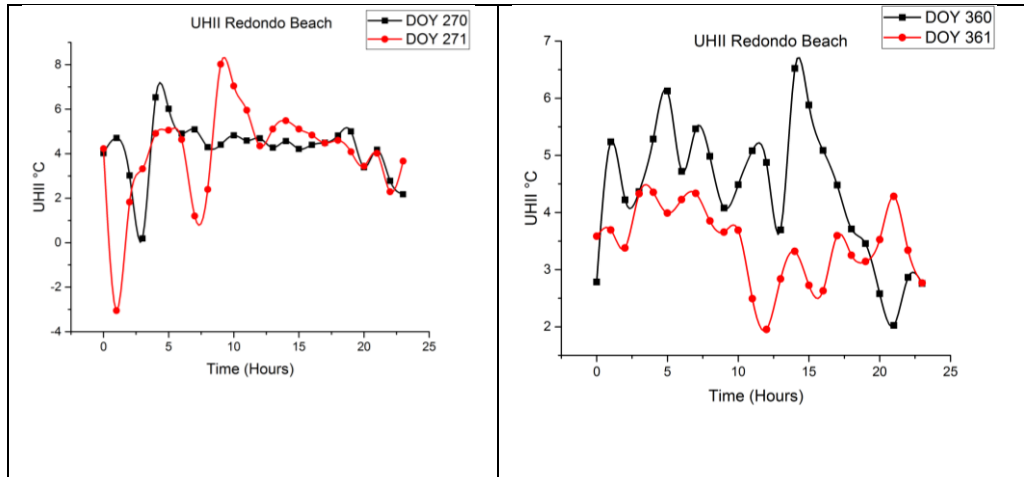
The daily profile of the UHI intensity is plotted in Figure 6.8-6.10. Each figure includes the plots of the UHII at different seasons.



**Figure 6.8.** UHII at station LBCH in Long Beach, California. 8 days distributed in the four seasons are plotted.

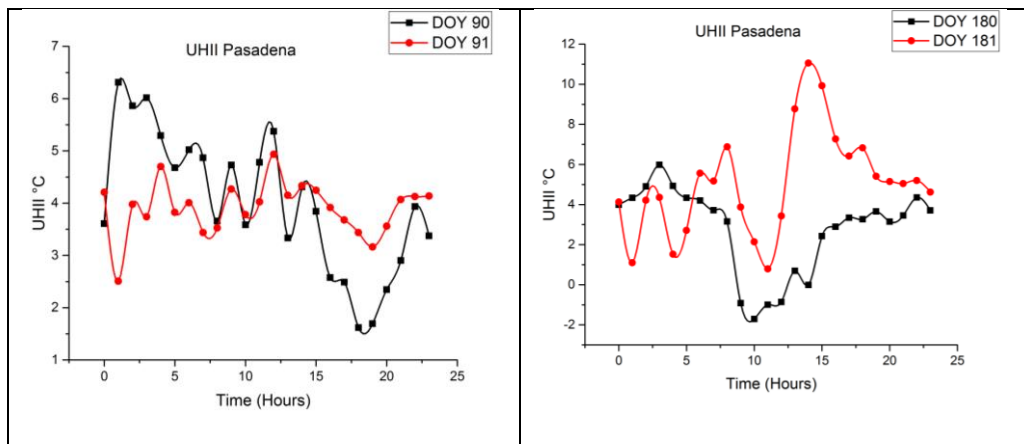
Figure 6.8 shows the UHII found with data from station LBCH. The profiles show a decrease of the UHII during the hours with sun, as the sun sets, the UHII increases.





**Figure 6.9.** UHII at station BILL in Redondo Beach, California. 8 days distributed in the four seasons are plotted

Figure 6.9 shows the profile of the UHII found at the station in Redondo Beach, California. The profiles during DOY 180, 181, 360 and 361 show the decrease of the intensity of the Urban Heat Island as the sun heat heats the built structures. As the sun sets, the UHII increases.



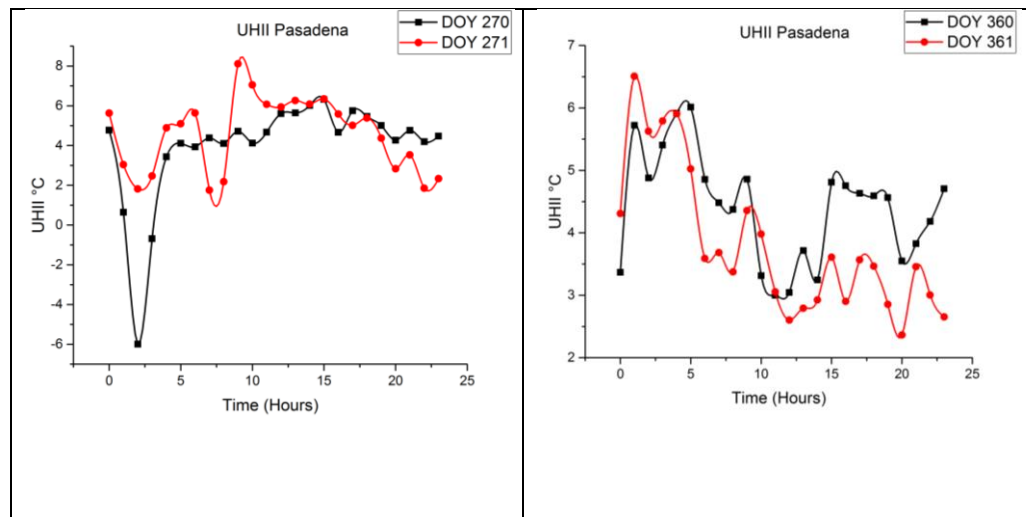


**Figure 6.10.** UHII at station CIT1 in Pasadena, California. 8 days distributed in the four seasons are plotted

Figure 6.10 shows the profile of the UHII at the station in Pasadena California for 8 days distributed in the 4 seasons. DOY 180 and 360 show the expected profile. As the sun sets, the UHII increases.

## 6.4 Validation of algorithm

Two validations of the output of the algorithm used to monitor the uHII with GNSS data are presented here. First, the validation of the temperature estimation is presented, followed by the validation of the UHII. The first validation is done by comparing the estimated temperature with the algorithm with temperature measured with weather stations near the GNSS stations. The second validation is achieved by comparing the UHI intensity measured with temperature data from weather stations and temperature estimated with the algorithm.

### 6.4.1 Validation of the temperature estimated from GNSS data

The estimated temperature with the algorithm is compared with data from T2m temperature sensors housed in meteorological stations. The

comparison of temperature is done for 8 days of the year (DOY) covering the four seasons: DOY 90, 91 during the spring, DOY 180,181 during the summer, DOY 270,271 during the autumn and DOY 360, 361 during the winter. The magnitude of the differences per station are shown in Figure 6.11-6.14. Figure 6.11 shows the magnitude of the differences of temperature measured with a weather station and estimated with the algorithm in Long Beach, California. Figure 6.12 shows the same differences of temperature in Pasedena, California. Figure 6.13 shows the differences for the stations in Redondo Beach, California. Finally, the magnitude of temperature differences for the stations in Temecula, California, are shown in Figure 6.14.

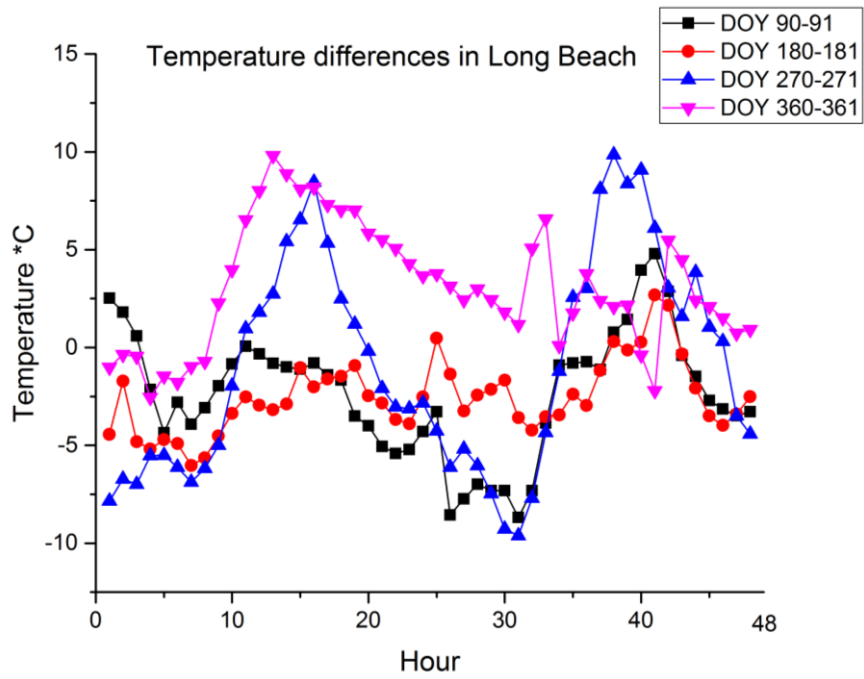


**Figure 6.11.** Difference of temperature obtained from the algorithm and from weather station data for the station in Long Beach, during 8 days of the year.

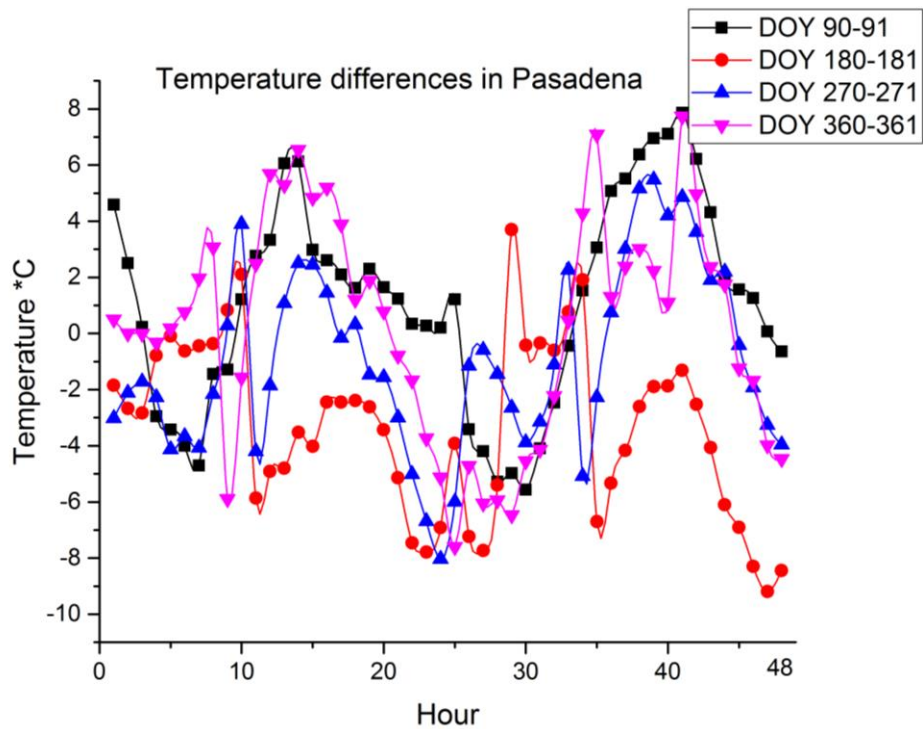


**Figure 6.12.** Difference of temperature obtained from the algorithm and from weather station data for the station in Pasadena, during 8 days of the year.

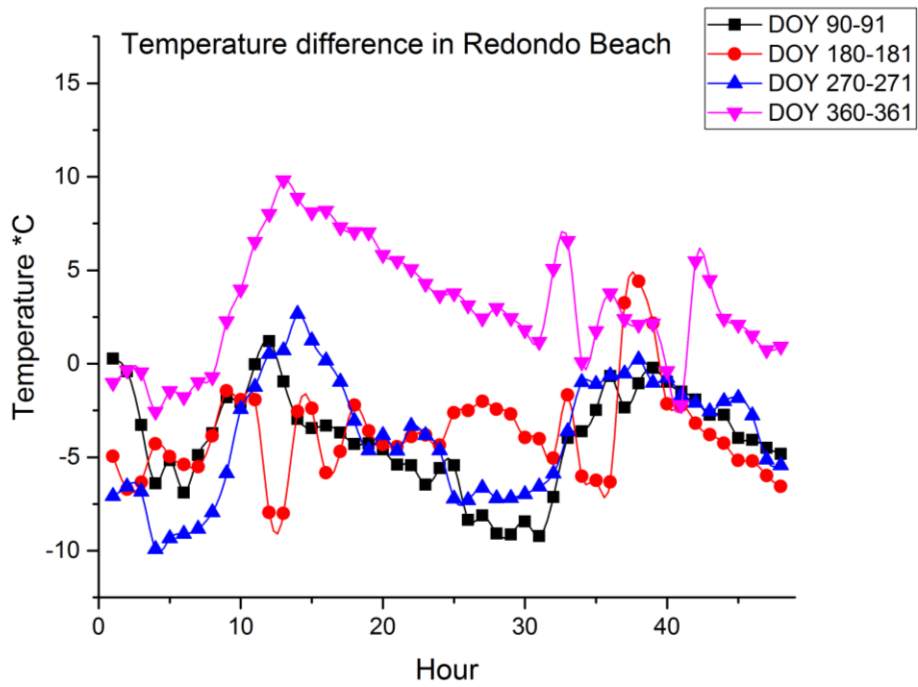


**Figure 6.13.** Difference of temperature obtained from the algorithm and from weather station data for the station in Redondo Beach, during 8 days of the year.

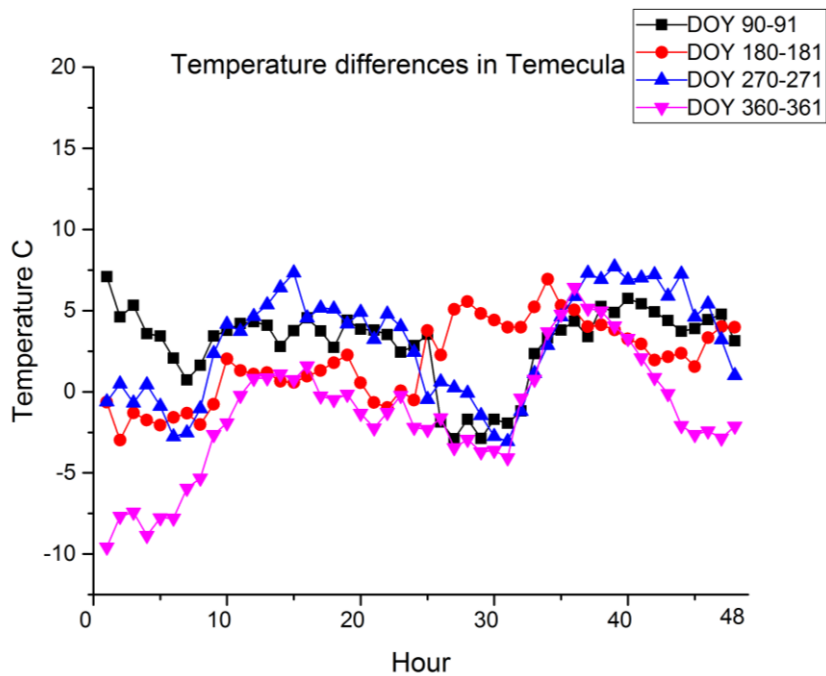


**Figure 6.14.** Difference of temperature obtained from the algorithm and from weather station data for the station in Temecula, during 8 days of the year.

Figures 6.11-6.14 show that the temperature differences during the days chosen for the study increase as the hour increase, during the middle of the day (hours 12 and 36) the maximum differences are found. In all cases the difference of temperature is smaller than 10 °C.

The mathematical validation of the algorithm is done by calculating the mean and the Root Mean Square (RMS) of the differences. The statistical analysis is shown in Table 6.2 and Table 6.3.

**Table 6.2.** Mean of the differences in °C between temperature estimated with the algorithm and measured with T2m sensors in a weather station.

	Temperature °C			
	Spring	Summer	Autumn	Winter
<b>Temecula</b>	3.00	1.90	2.95	-1.38
<b>Long beach</b>	-2.37	-2.53	-0.98	4.72
<b>Redondo</b>	-3.96	-3.74	-3.87	4.86
<b>Pasadena</b>	1.11	-3.32	-0.97	1.27

**Table 6.3.** RMSE in °C of the differences between temperature estimated with the algorithm and measured with T2m sensors in a weather station.

	Temperature °C			
	Spring	Summer	Autumn	Winter
<b>Temecula</b>	3.80	3.08	4.37	3.98
<b>Long beach</b>	3.94	3.13	5.50	6.28
<b>Redondo</b>	4.76	4.48	4.99	6.27
<b>Pasadena</b>	3.79	4.51	3.36	5.47

The values of the average differences and the RMSE are within the range found in the validation of the algorithm shown in Chapter 5. RMSE < 5°C is considered a good estimation. The stations in Redondo Beach have the highest discrepancies while those in Temecula have the smallest discrepancies. Also, during the winter, the RMSE is greater than 5 °C for

three of the four stations. This can be explained because during the winter the temperatures are low so the change of water vapor partial pressure is difficult to model accurately.

#### **6.4.2 Validation of the estimation of UHI intensity.**

The UHI intensity has been calculated with the temperatures estimated with the algorithm and with temperatures measured with T2m sensors in weather stations. The difference of the intensity ( $Diff\_UHII(t)$ ) has been compared by doing the following mathematical procedure:

$$Diff\_UHII(t) = UHII\_alg(t) - UHII\_met(t) \quad (6.3)$$

Where  $UHII\_alg(t)$  is the intensity of the UHI obtained with the algorithm at epoch  $t$  and  $UHII\_met(t)$  is the intensity of the UHI obtained with meteorological data at epoch  $t$ . According to Ramamurthy and Sangobanwo (2016), the UHI in Los Angeles increases at night up to 2 °C and during the day the intensity of the UHI becomes negative at some times. They studied the UHI in different U.S cities, among them in LA using surface temperature measurements from a station in a rural and one in an urban area. The profile of the UHII in LA is shown in Figure 6.15 with the time referenced to UTC. LA's local time is UTC-8.

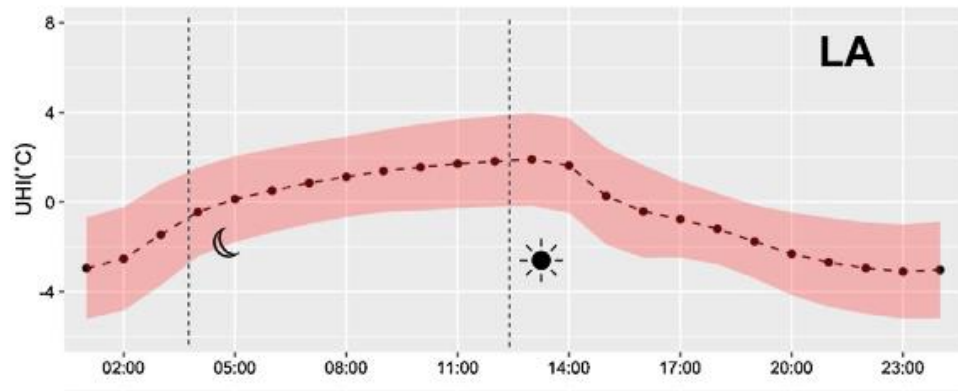


**Figure 6.15.** UHI intensity of LA in UTC time. LA local time is UTC-8. Taken from (Ramamurthy & Sangobanwo, 2016).

Figure 6.15 shows the UHI intensity in LA for a day during the spring. The intensity increases at night, when the built structures release heat to its surroundings. During the day, the built structures absorb heat from the radiation of the sun and the sun heats up the air as well, therefore the intensity of the UHI decreases during daytime. Figure 6.16-6.19 summarize the UHI intensity found with meteorological data during eight days of the year 2017.

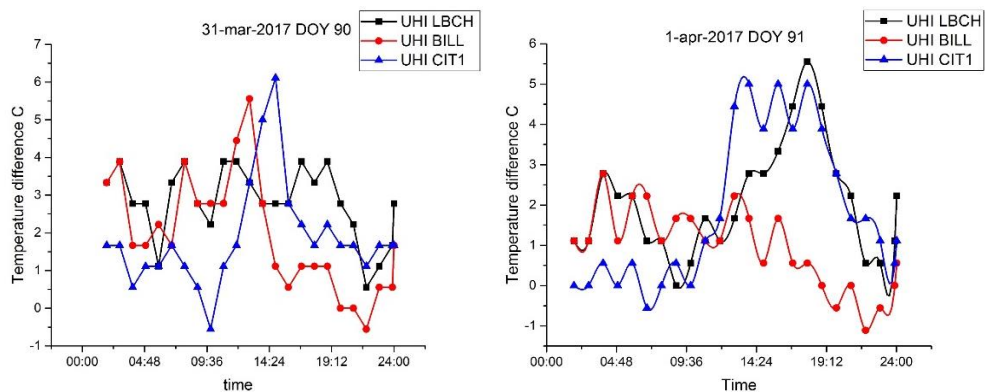


**Figure 6.16.** Intensity of the UHI between three urban and one rural station during DOY 90 and 91 2017.

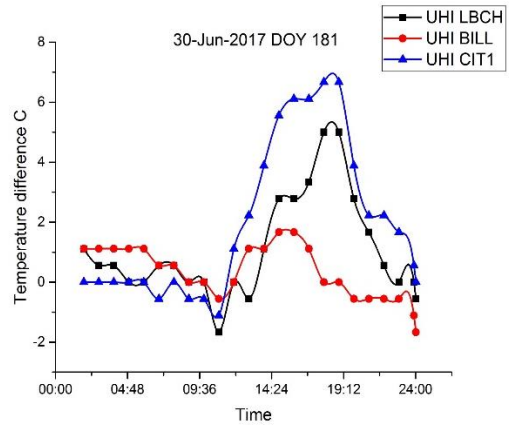
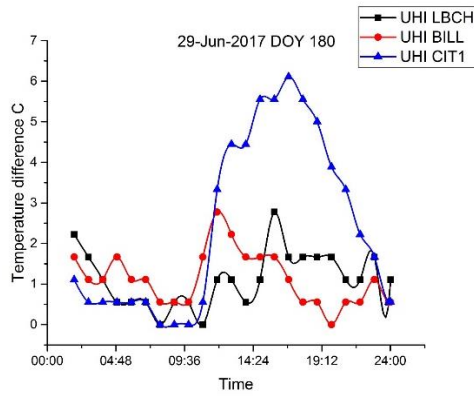


**Figure 6.17.** Intensity of the UHI between three urban and one rural station during DOY 180 and 181 2017.

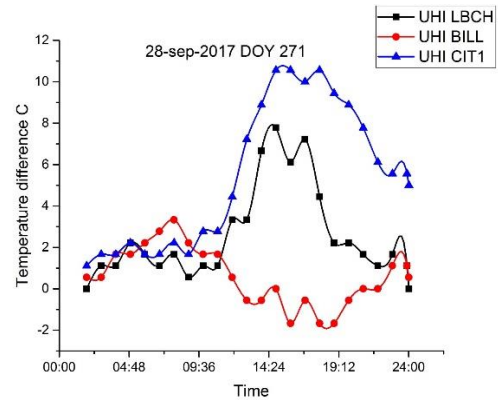
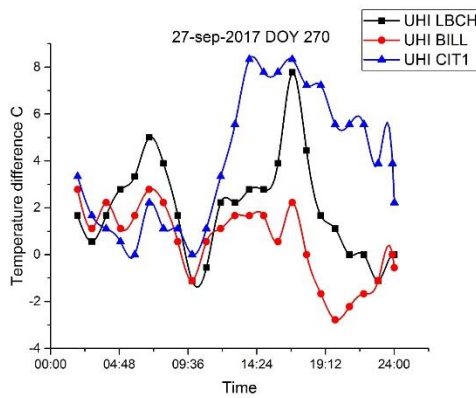


**Figure 6.18.** Intensity of the UHI between three urban and one rural station during DOY 270 and 271 2017.

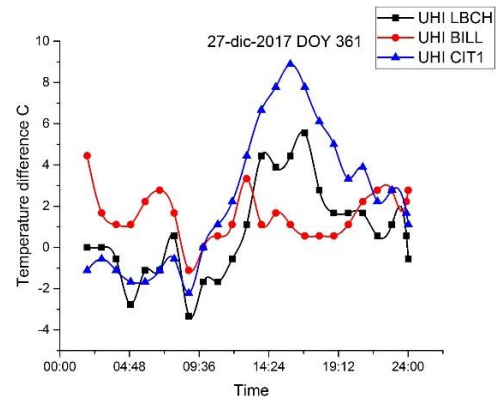
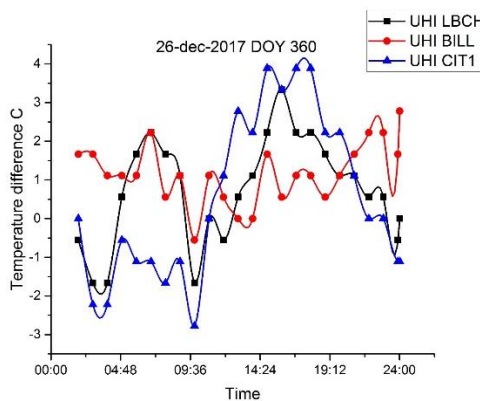


**Figure 6.19.** Intensity of the UHI between three urban and one rural station during DOY 360 and 361 2017.

The hourly profiles of the UHI depicted in Figures 6.16-6.19 show that after 12:00 local time, the intensity of the UHI increases to a maximum of 10 °C during the autumn and winter. At around 16:00 the intensity starts to decrease until midnight. The UHI is more notorious during the autumn.

The intensity of the UHI (UHII) obtained with meteorological data from weather stations is compared with the UHII estimated with the algorithm.

The average of the differences and the RSME are used as indicators of the quality of the estimation.

**Table 6.4.** Average of the differences in °C for UHI intensity in Long Beach, Redondo Beach and Pasadena

Average differences			
DOY	Long Beach	Redondo	Pasadena
90	0.23	-1.45	2.16
91	-0.97	-2.74	2.08
180	-3.01	-3.18	0.39
181	-3.26	-4.72	3.14
270	-0.99	-3.70	-0.002
271	-0.80	-3.85	-0.86
360	-3.65	-3.18	3.92
361	-2.76	-1.86	1.52

All data is compared epoch by epoch. Table 6.5 shows the average of the differences of the UHI intensity estimated from GNSS data and the UHI intensity measured from meteorological data.

**Table 6.5.** RMS value in °C for the differences of UHI intensity in Long Beach, Redondo Beach and Pasadena.

RMSE			
DOY	Long Beach	Redondo	Pasadena
90	1.72	1.95	2.88
91	1.76	2.81	2.71
180	4.14	3.61	3.75

<b>181</b>	3.57	4.97	3.80
<b>270</b>	2.35	4.16	2.55
<b>271</b>	2.58	4.88	3.27
<b>360</b>	3.90	3.61	4.69
<b>361</b>	3.88	2.32	4.41

Table 6.5 show the RMSE in °C of the differences. All values are under 5 °C. The main limitation of the algorithm is the low availability of water vapor partial pressure data. The water vapor partial pressure is estimated from radiosonde data available twice a day at 00:00 UTC and 12:00 UTC (16:00 and 04:00 local time). In order to find a precise validation of the algorithm, the UHII estimated at 04:00 and 16:00 every day was compared with the UHII measured from weather stations at the same times.

Since, only two values are used for the validation, more data has been processed and used in the comparison. Data from 5 days in each season was analyzed and compared to the UHII from meteorological data. 5 days during the spring have been selected: DOY 88,89,90,91 and 92. 5 days during the summer have been selected: DOY 178,179,180,181 and 182. During the summer 5 days have been selected: DOY 268,269,270,271 and 272. And, during the winter 5 days have been selected: DOY 358,359,360,361 and 362. The averages of these differences are shown in Table 6.6

**Table 6.6.** Average of the differences of UHI intensity in °C, for stations in Long Beach, Redondo Beach and Pasadena at 04:00 and 16:00 local time.

		<b>Long Beach</b>	<b>Redondo Beach</b>	<b>Pasadena</b>
<b>Spring</b>	<b>04:00</b>	-0.30	-1.04	3.07

	<b>16:00</b>	-0.60	-1.84	0.15
<b>Summer</b>	<b>04:00</b>	-1.32	-2.19	3.51
	<b>16:00</b>	-4.51	-1.23	-2.88
<b>Autumn</b>	<b>04:00</b>	-2.95	-2.46	2.98
	<b>16:00</b>	0.63	-3.96	-2.84
<b>Winter</b>	<b>04:00</b>	-3.46	-0.13	4.39
	<b>16:00</b>	-0.64	-2.86	-1.62

The average of the differences of UHI using all available data is shown in Table 6.7.

**Table 6.7.** Average of the differences in °C of all available data at 04:00 and 16:00.

	<b>Long Beach</b>	<b>Redondo Beach</b>	<b>Pasadena</b>
<b>04:00</b>	-2.01	-1.45	3.49
<b>16:00</b>	-1.28	-1.80	-1.80

## 6.5 UHI monitoring in HK

A second implementation of the developed algorithm is presented in this section, using HK GNSS data. The location has been described in Chapter 3. Hong Kong has been chosen as a test site because it has many heavy populated urban areas with lots of buildings close together. However, it has also areas with less population and few buildings.

The GNSS data used to test the algorithm has been described in Chapter 3. Furthermore, in the same chapter, the meteorological data used for validation has been also described. The UHI is monitored using the same procedure as the one described in section 6.2 to monitor the UHI in LA. The first step is the classification of type of stations.

### **6.5.1 Classification of type of GNSS station**

The station classification type, either rural or urban, was done following the same visual procedure applied to the LA metropolitan area stations. The classification procedure is shown in Appendix 3. Due to few meteorological stations with data available for Hong Kong, only two stations in an urban environment and two stations in a rural environment have been chosen for the HK UHI study, as data was neither easily available nor easily downloadable. Data can only be downloaded day by day, and only up to 15 MB of information can be downloaded at a time. Due to this limitation, stations were chosen manually from the list of available sites.

### **6.5.2 UHI monitoring in Hong Kong: methodology**

The HK UHI was monitored using a similar methodology to that applied to the LA UHI. The algorithm is described in figure 6.20.

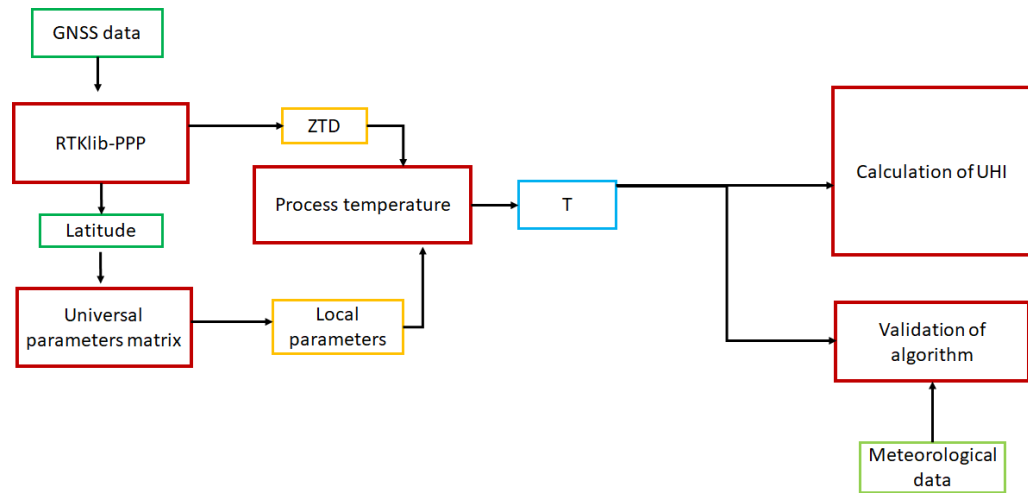


**Figure 6.20.** Block diagram of the methodology followed to monitor the HK UHI.

## 6.6 Implementation of the algorithm with data from HK

### 6.6.1 Process Raw data

The free source software RTKLIB has been used to process raw GNSS data and estimate the position and the ZTD using the PPP technique—with RTKLIB in PPP-kinematic mode. The final precise ephemeris and navigation data provided by the IGS were used as input in RTKLIB. Since there was observation data every 30 s, there are parameter estimates (position coordinates and ZTD) available every 30 s.

### 6.6.2 Process ZTD

A MATLAB routine has been implemented to read the ZTD from each of the RTKLIB output files generated. There are 2880 daily ZTD values. The ZTD estimated with RTKLIB are plotted in Figure 6.21-6.24.

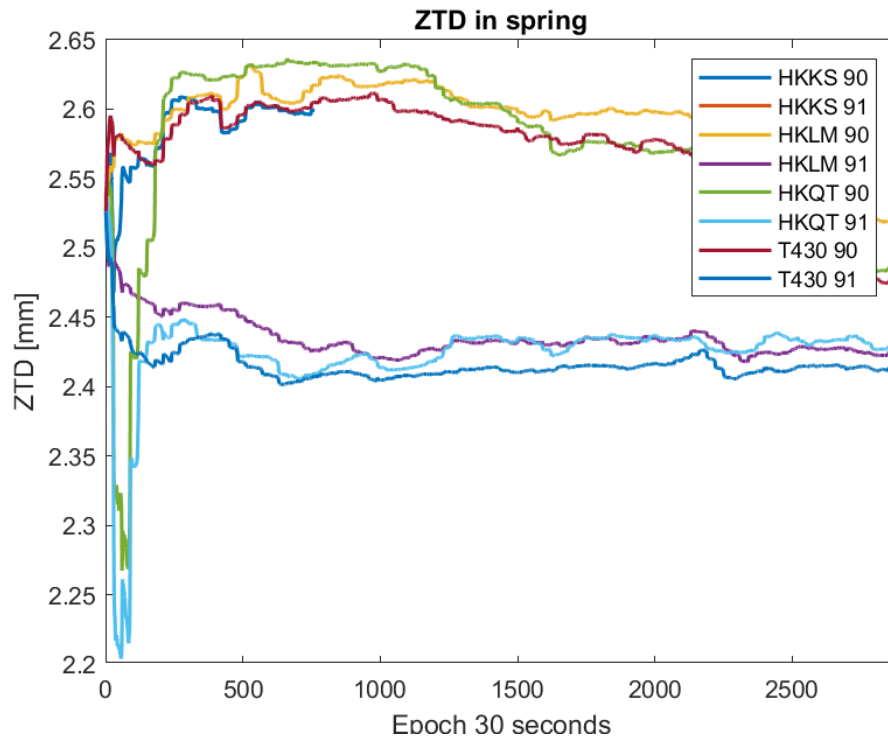


**Figure 6.21.** ZTD of stations in HK during the spring in 2017.

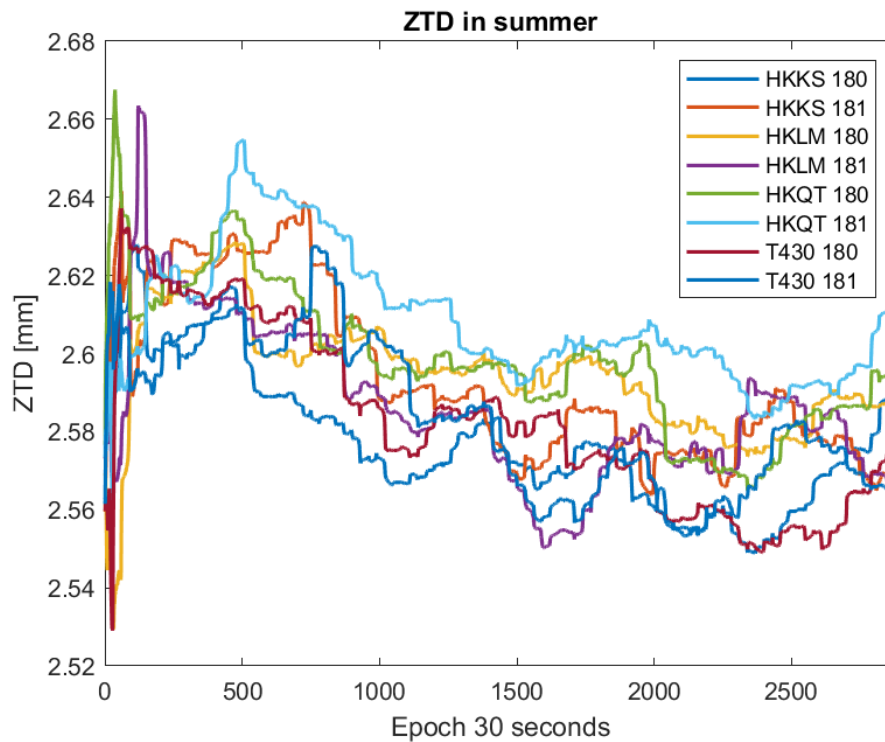


**Figure 6.22.** ZTD of stations in HK during the summer 2017.

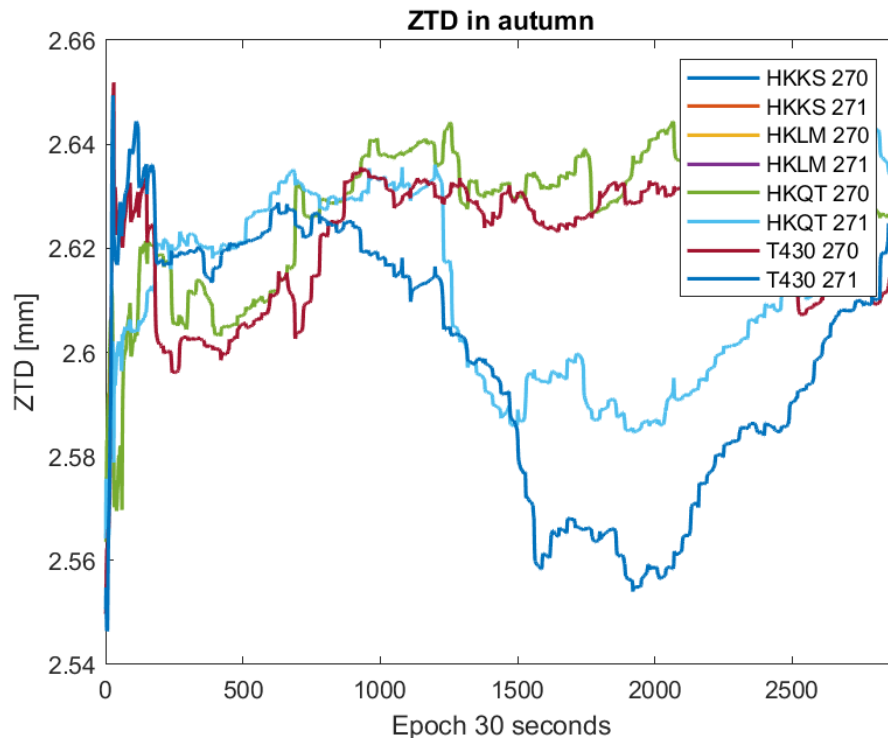


**Figure 6.23.** ZTD of stations in HK during the autumn in 2017.

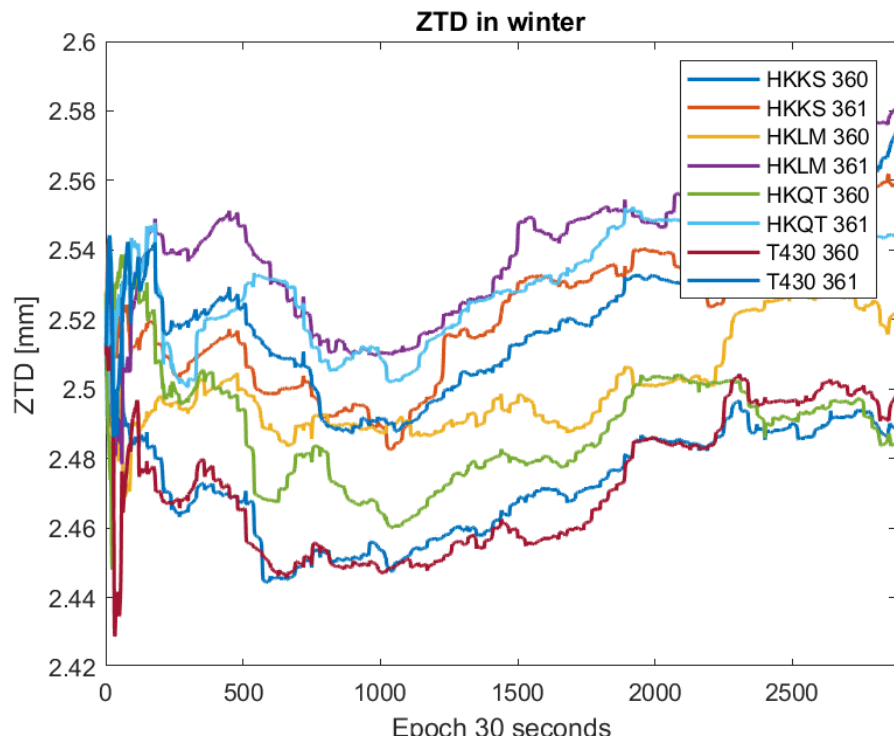


**Figure 6.24.** ZTD of stations in HK during the winter in 2017.

Figure 6.21-6-24 show the ZTD for Hong Kong GNSS stations, for 8 days of 2017. The ZTD has been estimated with RTKLIB, it takes 15 minutes

for the algorithm implemented in RTKLIB to converge to the ZTD value. Therefore, in all graphs at the beginning a big change of value can be detected.

### **6.6.3 Load Local Parameters**

HK is located at latitude 22° N, therefore, radiosonde environmental parameters calculated for latitude 20° N have been used as calculated before. The  $N_h$ ,  $N_0$ ,  $e$  and  $P$  have been taken from the matrix introduced in Chapter 4.

### **6.6.4 Process local $N_0$**

As described in Chapter 4, using  $N_h$ ,  $Z_{trop}$ , troposphere height and the ZTD, values for the local  $N_0$  were found, using the equations presented in that Chapter.

### **6.6.5 Calculation of temperatures from $N_0_{local}$**

Temperatures have been calculated using the universal parameters, local refractivity profile and equation (4.4) defined in Chapter 4. Figure 6.25-6.28 show the temperatures obtained using GNSS data from HK stations.

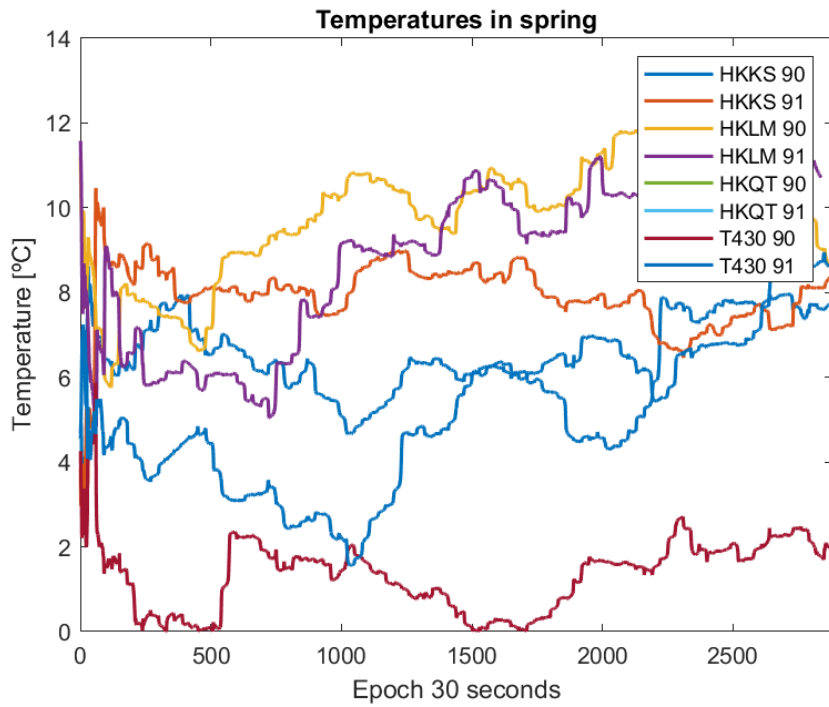


**Figure 6.25.** Temperatures during the spring, 4 stations in HK.

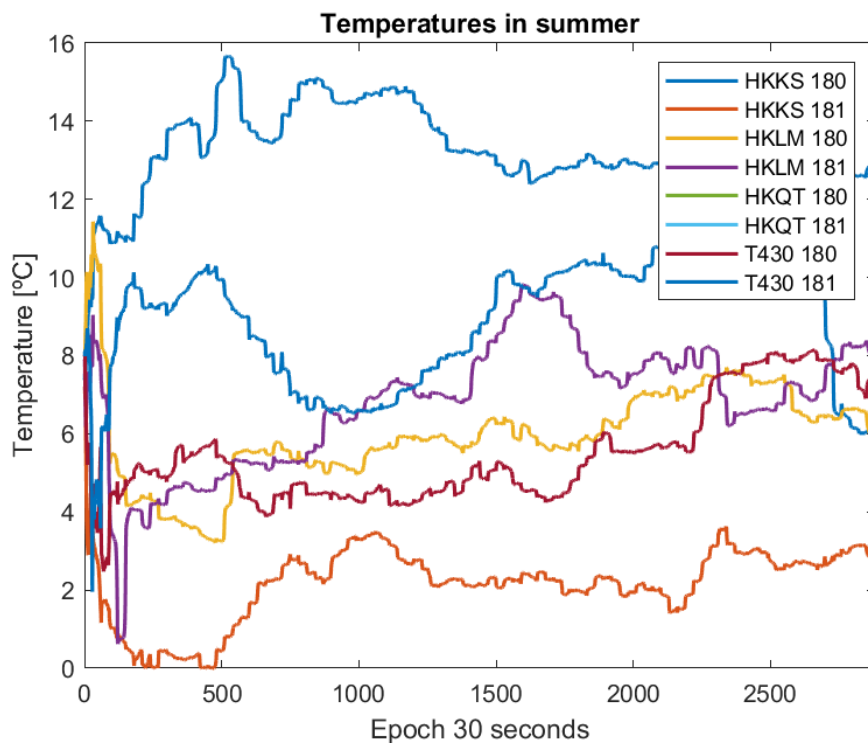


**Figure 6.26.** Temperatures during the summer, 4 stations in HK.

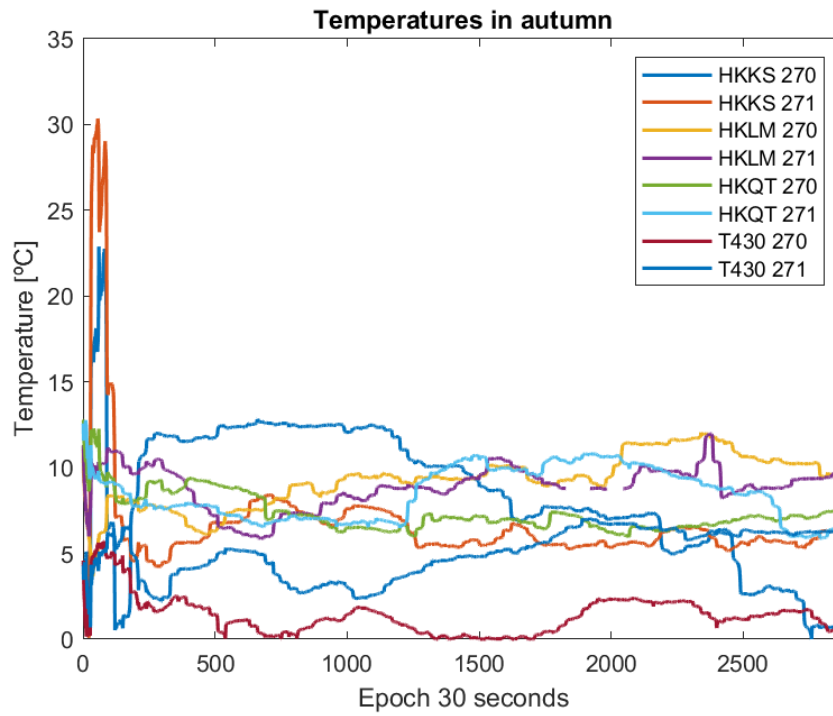


**Figure 6.27.** Temperatures during the autumn, 4 stations in HK.

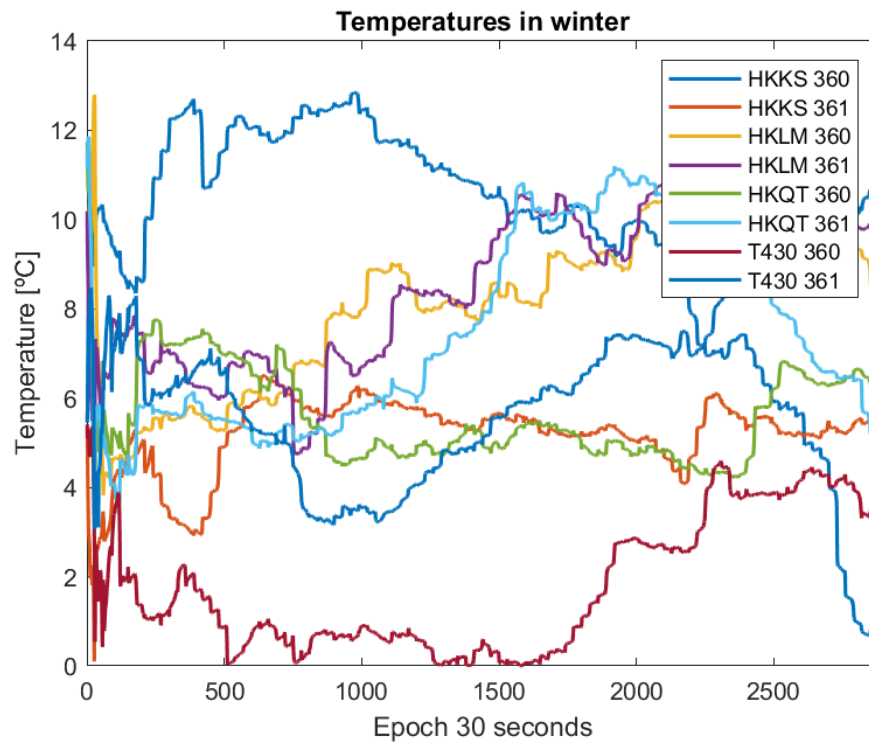


**Figure 6.28.** Temperatures during the winter, 4 stations in HK.

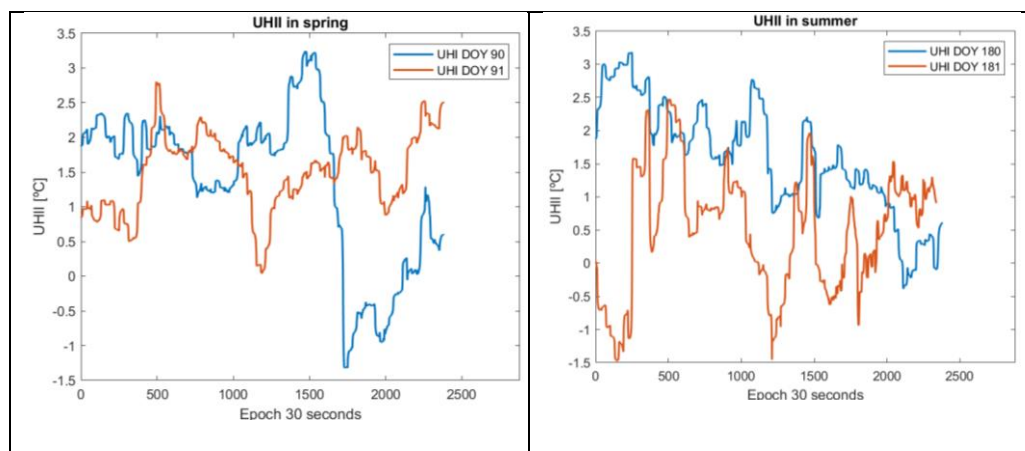
Figures 6.25-6.28 show the output of the algorithm. That is the temperature estimated from ZTD at 4 locations in Hong Kong during DOY 90, 91 (spring), 180, 181 (summer), 260,261 (autumn) and 360, 361 (winter). Since the ZTD requires 15 minutes to converge, the first 15 minutes of the estimated temperature present a highly variable result.

### 6.6.6 Estimation of UHI intensity

The UHI intensity is obtained by subtracting the temperature at an urban station with the temperature at a rural station. In this case, the rural station is in Hong Kong international airport and the urban station is in Hong Kong Observatory. The following mathematical relations is used to monitor the UHI intensity (UHII) at DOY 90,91,180,181,270,271,360,361:

$$UHII_{HK} = T_{alg}(T430) - T_{alg}(HKSL) \quad (6.4)$$

The daily profile of the UHI intensity is plotted in Figure 6.29. Each plot includes the profile of the UHI during two consecutive days.



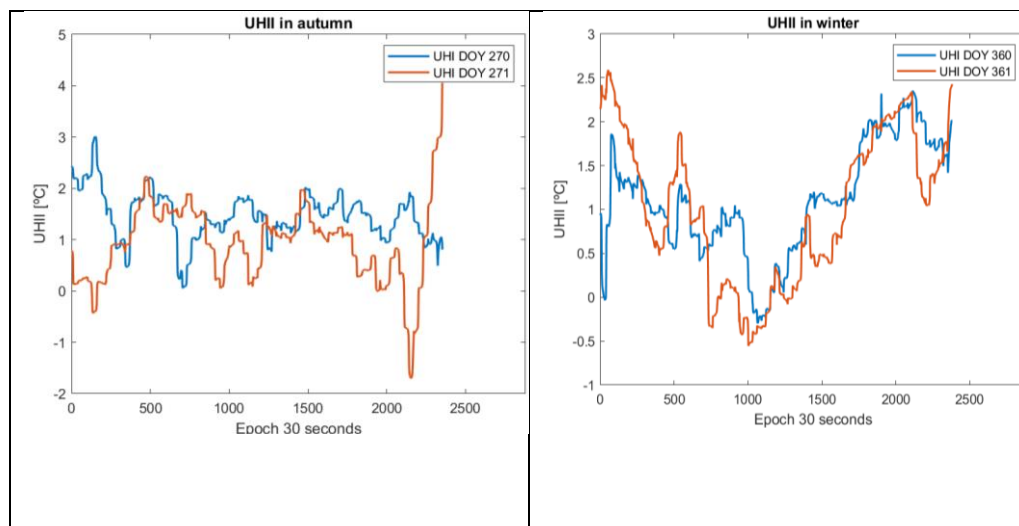


**Figure 6.29.** UHI intensity from GNSS data stations in HK.

The profiles of the UHI during different days of the year in Hong Kong are shown in figure 6.29. The stations used for the analysis are T430 which is in Hong Kong Observatory and HKKS which is in Hong Kong International Airport. The output is presented depending on the season, DOY 90 and 91 are days in spring. DOY 180 and 181 are days in summer. DOY 270 and 271 are days in autumn. DOY 360 and 361 are days in winter.

The shape found during the winter is very similar to the shape found with meteorological data. That is, as midday approaches, the UHI intensity (UHI) decreases. Past 16:00 the UHI increases. Similar behaviour is found with data from other days of the year; however, the shape is not as clear as during the winter.

## 6.7 Validation of algorithm

The validation of the algorithm used to monitor the UHI in HK is done by comparing the UHI intensity estimated with GNSS data implementing the algorithm with the UHI measured from weather stations.

A previous study done by Wai Siu and Hart (2013) shows the profile of the UHI in Hong Kong. The profile of the UHI obtained from surface temperatures in their study is shown in Figure 6.30.

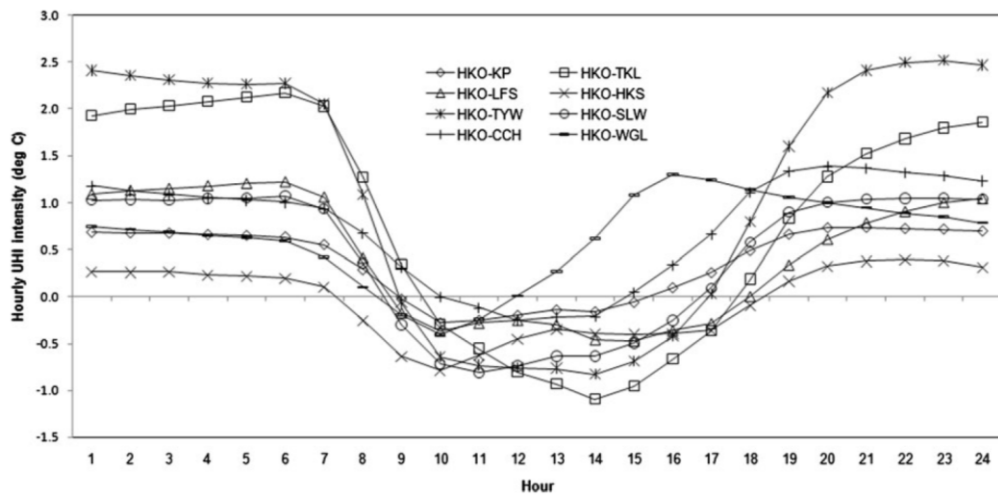


**Figure 6.30.** Profile of the UHI intensity in HK, taken from (Wai Siu & Hart, 2013)

The profile of the UHI presented in Figure 6.30 show a maximum intensity around 20:00. From 17:00 to 20:00 the UHI intensity increases, as at this time the buildings start to release heat to the atmosphere. After 7 am the UHI intensity decreases because the sun heats up the air and the built structures. The lowest intensity is found around 12:00 in most cases presented in Figure 6.30.

### 6.7.1 UHI intensity from meteorological stations

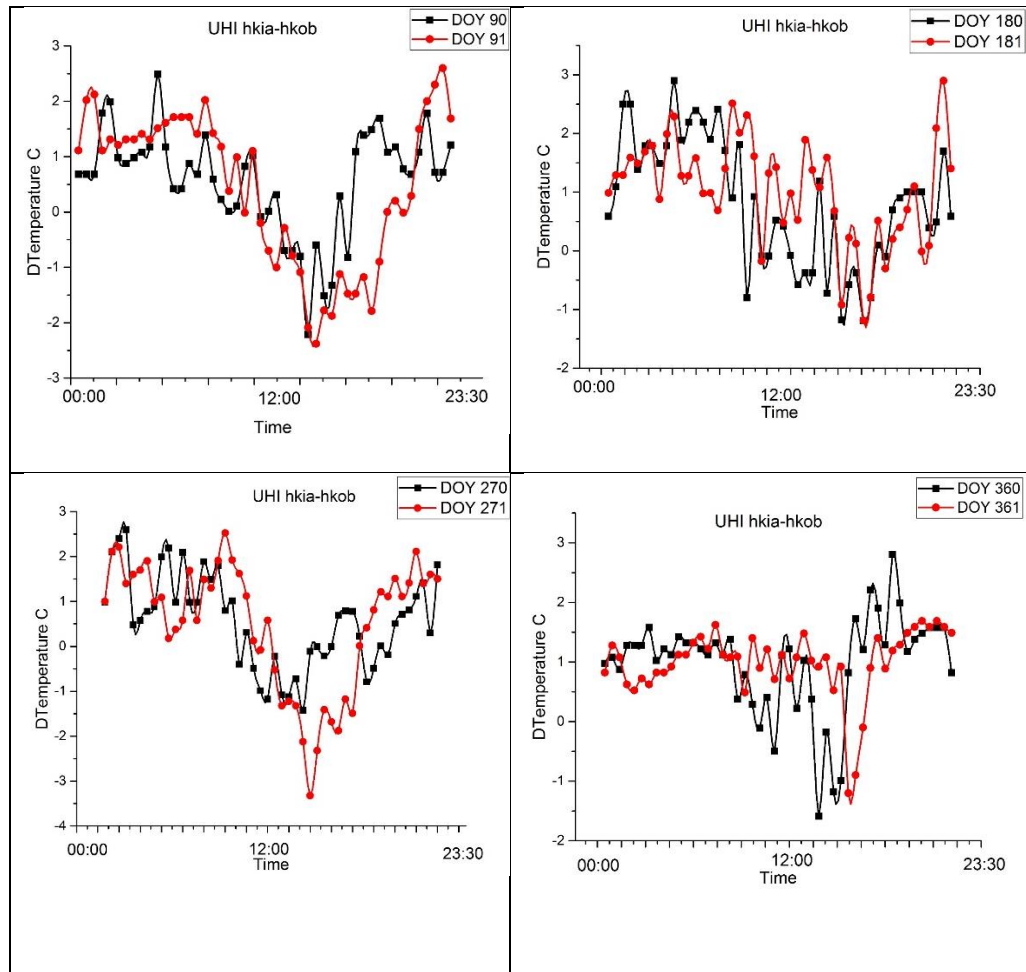


**Figure 6.31.** Profile obtained with meteorological data of UHII during 4 seasons.

The profile of the UHII found with meteorological data follows the same pattern as the one found in literature. The intensity found with meteorological data and the intensity estimated from GNSS data are compared using the following mathematical relation.

$$DUHII = UHII_{algo}(t) - UHII_{met}(t) \quad (6.5)$$

The mean of the differences (DUHII) and the RMSE are used as validation parameters. The daily mean of the differences and RSME of the differences are shown in Table 6.8. All values presented are in °C.

**Table 6.8.** Average and RMSE of the differences of UHII\_GNSS and UHII\_MET. In °C.

DOY	90	91	180	181	270	271	360	361
Average	<b>0.61</b>	<b>0.73</b>	<b>0.23</b>	<b>1.22</b>	<b>2.29</b>	<b>1.59</b>	<b>0.45</b>	<b>1.17</b>
RMSE	<b>1.93</b>	<b>2.81</b>	<b>1.36</b>	<b>2.36</b>	<b>2.69</b>	<b>2.71</b>	<b>1.34</b>	<b>1.67</b>

More data was analysed in order to study the behaviour of the algorithm with data from different seasons. The DOY selected during spring were: 88,89,90,91 and 92. In summer, the selected DOY were 178,170,180,181 and 182. In autumn the selected DOY were 268,269,270,271 and 272. In winter, the DOY selected were 358,359,360,361 and 362. The averages of the differences and the RMSE per season are presented in Table 6.9.

**Table 6.9.** Average and RMSE of the seasonal differences UHII\_GNS-UHII\_MET in °C.

	Spring	Summer	Autumn	Winter
Average	<b>0.67</b>	<b>0.72</b>	<b>1.94</b>	<b>0.81</b>
RMSE	<b>2.37</b>	<b>1.86</b>	<b>2.70</b>	<b>1.51</b>

The main limitation of the algorithm is the lack of real time data for water vapor partial pressure  $e$ . The values of  $e$  are obtained from radiosonde data available only twice a day, at 00:00 UTC and 12:00 UTC. Therefore, a validation had to be done by comparing the UHI intensity at those times. Local time in Hong Kong SAR is UTC+8, therefore, the radiosonde data is available at 08:00 and 20:00 local time (HKT). The validation is done with the following mathematical relations:

$$Average = \sum_1^{DOY} \frac{UHII\_GNSS(08:00HKT) - UHII\_MET(08:00HKT)}{DOY} \quad (6.6)$$

$$Average = \sum_1^{DOY} \frac{UHII\_GNSS(20:00HKT) - UHII\_MET(20:00HKT)}{DOY}$$

**Table 6.10.** Average in °C of the differences defined in Equation 6.6

	Spring	Summer	Autumn	Winter
00:00	<b>0.63</b>	<b>0.62</b>	<b>2.07</b>	<b>0.87</b>
12:00	<b>-0.55</b>	<b>-0.25</b>	<b>1.94</b>	<b>1.02</b>

It is possible to monitor the UHI intensity with GNSS data with a precision 3 °C. This has been demonstrated with the implementation of the algorithm with LA and HK data. However, the limitation of the algorithm is the low availability of *e* data. The real time implementation of the algorithm is limited by the lack of real time data of water vapor partial pressure. The next section demonstrates the possibility of using the algorithm to monitor UHI intensity at precise times with an estimated *e*.

## 6.8 UHI monitoring in Ningbo, China

Ningbo is situated in the coastal plain of the Yong River, approximately 25 km upstream from its mouth in Hangzhou Bay. Its land area is 9,816 km<sup>2</sup>, and its oceanic territory amounts to 9,758 km<sup>2</sup>. In total, the territory has 1,562 km of coastline, consisting of 788 km of mainland coastline and 774 km of island coastline. There are 531 islands under the city's administration (Britannica, 2019), and the 2012 population estimate for Ningbo was 7,639,000 inhabitants. The site and the data used in this section are described in Chapter 3.

### **6.8.1 UHI monitoring in Ningbo: Methodology**

The UHI in Ningbo was monitored using the same procedure described for the UHI monitoring in HK, including the same six steps:

- Process raw GNSS data with RTKLIB
- Obtain a daily ZTD
- Load local parameters based on the latitude
- Process local  $N_0$ ,
- Estimate temperature from local  $N_0$ ,
- Calculate UHI intensity.

The data available for this case study had different time intervals. There were 2 h of 1 s GNSS observation data, 2 h of 5 min meteorological data and daily averages of the universal parameters. Therefore, the daily changes of universal parameters were not accounted for when the GNSS and the meteorological data exhibited hourly fluctuations.

### **6.8.2 Process raw data**

The raw data collected with the GNSS Leica receiver has been processed with RTKLIB. Thus, the position of the receiver and the ZTD have been estimated as part of the RTKLIB solution. The options used in RTKLIB were: Kinematic forward positioning, a cut-off angle of  $10^\circ$  and the precise ephemeris from the IGS. The RTKLIB-estimated ZTDs are plotted in Figure 6.32.

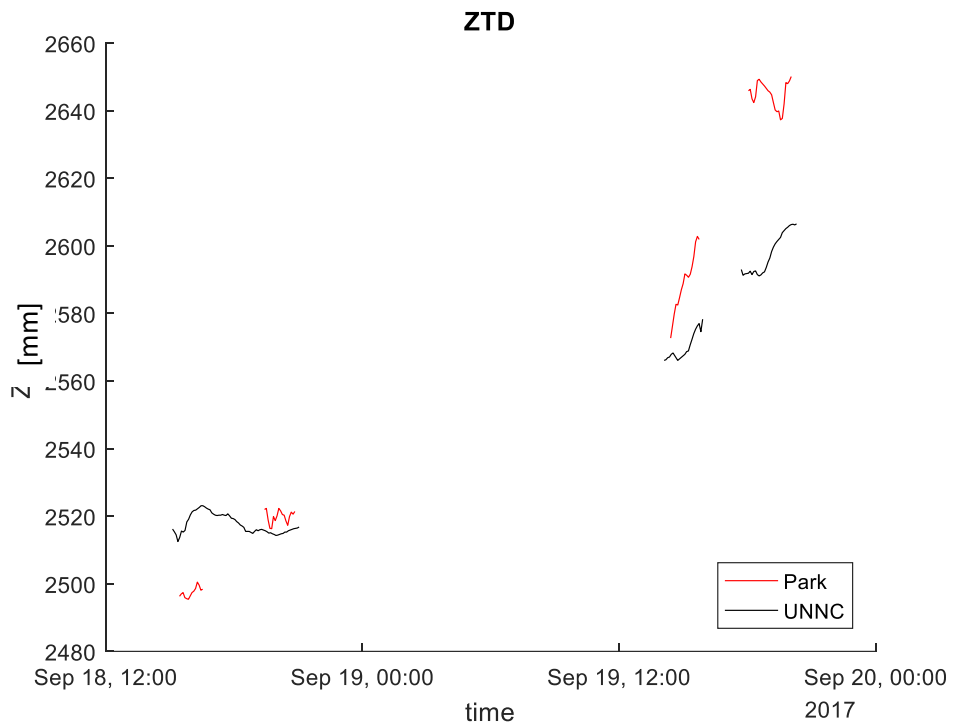


**Figure 6.32.** ZTD estimated from raw data collected in the park and at UNNC campus.

The ZTDs estimated as a by-product of the PPP technique implemented in RTKLIB are depicted in Figure 6.32. Two hours' worth of data was collected on September 18 and 19, 2017. (DOY 260 and 261)

### 6.8.3 Process ZTD

MATLAB was used to extract the ZTD value from RTKLIB's output. Every epoch of raw data yielded a value of ZTD. In total 1806 values of ZTD were estimated with RTKLIB.

### 6.8.4 Load local parameters

The parameters needed to estimate the temperature from GNSS data are the  $Z_{\text{trop}}$ ,  $N_h$ ,  $N_0$ ,  $P$  and  $e$ , which were available daily (one value per day). It was assumed that  $Z_{\text{trop}}$  and  $N_h$  didn't vary significantly during the day, so the value available for these parameters will be constant

during the hours of data collected. Water vapour partial pressure was the only parameter that changed significantly through a 24 h period.

### 6.8.5 Process local $N_0$

The  $N_h$  and  $Z_{trop}$  are imported from the matrix containing the universal parameters, using a MATLAB code similar to the one used for the previous two cases.  $N_{0\_local}$  is calculated using the formula:  $N_{0\_local} =$

$\frac{ZTD}{\int_{Z_{site}}^{Z_{trop}} e^{N_h} dz}$ . In this case, the receivers are at the same height and the same

latitude, so the integral in the denominator is a constant for both days.

The same  $Z_{trop}$ ,  $Z_{site}$  and  $N_h$  are used for both stations each day, and so it is concluded that, when working in a time span of less than 24 h, the  $N_0$  is directly proportional to the ZTD. Figure 6.33 shows the  $N_0$  values calculated with the available data.

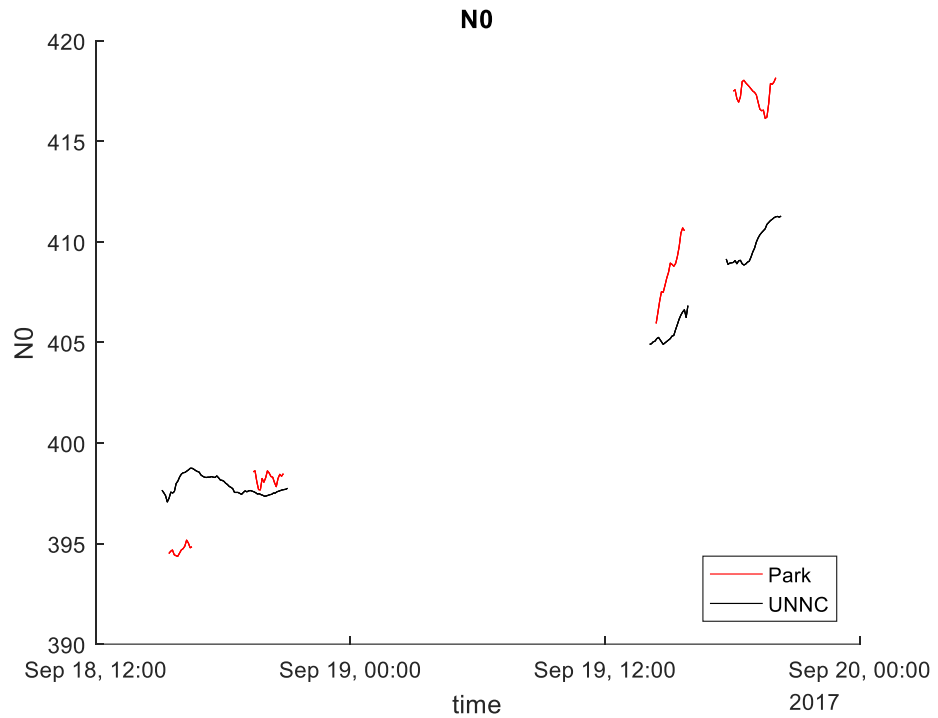


**Figure 6.33.** Profile of local  $N_0$  obtained from ZTD data and universal parameters.

The calculated local  $N_0$  shows that during the evening of September 19, the difference of values between both stations is clear, and so it is expected that a temperature difference between the stations would be found for that day.

### 6.8.6 Calculation of Temperature from $N_0_{local}$

Temperature is calculated following the procedure explained in Chapter 5. The profile of the  $e$  for year 2017 is shown in Figure 6.34.

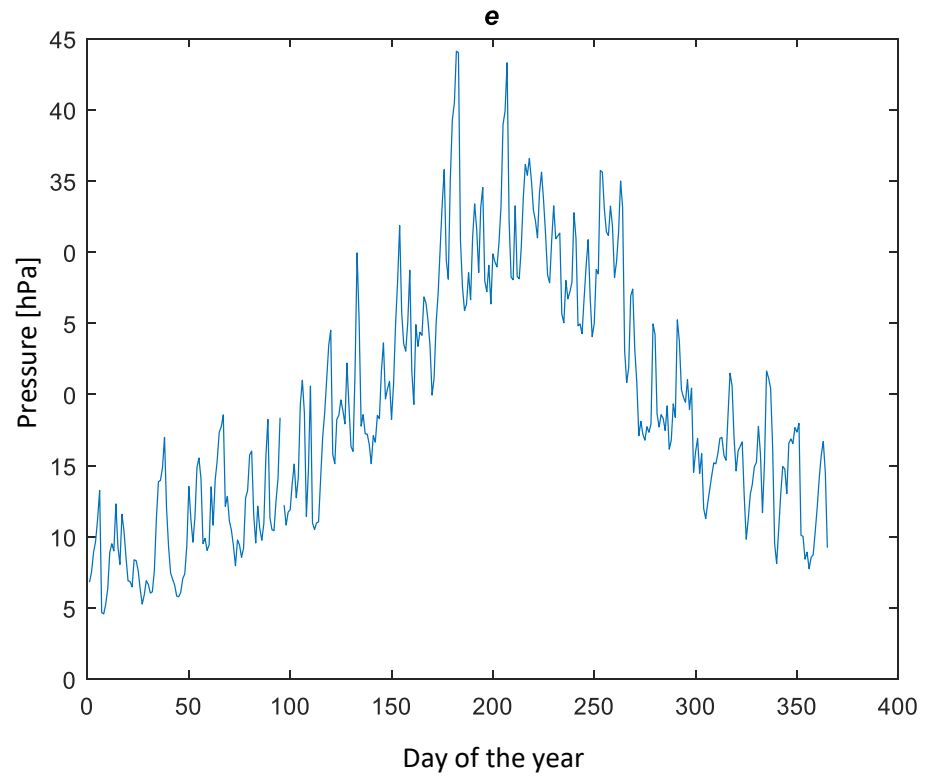


**Figure 6.34.** Profile of  $e$ , for 2017

The profile of  $e$  shows that its value changes through the year and also during the day. It was computed using radiosonde data from a radiosonde station located at a latitude similar to that of the GNSS receivers. Since GNSS data was collected for 2017 DOY 262 and 263 (September 18 and 19, 2017), we used the  $e$  values for DOY 262 and 263 to calculate the temperatures for those days.

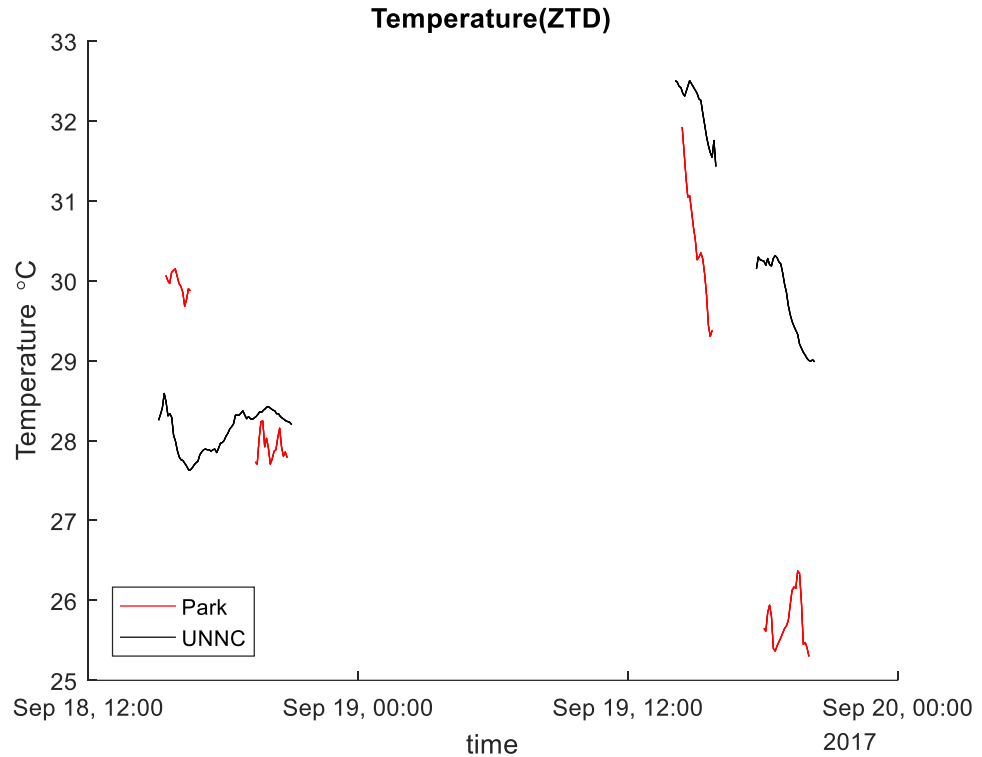


**Figure 6.35.** Temperatures estimated from ZTD at two locations: a park in Ningbo and at the UNNC campus.

The results displayed in Figure 6.35, for September 18, show a difference between the temperatures during the afternoon, when the park was warmer than the UNNC campus. Inside the campus, the temperature remained almost constant during the measurement period. In September 19, the temperature at UNNC campus was consistently higher than that of the park, indicating that the UHI was detected for that day.

### 6.8.7 Estimation of the UHI Intensity

The results from September 19 show that the campus temperature was always higher than the park temperature, especially during the evening, when the temperature difference was around 4 °C—which falls within the UHI definition.

## 6.9 Validation of output of algorithm

To validate the results, the temperatures obtained with the algorithm were compared to the temperatures measured with temperature sensors placed at the same locations as the GNSS receivers. Figure 6.36 shows the results of this comparison.

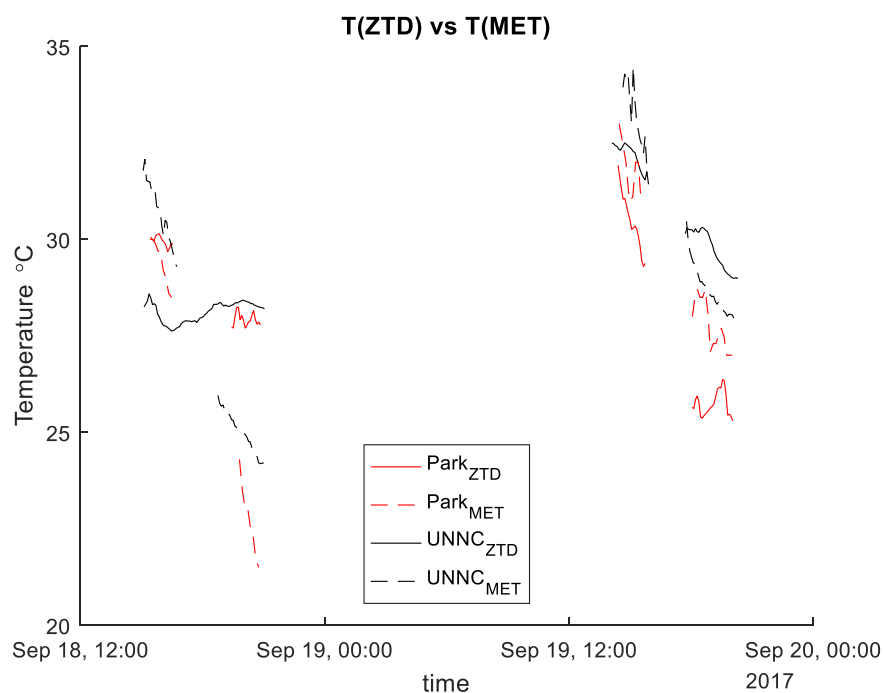


**Figure 6.36.** Temperatures calculated with the algorithm and with GNSS data (PARK<sub>ZTD</sub> and UNNC<sub>ZTD</sub>), and temperatures measured with a temperature sensor (PARK<sub>MET</sub> and UNNC<sub>MET</sub>).

Figure 6.36 shows the temperatures estimated with the algorithm at UNNC and PARK, and the temperatures measured with a temperature sensor at both locations. The red lines represent the temperature in the park, while the black lines are those in the campus. The continuous lines represent the results from GNSS data, and the dotted lines represent the temperatures measured at meteorological stations.

The results for the evening of September 19, 2017 are clear; the temperatures calculated with the algorithm and those measured with meteorological sensors followed the same shape in the park, with the UNNC temperature always higher than that of the park.

## **6.10 Analysis of discrepancies**

The discrepancies found with data from LA, HK and NB can be explained because of two main reasons:

1. Low availability of radiosonde data for calculation of the water vapor partial pressure. The amount of water vapor in the troposphere varies a lot through the day of the year depending on the season and the weather conditions. Therefore, the water vapor partial pressure also varies throughout the day. Since there are only two daily radiosonde soundings the value of  $e$  is calculated at those times, when radiosonde data is not available the value of  $e$  is estimated. Therefore, a better model to calculate  $e$  is required.
2. Special weather conditions are not accounted for in this algorithm. Specially in Hong Kong, there are typhoons passing through the territory. The algorithm and the validation technique need to be improved to take into consideration special weather conditions.

According to Ramamurthy and Sangobanwo (2016) the Standard Deviation (STD) of the UHII in LA that they found using remote sensing techniques is 4 °C. The STD of the UHII found from the results of the algorithm is 3.6 °C when radiosonde data is available. Even though, there

are discrepancies in the results, the algorithm had the same accuracy as the remote sensing technique used to monitor the UHI in LA.

The discrepancies for data from Hong Kong are less than 3 °C when radiosonde data is available. The results presented by (Wai Siu & Hart, 2013) show the UHI intensity with a deviation of 2.5°C depending on the sites. Therefore, the performance of the algorithm is within acceptable range compared with remote sensing techniques.

The UHI found in Ningbo is 4 °C. This value cannot be compared to other UHI studies in Ningbo because there are no previous studies. Furthermore, more data is required to monitor the UHI during the whole year in Ningbo.

## **6.11 Discussion**

The three case studies presented in this chapter show that it is possible to monitor UHI intensity using GNSS data and universal parameters derived previously from radiosonde data. The algorithm implemented with data from three cities (LA, HK and NB) has the same steps in all cases:

- Process raw data
- Process ZTD
- Load local parameters
- Process local  $N_0$
- Calculation of temperature from  $N0\_local$
- Estimation of the UHI intensity

Raw data is either collected using GNSS receivers such as in the case of NB or obtained from reliable sources such as the IGS or Hong Kong Observatory. The ZTD is estimated using RTKLIB which implements PPP in the three cases. Previously, radiosonde data has been processed from stations around the world to calculate pressure, and the profile of the refractivity of the troposphere at different latitudes. These parameters are recorded in a matrix indexed by latitude. The algorithm requires the parameters and the ZTD at the latitude of measurement to estimate the temperature from the relation of the tropospheric delay and environmental variables. Finally, the UHI intensity is obtained by subtracting the temperature at an urban area minus the temperature at a rural area.

The validation of the algorithm is done by comparing the UHI estimated from GNSS data and the UHI measured with data from weather stations. At the times when there is radiosonde data (00:00 UTC and 12:00 UTC). The UHI measured from weather stations show a pattern which agrees with theory. However, the output of the algorithm does not follow the same pattern clearly. The limitations of the algorithm are the inputs, the pressure is considered to be a constant and the water vapor partial pressure is obtained from radiosonde soundings which are available twice a day in the best cases. The results would be improved if these variables can be measured in real time. The pressure can be measured from a barometer which can be found embedded in hand-held devices. However,  $e$  poses the greatest challenge as its models depend on

temperature. The possibility of using Numeric Weather Prediction models can help to estimate  $e$  with greater frequency.

Another factor that induces error to the UHI estimation from GNSS data is the difference of height between the GNSS receiver and the height of the weather sensor used for validation. All weather stations are located 2 meters above the ground, however, the GNSS receivers can be located on top of buildings because a clear view to the sky is necessary in precise positioning. The altitude affects the measurement of temperature, according to the WMO the temperature decreases 6 °C every kilometre of altitude. The difference of altitude of the GNSS sensor and the meteorological sensor need to be taken into consideration when doing the validation of the output of the algorithm.

Other reasons for the discrepancies found in the validation of the output of the algorithm are: extreme weather conditions, lack of data because of technical difficulties, errors in the PPP technique, lack of data to implement the PPP technique. In conclusion, the more GNSS data available allows to monitor the UHI with more precision and to detect small changes of temperature within the city. Therefore, it is desirable to have a dense GNSS network, and this can be achieved using crowdsourcing or participatory sensing techniques.

# CHAPTER 7

## CONCLUSIONS AND FUTURE WORK

### 7.1 Summary

The aim of this research has been to develop an algorithm to monitor the UHI intensity from GNSS data. The aim has been achieved by developing two algorithms, one to compute surface temperature from GNSS data, and one to calculate the UHI intensity from GNSS data. The UHI monitoring algorithm operation involves six steps:

- 1 The first step is the estimation of the ZTD from GNSS data using the Precise Point Positioning technique. In this thesis, the open-source software RTKLIB is used as the implementation of PPP to estimate ZTD. GNSS data from LA, HK and NB has been processed to test the algorithm.
- 2 The second step of the algorithm is to import the output of RTKLIB into a matrix using MATLAB. The matrix is indexed by latitude.
- 3 The third step is the derivation of the profile of the water vapour partial pressure,  $e$ , the refractivity of air at surface level,  $N_0$ , the ratio of decay of the refractivity with height,  $N_h$ , and the air pressure,  $P$  in the troposphere. These profiles are obtained for different latitudes using radiosonde data. This step only needs to be performed once because

all variables have an annual cycle. A re-computation of these parameters is needed in 5 years to account for climate change. All data used in this research is from the year 2017.

- 4 The fourth step is the calculation of the height of the troposphere. This is achieved using radiosonde data and the definition of LRT1 and LRT2 given by the WMO. Furthermore, in this research, a formula has been derived to calculate the height of the troposphere from GNSS data.
- 5 The fifth step is the calculation of the temperature using the ZTD, parameters estimated in the third step and the height of the troposphere. The process is explained in Chapter 5 of the thesis.
- 6 Lastly, the intensity of the UHI is calculated by comparing the temperature at an urban site with that of a rural site. The intensity of the UHI has been validated using datasets of GNSS and meteorological data for the year 2017 from LA, HK and NB.

## **7.2 Conclusions**

The algorithm to estimate temperature from ZTD has been introduced and validated in Chapter 5. The accuracy of the estimation is indicated by the average of the difference of values estimated with algorithm and values measured with meteorological stations. Moreover, the RMSE of the differences is also used as an indicator of the quality of the estimations. The validation shows that at times when e data is available (from radiosonde, twice a day in some stations), the accuracy of the estimation increases up to 3 °C.

The algorithm to monitor UHII from GNSS data has been introduced and validated in Chapter 6. GNSS data from LA and HK has yielded the expected daily profile of the UHII. In LA, the urban station in Long Beach and the rural station nearby yield an UHI intensity which differs only 2 °C with the UHI intensity found with meteorological data. There is data from radiosonde at 00:00 and 12:00 UTC. At 00:00 the difference between the output of the algorithm and UHII from meteorological data has an average difference of 2 °C while at 12:00 the average difference is reduced to 1 °C. The lower discrepancy between estimated and measured value has been found with data at 12:00 UTC during the spring, autumn and winter. In the summer the average differences at 00:00 UTC and 12:00 is the highest. Therefore, the algorithm needs to be improved for summer conditions.

In HK, the UHII from GNSS data follows the same pattern as the UHII found in previous studies with surface temperature sensors. Only two stations are used in HK, one in Hong Kong Observatory and one in Hong Kong International Airport. The output of the algorithm differs in average 1.04 °C. During the spring, summer and winter, the difference is lower than 1 °C while during the autumn the difference is between 1 °C and 2 °C. The radiosonde station nearby provides data at 00:00 UTC and 12:00 UTC which enables to estimate a precise value of  $e$  at those times. At 00:00 the differences during spring, summer and winter are less than 1 °C while during the autumn the average difference is 2 °C. At 12:00 UTC the highest average difference was during autumn, approximately 1.9 °C.

Therefore, improvements are needed for the weather conditions of Hong Kong during the autumn.

For Ningbo, the data available was from two campaigns, of 2 h each, during two days of September 2017. The intensity of the UHI on September 19, 2017 has been found to be 4°C during the evening, which fulfils the UHI intensity definition. Thus, the ability of the algorithm to monitor temperature using GNSS data at different rates has been demonstrated.

### **7.3 Main contributions of this research**

During the course of this research, the following original work has been conducted:

- Study of the ZTD estimation quality achieved using different software and online PPP services, in order to justify the use of RTKLIB in this research. Details of this work may be seen in Mendez Astudillo et al (2018).
- Software developed in MATLAB to process radiosonde data and ZTD data. This software was used to compute profiles for the environmental parameters, temperature, water vapour and pressure, with respect to altitude. In addition, radiosonde data was processed, to obtain the universal parameters needed as inputs for the algorithm.
- An algorithm, and its software implementation have been developed, to estimate tropopause height using GNSS data. It is based on the definition of the second lapse rate tropopause.

- Theoretical development, and software implementation, of an algorithm to calculate temperature from GNSS data.
- Theoretical development, and software implementation, of an algorithm to measure UHI intensity.

#### **7.4 Future work**

In order to implement the algorithm in real time, it is necessary to have water vapour partial pressure data, at almost real time. This parameter cannot be directly measured. Therefore, new models for  $e$  need to be used to estimate its value at different latitudes such as Numeric Weather Prediction models.

The GNSS network needed to monitor UHI can be implemented with handheld devices incorporating GNSS receivers, such as smartphones. Firstly though, the algorithm needs to be adapted for use with single frequency GNSS receivers. For this case, it is necessary to design a strategy to compensate and account for the effect of the ionosphere, which cannot be eliminated within the PPP technique with double-frequency GNSS data.

If single frequency GNSS receivers can be used to monitor UHI intensity, a system based on crowdsourcing techniques can be implemented. The user will have to characterize whether the location of the handheld device he is carrying is rural or urban, based on the basic definition of urban and rural areas. Then, the user will have to share GNSS data collected with his/her device. The GNSS data collected would need to be sent via an internet link to a server in charge of implementing the PPP to estimate

location coordinates and ZTD. The ZTD and latitude of the receiver's position would then need to be sent to a software implementation of the algorithm described in this thesis, to estimate temperature from the ZTD. The ZTD would be labelled ZTD\_urban or ZTD\_rural, as appropriate, after which the algorithm would obtain T\_urban and T\_rural. These two temperatures would then be compared, and the difference recorded using the algorithm to monitor UHI, as discussed in Chapter 6. Finally, the temperature differences could be mapped, using a mapping service on the server. The map could be retrieved by the user via an internet link and a mapping application in the user's device.

A system such as this would empower users to know the exact the temperature at their location, instead of getting a "generic" temperature from a weather station that might not be close by. Furthermore, the system would enable to monitor the UHI in real-time, which would be valuable for city planners and environmental researchers.

# REFERENCES

- Awange, J. L. (2012). *Environmental Monitoring Using GNSS: Global Navigation Satellite Systems*. Heidelberg, Germany: Springer.
- Bevis, M., Businger, S., & Chiswell, S. (1994). GPS meteorology: Mapping Zenith Wet Delays onto precipitable water. *Journal of Applied Meteorology*, **33**, 379-386.
- Bisnath, S., & Langley, R. (2003). High-Precision Single Frequency GPS Point Positioning. Paper presented in: Institute of Navigation. *ION-GPS/GNSS+ Portland, Oregon*.
- Boehm, J., Niell, A., Tregoning, P., & Schuh, H. (2006). Global Mapping Function (GMF): A new empirical mapping function based on numerical weather model data. *Geophysical Research Letters*, **33**. doi:10.1029/2005GL025546
- Böhm, J., Heinkelmann, R., & Schuh, H. (2007). Short Note: A global model of pressure and temperature for geodetic applications. *Journal of Geodesy*, **81**, 679-683.
- Boufidou, E., Commandeur, T. J. F., Nedkov, S. B., & Zlatanova, S. (2011). Measure the Climate, Model the City. *Remote Sensing and Spatial Information Service*, **XXXVIII**.
- Encyclopedia Britannica., (2019a). *Hong Kong Administrative Region, China*. Retrieved from <https://www.britannica.com/place/Hong-Kong>
- Encyclopedia Britannica., (2019b). *Los Angeles, California, United States*. Retrieved from <https://www.britannica.com/place/Los-Angeles-California>
- Encyclopedia Britannica., (2019c). *Ningbo, China*. Retrieved from <https://www.britannica.com/place/Ningbo>
- Natural Resources Canada. (2019). *Precise Point Positioning*. Retrieved from <https://webapp.geod.nrcan.gc.ca/geod/tools-outils/ppp.php>
- The Keystone Center., (2007). State Clean Energy-Environment Technical Forum: Urban Heat Islands (UHI), Clean Energy and Air Quality. Colorado
- Davies, K., & Hartmann, G. K. (1997). Studying the ionosphere with the Global Positioning System. *Radio Science*, **32**(4), 1695-1703. doi:<https://doi.org/10.1029/97RS00451>
- Davis, J., Herring, T., Shapiro, I., Rogers, A., & Elgered, G. (1985). Geodesy by radio interferometry: effects of atmospheric modeling errors on estimates of baseline length. *Radio Science*, **20**, 1593-1607.
- Dong, Z., & Jin, S. (2018). 3-D water vapor tomography in Wuhan from GPS, BDS and GLONASS observations. *Remote Sensing*, **10**(62).
- EGSA. (2019). Galileo Programme. Retrieved from <https://www.gsa.europa.eu/galileo/programme>
- Essen, L., & Froome, K. D. (1951). Dielectric Constant and Refractive Index of Air and its Principal Constituents at 24,000 Mc./s. *Nature*(**167**), 512-513.

- Feng, S., Fu, Y., & Xiao, Q. (2012). Trends in the global tropopause thickness revealed by radiosondes. *Geophysical Research Letters*. **39**,(L20706), 6. doi:10.1029/2012GL053460
- Fernandes, M. J., Lazaro, C., Ablain, M., & Pires, N. (2015). Improved wet path delays for all ESA and reference altimetric mission. *Remote Sensing of Environment*. **169**, 50-74.
- Gago, E. J., Roldan, J., Pacheco-Torres, R., & Ordóñez, J. (2013). The city and urban heat islands: A review of strategies to mitigate adverse effects. *Renewable and Sustainable Energy Reviews*. **25**, 749-758. doi:10.1016/j.rser.2013.05.057
- Gao, Y. (2006). GNSS solutions: Precise Point Positioning and its challenges. *Inside GNSS*(November/December), 16-18.
- Gao, Y., & Shen, X. (2002). A New Method for Carrier-Phase-Based Precise Point Positioning *Navigation*. **49**(2), 109-116.
- Gelb, A. (1974). *Applied Optimal Estimation*: MIT press.
- GMV. (2019). *Magic GNSS*. Retrieved from <https://magicgnss.gmv.com/>
- Golden, J. S., Carlson, J., Kaloush, K. E., & Phelan, P. (2007). A comparative study of the thermal and radiative impacts of photovoltaic canopies on pavement surface temperatures. *Solar Energy*. **81**(7), 872-883. doi:10.1016/j.solener.2006.11.007
- Google. (2019). *Gloogle Maps*. Retrieved from <https://www.google.com/permissions/geoguidelines/>
- Grimmond, C. S. B., Roth, M., Oke, T. R., Au, Y. C., Best, M., Betts, R., et al. (2010). Climate and More Sustainable Cities: Climate Information for Improved Planning and Management of Cities. *Environmental Sciences*. **1**, 247-272.
- Haase, J. S., Dautermann, T., Taylor, M. J., Chapagain, N., Calais, E., & Pautet, D. (2011). Propagation of plasma bubbles observed in Brazil from GPS and airglow data. *Advances in Space Research*. **47**(10), 1758-1776.
- Hall, C. M., Hansen, G., Sigerenes, F., & Kuyeng Ruiz, K. M. (2011). Tropopause height at 78 N 16 E: average seasonal variation 2007-2010. *Atmospheric Chemistry and Physics*. **11**, 5485--5490.
- Harris, R., & Coutts, A. (2011). Airborne Thermal Remote Sensing for Analysis of the Urban Heat Island. In *Victoria Center for Climate Change Research*.
- Heroux, P., & Kouba, J. (2001). GPS Precise Point Positioning Using IGS Orbit Products. *Physics and Chemistry of the Earth (A)*. **26**(6-8), 573-578.
- HKGSS. (2019). *Hong Kong Satellite Positioning Reference Station Network*. Retrieved from <https://www.geodetic.gov.hk/en/satref/satref.htm>
- Hoffmann, P., Krueger, O., & Schlünzen, K. H. (2012). A statistical model for the urban heat island and its application to a climate change scenario. *International Journal of Climatology*. **32**(8), 1238-1248. doi:10.1002/joc.2348
- Hofmann-Wellenhof, B., Lichtenegger, H., & Wasle, E. (2008). *GNSS-Global Navigation Satellite Systems GPS, Glonass, Galileo and more*. Vienna, Austria: Springer.

- Hoinka, K. P. (1998). Statistics of the Global Tropopause Pressure. *Monthly Weather Review*. **126**, 3303-3325.
- Hopfield, H. (1969). Two-quartic tropospheric refractivity profile for correcting satellite data. *Journal of Geophysical Research*. **74**, 4487-4499.
- Hu, L., & Brunsell, N. A. (2015). A new perspective to assess the urban heat island through remotely sensed atmospheric profiles. *Remote Sensing of Environment*. **158**, 393-406. doi:10.1016/j.rse.2014.10.022
- Ifadis, I. (1986). *The atmospheric delay of radio waves: Modelling the elevation dependence on a global scale*. Chalmers University of Technology, Göteborg Sweden.
- IGS. (2019). *IGS Network*. Retrieved from <http://www.igs.org/network>
- ISO. (1975). *International Standard Atmosphere*. In ISO/TC 20/SC 6.
- Jain, S. P., & Rao, K. R. (1974). Experimental Study on the Effect of Roof Spray Cooling on Unconditioned and Conditioned Buildings. *Building Science*. **9**(1), 9-16.
- Jauregui, E. (1997). Heat Island Development in Mexico City. *Atmospheric Environment*, **31**(22), 3821-3831.
- Jin, M. S. (2012). Developing an Index to Measure Urban Heat Island Effect Using Satellite Land Skin Temperature and Land Cover Observations. *Journal of Climate*. **25**(18), 6193-6201. doi:10.1175/jcli-d-11-00509.1
- Jin, S., Feng, G. P., & Gleason, S. (2011). Remote sensing using GNSS signals: Current status and future directions. *Advances in Space Research*. **47**, 1645-1653. doi:10.1016/j.asr.2011.01.036
- Jin, S. G., Luo, O. F., & Park, P. (2008). GPS observations of the Ionospheric F2 layer behavior during the 20th November 2003 geomagnetic storm over South Korea. *Journal of Geodesy*. **82**(12), 883-892.
- JPL. (2019). *The Automatic Precise Positioning Service*. Retrieved from <http://apps.gdgps.net/>
- Juan, J. M., Hernandez-Pajares, M., Sanz, J., Ramos-Bosch, P., Aragon-Angel, A., Orus, R., et al. (2012). Enhanced Precise Point Positioning for GNSS users. *IEEE Transactions on Geoscience and Remote Sensing*. **50**(10), 1--11.
- Kikegawa, Y., Genchi, Y., Yoshikado, H., & Kondo, H. (2003). Development of a numerical simulation system toward comprehensive assessments of urban warming countermeasures including their impacts upon the urban buildings' energy-demands. *Applied Energy*. **76**, 449-466. doi:10.1016/s0306-2619(03)00009-6
- Klysiak, K., & Fortuniak, K. (1999). Temporal and spatial characteristics of the urban heat island of Łódź, Poland. *Atmospheric Environment*. **33**, 3885-3895.
- Langley, R. (1998). Propagation of the GPS signals. In P. J. G. Teunissen & A. Kleusberg (Eds.), *GPS for Geodesy*. Berlin, Heidelberg: Springer.
- Leandro, R. (2009). *Precise Point Positioning with GPS: A new Approach for Positioning, Atmospheric Studies and Signal Analysis*. (PhD),

- University of New Brunswick, Fredericton, New Brunswick, Canada.
- Leandro, R., Langley, R., & Santos, M. (2007). Estimation of P2-C2 biases by means of Precise Point Positioning. Paper presented at the *ION annual meeting 2007*.
- Liang, J. (2013). *Chemical Modeling for Air Resources Fundamentals, applications and corroborative analysis*: Academic Press.
- McCarthy, D., & Pétit, G. (2004). IERS conventions (2003).
- Memon, R. A., Leung, D. Y. C., & Liu, C.-H. (2009). An investigation of urban heat island intensity (UHII) as an indicator of urban heating. *Atmospheric Research*. **94**(3), 491-500. doi:10.1016/j.atmosres.2009.07.006
- Mendes, V. (1999). *Modeling the neutral atmosphere propagation delay in radiometric space techniques*. (PhD), University of New Brunswick, Fredericton, New Brunswick, Canada.
- Mendes, V., & Langley, R. (1998, June 1-3, 1998). Tropospheric zenith delay prediction accuracy for airborne GPS high-precision positioning. Paper presented at the *Proceedings of the Institute of Navigation 54th annual meeting*, Denver, USA.
- Mendez Astudillo, J., Lau, L., Tang, Y. T., & Moore, T. (2018). Analysing the Zenith Tropospheric Delay Estimates in On-line Precise Point Positioning (PPP) Services and PPP Software Packages. *Sensors (Basel)*. **18**(2). doi:10.3390/s18020580
- Mohammed, J., Moore, T., Hill, C., Bingley, R. M., & Hansen, D. N. (2016). An assessment of static precise point positioning using GPS only, GLONASS only and GPS plus GLONASS. *Measurement*. **88**, 121-130.
- Moritz, H. (1972). *Advanced Least-Squares Methods*. Retrieved from: <https://earthsciences.osu.edu/sites/earthsciences.osu.edu/files/report-175.pdf>, Columbus, Ohio
- Moritz, H. (1978). Least-Squares Collocation. *Reviews of Geophysics and Space Physics*. **16**(3), 421-431.
- National Coordination Office for Space-Based Positioning, N., and Timing. (2019). GPS: The Global Positioning System. Retrieved from <https://www.gps.gov/systems/gps/space/>
- Niell, A. E. (2000). Improved atmospheric mapping functions for VLBI and GPS. *Earth Planets Space*. **52**, 699-702.
- NOAA. (2019). Integrated Global Radiosonde Archive (IGRA) Retrieved from <https://www.ncdc.noaa.gov/data-access/weather-balloon/integrated-global-radiosonde-archive>
- Nuruzzaman, M. (2015). Urban Heat Island: Causes, Effects and Mitigation Measures - A Review. *International Journal of Environmental Monitoring and Analysis*. **3**(2), 67. doi:10.11648/j.ijema.20150302.15
- Oke, T. R. (1976). The Distinction Between Canopy and Boundary-Layer Urban Heat Islands. *Atmosphere*. **14**(4). doi:10.1080/00046973.1976.9648422
- Peng, S., Piao, S., Ciais, P., Friedlingstein, P., Otle, C., Breon, F. M., et al. (2012). Surface urban heat island across 419 global big cities. *Environ Sci Technol*. **46**(2), 696-703. doi:10.1021/es2030438

- Pichierri, M., Bonafoni, S., & Biondi, R. (2012). Satellite air temperature estimation for monitoring the canopy layer heat island of Milan. *Remote Sensing of Environment*. **127**, 130-138. doi:10.1016/j.rse.2012.08.025
- EPA Atmospheric Programs (2017). *Reducing Urban Heat Islands: Compendium of Strategies. Urban Heat Island Basics*. Climate Protection Partnership Division in the U.S Retrieved from <https://goo.gl/1Ckkt9>
- Ramamurthy, P., & Sangobanwo, M. (2016). Inter-annual variability in urban heat island intensity over 10 major cities in the United States. *Sustainable Cities and Society*. **26**, 65-75.
- Rieckh, T., Scherllin-Pirscher, B., Ladstädter, F., & Foelsche, U. (2014). Characteristics of tropopause parameters as observed with GPS radio occultation. *Atmospheric Measurement Techniques*. **7**, 3847-3958.
- Rizwan, A. M., Dennis, L. Y. C., & Liu, C. (2008). A review on the generation, determination and mitigation of Urban Heat Island. *Journal of Environmental Sciences*. **20**(1), 120-128. doi:10.1016/s1001-0742(08)60019-4
- Rocken, C., van Hove, T., Johnson, J., Solheim, F., Ware, R., Bevis, M., et al. (1995). GPS/STORM-GPS sensing of atmospheric water vapor for meteorology. *Journal of Atmospheric and Oceanic Technologies*. **12**, 468-478.
- Roth, M. (2013). Urban Heat Island. In H. J. S. Fernando (Ed.), *Handbook of Environmental Fluid Dynamics* (Vol. II, pp. 143-159): Taylor & Francis Group.
- Saastamoinen, J. (1972). Atmospheric correction for the troposphere and stratosphere in radio ranging of satellites. In *The use of artificial satellites for Geodesy* (Vol. 15, pp. 247-251): AGU.
- Sanz Subirana, J., Juan Zornoza, J. M., & Hernandez-Pajares, M. (2013a). *GNSS Data Processing Volume II: Laboratory Exercises* (Vol. 2). Noordwijk, The Netherlands: ESA communications.
- Sanz Subirana, J., Juan Zornoza, J. M., & Hernandez-Pajares, M. (2013b). *GNSS Data Processing: Volume I, Fundamentals and Algorithms* (Vol. 1). Noordwijk, The Netherlands: ESA communications.
- Schwarz, N., Lautenbach, S., & Seppelt, R. (2011). Exploring indicators for quantifying surface urban heat islands of European cities with MODIS land surface temperatures. *Remote Sensing of Environment*. **115**(12), 3175-3186. doi:10.1016/j.rse.2011.07.003
- Seeber, G. (2008). *Satellite Geodesy Foundations, Methods and Applications* (2nd ed.): de Gruyter
- Seidel, D. J., & Randel, W. J. (2006). Variability and trends in the global tropopause estimated from radiosonde data *Journal of Geophysical Research*. **11**.
- Shahmohamadi, P., Che-Ani, A. I., Maulud, K. N. A., Tawil, N. M., & Abdullah, N. A. G. (2011). The Impact of Anthropogenic Heat on Formation of Urban Heat Island and Energy Consumption Balance. *Urban Studies Research*, **2011**, 1-9. doi:10.1155/2011/497524

- Smith, E., & Weintraub, S. (1953). The constants in the equation of atmospheric refractive index at radio frequencies. *Proceedings of the Institute of Radio Engineers*. **41**(8), 1035-1037.
- Speight, J. G. (2017). *Environmental organic chemistry for engineers*. Amsterdam Boston: Elsevier/Butterworth-Heinemann.
- Streutker, D. R. (2003). Satellite-measured growth of the urban heat island of Houston, Texas. *Remote Sensing of Environment*. **85**, 282-289. doi:10.1016/s0034-4257(03)00007-5
- BeiDou Navigation System (2019). *BeiDou Navigation Satellite System*. Retrieved from <http://en.beidou.gov.cn/>
- Szymanowski, M., & Kryza, M. (2011, April 11-13). Application of remotely sensed data for spatial approximation of urban heat island in the city of Wroclaw, Poland. Paper presented at *the Joint Urban Remote Sensing Event*, Munich, Germany.
- Takebayashi, H., & Moriyama, M. (2007). Surface heat budget on green roof and high reflection roof for mitigation of urban heat island. *Building and Environment*. **42**(8), 2971-2979. doi:10.1016/j.buildenv.2006.06.017
- Thayer, G. (1974). An improved equation for the radio refractive index of air. *Radio Science*. **9**, 211-222. doi:<https://doi.org/10.1029/RS009i010p00803>
- Tolman, B. W. (2008). GPS Precise Absolute Positioning via Kalman Filtering. Paper presented at *The ION GNSS 21st International technical meeting of the satellite division*, Savannah, GA.
- Weather Underground. (2019). *Sensor Network*. Retrieved from <https://www.wunderground.com/weatherstation/overview.asp>
- Unger, J., Gál, T., Rakonczai, J., Mucsi, L., Szatmári, J., Tobak, Z., et al. (2010). Modeling of the urban heat island pattern based on the relationship between surface and air temperatures. *Quarterly Journal of the Hungarian Meteorological Service*. **114**(4), 287-302.
- Vedel, H., Mogensen, K. S., & Huang, X.-Y. (2001). Calculation of zenith delays from meteorological data comparison of NWP model, radiosonde and GPS delays. *Physics and Chemistry of the Earth (A)*. **26**(6-8), 497-502.
- Voogt, J. A. (2014). How Researchers Measure Urban Heat Islands. In University of Western Ontario (Ed.), *Department of Geography*. London, Canada: University of Western Ontario.
- Wahr, J. M. (1981). The forced nutation of an elliptical, rotating, elastic, and oceanless Earth. *Geophysical Journal Royal Astronomical Society*. **64**, 705-727.
- Wai Siu, L., & Hart, M. A. (2013). Quantifying urban heat island intensity in Hong Kong SAR, China. *Environment Monitoring Assessment*. **185**, 4383-4398.
- Wang, L., & Xu, H.-q. (2008). Study on the Information Extraction of Evapotranspiration and Its Relation with the Urban Heat Island and Urban Expansion in Fuzhou City with Its Surrounding Areas of SE China. Paper presented at the *International Workshop on Earth Observation and Remote Sensing Applications*.
- Wilgan, K., Hurter, F., Geiger, A., Rohm, W., & Bosy, J. (2016). Tropospheric refractivity and zenith path delays from least-square

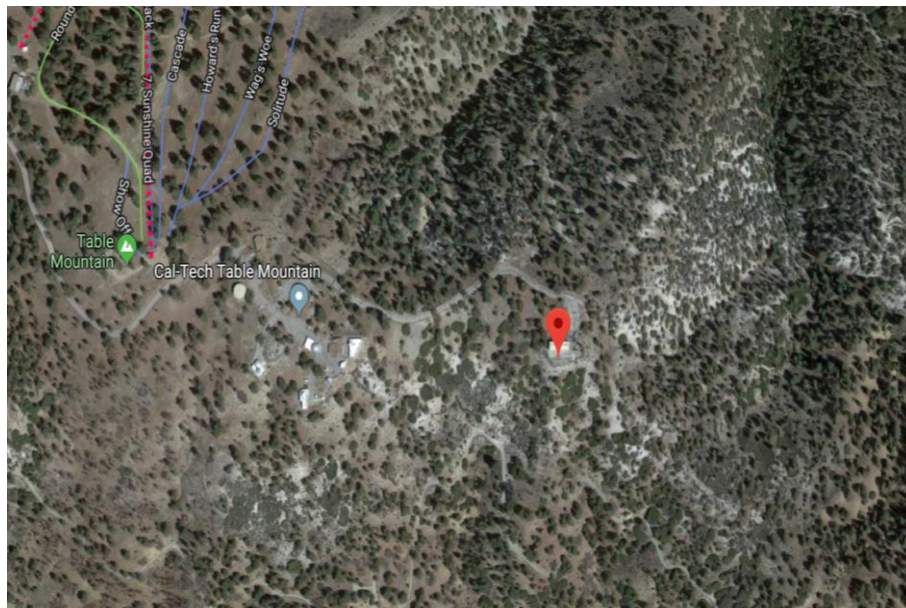
- collocation of meteorological and GNSS data. *Journal of Geodesy*. **91**(2), 1-18.
- WMO. (1957). *Lapse rate tropopause*. In: World Meteorological Organization.
- Wu, J. T., Wu, S. C., Hajj, G. A., Bertiger, W. I., & Lichten, S. M. (1993). Effects of antenna orientation on GPS carrier phase. *Manuscripta geodetica*. **18**, 91-98.
- Younes, S. A.-M. (2016). Modeling investigation of wet tropospheric delay error and precipitable water vapor content in Egypt. *The Egyptian Journal of Remote Sensing and Space Sciences*. **19**, 333-342.
- Yu, C., & Hien, W. N. (2006). Thermal benefits of city parks. *Energy and Buildings*. **38**(2), 105-120. doi:10.1016/j.enbuild.2005.04.003
- Yu, K., Rizos, C., Burrage, D., Dempster, A. G., Zhang, K., & Markgraf, M. (2014). An overview of GNSS remote sensing. *EURASIP Journal on Advances in Signal Processing*. **2014**(134).
- Zumberge, J. F., Heflin, M. B., Jefferson, D. C., Watkins, M. M., & Webb, F. H. (1997). Precise point positioning for the efficient and robust analysis of GPS data from large networks. *Geophysical Research*. **12**, 5005-5017.

# APPENDIX 1

## Classification of environment around GNSS stations in LA



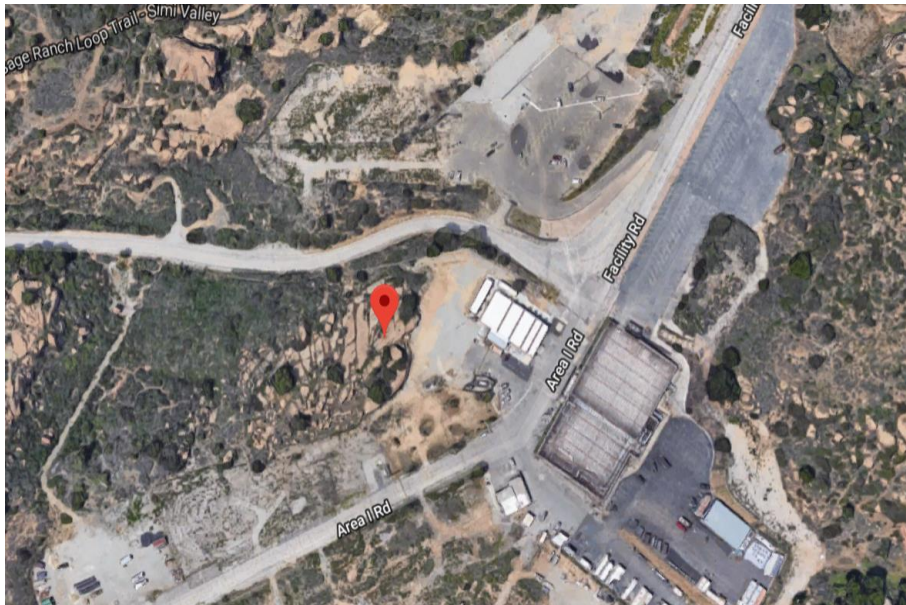
SFDM is located near some built structures, near a water-body and high in the mountain. Therefore, it is considered to be in a rural area



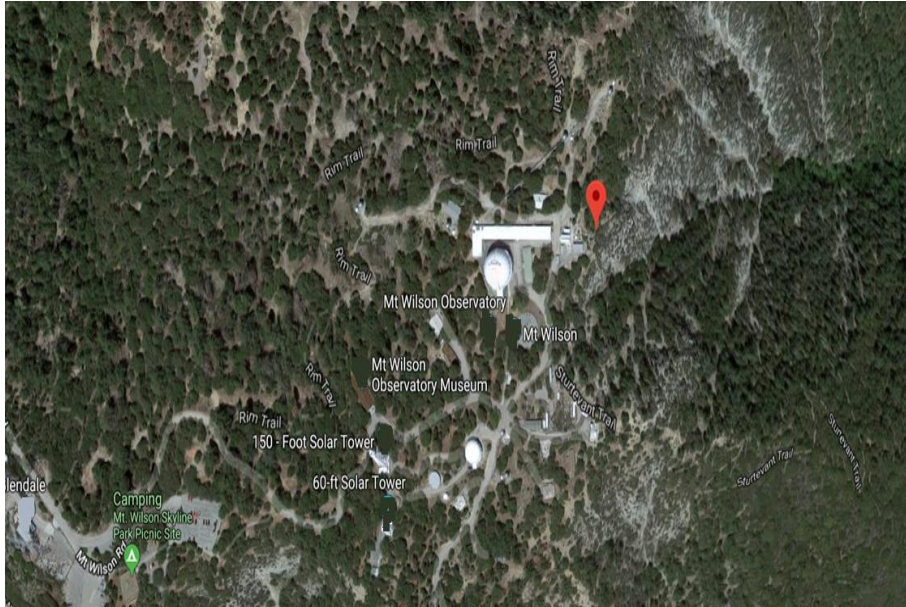
TABL is in a rural area. Surrounded by nature on top of a mountain



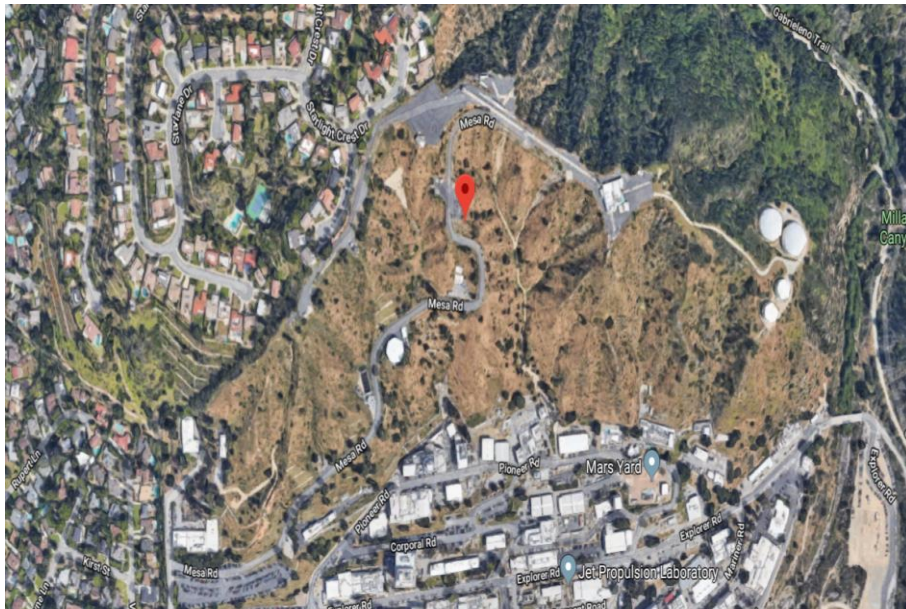
CMP9 is in a rural area. Surrounded by nature in a mountain top site.



ROCK is classified as being in a rural area as it is surrounded by nature.



WLSN: is on top of Mount Wilson, and is therefore classified as a rural area



JPLM. Rural area, empty surroundings

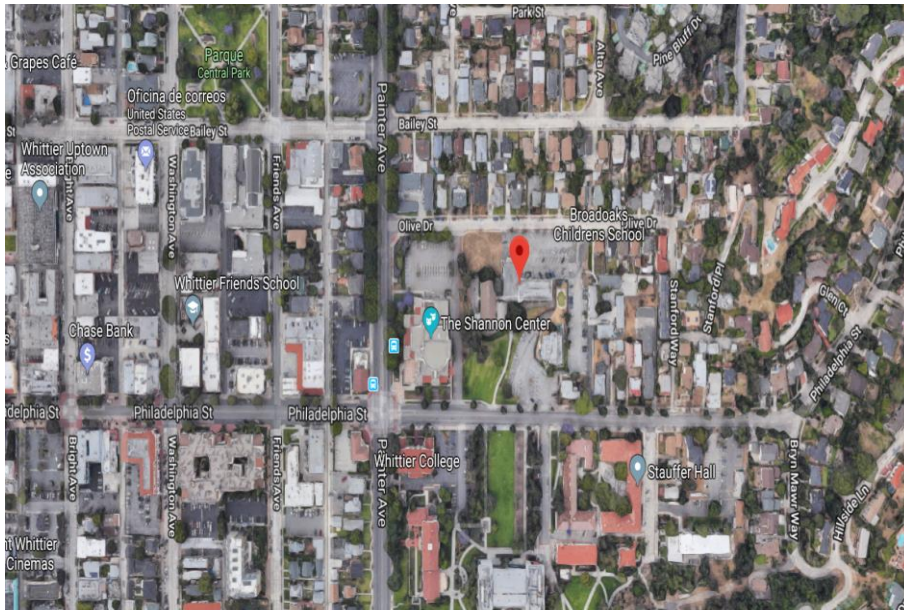




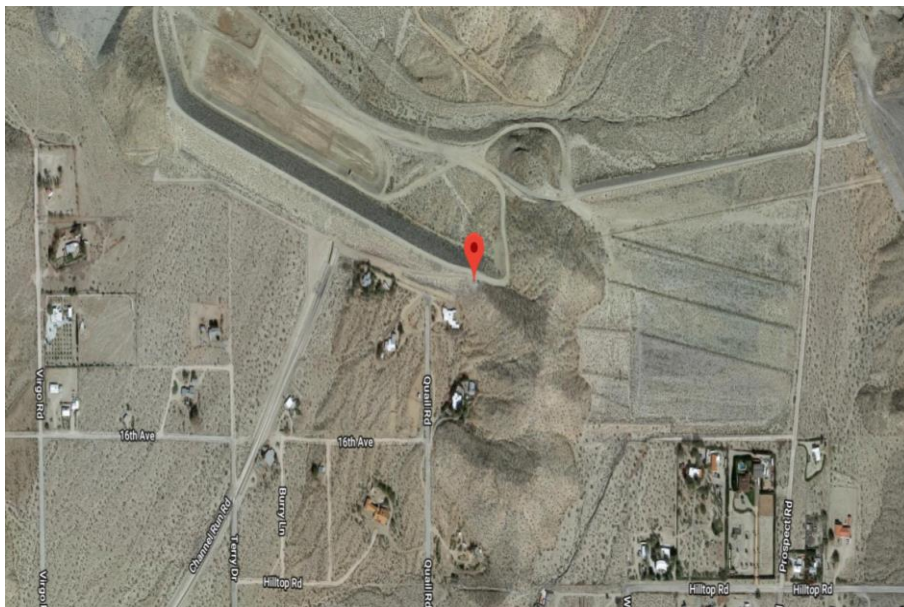
SPK1: rural area, surrounded by nature



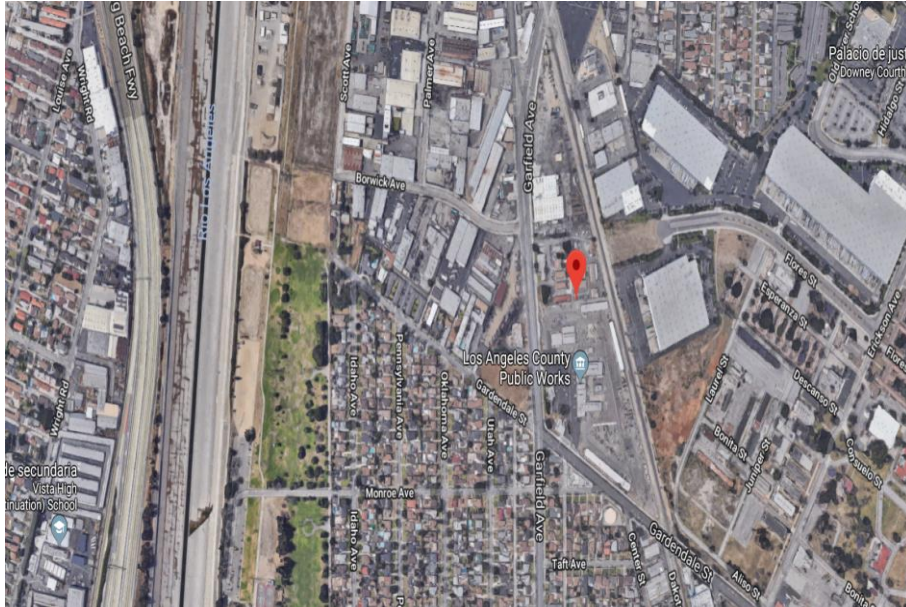
CRFP: rural area, the receiver is surrounded by only a few buildings



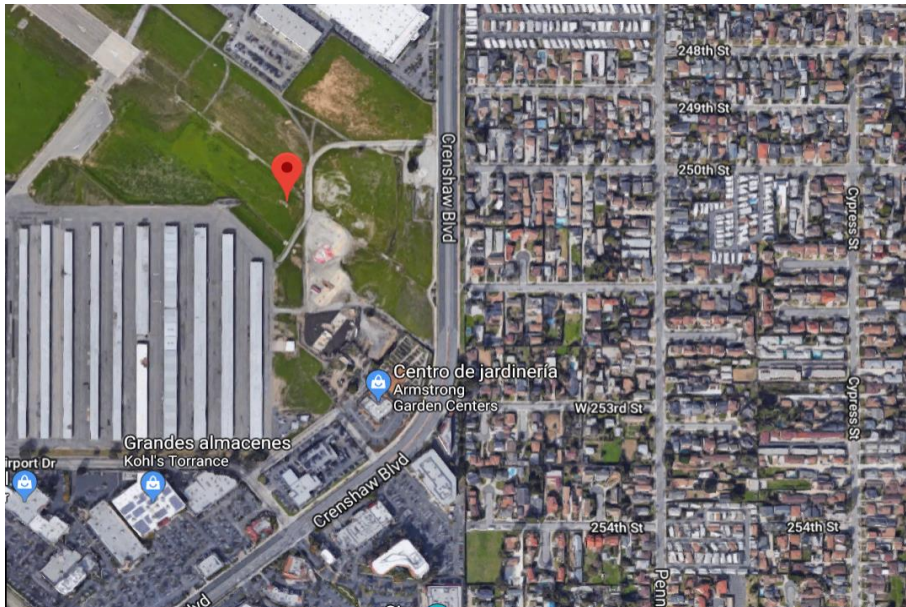
WHC1:  
urban area,  
as the  
receiver is  
surrounded  
by buildings



WIDC: rural  
area.  
Receiver  
surrounded  
by nature



HOLP:  
 urban area.  
 Receiver  
 surrounded  
 by buildings  
 in the city



TORP: rural,  
 the receiver  
 is located in  
 an airport

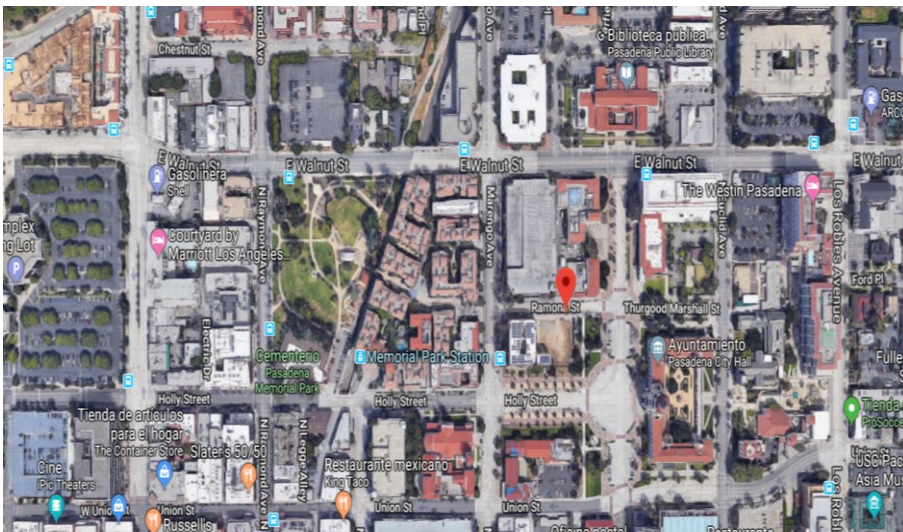


# APPENDIX 2

## Classification of surroundings of meteorological stations in LA

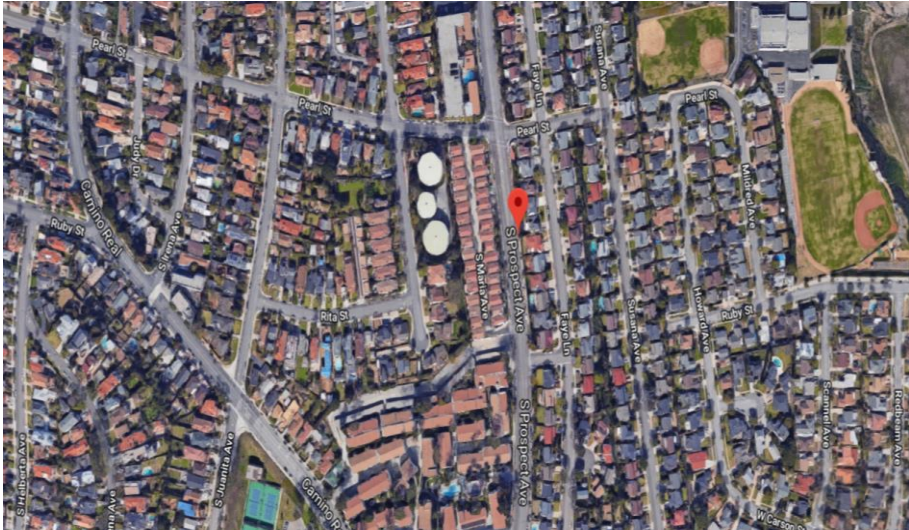


USC00046006:  
rural,  
surrounded by  
nature

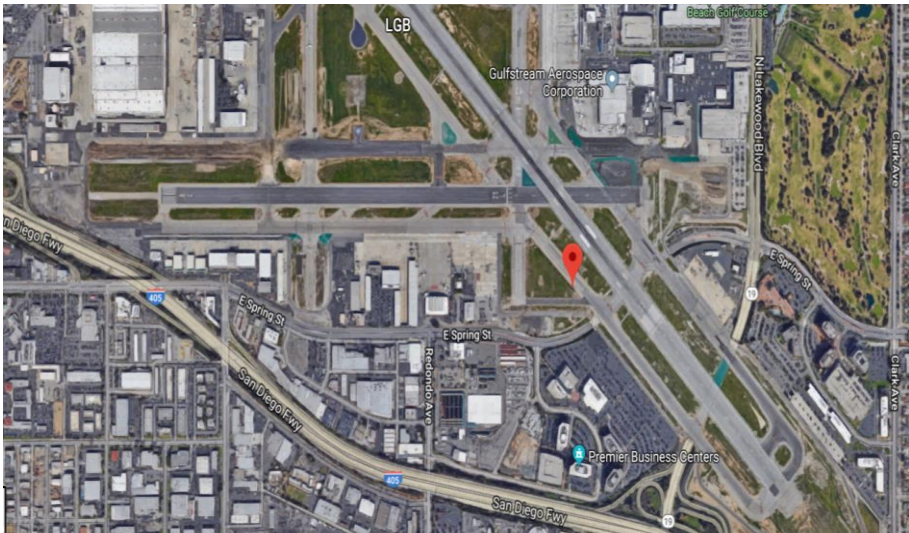


USC00046719:  
urban. The  
sensor is  
surrounded by  
buildings





USC00047326:  
urban area,  
surrounded by  
buildings



USW00023129  
: urban, as the  
receiver is in an  
airport

# APPENDIX 3

Classification of GNSS station in Hong Kong according to their surroundings.



HKCL.  
Rural area because of open space



HKFN/t430:  
urban area because it is surrounded by built structures



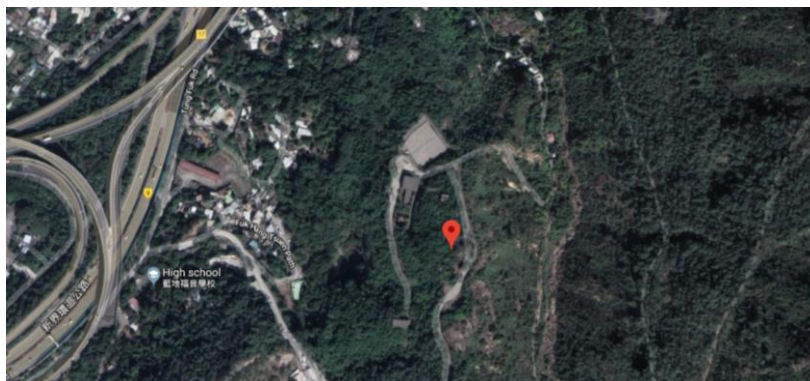
HKKS:  
Station surrounded by nature. Therefore, rural area



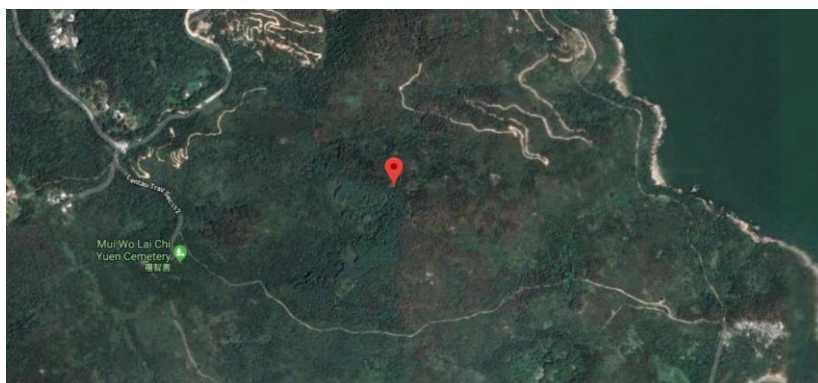
HKKT: rural as it is in a park surrounded by nature



HKLM: near a body of water and nature, therefore, rural



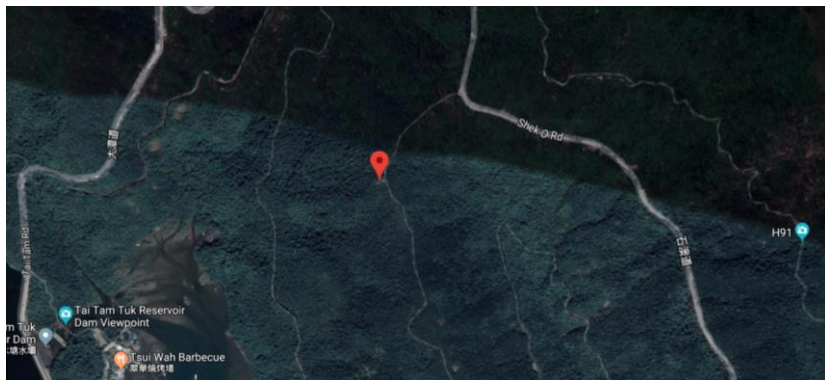
HKLT: the station is surrounded by nature; therefore, it is a rural station



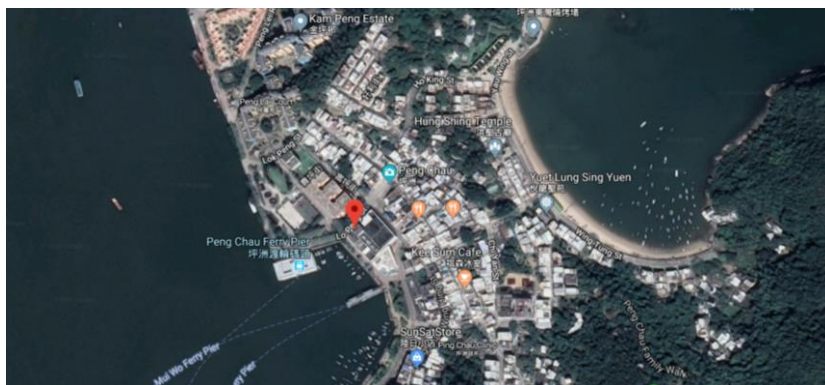
HKMW: station in a rural area, as no built structures are near



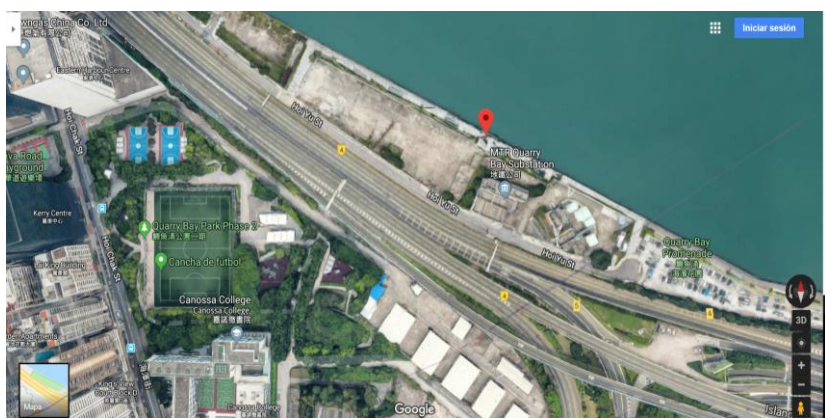
HKPN:  
station is in  
a rural area  
surrounded  
by nature



HKOH:  
station  
surrounded  
by nature,  
therefore is  
in a rural  
area



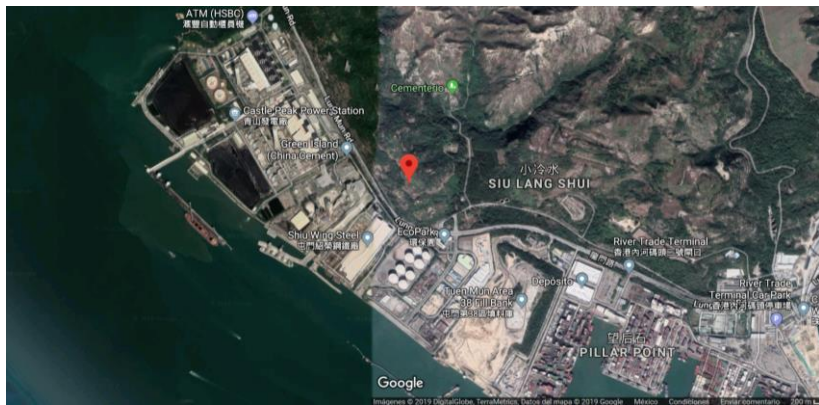
HKPC:  
station is in  
a port, near  
built  
structures  
so  
considered  
to be in an  
urban area



HKQT:  
considered  
to be in an  
urban area  
because of  
built  
structures  
nearby



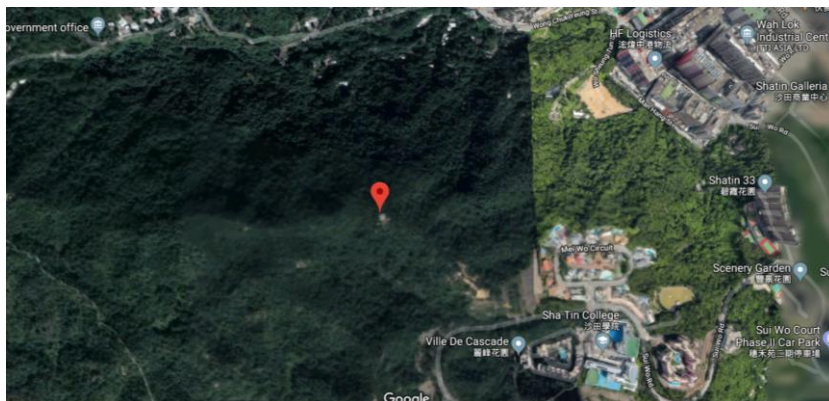
HKSC:  
 considered to be in an urban setting because it is near built structures



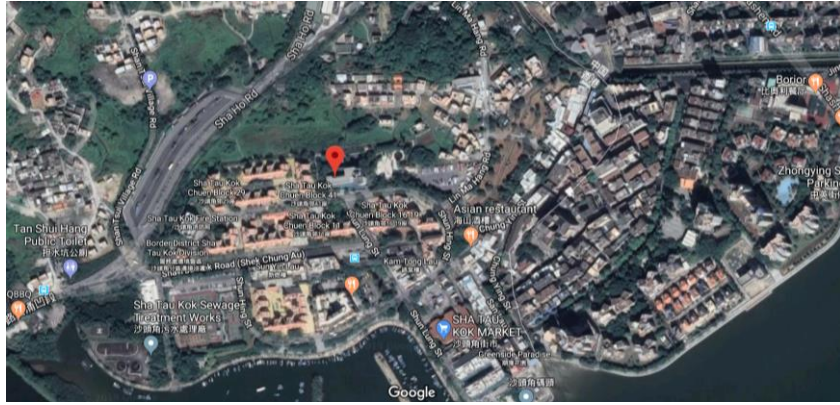
HKSL:  
 station is on a hill, therefore considered to be in a rural area



HKSS:  
 urban area because it is surrounded by nature



HKST:  
 station is on a mountain surrounded by nature, therefore classified as rural



**HKTK:**  
 station is in  
 an urban  
 area  
 because it is  
 surrounded  
 by tall  
 buildings



**HKWS:**  
 station is  
 considered  
 to be a rural  
 area  
 because it is  
 surrounded  
 by nature.